frontiers | Research Topics

PET/CT and MRI in prostate cancer

Edited by
Fabio Grizzi and Gianluigi Taverna

Published in
Frontiers in Oncology

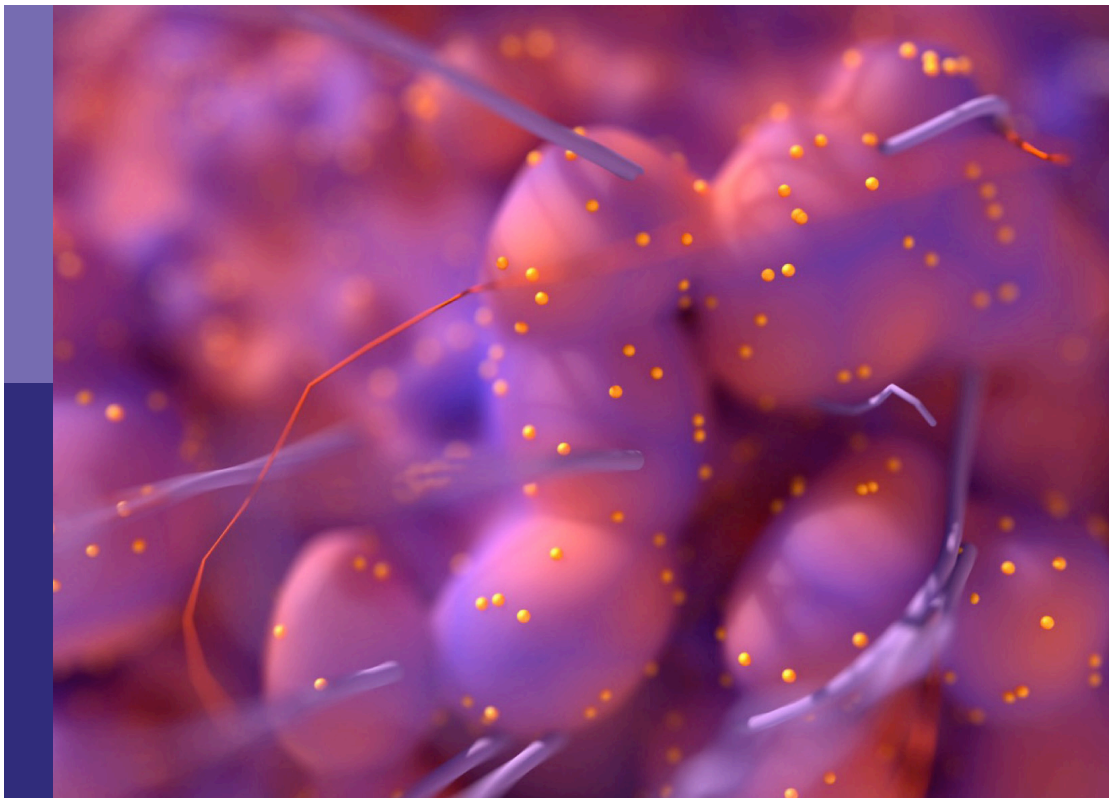

ISSN 1664-8714
ISBN 978-2-8325-4984-1
DOI 10.3389/978-2-8325-4984-1

About Frontiers

Frontiers is more than just an open access publisher of scholarly articles: it is a pioneering approach to the world of academia, radically improving the way scholarly research is managed. The grand vision of Frontiers is a world where all people have an equal opportunity to seek, share and generate knowledge. Frontiers provides immediate and permanent online open access to all its publications, but this alone is not enough to realize our grand goals.

Frontiers journal series

The Frontiers journal series is a multi-tier and interdisciplinary set of open-access, online journals, promising a paradigm shift from the current review, selection and dissemination processes in academic publishing. All Frontiers journals are driven by researchers for researchers; therefore, they constitute a service to the scholarly community. At the same time, the *Frontiers journal series* operates on a revolutionary invention, the tiered publishing system, initially addressing specific communities of scholars, and gradually climbing up to broader public understanding, thus serving the interests of the lay society, too.

Dedication to quality

Each Frontiers article is a landmark of the highest quality, thanks to genuinely collaborative interactions between authors and review editors, who include some of the world's best academicians. Research must be certified by peers before entering a stream of knowledge that may eventually reach the public - and shape society; therefore, Frontiers only applies the most rigorous and unbiased reviews. Frontiers revolutionizes research publishing by freely delivering the most outstanding research, evaluated with no bias from both the academic and social point of view. By applying the most advanced information technologies, Frontiers is catapulting scholarly publishing into a new generation.

What are Frontiers Research Topics?

Frontiers Research Topics are very popular trademarks of the *Frontiers journals series*: they are collections of at least ten articles, all centered on a particular subject. With their unique mix of varied contributions from Original Research to Review Articles, Frontiers Research Topics unify the most influential researchers, the latest key findings and historical advances in a hot research area.

Find out more on how to host your own Frontiers Research Topic or contribute to one as an author by contacting the Frontiers editorial office: frontiersin.org/about/contact

PET/CT and MRI in prostate cancer

Topic editors

Fabio Grizzi – Humanitas Research Hospital, Italy

Gianluigi Taverna – Humanitas Research Hospital, Italy

Citation

Grizzi, F., Taverna, G., eds. (2024). *PET/CT and MRI in prostate cancer*. Lausanne: Frontiers Media SA. doi: 10.3389/978-2-8325-4984-1

Table of contents

05 Editorial: PET/CT and MRI in prostate cancer
Fabio Grizzi and Gianluigi Taverna

12 A Pilot Study of ^{18}F-DCFPyL PET/CT or PET/MRI and Ultrasound Fusion Targeted Prostate Biopsy for Intra-Prostatic PET-Positive Lesions
Yachao Liu, Hongkai Yu, Jiajin Liu, Xiaojun Zhang, Mu Lin, Holger Schmidt, Jiangping Gao and Baixuan Xu

21 Whole-Body MRI vs. PET/CT for the Detection of Bone Metastases in Patients With Prostate Cancer: A Systematic Review and Meta-Analysis
Yuefu Zhan, Guangming Zhang, Mingliang Li and Xiaobo Zhou

29 Safety profile of robotic-assisted transperineal MRI-US-fusion guided biopsy of the prostate
Manuel Walter, Pawel Trotsenko, Hanns-Christian Breit, Nicola Keller, Anja Meyer, David Jean Winkel, Hans Helge Seifert and Christian Wetterauer

36 Study of iron metabolism based on T2* mapping sequences in PI-RADS 3 prostate lesions
Wenhao D, Guangzheng L, Zhen T, Xuedong W, Yonggang L, Xuefeng Z, Weijie Z, Gang L and Yuhua H

44 Multiparametric magnetic resonance imaging for the differential diagnosis between granulomatous prostatitis and prostate cancer: a literature review to an intriguing diagnostic challenge
Caterina Gaudiano, Benedetta Renzetti, Cristina De Fino, Beniamino Corcioni, Federica Ciccarese, Lorenzo Bianchi, Riccardo Schiavina, Matteo Droghetti, Francesca Giunchi, Eugenio Brunocilla and Michelangelo Fiorentino

53 ^{68}Ga-PSMA-11 PET/CT versus ^{68}Ga-PSMA-11 PET/MRI for the detection of biochemically recurrent prostate cancer: a systematic review and meta-analysis
Ruizhe Huang, Yizhen Li, Haowen Wu, Boyi Liu, Xuanjun Zhang and Zhongxi Zhang

68 Pelvic PET/MR attenuation correction in the image space using deep learning
Bendik Skarre Abrahamsen, Ingerid Skjei Knudtsen, Live Eikenes, Tone Frost Bathen and Mattijs Elschot

78 Improving diagnostic efficacy of primary prostate cancer with combined ^{99m}Tc-PSMA SPECT/CT and multiparametric-MRI and quantitative parameters
Yu Zhang, Yuanying Shi, Liefu Ye, Tao Li, Yongbao Wei, Zhiyi Lin and Wenxin Chen

89 A classifier model for prostate cancer diagnosis using CNNs and transfer learning with multi-parametric MRI
Mubashar Mehmood, Sadam Hussain Abbasi, Khursheed Aurangzeb, Muhammad Faran Majeed, Muhammad Shahid Anwar and Musaed Alhussein

102 Magnetic resonance imaging radiomics-based prediction of clinically significant prostate cancer in equivocal PI-RADS 3 lesions in the transitional zone
Ying-Ying Zhao, Mei-Lian Xiong, Yue-Feng Liu, Li-Juan Duan, Jia-Li Chen, Zhen Xing, Yan-Shun Lin and Tan-Hui Chen

115 Multimodal data integration for predicting progression risk in castration-resistant prostate cancer using deep learning: a multicenter retrospective study
Chuan Zhou, Yun-Feng Zhang, Sheng Guo, Yu-Qian Huang, Xiao-Ni Qiao, Rong Wang, Lian-Ping Zhao, De-Hui Chang, Li-Ming Zhao, Ming-Xu Da and Feng-Hai Zhou

frontiers | Frontiers in Oncology

TYPE Editorial
PUBLISHED 24 May 2024
DOI 10.3389/fonc.2024.1421542

OPEN ACCESS

EDITED AND REVIEWED BY
Ronald M. Bukowski,
Cleveland Clinic, United States

*CORRESPONDENCE
Fabio Grizzi
fabio.grizzi@humanitasresearch.it
Gianluigi Taverna
gianluigi.taverna@humanitas.it

RECEIVED 22 April 2024
ACCEPTED 24 April 2024
PUBLISHED 24 May 2024

CITATION
Grizzi F and Taverna G (2024) Editorial: PET/CT and MRI in prostate cancer. *Front. Oncol.* 14:1421542. doi: 10.3389/fonc.2024.1421542

Editorial: PET/CT and MRI in prostate cancer

Fabio Grizzi[1,2]* and Gianluigi Taverna[3]*

[1]Department of Immunology and Inflammation, IRCCS Humanitas Research Hospital, Milan, Italy, [2]Department of Biomedical Sciences, Humanitas University, Milan, Italy, [3]Department of Urology, Humanitas Mater Domini, Castellanza, Varese, Italy

KEYWORDS

prostate cancer, diagnosis, PET/CT, MRI, artificial intelligence

Editorial on the Research Topic
PET/CT and MRI in prostate cancer

Prostate cancer (PCa) represents one of the leading causes of cancer-related mortality (1). Age, African ancestry, and a family history of PCa are widely recognized as established risk factors (2). PCa exhibits a wide spectrum of aggressiveness, ranging from slow-growing to highly life-threatening. Large-scale trials have demonstrated that low-grade PCa (grade group 1) is associated with a very low risk of cancer-specific death. On the other hand, cancers classified in grade groups 3 through 5 display significantly higher metastatic potential and accounted for the majority of the estimated deaths from PCa (3). This diversity in the lethality of different PCa subtypes underscores the critical need for precise and accurate diagnosis of PCa. At diagnosis, 13% of PCa patients will have regional lymph node involvement and 8% will have distant metastasis (4). The most common site of metastatic PCa (mPCa) involvement is the bone, accounting for up to 90% of mPCa. Visceral organ involvement, such as in the lung, liver, adrenal gland, and brain, is less common. When compared to localized PCa, the 5-year survival rate of mPCa declines significantly from 100% to 34.1%. Early detection of mPCa is crucial for treatment. The U.S. Food and Drug Administration (FDA) sanctioned the assessment of prostate-specific antigen (PSA), a protein discharged by both healthy and cancerous prostate cells, in 1986 (5). Initially authorized for tracking patients with confirmed PCa, it was later endorsed in 1994 to assist in detecting PCa alongside digital rectal examination (DRE) in individuals aged 50 and above. Recently, screening for PCa using serum PSA has come under considerable criticism due to several trials demonstrating that using PSA serum levels often leads to overdiagnosis and overtreatment, as well as the inability to accurately differentiate between low-, intermediate-, and high-risk aggressive disease. PCa diagnosis is currently based on the gold standard invasive procedure of transrectal ultrasound (TRUS)-guided needle biopsy of the prostate. The diagnostic biopsy is informed by the combination of any of the following: elevated PSA serum levels, PSA kinetics, abnormal DRE, family history, race, or abnormal previous biopsy. Gleason score, cancer stage, and cancer core information are all obtained from biopsy, and frequent or periodic biopsies are not amenable for patients. Individuals with elevated PSA levels upon screening have the option to pursue additional examinations to determine the necessity for biopsy, multiparametric magnetic resonance imaging (MRI) to pinpoint biopsy sites, or both. Those diagnosed with low-risk or favorable intermediate-risk PCa may opt for active surveillance, involving periodic PSA tests and biopsies, instead of immediate curative

treatments such as surgery or radiation therapy (5). Using a 12-core systematic prostate biopsy tends to yield inaccuracies in diagnosis, leading to both overdiagnosis and underdiagnosis of prostate cancer (3). Employing MRI targeting during biopsies can potentially mitigate the misclassification of PCa, especially in men with MRI-visible lesions. In patients displaying MRI-visible lesions, utilizing a combined biopsy approach resulted in increased detection of PCa. Nevertheless, relying solely on MRI-targeted biopsy led to an underestimation of the histologic grade for certain tumors. Following radical prostatectomy, the occurrence of upgrades to grade group 3 or higher during histopathological analysis was notably reduced after implementing combined biopsy techniques (3). The European Association of Nuclear Medicine (EANM) has recently introduced a molecular imaging TNM (miTNM) classification utilizing prostate-specific membrane antigen (PSMA) positron emission tomography (PET) scan/computed tomography (CT) observations (6). It is anticipated that the prognosis of the miT, miN, and miM substages will likely be more favorable compared to their conventional T, N, and M counterparts due to the enhanced sensitivity of PSMA PET/CT over standard bone scans and abdominopelvic CT scans. However, the extent of this prognostic improvement and its practical significance and implications remain to be thoroughly evaluated. MRI of the prostate has been, however, recommended as the initial diagnostic test for men presenting with suspected PCa, with a negative MRI enabling safe avoidance of biopsy and a positive result enabling MRI-directed sampling of lesions (7). Evidence supports the role of the MRI-directed pathway for PCa diagnosis, with improved performance over the previous clinical standard of systematic TRUS needle biopsy of the prostate. In terms of localizing the primary tumor for diagnostic biopsy, MRI prior to biopsy is becoming common practice to identify more clinically significant PCa (International Society of Urological Pathology [ISUP] grade group ≥2) and reduce the diagnosis of non-clinically significant disease (8). The main role of prostate MRI is to detect only clinically significant PCa. The prevalence of clinically significant PCa in men referred to urology clinics has been reported as ~30%, indicating that a substantial proportion of patients might unnecessarily undergo an invasive biopsy procedure; however, a negative MRI would enable up to half of these patients to safely avoid biopsy (9). Conversely, a positive MRI can directly target tumor lesions to provide pathologically accurate tissue sampling (9). The negative predictive value (NPV) of MRI is high (~90%) and has little variability among centers, whereas a comparatively low positive predictive value (PPV) of 17%, 46%, and 75% has been reported for lesions with a Prostate Imaging- Reporting and Data System (PI-RADS) score of 3, 4, and 5, respectively (9). MRI lesions are assessed using the PI-RADS score, ranging from 1 to 5. Higher scores signify lesions that are more clinically suspicious, aiding in the stratification of PCa risk. Prostate MRI, when interpreted using the PI-RADS, enhances the initial detection of clinically significant PCa (csPCa) compared to standard biopsy, thus aiding in the reduction of overdiagnosis. However, despite these benefits, approximately 15% of csPCa cases may still evade detection. Additionally, the PPV of PI-RADS can vary among different institutions. To tackle these challenges effectively, strategies must be implemented to minimize interobserver variability in interpretation. Recognizing the evolving demands in prostate MRI interpretation, specialized scoring systems have emerged beyond PI-RADS to address specific scenarios and unmet needs. Examples include the Prostate Imaging Quality (PI-QUAL) score, designed for assessing the image quality of mpMRI examinations. Additionally, the Prostate Cancer Radiologic Estimation of Change in Sequential Evaluation (PRECISE) recommendations offer guidance for evaluating serial mpMRI examinations during active surveillance. For assessing local recurrence after radical prostatectomy or radiation therapy, the Prostate Imaging for Recurrence Reporting System (PI-RR) score is utilized, while the Prostate Imaging after Focal Ablation (PI-FAB) score is employed to assess local recurrence after focal therapy. These specialized scoring systems cater to specific clinical scenarios, providing tailored and comprehensive evaluation methods beyond the scope of traditional PI-RADS (10). It has been shown that MRI performs best as a rule- out test; however, results from studies in which MRI-detected lesions were compared with histopathology on prostatectomy specimens showed that 8–24% of Grade Group 2 PCa might be MRI occult (9), which could mainly be ascribed to technical limitations, the presence of cribriform glands, and/or a sparse pattern of tumor growth. It has been reported that the diagnostic strategy involving PSAs low sensitivity, the invasiveness of prostate biopsy sampling, and the variability in performing and interpreting MRI is constrained by various factors. Successful implementation of this approach necessitates experienced clinicians, optimized equipment, effective interdisciplinary communication, and standardized workflows. Each component of the pathway must be carefully executed to achieve the anticipated results. PCa can vary tremendously in its clinical behavior and response to treatment. Due to this and its substantial global incidence, there is an ongoing need for improved diagnostic, risk-stratification, and therapeutic approaches to optimize patient outcomes. PSMA PET has begun to revolutionize the landscape of PCa management from both a diagnostic and therapeutic perspective. PSMA, a transmembrane glycoprotein (11), was initially identified on prostate cells in 1987 (12) and cloned and characterized in 1993 (13). It was further noted to be preferentially expressed on malignant versus benign prostate cells, prompting researchers to develop it as a target for molecular imaging and theranostic applications (14). The expression of PSMA in tumors is, however, absent in 15–20% of men diagnosed with castration-resistant prostate cancer (CRPC), but the precise mechanisms behind this phenomenon are still unclear (15). PSMA PET has evolved as an imaging tool capable of driving more accurate and targeted approaches to PCa management. Recently, Weiner et al. detailed the historical development and contemporary impact of PSMA PET in PCa care, highlighting the advancements made and promising future directions which will be guided by clinical trials (16). In a pooled analysis of multiple prospective studies, Kawada et al. (17) showed PSMA PET increased sensitivity for detecting csPCa from 84 to 91% compared to MRI alone. Prior work has shown that PSMA PET is better able to detect more PCa in patients with biochemical recurrence compared to Choline- or Fluciclovine-based PET after

primary radiation or surgery (18, 19). Specifically, when the PSA is ≤0.5 ng/mL in these patients, the detection rate is only 12.5% for Choline-based PET and 50% for PSMA PET. In a similarly designed prospective study of patients with PSA 0.2-2.0 ng/mL following surgery for PCa, the detection rate for Fluciclovine-based PET was 26%, while PSMA-based PET detected PCa in 56% (18). Additional phase III trials are required to further investigate whether PSMA PET imaging can effectively guide patients in avoiding unnecessary prostate biopsies.

Recent years have witnessed substantial progress in leveraging artificial intelligence (AI) and computer-aided diagnosis to enhance the diagnosis of PCa, encompassing both radiological and histological domains (Figure 1). These AI-based tools have demonstrated potential in enhancing the efficiency and precision of radiologists by streamlining or enhancing human workflow. Likewise, longstanding challenges in PCa histopathology, such as limited interobserver and intraobserver agreement in measurements and Gleason grading, are being addressed through the integration of these innovative techniques (20–23).

This Research Topic has provided an open discussion of how PET/CT and MRI impact the diagnosis of PCa. Liu et al. evaluated the feasibility and diagnostic performance of PSMA based 18F-DCFPyL PET/CT-ultrasound (PET/CT-US) or PET/MRI-ultrasound (PET/MRI-US) fusion targeted biopsy for intra-prostatic PET-positive lesions. From April 2018 to November 2019, they prospectively enrolled 55 subjects to perform PET/CT-US or PET/MRI-US fusion targeted biopsies for solitary PET-positive prostate lesions (two to four cores/lesion). The positive rates of PCa based on patients and biopsy cores were calculated respectively. With reference to the pathological results of biopsy cores, the MR signal characteristics in the area of the PET-positive lesion were analyzed for the patients who underwent PET/MRI. One hundred forty-six biopsy cores (82.0%) from 51 (92.7%) patients were positive for PCa; 47 (85.5%) were positive for csPCa. It is noteworthy that nine patients underwent both 18F-DCFPyL PET/CT and PET/MRI examinations; the seven patients with PCa showed abnormal MR signal in the area of the PET-positive lesion while the other two patients with prostatic hyperplasia and prostatitis showed normal MR signal in the area of the PET-positive lesion. This study indicated that 18F-DCFPyL PET/CT-US or PET/MRI-US fusion targeted prostate biopsies may be valuable for PCa diagnosis and have a high detection rate of clinically significant PCa for PET-positive lesions. PET/MR can rule out some false PET-positive lesions, which may potentially reduce unnecessary prostate biopsies.

In a recent meta-analysis involving patients with non-small cell lung cancer, there was no discernible contrast between whole-body magnetic resonance imaging (WBMRI) and PET/CT. However, such a comparative study is lacking in the context of PCa. Zhan et al. undertook a comparison between WBMRI and PET/CT for detecting bone metastases in PCa patients. Their analysis encompassed four prospective and one retrospective study, involving a total of 657 patients. Significant disparities were noted between WBMRI and PET/CT concerning sensitivity and negative likelihood ratios, whereas no notable differences were observed for specificity and positive likelihood ratios. The diagnostic odds ratio for WBMRI was found to be similar to that of PET/CT. PET/CT demonstrated higher sensitivity and negative likelihood ratios in detecting bone metastases from PCa compared to WBMRI, while no significant distinctions were detected for specificity and positive likelihood ratios. Walter et al. conducted an assessment of the MonaLisa prostate biopsy system focusing on safety, tolerability, and patient-related outcomes. This prospective study involved 228 patients who underwent Robotic-assisted transperineal MRI-US-fusion guided biopsy of the prostate. The study evaluated peri-operative side effects, functional outcomes, and patient satisfaction. On the day of biopsy, the mean pain score was 1.3 points on the Visual Analog Scale (VAS), which remained consistent on the

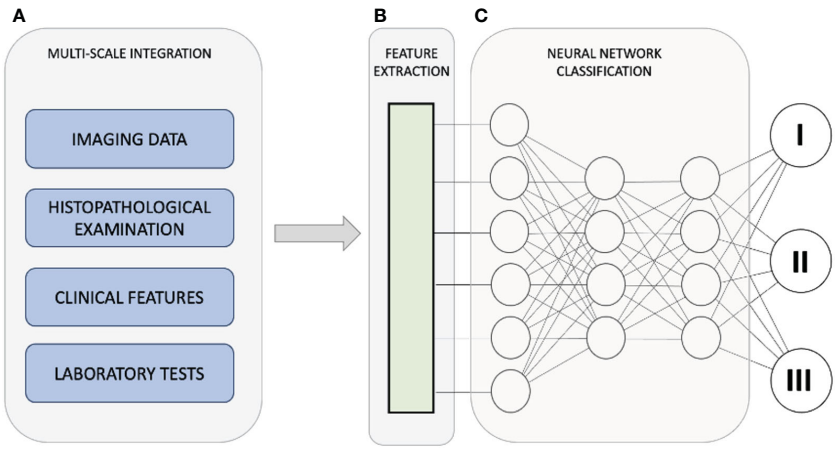

FIGURE 1
The diagnostic pathway for PCa strives to achieve timely identification of clinically significant PCa while minimizing the detection of insignificant cases. This approach seeks to strike a balance between diagnostic accuracy and the potential burden on individuals and healthcare providers. Utilizing artificial intelligence, we integrate data from various scales **(A)** to enhance the diagnosis and treatment of prostate cancer. Within the collected dataset, the AI-driven system identifies and extrapolates the features and data points most pertinent to generating the ultimate outcome **(B)**. The integration of diverse data and features culminates in a refined categorization of the condition **(C)**, emphasizing that integration involves intricate connections among diverse characteristics observed across multiple scales, rather than a mere summation of individual outcomes.

following day. Overall, 14% of patients experienced grade I complications according to the Clavien-Dindo classification, with no higher-grade complications reported. Gross hematuria, hematospermia, and acute urinary retention occurred in 63.6%, 43%, and 14% of patients, respectively, while only one patient developed urinary tract infection. The authors concluded that robotic-assisted transperineal MRI-US-fusion guided biopsy of the prostate, performed under general anesthesia, is a safe and well-tolerated procedure. They attribute this favorable risk profile and tolerability to the minimally invasive approach involving two entry points, which allows for the omission of perioperative prophylaxis while minimizing the risk of infectious complications. In their manuscript, Gaudiano et al. provided an overview of both the common and rare features of different types of granulomatous prostatitis (GP) on mpMRI through a comprehensive literature review. Their aim was to identify radiological criteria for distinguishing this inflammatory condition from PCa and reducing the need for TRUS prostate biopsy whenever possible. Specifically, they focused on evaluating GP features within the multiparametric study protocol, which includes T2-weighted (T2w) imaging, diffusion-weighted imaging (DWI) with apparent diffusion coefficient (ADC) mapping, and dynamic contrast-enhanced (DCE) sequences. The primary limitation they encountered was the scarcity of large-scale studies on this topic due to the rarity of the disease. Consequently, the literature predominantly comprises case reports and small case series, which precluded a detailed statistical analysis. Through their literature review, they concluded that mpMRI of the prostate could be instrumental in distinguishing Bacille Calmette-Guérin (BCG)-induced GP from PCa, particularly by accurately assessing the characteristic "ring enhancement" of prostate lesions on multiphase contrast-enhanced MRI within a specific clinical context. They suggested that an mpMRI follow-up of prostatic lesions could be safely conducted in such cases. However, they noted that differentiating other types of non-necrotic GP, such as nonspecific granulomatous prostatitis, xanthogranulomatous prostatitis, and diffuse or nodular BCG-induced GP, based solely on mpMRI features, including PSA values, was not feasible. In these instances, a targeted biopsy remained the necessary approach for accurate diagnosis.

In their study, Wenhao et al. assessed the utility of quantitative T2 star (T2*) values derived from T2* mapping sequences in mpMRI for diagnosing and grading PI-RADS 3 PCa. They prospectively enrolled patients with PCa or benign prostatic hyperplasia (BPH) and collected imaging indicators, including T2* values and ADC values. Additionally, they measured levels of proteins involved in iron metabolism using enzyme-linked immunosorbent assays. Their findings revealed significant differences in three iron metabolism indexes - ferritin, hepcidin, and ferric ion (Fe) - as well as T2* values between the PCa and BPH groups and between the low ISUP group (ISUP ≤ 2) and the high ISUP group (ISUP > 2). Moreover, a significant correlation was observed between the levels of these three indicators and T2* values. Further receiver operating characteristic analysis demonstrated that the levels of iron metabolism-related indexes and T2* values exhibited strong performance in diagnosing and grading PCa. Their study highlighted the potential of T2* values in detecting and predicting the grade of PCa, as they reflect the tumor's iron metabolism. This finding suggests that T2* values could serve as a valuable tool in the future for diagnosing and grading PCa, providing a foundation for improved clinical decision-making in PCa management. Zhang et al. conducted a comparative analysis between 99mTc-PSMA single-photon emission computed tomography (SPECT)/CT and mpMRI in detecting primary PCa. Their prospective study involved fifty-six men with suspected PCa, categorized into high- (Gleason score > 7), intermediate- (Gleason score = 7), and low-risk groups (Gleason score < 7). All patients underwent both 99mTc-PSMA SPECT/CT and mpMRI within an average interval of 3 days. They utilized maximum standardized uptake value (SUV_{max}), minimum ADC_{min}, and their ratio (SUV_{max}/ADC_{min}) as imaging parameters to differentiate between benign and malignant prostatic lesions. Their findings indicated that 99mTc-PSMA SPECT/CT and mpMRI exhibited comparable performance in detecting primary PCa, with sensitivities of 97.7% and 90.9%, specificities of 75.0% and 75.0%, and areas under the curve (AUC) of 97.4% and 95.1%, respectively. Moreover, the AUC of SUV_{max}/ADC_{min} surpassed those of SUV_{max} or ADC_{min} alone. The authors identified a threshold of $>7.0\times10^3$ for SUV_{max}/ADC_{min} in prostatic lesions, indicating a higher likelihood of malignancy. Additionally, when SUV_{max}/ADC_{min} exceeded $>27.0\times10^3$, patients with PCa might exhibit lymph node and bone metastases. SUV_{max} exhibited a positive correlation with the Gleason score, while ADC_{min} displayed a negative correlation. SUV_{max}/ADC_{min} showed a positive correlation with the Gleason score and emerged as the primary predictor of the high-risk group. The combination of 99mTc-PSMA SPECT/CT and mpMRI yielded improved diagnostic efficacy for PCa compared to either modality alone. Notably, SUV_{max}/ADC_{min} emerged as a valuable differential diagnostic imaging parameter in this context.

Huang et al. conducted a comprehensive meta-analysis and systematic review to compare the diagnostic effectiveness of 68Ga-PSMA-11 PET/CT and 68Ga-PSMA-11 PET/MRI in patients with biochemically recurrent PCa after radical prostatectomy and hybrid radiotherapy and radical prostatectomy. Their analysis included studies evaluating the utility of 68Ga-PSMA-11 PET/CT or PET/MRI as a screening tool for detecting biochemically recurrent PCa. A total of 37 studies involving 8409 patients were scrutinized. To assess heterogeneity, the I^2 statistic was employed, with the random effect model used in cases of substantial heterogeneity ($I^2 > 50\%$) and the fixed model in other instances. Additionally, the authors evaluated the quality of the included studies using the Quality Assessment of Diagnostic Accuracy Studies 2 (QUADAS-2) method. The combined total detection rates for 68Ga-PSMA-11 PET/CT and PET/MRI were 0.70 (95% CI: 0.65-0.75) and 0.71 (95% CI: 0.67-0.75), respectively. The authors found no significant difference in the overall detection rates for biochemical relapse between 68Ga-PSMA-11 PET/CT and PET/MRI. Moreover, the detection rates were unaffected by PSA values. Their analysis suggests that the diagnostic efficacy of 68Ga-PSMA-11 PET/CT is comparable to that of 68Ga-PSMA-11 PET/MRI in detecting biochemically recurrent PCa. However, they cautioned that not all studies employed pathological biopsies as the gold standard,

highlighting the need for additional larger prospective studies to address this limitation.

In 2023, Mehmood et al. addressed the challenges posed by high-resolution and multiresolution MRI in PCa diagnosis by leveraging computer-aided diagnostic (CAD) methods. With the rapid advancement of medical technology, deep learning methods have gained prominence in this domain. These techniques not only improve diagnostic efficiency but also mitigate observer variability, consistently surpassing traditional approaches. However, resource constraints remain a significant hurdle in distinguishing aggressive from non-aggressive cancers in PCa treatment. Their study aimed to harness MRI images for PCa identification by integrating deep learning and transfer learning. They explored various convolutional neural network (CNN)-based deep learning methods for classifying PCa-related MRI images. In their approach, they developed a method for PCa classification using transfer learning on a limited image dataset to achieve high performance, aiding radiologists in prompt PCa identification. Their proposed methodology utilized the EfficientNet architecture pre-trained on the ImageNet dataset, incorporating three branches for feature extraction from different MRI sequences. The fusion of these extracted features significantly enhanced the model's ability to accurately distinguish MRI images. Their model achieved a notable accuracy rate of 88.89% in classifying PCa. Comparative analysis revealed that their approach outperformed both traditional hand-crafted feature techniques and existing deep learning methods in PCa classification. This underscores the efficacy of their methodology in learning distinctive features from prostate images and accurately identifying cancerous regions.

Zhao et al. aimed to develop a robust model for predicting csPCa (pathological grade group ≥ 2) in PI-RADS 3 lesions within the transition zone by comparing the performance of combination models. Their study involved 243 men who underwent 3-Tesla MRI and ultrasound-guided transrectal biopsy, divided into a training cohort of 170 patients and a separate testing cohort of 73 patients. Manual segmentation of T2-weighted imaging (T2WI) and diffusion-weighted imaging (DWI) images was performed for PI-RADS 3 lesions to extract mean apparent diffusion coefficient (ADC) values and conduct radiomic analysis. Predictive clinical factors were identified using both univariate and multivariate logistic models, and the least absolute shrinkage and selection operator (LASSO) regression models were employed for feature selection and constructing radiomic signatures. The authors developed nine models combining clinical factors, radiological features, and radiomics, utilizing logistic and XGboost methods. The performance of these models was evaluated using ROC analysis and the Delong test. Among the 243 participants with a median age of 70 years, 30 were diagnosed with csPCa, leaving 213 without a csPCa diagnosis. PSA density (PSAD) emerged as the sole significant clinical factor, identified through univariate and multivariate logistic models. Seven radiomic features correlated with csPCa prediction. The XGboost model exhibited superior performance compared to eight other models (AUC of the training cohort: 0.949, and validation cohort: 0.913). However, it did not surpass the PSAD+MADC model in both the training and testing cohorts. Their findings demonstrated that the machine learning XGboost model performed best in predicting csPCa in PI-RADS 3 lesions within the transitional zone. However, the addition of radiomic classifiers did not significantly enhance the performance over the compound model of clinical and radiological findings. Thus, the Mean ADC+PSAD model was deemed the most effective and generalizable option for quantitative prostate evaluation.

Zhou et al. developed an artificial intelligence (AI)-based model for predicting the progression of castration-resistant prostate cancer (CRPC) by integrating multimodal data. They retrospectively collected data from 399 patients diagnosed with PCa across three medical centers. Regions of interest (ROIs) were delineated from three MRI sequences, namely T2WI, diffusion-weighted imaging (DWI), and ADC, and the largest section of each ROI was extracted using a cropping tool. Representative pathological hematoxylin and eosin-stained slides were selected for training a deep-learning model. Subsequently, a joint combined model nomogram was constructed. The predictive performance and goodness of fit of the model were evaluated using ROC curves and calibration curves. Decision curve analysis curves and Kaplan-Meier survival curves were generated to assess the clinical net benefit of the model and its association with progression-free survival. The AUC of the machine learning (ML) model was determined to be 0.755. The best-performing deep learning model for radiomics and pathomics was identified as the ResNet-50 model, achieving AUC values of 0.768 and 0.752, respectively. The nomogram graph illustrated that the DL model contributed the most, resulting in an AUC of 0.86 for the combined model. Calibration curves and DCA indicated that the combined model exhibited good calibration ability and provided a net clinical benefit. Additionally, the KM curve suggested that the model integrating multimodal data could guide patient prognosis and management strategies effectively. Overall, the integration of multimodal data significantly enhanced the prediction of PCa progression to CRPC. Abrahamsen et al. introduced a novel method of accounting for bone in pelvic PET/MR AC by directly predicting the errors in the PET image space caused by the lack of bone in four-class Dixon-based attenuation correction. A CNN was trained to predict the four-class AC error map relative to CT-based attenuation correction. Dixon MR images and the four-class attenuation correction μ-map were used as input to the models. CT and PET/MR examinations for 22 patients ([18F] FDG) were used for training and validation, and 17 patients were used for testing (6 [18F] PSMA-1007 and 11 [68Ga] Ga-PSMA-11). A quantitative analysis of PSMA uptake using voxel- and lesion-based error metrics was subsequently used to assess performance. In the voxel-based analysis, the proposed model reduced the median root mean squared percentage error from 12.1% and 8.6% for the four- and five-class Dixon-based AC methods, respectively, to 6.2%. The median absolute percentage error in the maximum standardized uptake value (SUV_{max}) in bone lesions improved from 20.0% and 7.0% for four- and five-class Dixon-based AC methods to 3.8%. The proposed method reduces the voxel-based error and SUV_{max} errors in bone lesions when compared to the four- and five-class Dixon-based AC models. It is indubitable that MRI and PCa-specific PET represent two widely applicable, rapidly developing technologies that are becoming increasingly important to PCa diagnosis and management. While

the adoption of these techniques will help us make the most informed decisions with patients, it is important to recognize that the clinical benefits and cost-effectiveness of their use are still being evaluated and debated. It should also underline that consistent image interpretation is crucial for ensuring comparable data across different clinical trials and for effectively translating research findings into routine clinical practice (24).

A significant increase in the annual number of new PCa cases is expected, with cases projected to rise from 1.4 million in 2020 to 2.9 million by 2040 (25). This rise is attributed to shifting age demographics and improvements in life expectancy, particularly driving increases in the disease burden. Late diagnosis of PCa is a widespread issue globally, with low- and middle-income countries (LMICs) particularly affected, where late diagnosis is common. To mitigate the adverse impact of this upward trend, urgent establishment of systems for earlier diagnosis in LMICs is imperative. Trials of screening are urgently required in these regions to provide valuable insights into improving early diagnosis strategies. Early diagnosis systems must incorporate innovative combinations of personnel and harness the growing capabilities of AI-based algorithms to assist in the interpretation of scans and biopsy samples. This multifaceted approach is essential to address the challenges posed by rising case numbers and improve outcomes for individuals affected by prostate cancer worldwide. Tackling the intricate dimensions of PCa, both in its temporal progression and spatial manifestations, holds the promise of uncovering deeper insights into its origins and evolution (26). This comprehensive approach stands to provide a more cohesive conceptual framework, enhance the interpretation of experimental findings, guide targeted research endeavors, and offer a systematic way to organize the vast array of existing knowledge by identifying commonalities or shared characteristics among different types of tumors. Encouragingly, collaboration among experts from diverse disciplines such as engineering, clinical medicine, biology, and mathematics continues to drive forward efforts towards achieving a unified and quantifiable understanding of cancer's complexities. Crucially, technology plays an indispensable role in this pursuit, serving as a vital catalyst for scientific progress.

Author contributions

FG: Writing – review & editing, Writing – original draft, Supervision, Conceptualization. GT: Writing – review & editing, Writing – original draft, Supervision, Conceptualization.

Acknowledgments

We extend our gratitude to all the scientists who have contributed to our Research Topic. The authors express sincere appreciation to Pizzium S.p.A. for their invaluable support in our research endeavors.

Conflict of interest

The authors declare that the research was conducted in the absence of any commercial or financial relationships that could be construed as a potential conflict of interest.

The author(s) declared that they were an editorial board member of Frontiers, at the time of submission. This had no impact on the peer review process and the final decision.

Publisher's note

References

1. Cornford P, van den Bergh RCN, Briers E, Van den Broeck T, Brunckhorst O, Darraugh J, et al. Eau-eanm-estro-esur-isup-siog guidelines on prostate cancer-2024 update. Part i: Screening, diagnosis, and local treatment with curative intent. *Eur Urol*. (2024). doi: 10.1016/j.eururo.2024.03.027

2. Albright F, Stephenson RA, Agarwal N, Teerlink CC, Lowrance WT, Farnham JM, et al. Prostate cancer risk prediction based on complete prostate cancer family history. *Prostate*. (2015) 75:390–85. doi: 10.1002/pros.22925

3. Ahdoot M, Wilbur AR, Reese SE, Lebastchi AH, Mehralivand S, Gomella PT, et al. Mri-targeted, systematic, and combined biopsy for prostate cancer diagnosis. *N Engl J Med*. (2020) 382:917–285. doi: 10.1056/NEJMoa1910038

4. Liu J, Cundy TP, Woon DTS, Lawrentschuk N. A systematic review on artificial intelligence evaluating metastatic prostatic cancer and lymph nodes on psma pet scans. *Cancers (Basel)*. (2024) 16. doi: 10.3390/cancers16030486

5. Pinsky PF, Parnes H. Screening for prostate cancer. *N Engl J Med*. (2023) 388:1405–145. doi: 10.1056/NEJMcp2209151

6. Ceci F, Oprea-Lager DE, Emmett L, Adam JA, Bomanji J, Czernin J, et al. E-psma: The eanm standardized reporting guidelines v1.0 for psma-pet. *Eur J Nucl Med Mol Imaging*. (2021) 48:1626–385. doi: 10.1007/s00259-021-05245-y

7. McKone EL, Sutton EA, Johnson GB, Phillips RM. Application of advanced imaging to prostate cancer diagnosis and management: A narrative review of current practice and unanswered questions. *J Clin Med*. (2024) 13. doi: 10.3390/jcm13020446

8. Kasivisvanathan V, Rannikko AS, Borghi M, Panebianco V, Mynderse LA, Vaarala MH, et al. Mri-targeted or standard biopsy for prostate-cancer diagnosis. *N Engl J Med*. (2018) 378:1767–775. doi: 10.1056/NEJMoa1801993

9. Johnson LM, Turkbey B, Figg WD, Choyke PL. Multiparametric mri in prostate cancer management. *Nat Rev Clin Oncol*. (2014) 11:346–535. doi: 10.1038/nrclinonc.2014.69

10. Dias AB, Chang SD, Fennessy FM, Ghafoor S, Ghai S, Panebianco V, et al. New prostate mri scoring systems (pi-qual, precise, pi-rr, and pi-fab): Ajr expert panel narrative review. *AJR Am J Roentgenol*. (2024). doi: 10.2214/AJR.24.30956

11. Ghosh A, Heston WDW. Tumor target prostate specific membrane antigen (psma) and its regulation in prostate cancer. *J Cell Biochem*. (2003) 91:528–395. doi: 10.1002/jcb.10661

12. Horoszewicz JS, Kawinski E, Murphy GP. Monoclonal antibodies to a new antigenic marker in epithelial prostatic cells and serum of prostatic cancer patients. *Anticancer Res*. (1987) 7:927–355.

13. Israeli RS, Powell CT, Fair WR, Heston WD. Molecular cloning of a complementary DNA encoding a prostate-specific membrane antigen. *Cancer Res*. (1993) 53:227–305.

14. Al Saffar H, Chen DC, Delgado C, Ingvar J, Hofman MS, Lawrentschuk N, et al. The current landscape of prostate-specific membrane antigen (psma) imaging biomarkers for aggressive prostate cancer. *Cancers (Basel)*. (2024) 16. doi: 10.3390/cancers16050939

15. Bakht MK, Yamada Y, Ku SY, Venkadakrishnan VB, Korsen JA, Kalidindi TM, et al. Landscape of prostate-specific membrane antigen heterogeneity and regulation in ar-positive and ar-negative metastatic prostate cancer. *Nat Cancer*. (2023) 4:699–7155. doi: 10.1038/s43018-023-00539-6

16. Weiner AB, Agrawal R, Valle LF, Sonni I, Kishan AU, Rettig MB, et al. Impact of psma pet on prostate cancer management. *Curr Treat Options Oncol*. (2024) 25 (2):191-205. doi: 10.1007/s11864-024-01181-9

17. Kawada T, Yanagisawa T, Rajwa P, Sari Motlagh R, Mostafaei H, Quhal F, et al. Diagnostic performance of prostate-specific membrane antigen positron emission tomography-targeted biopsy for detection of clinically significant prostate cancer: A systematic review and meta-analysis. *Eur Urol Oncol*. (2022) 5:390–4005. doi: 10.1016/j.euo.2022.04.006

18. Calais J, Ceci F, Eiber M, Hope TA, Hofman MS, Rischpler C, et al. (18)f-fluciclovine pet-ct and (68)ga-psma-11 pet-ct in patients with early biochemical recurrence after prostatectomy: A prospective, single-centre, single-arm, comparative imaging trial. *Lancet Oncol*. (2019) 20:1286–945. doi: 10.1016/S1470-2045(19)30415-2

19. Morigi JJ, Stricker PD, van Leeuwen PJ, Tang R, Ho B, Nguyen Q, et al. Prospective comparison of 18f-fluoromethylcholine versus 68ga-psma pet/ct in prostate cancer patients who have rising psa after curative treatment and are being considered for targeted therapy. *J Nucl Med*. (2015) 56:1185–905. doi: 10.2967/jnumed.115.160382

20. Pepe P, Fandella A, Barbera M, Martino P, Merolla F, Caputo A, et al. Advances in radiology and pathology of prostate cancer: A review for the pathologist. *Pathologica*. (2024) 116:1–125. doi: 10.32074/1591-951X-925

21. Park KS. Recent updates on applications of artificial intelligence for nuclear medicine professionals: Prostate cancer and pet/ct. *Nucl Med Mol Imaging*. (2024) 58:97–1005. doi: 10.1007/s13139-024-00856-3

22. Zhu L, Pan J, Mou W, Deng L, Zhu Y, Wang Y, et al. Harnessing artificial intelligence for prostate cancer management. *Cell Rep Med*. (2024) 5:1015065. doi: 10.1016/j.xcrm.2024.101506

23. Hegazi M, Taverna G, Grizzi F. Is artificial intelligence the key to revolutionizing benign prostatic hyperplasia diagnosis and management. *Arch Esp Urol*. (2023) 76:643–565. doi: 10.56434/j.arch.esp.urol.20237609.79

24. Swiha M, Ayati N, Oprea-Lager DE, Ceci F, Emmett L. How to report psma pet. *Semin Nucl Med*. (2024) 54:14–295. doi: 10.1053/j.semnuclmed.2023.07.007

25. James ND, Tannock I, N'Dow J, Feng F, Gillessen S, Ali SA, et al. The lancet commission on prostate cancer: Planning for the surge in cases. *Lancet*. (2024) 403 (10437):1683–722. doi: 10.1016/S0140-6736(24)00651-2

26. Grizzi F, Bax C, Capelli L, Taverna G. Editorial: Reshaping the diagnostic process in oncology: Science versus technology. *Front Oncol*. (2023) 13:1321688. doi: 10.3389/fonc.2023.1321688

frontiers in Oncology

ORIGINAL RESEARCH
published: 05 March 2021
doi: 10.3389/fonc.2021.612157

A Pilot Study of ^{18}F-DCFPyL PET/CT or PET/MRI and Ultrasound Fusion Targeted Prostate Biopsy for Intra-Prostatic PET-Positive Lesions

Yachao Liu[1†], Hongkai Yu[2†], Jiajin Liu[1], Xiaojun Zhang[1], Mu Lin[3], Holger Schmidt[4], Jiangping Gao[2] and Baixuan Xu[1*]*

[1] Department of Nuclear Medicine, Chinese People's Liberation Army General Hospital, Beijing, China, [2] Department of Urology Surgery, Chinese People's Liberation Army General Hospital, Beijing, China, [3] Magnetic Resonance Collaboration, Diagnostic Imaging, Siemens Healthineers Ltd., Shanghai, China, [4] Magnetic Resonance Education, Customer Services, Siemens Healthcare GmbH, Erlangen, Germany

OPEN ACCESS

Edited by:
Scott T. Tagawa, Cornell University, United States

Reviewed by:
Ning Zhang, Peking University Cancer Hospital, China
Alessandro Tafuri, University of Verona, Italy

***Correspondence:**
Baixuan Xu
xbx301@163.com
Jiangping Gao
jpgao301@163.com

[†]These authors share first authorship

Specialty section:
This article was submitted to Genitourinary Oncology, a section of the journal Frontiers in Oncology

Received: *30 September 2020*
Accepted: *11 January 2021*
Published: *05 March 2021*

Citation:
Liu Y, Yu H, Liu J, Zhang X, Lin M, Schmidt H, Gao J and Xu B (2021) A Pilot Study of ^{18}F-DCFPyL PET/CT or PET/MRI and Ultrasound Fusion Targeted Prostate Biopsy for Intra-Prostatic PET-Positive Lesions. Front. Oncol. 11:612157. doi: 10.3389/fonc.2021.612157

Objectives: The purpose of this study was to evaluate the feasibility and diagnostic performance of prostate-specific membrane antigen (PSMA) based ^{18}F-DCFPyL PET/CT-ultrasound (PET/CT-US) or PET/MRI-ultrasound (PET/MRI-US) fusion targeted biopsy for intra-prostatic PET-positive lesions.

Methods: From April 2018 to November 2019, we prospectively enrolled 55 candidates to perform PET/CT-US or PET/MRI-US fusion targeted biopsies for solitary PET-positive prostate lesions (two to four cores/lesion). The positive rates of prostate cancer based on patients and biopsy cores were calculated respectively. With reference to the pathological results of biopsy cores, the MR signal characteristics in the area of the PET-positive lesion were analyzed for the patients who underwent PET/MRI.

Results: A total of 178 biopsy cores were taken on the 55 patients. One hundred forty-six biopsy cores (82.0%, 146/178) from 51 (92.7%, 51/55) patients were positive for prostate cancer; 47 (85.5%, 47/55) were clinically significant prostate cancer. It is noteworthy that nine patients underwent both ^{18}F-DCFPyL PET/CT and PET/MRI examinations; the seven patients with prostate cancer showed abnormal MR signal in the area of the PET-positive lesion while the other two patients with prostatic hyperplasia and prostatitis showed normal MR signal in the area of the PET-positive lesion.

Conclusion: This study indicated that ^{18}F-DCFPyL PET/CT-US or PET/MRI-US fusion targeted prostate biopsies may be valuable for prostate cancer diagnosis and have a high detection rate of clinically significant prostate cancer for PET-positive lesions. PET/MR can rule out some false PET-positive lesions, which may potentially reduce unnecessary prostate biopsies.

Keywords: ^{18}F-DCFPyL, PET/CT, PET/MR, biopsy, prostate cancer

INTRODUCTION

Prostate cancer remains one of the most common male malignancies worldwide. Systematic 12-core transrectal ultrasound-guided prostate biopsy and histopathology are the most commonly used techniques for the diagnosis of prostate cancer before radical prostatectomy (1). However, biopsies are invasive, painful, and prone to potential complications. Normal prostate tissue, benign prostate diseases, and clinically insignificant prostate cancer are often detected by this conventional biopsy scheme. In addition, this conventional approach is poor at sampling the anterior, midline, and apex of the prostate, which leads to the underdiagnosis of patients with clinically significant prostate cancer.

Much progress has been made in recent years towards developing a targeted prostate biopsy. Clinicians are constantly exploring new methods, such as direct in-bore MRI guidance and image fusion guidance targeted prostate biopsy, to improve the detection of clinically significant prostate cancer and reduce the number of biopsy procedures and associated complications (2). However, 24% of men with negative multiparametric MRI have a significant risk of harboring clinically significant prostate cancer (3).

PSMA is a type II transmembrane glycoprotein with enzymatic carboxypeptidase activity. PSMA is overexpressed on almost all types of prostate cancer cells, making PMSA an ideal target for the diagnosis and treatment of prostate cancer. Compared with conventional imaging modalities, such as CT and MR, both ^{68}Ga and ^{18}F labeled PSMA PET imaging has a higher sensitivity and specificity for prostate cancer (4–7). ^{18}F-DCFPyL is a very promising ^{18}F-labeled PSMA tracer that is currently under investigation. A previous study showed that ^{18}F labeled PSMA provides better image quality and the ability to display small lesions (8). The purpose of our study was to explore the feasibility and diagnostic performance of ^{18}F-DCFPyL PET/CT or PET/MRI and ultrasound (PET/CT-US or PET/MRI-US) fusion-targeted prostate biopsy for intra-prostatic PET-positive lesion diagnosis.

MATERIALS AND METHODS

Study Population

Between April 2018 and November 2019, 213 consecutive patients performed ^{18}F-DCFPyL PET/CT or PET/MRI because of elevated PSA, digital rectal examination, ultrasound, or MRI suspected prostate cancer. The patients with solitary PET-positive prostate lesions were assessed for eligibility for ^{18}F-DCFPyL PET targeted biopsy and informed of the potential harms and benefits of this method. The inclusion criteria were: (1) ^{18}F-DCFPyL PET/CT or PET/MRI showed solitary radioactive concentration (PET-positive lesion) in the prostate; and, (2) the solitary PET-positive lesion involved less than one half of one lobe; and, (3) a targeted biopsy performed by ^{18}F-DCFPyL PET/CT-US or PET/MRI-US targeted at the solitary intraprostatic PET-positive lesion. Patients were excluded if (1)^{18}F-DCFPyL PET/CT or PET/MRI showed multiple or no PET-positive lesion in the prostate; and (2) they chose systematic biopsy instead of our targeted biopsy way or refused any prostate biopsy. All procedures were approved by the local ethics board and all the enrolled subjects provided informed consent.

18F-DCFPyL PET/CT and PET/MRI Examinations

^{18}F-DCFPyL was synthesized by our nuclear medicine department (radiochemical purity > 98%, specific activity 54–90 GBq/μmol). Quality control report was provided in **Table 1**.

PET/CT was performed from the ears to the upper thigh on a Siemens Biograph 64 operating in 3D emission mode with CT-derived attenuation correction (120 kV, 100 mAs, 5.0 mm Slice, 0.9 Pitch). The PET acquisition time was 2 min per bed position. CT maps were used for PET attenuation correction. PET data were reconstructed using ordered subset expectation maximization (OSEM; 3 iterations, 21 subsets, 168 × 168 matrix) and a transaxial resolution of 5.0 mm (full-width at half-maximum).

PET/MRI was performed on a hybrid PET/MRI scanner (Biograph mMR, Siemens Healthcare, Erlangen). The MR protocol consisted of T1W fast spin echo (2D, transversal, TR

TABLE 1 | Quality control report.

Test	Specification	Average Original (n = 4)
Initial appearance	Clear, colorless solution, no visible particulate matter	Conforms
Appearance, 240 min after end of synthesis	Clear, colorless solution, no visible particulate matter	Conforms
Initial radiochemical purity, %	≥95%	100%
pH, initial	4.5–8.5	6.5
Chemical purity	DCFPyL	3.87 ± 0.13 μg/ml
Yield	≥20 mCi [18F]DCFPyL (referenced to assay recorded at end of filtration)	347 ± 45 mCi
Specific activity	≥1,000 mCi/μmol of [18F]DCFPyL (referenced to end of filtration)	65 ± 23 GBq/μmol
Residual solvent analysis	Acetonitrile ≤400 ppm	0 ppm
	Tetrabutylammonium ≤400 ppm	0 ppm
Radionuclidic identity	t1/2 = 105–115 min	109.8 ± 2.3 min
Radionuclidic purity	99.5% associated with ^{18}F (0.511 and 1.022 MeV)	Conforms
Identity (high-performance liquid chromatography, HPLC)	HPLC retention time matches reference standard	Conforms
Filter integrity	Bubble point ≥13 psi	17.3 ± 0.6 psi
Endotoxin	≤15 EU/ml	<5 EU/ml
Sterility	No growth observed	Conforms

500 ms, TE 13 ms, flip angle 150°, 15 slices, Slice thickness 5 mm, field of view (FOV) 300 × 300, voxel size 1.2 × 1.2 × 5.0 mm^3), T2W (transversal, TR 3810 ms, TE 78 ms, flip angle 150°, 20 slices, Slice thickness 3 mm, FOV 240 × 240, voxel size 0.8 × 0.8 × 3.0 mm^3) fast spin echo, high b value DWI (2D, transversal, TR 6500 ms, TE 93 ms, 20 slices, Slice thickness 3 mm, FOV 380 × 380, voxel size 2.4 × 2.4 × 3.0 mm^3, b-values 0, 1,000 and 2,000 s/mm^2), and PET acquisition for the pelvic region. PET images were reconstructed with 3 iterations and 21 subsets. MRI-based attenuation correction was applied using DIXON-volume interpolated breath-hold examination (VIBE) sequences comprising in- and opposed-phase as well as fat- and water-saturated images.

Prostate Biopsy Procedure

^{18}F-DCFPyL PET/CT-US or PET/MRI-US fusion targeted prostate biopsy for the intra-prostatic PET-positive lesions were performed with the BK Predictive Fusion prostate biopsy system (BK Medical Technology Shanghai Co., Ltd). Patients were given fluoroquinolone antibiotic prophylaxis and prescribed enemas on the day before the procedure, and again 3 h before the procedure. Before the targeted biopsy, the ^{18}F-DCFPyL PET/CT or PET/MRI imaging data were imported into the BK Predictive Fusion prostate biopsy system workstation, and the boundaries of the prostate were delineated on CT or T2W images. A standardized uptake value (SUV) of 2.5 was used to delineate the boundary of PET-positive lesions marked as targets for biopsy. The SUVmax, SUVmean, and volume of lesions were also recorded for further analysis. The patients were placed in the Trendelenburg position and administered local anesthesia of 1% lidocaine. During the biopsy procedure, the previous delineated prostate volume from the CT or T2W images was then registered with the prostate volume acquired from the three-dimensional transrectal ultrasonography with real-time tracking of the ultrasound probe. Subsequently, an algorithm determined the precise three-dimensional real-time information about the localization of targets in the PET-positive lesion for needle placement during the ultrasound-guided biopsy. Transrectal biopsies were performed with two to four cores for each PET-positive lesion. A schematic diagram of a targeted prostate biopsy procedure is shown in **Figure 1**.

Compared with targeted biopsy, systematic biopsy causes greater suffering to patients, both psychologically and physically (post-biopsy complications). Some patients, particularly elders, are unwilling to undergo systematic biopsy. In contrast, ^{18}F-DCFPyL PET positive lesions have high diagnostic value for prostate cancer. For patients with single PET positive lesion, targeted biopsy (two to four cores) alone can achieve good detection rate and reduce patients' pain. However, only targeted biopsy for PET-positive lesion might miss some PET-negative prostate cancer lesions. The advantages and disadvantages of the two biopsy methods were informed to the patients.

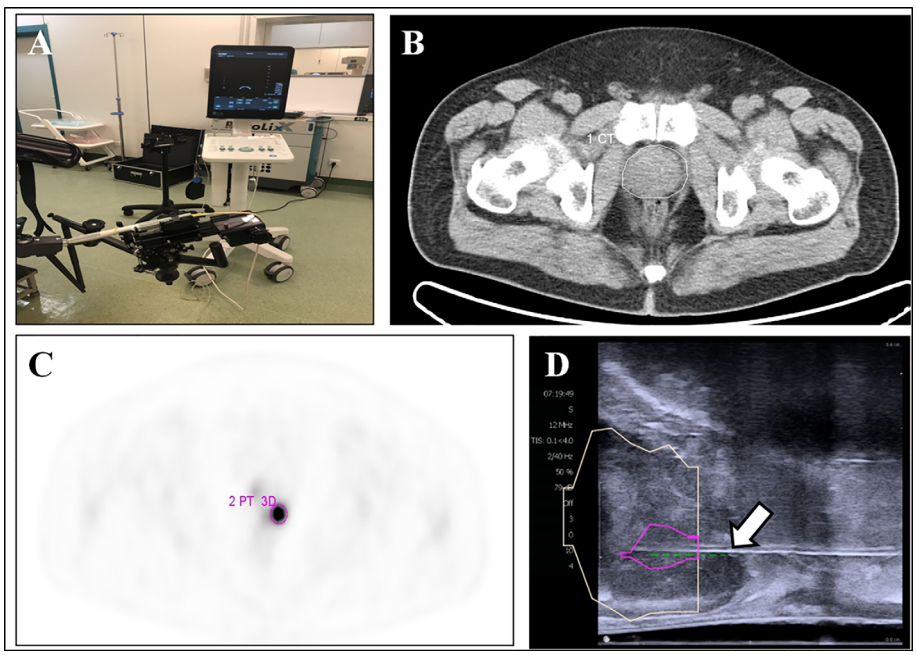

FIGURE 1 | ^{18}F-DCFPyL PET/CT-US or PET/MRI-US fusion targeted prostate biopsy for the intraprostatic PET-positive lesions were performed with the BK Predictive Fusion prostate biopsy system **(A)**. The boundaries of the prostate were delineated on the CT image (**B**, white circle). The PET-positive lesion was marked as the target for biopsy (**C**, pink circle). The previous delineated prostate and PET-positive lesion from PET/CT was registered to the prostate volume acquired from the three-dimensional transrectal ultrasonography; the puncture needle (**D**, arrow) then reached the target biopsy area.

Histopathologic Analysis

The prostate biopsies were analyzed by two pathologists, each with over 10 years of experience in prostate pathology. Analyzed biopsy features include the total number of biopsy cores, percentage of cores involving adenocarcinoma, and the number of positive biopsy cores. In our study, clinically significant prostate cancer was defined as the presence of a single biopsy core indicating disease of Gleason score 3 + 4 (Gleason sum of 7) or greater (the Gleason score is composed of a primary [most predominant] grade plus a secondary [highest non-predominant] grade); the range for a primary or secondary grade is from 3 to 5, with the Gleason sum ranging from 6 to 10 (3, 9–12).

RESULTS

A total of 55 patients (mean age: 67, range: 49–84) with solitary PET-positive prostate lesions agreed to undergo ^{18}F-DCFPyL PET/CT-US or PET/MRI-US fusion targeted prostate biopsy were enrolled in this study (**Figure 2**). Among them, two cases had previous negative prostate biopsy and 53 cases were biopsy-naive. Finally, no significant complications occurred in any patient after the biopsy. An overview of the study population is shown in **Table 2**.

Among the 55 patients, 32 patients received PET/CT examinations along, 14 patients received PET/MRI examinations along, and 9 patients underwent both PET/CT and PET/MRI scans sequentially within 2 h. The average volume of the target biopsy area was 3.68 ± 2.18 cm^3 (range: 0.7–9.82 cm^3). The average SUVmax ± SD was 15.47 ± 12.25 (range: 4.36–59.34), and the average SUVmean ± SD was 7.07 ± 4.68 (range: 3.39–30.30).

A total of 178 core biopsies were performed, 146 (82.0%, 146/178) samples were malignant. According to the biopsy pathology, fusion-targeted biopsy identified 51 (92.7%, 51/55) patients as having prostate cancer; 47 (85.5%, 47/55) of these 55 patients were clinically significant prostate cancer while 4 (7.3%, 4/55) were clinically insignificant prostate cancer. The detection rates of clinically significant prostate cancer by PET/CT-US and PET/MRI-US were 87.5% (28/32) and 82.6% (19/23), respectively.

Among the 55 patients, 32 were examined using only ^{18}F-DCFPyL PET/CT; 28 were diagnosed with clinically significant cancer, 2 with clinically insignificant cancer, and 2 with benign prostatic hyperplasia.

Of the 14 patients examined using only ^{18}F-DCFPyL PET/MR, 13 were diagnosed with clinically significant cancer, and 1 was diagnosed with clinically insignificant cancer. All of these 14 patients showed abnormal MR signals (low T2 signal, high DWI signal, decreased ADC value) in the area of PET-positive lesions.

TABLE 2 | Clinical characteristics of the 55 patients enrolled in the study.

Patient characteristics	Total (n = 55)	PET/CT-US (n = 32)	PET/MRI-US (n = 23)
Age (year; mean ± SD)	67.02 ± 9.05	67.91 ± 9.43	65.78 ± 8.53
PSA (ng/ml; mean ± SD)	14.37 ± 10.31	13.82 ± 7.97	15.13 ± 13.05
Target volume (cm^3; mean ± SD)	3.68 ± 2.18	4.14 ± 2.17	3.04 ± 2.08
SUVmax (mean ± SD)	15.47 ± 12.25	15.19 ± 12.53	15.85 ± 12.10
SUVmean (mean ± SD)	7.07 ± 4.68	7.37 ± 5.22	6.65 ± 3.87
Total number of cores from targeted biopsy	178	103	75
Positive cores on targeted biopsy (%)	146 (82.0%)	85 (82.5%)	61 (81.3%)
Men with prostate cancer	51 (92.7%)	30 (93.8%)	21 (91.3%)
No. Gleason score			
Gleason 3 + 3	4	2	2
Gleason 3 + 4	13	5	8
Gleason 4 + 3	16	10	6
Gleason 4 + 4	10	5	5
Gleason 5 + 3	1	1	0
Gleason 4 + 5	7	7	0
Men with clinically significant prostate cancer (%)	85.5% (47/55)	87.5% (28/32)	82.6% (19/23)

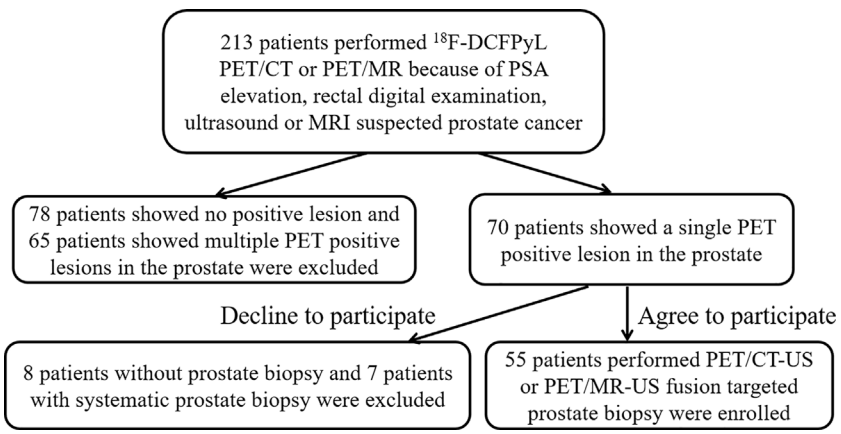

FIGURE 2 | Prostate biopsy algorithm of study subjects.

Of the nine patients that underwent successive examinations of ^{18}F-DCFPyL PET/CT and PET/MRI, seven examinations showed abnormal MR signal (decreased T2 signal, low ADC value, and increased DWI signal at both 1,000 and 2,000 s/mm^2) in the area of the PET-positive lesions (a typical case is shown in **Figure 3**), and the subsequent pathology confirmed prostate cancer in all cases. The other two patients showed normal MR signal in the area of the PET-positive lesions (a typical case is shown in **Figure 4**), and the subsequent biopsy confirmed prostatic hyperplasia and prostatitis.

DISCUSSION

This preliminary study demonstrates that for patients with clinical suspicion of prostate cancer and PSMA (^{18}F-DCFPyL) PET-positive lesions, using PET/CT-US or PET/MRI-US fusion-targeted prostate biopsy had a high detection rate of clinically significant prostate cancer. Furthermore, PET/MRI was able to identify the false positive lesions by PSMA PET. To our knowledge, this is the first study to explore the feasibility and diagnostic performance of PSMA PET/CT-US and PET/MRI-US fusion targeted prostate biopsy.

The trade-off between detection rate and the number of biopsy cores is a major concern with men suspected of prostate cancer. As the number of biopsy cores increases, the detection rate of prostate cancer increases but the portion of low-grade prostate cancer detected also increases. In addition, more biopsies lead to post-biopsy complications, including urinary retention, infection, hematuria, and hematochezia. Although prostate cancer screening strategies with repeated PSA testing and an extended-core prostate biopsy protocol reduces the incidence and mortality of advanced disease, it also leads to a significant proportion of overdiagnosis and consequently overtreatment for some low-risk tumors that may not result in symptoms or death from the disease during a patient's lifetime (13). Overdiagnosis and overtreatment of non-lethal tumors expose patients with insignificant prostate cancer to unnecessary side-effects. Thus, it is critical that the location and characteristics of prostate cancer are known before making treatment decisions.

A systematic 12-core transrectal ultrasound-guided biopsy is clinically recommended (14), and the rate of prostate cancer detection for a first systematic transrectal ultrasound-guided biopsy is typically 30–50% (15). Even the extended biopsy schemes with more than 12 cores may still miss almost a third of prostate cancers (16). Magnetic resonance imaging and ultrasonography (MRI-US) fusion targeted prostate biopsy has the advantages of accurate localization of lesions and real-time imaging, and it has been gradually applied to clinical practice. According to one systematic review, the median detection rate of prostate cancer was 43.4% with the standard biopsy strategy

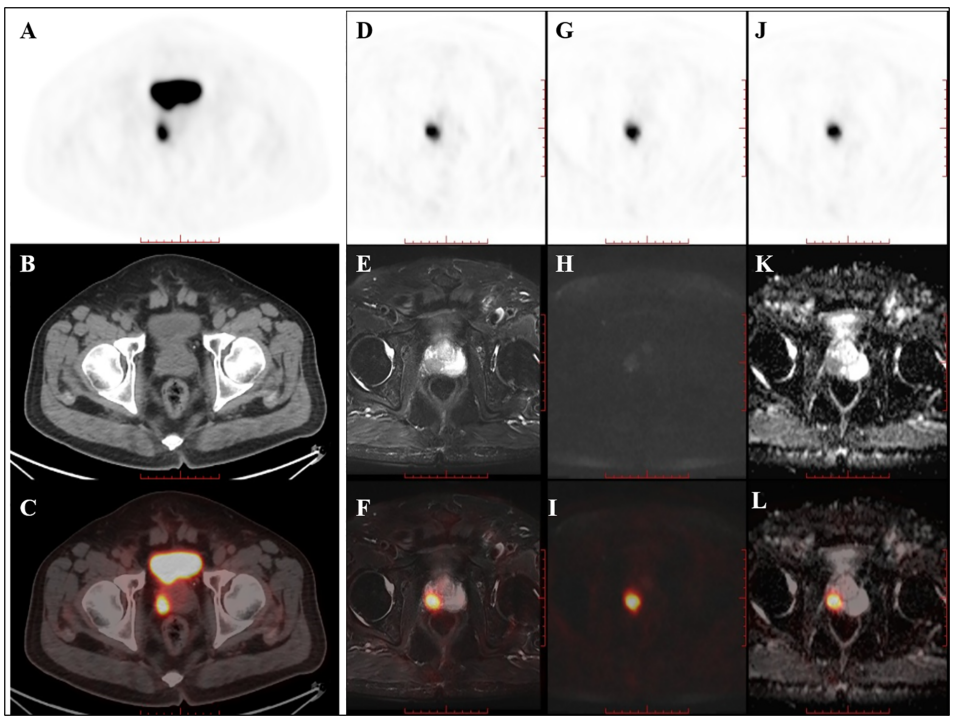

FIGURE 3 | PET/CT found one PET-positive lesion in the prostate gland (**A:** PET, **B**: CT, **C**: fused PET/CT). PET/MRI showed short T2 signal (**D**: PET, **E**: T2WI, **F**: fused PET/T2WI), high DWI signal (**G**: PET, **H**: DWI, **I**: fused PET/DWI), and a decreased ADC value at the site of the PET-positive lesion (**J**: PET, **K**: ADC map, **L**: fused PET/ADC map). The subsequent pathology confirmed prostate cancer.

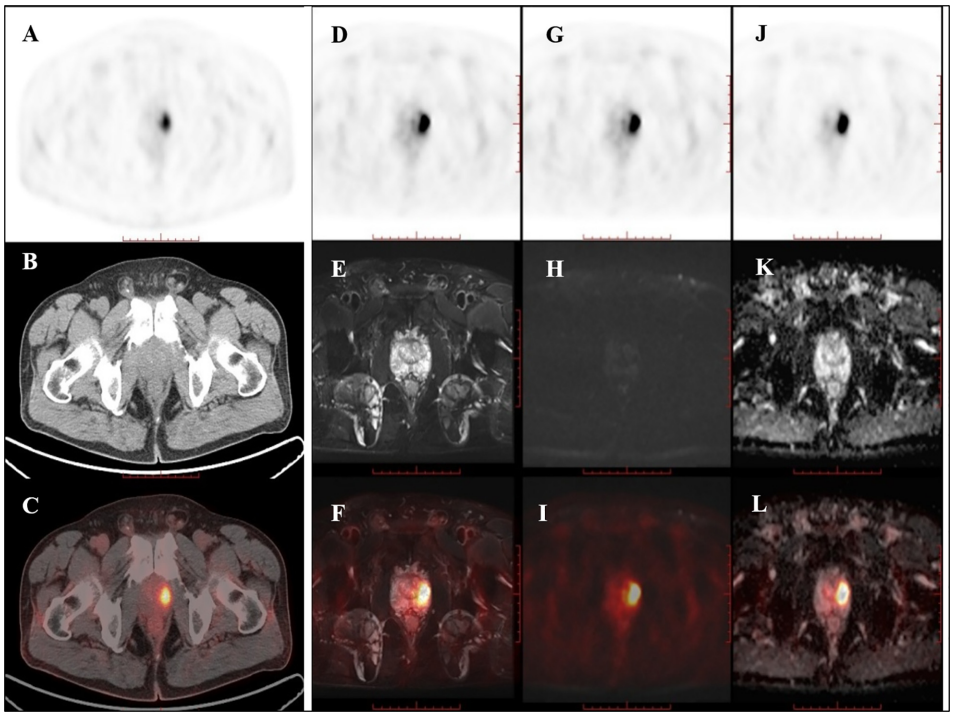

FIGURE 4 | PET/CT found one PET-positive lesion in the prostate gland (**A**: PET, **B**: CT, **C**: fused PET/CT). PET/MRI showed no obviously abnormal signal on T2WI (**D**: PET, **E**: T2WI, **F**: fused PET/T2WI), DWI (**G**: PET, **H**: DWI, **I**: fused PET/DWI), or the ADC map at the site of the PET-positive lesion (**J**: PET, **K**: ADC map, **L**: fused PET/ADC map). The subsequent pathology confirmed prostatic hyperplasia and prostatitis.

versus 50.5% with MRI-US image fusion targeted biopsy (17). No obvious advantage of MRI/US fusion-guided biopsy was observed in terms of the cancer detection rate compared to a standard systematic biopsy (18).

The accurate detection and delineation of intra-prostatic tumors are important for diagnosis and treatment decisions for patients with primary prostate cancer. Radionuclide ^{18}F or ^{68}Ga labeled PSMA PET imaging has great value in the diagnosis of prostate cancer. After prostatectomy, a histology map of the prostate was reconstructed, and the histological extension of each segment (132 segments from six patients) of the prostate was compared with PSMA PET images, the correlation of histological results with PSMA PET images showed a specificity and sensitivity of 92%, respectively (19). Some studies have validated the performance of PSMA PET/CT to define the gross tumor volume (GTV) through comparison with histology and have reported good results with high sensitivity and specificity in the detection of primary prostate cancer (19–21). In a recent study, 31 patients with previously negative prostate biopsy, but persistently elevated serum PSA, were imaged with ^{68}Ga-labeled PSMA PET/CT and then underwent both standard systematic biopsy and PET/CT-US fusion targeted biopsy (9): Among the 13 patients who were negative on PSMA PET imaging, none were diagnosed with clinically significant cancer; in the 18 patients positive by PSMA PET imaging, PET/CT-US fusion targeted biopsy detected all 12 patients with clinically significant cancer while standard systematic biopsy detected only 10 patients. These preliminary results suggest that PSMA PET might be a useful tool to identify and define malignant lesions prior to prostate biopsy. The results of our study showed that fusion of ^{18}F-DCFPyL PET/CT or PET/MRI with ultrasound is beneficial and feasible for guiding targeted prostate biopsy. In addition, this preliminary result indicates that ^{18}F-DCFPyL PET/CT-US or PET/MRI-US fusion targeted prostate biopsy may be a good way to reduce over-diagnosis of clinically insignificant prostate cancer and improve detection of clinically significant cancer. This method allows urologists to progress from blind, systematic biopsies to biopsies that are mapped, targeted, and tracked. More rigorous and comprehensive studies should be designed to prove the clinical value of PET/CT-US and PET/MRI-US fusion targeted prostate biopsies.

In this study, there were only four patients whose biopsy pathology was negative for prostate cancer yielding a 7.3% (4/55) false-positive rate for the ^{18}F-DCFPyL PET-positive lesions. There are several possibilities why the PET-positive lesions were not malignant. According to a case report, a patient with 2two focal PSMA-positive areas in the prostate gland, one corresponded to prostate cancer (Gleason score 4 + 3), while the other had no evidence of malignancy despite high PSMA expression on immunohistochemistry (22). Another explanation for the false positive cases may be the motion

during PET/CT examinations. Even if a true prostate cancer lesion is correctly declared by ^{18}F-DCFPyL PET, there is a possibility that it may be missed on biopsy if PET and CT indicated different locations. In contrast, urologists can consider the lesion localization provided by MR images when performing PET/MRI-US fusion targeted prostate biopsies to help improve the target position precision of biopsy cores.

Prostate cancer is typically characterized by abnormal MR signal (low signal on T2-weighted images, high signal on DWI, and low ADC value) and high PSMA uptake on PET/MR. Benign prostate diseases such as prostatitis, benign prostatic hyperplasia (BPH), and scarring are heterogeneous and may sometimes appear similar to prostate cancer on MRI (23), but they generally do not show obvious PSMA uptake. Prostate tumors with small size and low grade can have atypical manifestations on PSMA PET/MR. When compared with the radical prostatectomy specimens pathology, 5.9% intra-prostatic tumors were non-avid for ^{68}Ga-PSMA PET, and 5.4% intra-prostatic tumors were not detected by mp-MRI (24). PET/MRI is a new multi-modal imaging technique that is expected to improve the diagnostic performance of imaging, especially in cases where soft-tissue evaluation is crucial, such as prostate cancer (4, 25). In our study, nine patients underwent both ^{18}F-DCFPyL PET/CT and PET/MRI successively, and seven of these patients had abnormal MR signal in the area of the PET-positive lesions that were prostate cancer. The other two cases showed no obvious abnormal MR signal in the area of the PET-positive lesions were hyperplasia and prostatitis. PET/MRI is expected to further improve the prostate biopsy efficacy by reducing unnecessary prostate biopsies in some patients with PET-positive and MR-negative lesions.

Theoretically, targeted biopsies only for PSMA PET-positive lesion cannot rule out the presence of prostate cancer lesion in the PET-negative area of prostate. Thus, systematic prostate biopsy can provide added value to PET targeted biopsy. Zhang LL et al. (26) performed targeted biopsies alone for 25 patients with PSMA-avid lesions, and 21 patients were diagnosed with prostate cancer by targeted biopsy. The other four patients with initially negative by targeted biopsy underwent supplementary systematic biopsy, two of them were still negative, and two patients were confirmed as prostate cancer by the supplementary systematic biopsy. To our knowledge, there is no published literature making direct comparison between systematic biopsy and targeted biopsy in the same patient cohort.

PSMA labeled ligands appear very promising for diagnosis and treatment of prostate cancer (27). While MRI has been effective in the detection of significant prostate cancer, its use in the identification and quantification of extra-prostatic disease is limited. This gap is now being filled by PSMA PET (28). Published studies (4, 29) have shown that PSMA PET (PET/CT or PET/MRI) exceeds MRI in the diagnosis and characterization of prostate cancer. A systematic review and meta-analysis from 13 studies showed the overall pooled sensitivity of PSMA PET/CT for staging in prostate cancer were 92% (30). MRI-US fusion-guided biopsies detected more clinically significant cancers than standard biopsy techniques (12, 17, 31–33). In our study, prostate biopsies performed on targeted ^{18}F-DCFPyL PET-positive lesions of 55 patients had a high detection rate (51/55, 92.7%) of prostate cancer, and a high proportion (85.5%, 47/55) were clinically significant prostate cancer.

There are several limitations to our study. Firstly, the sample size was small, and the subsets of those getting PET/CT-US and PET/MRI-US guided biopsy were not randomized and prospectively powered but were rather convenience sample. Considering the limited number of cases in this study, we were unable to compare the diagnostic value between PET/CT-US and PET/MRI-US. Secondly, this study only used ^{18}F-DCFPyL PET/CT-US and PET/MRI-US guided biopsy for targeted PET-positive lesions; therefore, we were unable to directly compare them with the systematic prostate biopsies. Thirdly, this study used the biopsy pathology for the diagnosis of prostate cancer and did not compare the pathological results of the biopsy with radical prostatectomy. This is because some patients included in this study were given endocrine therapy before the surgical operation, which will lead to the failure of the postoperative Gleason score evaluation, and other patients did not undergo radical prostatectomy due to advanced age or other factors. Lastly, although PSMA PET/CT-US or PET/MRI-US fusion targeted biopsy is of high diagnostic value, it is costly and can only be available in some general hospitals with the ability to synthesize PSMA labeled ligands and the equipment of PET/CT or PET/MRI scanner.

CONCLUSION

In this study, ^{18}F-DCFPyL PET/CT-US or PET/MRI-US fusion-targeted prostate biopsy proved to be feasible for prostate cancer diagnosis due to its high detection rate of clinically significant prostate cancer. PET/MR can rule out some false PET-positive lesions, which may potentially reduce unnecessary prostate biopsies. For patients with pacemakers or claustrophobia, ^{18}F-DCFPyL PET/CT-US guided prostate biopsy remains a good alternative.

DATA AVAILABILITY STATEMENT

The original contributions presented in the study are included in the article/supplementary material. Further inquiries can be directed to the corresponding authors.

ETHICS STATEMENT

The studies involving human participants were reviewed and approved by the Ethics Committee of Chinese PLA General Hospital. The patients/participants provided their written informed consent to participate in this study.

AUTHOR CONTRIBUTIONS

BX and JG conceived of the presented idea. YL and HY developed the theory and performed the computations. JL, XZ, HS, and ML verified the analytical methods. All authors provided critical feedback and helped shape the research, analysis, and manuscript and discussed the results. All authors contributed to the article and approved the submitted version.

FUNDING

This work was financially supported by the National Natural Science Foundation of China project (No. 81571715), Achievement Transformation project of Chinese PLA General Hospital (No. 2018-TM-07), and Special scientific research topic of health care of Chinese PLA General Hospital (No. 19BJZ19).

REFERENCES

1. Thompson I, Thrasher JB, Aus G, Burnett AL, Canby-Hagino ED, Cookson MS, et al. Guideline for the Management of Clinically Localized Prostate Cancer: 2007 Update. *J Urol* (2007) 177(6):2106–31. doi: 10.1016/j.juro.2007.03.003
2. Wegelin O, Exterkate L, van der Leest M, Kelder JC, Bosch J, Barentsz JO, et al. Complications and Adverse Events of Three Magnetic Resonance Imaging-based Target Biopsy Techniques in the Diagnosis of Prostate Cancer Among Men with Prior Negative Biopsies: Results from the FUTURE Trial, a Multicentre Randomised Controlled Trial. *Eur Urol Oncol* (2019) 2(6):617–24. doi: 10.1016/j.euo.2019.08.007
3. Wang RS, Kim EH, Vetter JM, Fowler KJ, Shetty AS, Mintz AJ, et al. Determination of the Role of Negative Magnetic Resonance Imaging of the Prostate in Clinical Practice: Is Biopsy Still Necessary? *Urology* (2017) 102 (1):190–7. doi: 10.1016/j.urology.2016.10.040
4. Eiber M, Weirich G, Holzapfel K, Souvatzoglou M, Haller B, Rauscher I, et al. Simultaneous (68)Ga-PSMA HBED-CC PET/MRI Improves the Localization of Primary Prostate Cancer. *Eur Urol* (2016) 70(5):829–36. doi: 10.1016/j.eururo.2015.12.053
5. Rowe SP, Macura KJ, Mena E, Blackford AL, Nadal R, Antonarakis ES, et al. PSMA-Based [(18)F]DCFPyL PET/CT Is Superior to Conventional Imaging for Lesion Detection in Patients with Metastatic Prostate Cancer. *Mol Imaging Biol* (2016) 18(3):411–9. doi: 10.1007/s11307-016-0957-6
6. Cornelis FH, Durack JC, Morris MJ, Scher H I, Solomon SB. Effective Prostate-Specific Membrane Antigen-Based 18F-DCFPyL-Guided Cryoablation of a Single Positive Site in a Patient Believed to Be More Metastatic on 11C-Choline PET/CT. *Clin Nucl Med* (2017) 42(12):e516–8. doi: 10.1097/RLU.0000000000001846
7. Bauman G, Martin P, Thiessen JD, Taylor R, Moussa M, Gaed M, et al. [(18)F]-DCFPyL Positron Emission Tomography/Magnetic Resonance Imaging for Localization of Dominant Intraprostatic Foci: First Experience. *Eur Urol Focus* (2018) 4(5):702–6. doi: 10.1016/j.euf.2016.10.002
8. Dietlein M, Kobe C, Kuhnert G, Stockter S, Fischer T, Schomäcker K, et al. Comparison of [18F]DCFPyL and [68Ga]Ga-PSMA-HBED-CC for PSMA-PET Imaging in Patients with Relapsed Prostate Cancer. *Mol Imaging Biol* (2015) 17(4):575–84. doi: 10.1007/s11307-015-0866-0
9. Liu C, Liu T, Zhang Z, Zhang N, Du P, Yang Y, et al. PSMA PET/CT and standard plus PET/CT-Ultrasound fusion targeted prostate biopsy can diagnose clinically significant prostate cancer in men with previous negative biopsies. *J Nuclear Med* (2020) jnumed.119.235333. doi: 10.2967/jnumed.119.235333
10. Lopci E, Saita A, Lazzeri M, Lughezzani G, Colombo P, Buffi NM, et al. (68) Ga-PSMA Positron Emission Tomography/Computerized Tomography for Primary Diagnosis of Prostate Cancer in Men with Contraindications to or Negative Multiparametric Magnetic Resonance Imaging: A Prospective Observational Study. *J Urol* (2018) 200(1):95–103. doi: 10.1016/j.juro.2018.01.079
11. Davenport MS, Montgomery JS, Kunju LP, Siddiqui J, Shankar PR, Rajendiran T, et al. (18)F-Choline PET/mpMRI for Detection of Clinically Significant Prostate Cancer: Part 1. Improved Risk Stratification for MRI-Guided Transrectal Prostate Biopsies. *J Nucl Med* (2020) 61(3):337–43. doi: 10.2967/jnumed.119.225789
12. Kasivisvanathan V, Rannikko AS, Borghi M, Panebianco V, Mynderse LA, Vaarala MH, et al. MRI-Targeted or Standard Biopsy for Prostate-Cancer Diagnosis. *N Engl J Med* (2018) 378(19):1767–77. doi: 10.1056/NEJMoa1801993
13. Loeb S, Bjurlin MA, Nicholson J, Tammela TL, Penson DF, Carter HB, et al. Overdiagnosis and overtreatment of prostate cancer. *Eur Urol* (2014) 65 (6):1046–55. doi: 10.1016/j.eururo.2013.12.062
14. Matoso A, Epstein JI. Defining clinically significant prostate cancer on the basis of pathological findings. *Histopathology* (2019) 74(1):135–45. doi: 10.1111/his.13712
15. Arsov C, Rabenalt R, Blondin D, Quentin M, Hiester A, Godehardt E, et al. Prospective randomized trial comparing magnetic resonance imaging (MRI)-guided in-bore biopsy to MRI-ultrasound fusion and transrectal ultrasound-guided prostate biopsy in patients with prior negative biopsies. *Eur Urol* (2015) 68(4):713–20. doi: 10.1016/j.eururo.2015.06.008
16. Scattoni V, Russo A, Di Trapani E, Capitanio U, La Croce G, Montorsi F. Repeated biopsy in the detection of prostate cancer: When and how many cores. *Archivio Italiano di Urol e Androl* (2014) 86(4):311. doi: 10.4081/aiua.2014.4.311
17. Valerio M, Donaldson I, Emberton M, Ehdaie B, Hadaschik BA, Marks LS, et al. Detection of Clinically Significant Prostate Cancer Using Magnetic Resonance Imaging–Ultrasound Fusion Targeted Biopsy: A Systematic Review. *Eur Urol* (2015) 68(1):8–19. doi: 10.1016/j.eururo.2014.10.026
18. Yarlagadda VK, Lai WS, Gordetsky JB, Porter KK, Nix JW, Thomas JV, et al. MRI/US fusion-guided prostate biopsy allows for equivalent cancer detection with significantly fewer needle cores in biopsy-naive men. *Diagn Interv Radiol* (2018) 24(3):115–20. doi: 10.5152/dir.2018.17422
19. Rahbar K, Weckesser M, Huss S, Semjonow A, Breyholz HJ, Schrader AJ, et al. Correlation of Intraprostatic Tumor Extent with (6)(8)Ga-PSMA Distribution in Patients with Prostate Cancer. *J Nucl Med* (2016) 57(4):563–7. doi: 10.2967/jnumed.115.169243
20. Zamboglou C, Schiller F, Fechter T, Wieser G, Jilg CA, Chirindel A, et al. (68) Ga-HBED-CC-PSMA PET/CT Versus Histopathology in Primary Localized Prostate Cancer: A Voxel-Wise Comparison. *Theranostics* (2016) 6(10):1619–28. doi: 10.7150/thno.15344
21. Rowe SP, Gage KL, Faraj SF, Macura KJ, Cornish TC, Gonzalez-Roibon N, et al. (1)(8)F-DCFBC PET/CT for PSMA-Based Detection and Characterization of Primary Prostate Cancer. *J Nucl Med* (2015) 56 (7):1003–10. doi: 10.2967/jnumed.115.154336
22. Ferraro DA, Rupp NJ, Donati OF, Messerli M, Eberli D, Burger IA. 68Ga-PSMA-11 PET/MR Can Be False Positive in Normal Prostatic Tissue. *Clin Nucl Med* (2019) 44(4):e291–3. doi: 10.1097/RLU.0000000000002473
23. Lovegrove CE, Matanhelia M, Randeva J, Eldred-Evans D, Tam H, Miah S, et al. Prostate imaging features that indicate benign or malignant pathology on biopsy. *Transl Androl Urol* (2018) 7(Suppl 4):S420–35. doi: 10.21037/tau.2018.07.06
24. Kalapara AA, Nzenza T, Pan HY, Ballok Z, Ramdave S, O'Sullivan R, et al. Detection and localisation of primary prostate cancer using (68) Ga-PSMA PET/CT compared with mpMRI and radical prostatectomy specimens. *BJU Int* (2020) 126(1):83–90. doi: 10.1111/bju.14858
25. Souvatzoglou M, Eiber M, Martinez-Moeller A, Furst S, Holzapfel K, Maurer T, et al. PET/MR in prostate cancer: technical aspects and potential diagnostic value. *Eur J Nucl Med Mol Imaging* (2013) 40 1(Suppl):79–88. doi: 10.1007/s00259-013-2445-4
26. Zhang LL, Li WC, Xu Z, Jiang N, Zang SM, Xu LW, et al. (68)Ga-PSMA PET/CT targeted biopsy for the diagnosis of clinically significant prostate cancer compared with transrectal ultrasound guided biopsy: a prospective randomized single-centre study. *Eur J Nucl Med Mol Imaging* (2020) 48 (2):483–92. doi: 10.1007/s00259-020-04863-2
27. Giovacchini G, Giovannini E, Riondato M, Ciarmiello A. PET/CT with 68Ga-PSMA In Prostate Cancer: Radiopharmaceutical Background And Clinical Implications. *Curr Radiopharm* (2017) 11(1):4–13. doi: 10.2174/1874471010666171101121803

28. Eapen RS, Nzenza TC, Murphy DG, Hofman MS, Cooperberg M, Lawrentschuk N. PSMA PET applications in the prostate cancer journey: from diagnosis to theranostics. *World J Urol* (2019) 37(7):1255–61. doi: 10.1007/s00345-018-2524-z
29. Arslan A, Karaarslan E, Güner A, Sağlican Y, Tuna M, Özişik O, et al. Comparison of MRI, PSMA PET/CT, and Fusion PSMA PET/MRI for Detection of Clinically Significant Prostate Cancer. *J Comput assisted Tomography* (2020). doi: 10.1097/rct.0000000000001116
30. Lin CY, Lee MT, Lin C L, Kao CH. Comparing the Staging/Restaging Performance of 68Ga-Labeled Prostate-Specific Membrane Antigen and 18F-Choline PET/CT in Prostate Cancer: A Systematic Review and Meta-analysis. *Clin Nucl Med* (2019) 44(5):365–76. doi: 10.1097/RLU.0000000000002526
31. Gayet M, van der Aa A, Beerlage HP, Schrier BP, Mulders PFA, Wijkstra H. The value of magnetic resonance imaging and ultrasonography (MRI/US)-fusion biopsy platforms in prostate cancer detection: a systematic review. *BJU Int* (2016) 117(3):392–400. doi: 10.1111/bju.13247
32. Jayadevan R, Zhou S, Priester AM, Delfin M, Marks LS. Use of MRI-ultrasound Fusion to Achieve Targeted Prostate Biopsy. *J Vis Exp* (2019) 9 (146):e59231–9. doi: 10.3791/59231
33. Cattarino S, Forte V, Salciccia S, Drudi FM, Cantisani V, Sciarra A, et al. MRI ultrasound fusion biopsy in prostate cancer detection: Are randomized clinical trials reproducible in everyday clinical practice? *Urologia* (2019) 86(1):9–16. doi: 10.1177/0391560319834490

Conflict of Interest: Author ML was employed by company Siemens Healthineers Ltd., China. Author HS was employed by company Siemens Healthcare GmbH, Germany.

The remaining authors declare that the research was conducted in the absence of any commercial or financial relationships that could be construed as a potential conflict of interest.

frontiers in Oncology

SYSTEMATIC REVIEW
published: 04 May 2021
doi: 10.3389/fonc.2021.633833

Whole-Body MRI vs. PET/CT for the Detection of Bone Metastases in Patients With Prostate Cancer: A Systematic Review and Meta-Analysis

Yuefu Zhan[1,2], *Guangming Zhang*[1]*, *Mingliang Li*[1] and *Xiaobo Zhou*[3]

[1] West China Biomedical Big Data Center, West China Hospital, Sichuan University, Chengdu, China, [2] Department of Radiology, Hainan Women and Children's Medical Center, Hainan, China, [3] School of Biomedical Informatics, The University of Texas Health Science Center at Houston, Houston, TX, United States

Purpose: A recent meta-analysis in patients with non-small cell lung cancer showed no difference between whole-body magnetic resonance imaging (WBMRI) and positron emission tomography/computed tomography (PET/CT), but no such study is available for prostate cancer (PCa). This study aimed to compare WBMRI and PET/CT for bone metastasis detection in patients with PCa.

Materials and Methods: PubMed, Embase, and the Cochrane library were searched for papers published up to April 2020. The population was the patients with untreated prostate cancer diagnosed by WBMRI or PET/CT. The outcomes were the true positive and negative and false positive and negative rates for WBMRI and PET/CT. The summarized sensitivity, specificity, positive likelihood ratios (PLR), negative likelihood ratios (NLR), and diagnostic odds ratios (DOR) were calculated with their 95% confidence intervals (CIs).

Results: Four prospective and one retrospective study are included (657 patients). Significant differences are observed between WBMRI and PET/CT for sensitivity (WBMRI/PET/CT: 0.896; 95% CI: 0.813–0.987; $P = 0.025$) and NLR (WBMRI/PET/CT: 2.38; 95% CI: 1.13–5.01; $P = 0.023$), but not for specificity (WBMRI/PET/CT: 0.939; 95% CI: 0.855–1.031; $P = 0.184$) and PLR (WBMRI/PET/CT: 0.42; 95% CI: 0.08–2.22; $P = 0.305$). WBMRI has a similar a DOR compared with PET/CT (WBMRI/PET/CT: 0.13; 95% CI: 0.02–1.11; $P = 0.062$). The summary area under the receiver operating characteristic curves for WBMRI is 0.88 (standard error: 0.032) and 0.98 (standard error: 0.013) for PET/CT for diagnosing bone metastases in PCa.

Conclusion: PET/CT presents a higher sensitivity and NLR for the bone metastasis detection from PCa, whereas no differences are found for specificity and PLR, compared with WBMRI.

Keywords: prostate cancer, magnetic resonance imaging, positron emission tomography, computed tomography, bone metastasis, meta-analysis

OPEN ACCESS

Edited by:
Fabio Grizzi,
Humanitas Research Hospital, Italy

Reviewed by:
Michele Marchioni,
University of Studies G. d'Annunzio Chieti and Pescara, Italy
Ekaterina Laukhtina,
I.M. Sechenov First Moscow State Medical University, Russia

***Correspondence:**
Guangming Zhang
gmwell@126.com

Specialty section:
This article was submitted to Genitourinary Oncology, a section of the journal Frontiers in Oncology

Received: *26 November 2020*
Accepted: *19 February 2021*
Published: *04 May 2021*

Citation:
Zhan Y, Zhang G, Li M and Zhou X (2021) Whole-Body MRI vs. PET/CT for the Detection of Bone Metastases in Patients With Prostate Cancer: A Systematic Review and Meta-Analysis. Front. Oncol. 11:633833. doi: 10.3389/fonc.2021.633833

INTRODUCTION

Prostate cancer (PCa) is the most common cancer in males and among the most lethal cancers in men worldwide (1, 2, 12). About 10% of patients with PCa have bone metastasis at presentation, with a rate as high as 80% for patients with advanced PCa (3, 4), and about 33% of the remaining patients will develop metastases during follow-up (5, 6). In addition, patients presenting small numbers of metastases have a better prognosis than those with a widespread disease (7) and may benefit from salvage targeted therapies in the metastatic setting (8, 12).

In patients with PCa in whom distant metastases are suspected, whole-body imaging (WBI) (head, neck, torso, and the proximal part of the limbs) can be used to guide the treatments (8, 12). Among the available modalities, ^{18}F-fluoride (NaF) positron emission tomography/computed tomography (PET/CT), ^{18}F-fluorocholine (FCH) PET/CT, and whole-body magnetic resonance imaging (WBMRI) have been proposed for PCa metastasis detection (9, 10, 38). WBMRI enables the detection of lymph node metastases and distant metastases in one test (11). Multi-parametric MRI has a better performance than a classical bone scan and targeted X-ray for detecting bone metastasis (12) and might have better performance than PET/CT (13, 14). Choline PET/CT may have a better detection rate of bone metastases compared to bone scans at the initial staging or restaging after a biochemical recurrence in men with PCa (15). ^{18}F-choline PET may have poor sensitivity but high specificity for bone metastasis detection in men with PCa (16).

A recent meta-analysis has compared the diagnostic performance in staging between WBMRI and PET/CT in patients with non-small cell lung cancer and showed no difference between the two imaging modalities (17). There are no guidelines specific to the diagnosis of bone metastases in PCa, and there are no meta-analyses comparing WBMRI and PET/CT in PCa.

Therefore, the aim of this meta-analysis was to compare WBMRI and PET/CT for bone metastasis detection in patients with PCa. The results could provide some guidance for the treatment strategy of patients with PCa.

MATERIALS AND METHODS

Literature Search

This meta-analysis was conducted according to the Preferred Reporting Items for Systematic Reviews and Meta-Analyses (PRISMA) guidelines (18). Papers published up to April 2020 were searched for in PubMed, Embase, and the Cochrane library using the MeSH term "Prostatic Neoplasms," and relevant keywords such as "whole-body magnetic resonance imaging." The relevant articles were searched for using the PICO principle (19), followed by screening based on the eligibility criteria: (1) population: patients with untreated primary PCa who underwent WBMRI or PET/CT for bone metastasis detection; (2) interventions: both WBMRI and PET/CT for the diagnosis of bone metastases; (3) outcomes: the numbers of patients with true positive, false positive, false negative, and true negative results for WBMRI and PET/CT; (4) study type: focused on humans; and (5) language: limited to English.

Data Extraction

The study characteristics (authors, year of publication, the country where the study was performed, type of study design, PSA levels, type of PET/CT, and sample size), treatment parameters (number of case analyses) were based on patients or lesions, standard reference per the study, and age of the patients, and primary outcomes (true positive, false positive, false negative, and true negative results for WBMRI and PET/CT) were extracted by two authors (Yuefu Zhan and Guangming Zhang) independently. Discrepancies were solved by the discussion.

Quality of the Evidence

Four prospective cohort studies and one retrospective cohort study could be included. The quality assessment was conducted independently by two authors (Yuefu Zhan and Guangming Zhang) using the Quality Assessment of Diagnostic Accuracy Studies-2 (QUADAS-2) for this particular review (20). The risk of bias was evaluated using the risk of bias in non-randomized studies of interventions tool (ROBINS-I) (21). Discrepancies in the quality assessment were solved by discussion.

Statistical Analysis

The summarized sensitivity, specificity, positive likelihood ratios (PLR), negative likelihood ratios (NLR), and diagnostic odds ratios (DOR) are presented with their corresponding 95% confidence intervals (CIs) and were obtained by means of a bivariate regression model using random effects based on the true positive and negative and false positive and negative rates in each study. The summary receiver operating characteristic (ROC) curve and the area under the curve (AUC) for WBMRI and PET/CT were calculated using a hierarchical regression model. The effect estimates and the corresponding 95% CIs of the diagnostic parameters were available for each study. The summary ratios between WBMRI and PET/CT and 95% CIs for sensitivity, specificity, PLR, NLR, DOR, and AUC were computed by random-effects models. The heterogeneity across the included studies was calculated using the I^2 and Q statistic, and a $P < 0.05$ was regarded as significant heterogeneity. Two-sided $P < 0.05$ are considered statistically significant across the studies included. The statistical analyses were conducted using the MetaDiSc software (version 1.4) and STATA SE 14.0 software (StataCorp, College Station, TX, USA). No publication analysis could be performed because the number of included studies was <10 (22).

RESULTS

Selection and Characteristics of the Studies

Figure 1 presents the study selection process. A total of 158 records were initially identified, and 141 were examined after the duplicates were removed. Twenty-nine were preliminarily excluded, and 112 full-text articles were evaluated for eligibility. Among them, 107 were excluded (32 because of study aim/design, 45 because of the population, 25 because of

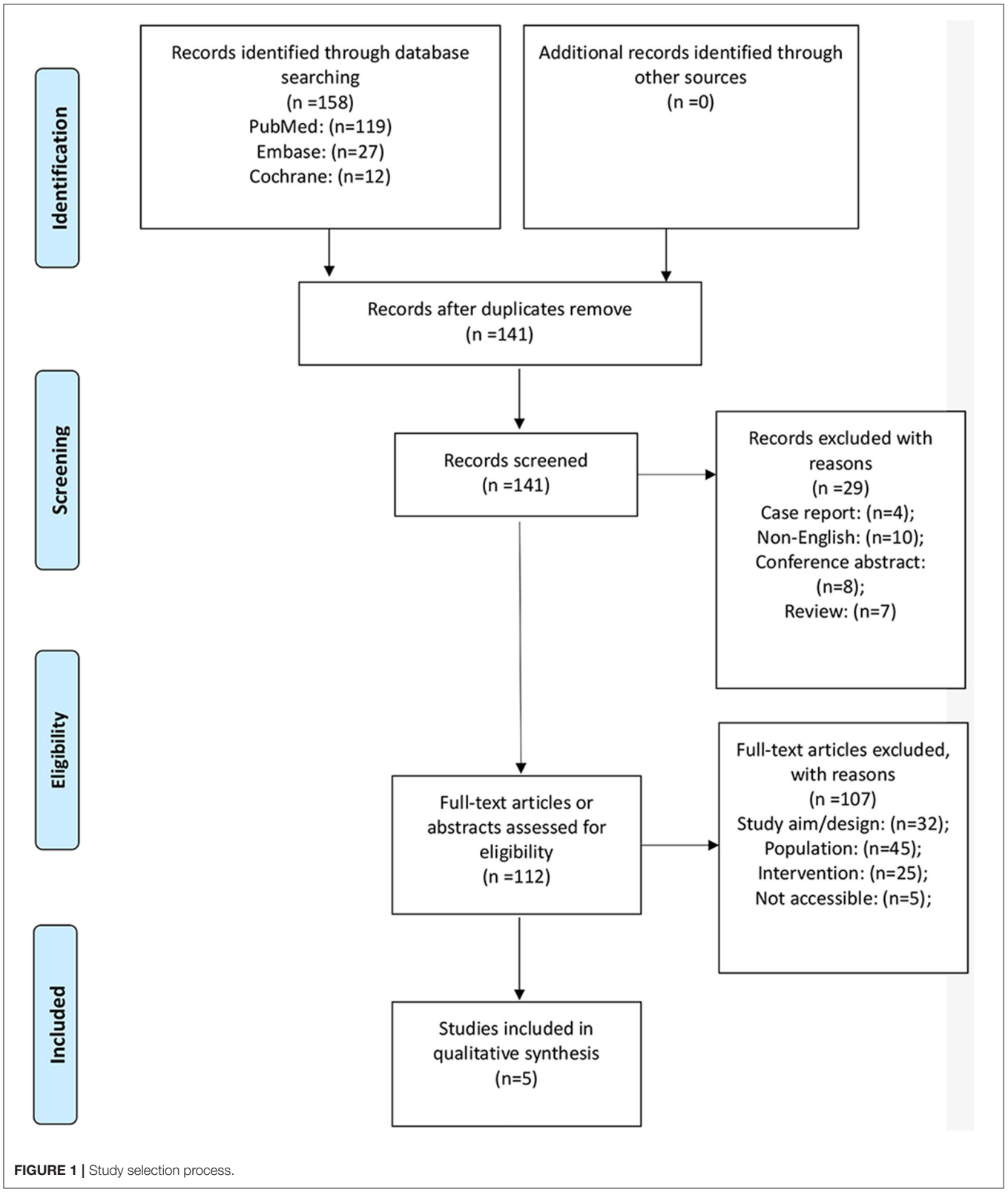

FIGURE 1 | Study selection process.

the intervention, and five because they were not accessible). Therefore, five studies were included (23–27).

There are four prospective studies (24–27) and one retrospective study (23). Three studies are based on the patient (24–27) and two on the lesions (23, 26). The five studies included 657 patients. **Table 1** presents the characteristics of the studies and the diagnostic values of WBMRI and PET/CT for each individual study. Two studies used ^{11}C-choline-PET/CT, two used F-NaF-PET/CT, and one used Ga-PSMA-PET/CT.

Table 2 presents the quality assessment of the studies included. One retrospective study (23) and three prospective studies (24–26) do not meet three criteria: avoidance of a case-control design, avoidance of inappropriate exclusions, and the use of a prespecified threshold. The study by Dyrberg et al. (27) meets only three criteria. For all five studies, it is uncertain whether the reference standard results were interpreted without knowledge of the results of the index test. **Supplementary Table 1** presents the ROBINS-I evaluation.

Sensitivity

The summary sensitivities for WBMRI and PET/CT for bone metastasis detection in PCa are 0.84 (95% CI: 0.77–0.89) and 0.94 (95% CI: 0.89–0.98), respectively (**Figure 2**). A significant difference is observed between WBMRI and PET/CT for sensitivity (ratio between WBMRI and PET/CT: 0.896; 95% CI: 0.813–0.987; $P = 0.025$; $I^2 = 0.0\%$, $P_{\text{heterogeneity}} = 0.686$) (**Supplementary Figure 1**; **Table 3**).

Specificity

The summary specificities for WBMRI and PET/CT for detecting bone metastases in PCa are 0.89 (95% CI: 0.86–0.91) and 0.98 (95% CI: 0.96–0.99), respectively (**Figure 3**). No significant difference is observed between WBMRI and PET/CT for specificity (ratio between WBMRI and PET/CT: 0.939; 95% CI: 0.855–1.031; $P = 0.184$; $I^2 = 78.8\%$, $P_{\text{heterogeneity}} = 0.001$) (**Supplementary Figure 2**; **Table 3**).

Positive Likelihood Ratio

The summary PLRs for WBMRI and PET/CT for detecting bone metastases in PCa are 6.89 (95% CI: 3.59–13.25) and 23.39 (95% CI: 2.56–214.03), respectively (**Supplementary Figure 3**). WBMRI is not associated with a significant difference in PLR compared with PET/CT (ratio between WBMRI and PET/CT: 0.42; 95% CI: 0.08–2.22; $P = 0.305$; $I^2 = 76.1\%$, $P_{\text{heterogeneity}} = 0.002$) (**Supplementary Figure 5**; **Table 3**).

Negative Likelihood Ratio

The summary NLRs for WBMRI and PET/CT for detecting bone metastases in PCa are 0.21 (95% CI: 0.14–0.29) and 0.07 (95% CI: 0.04–0.13), respectively (**Supplementary Figure 4**). WBMRI was associated with a significant difference in NLR compared with PET/CT (ratio between WBMRI and PET/CT: 2.38; 95% CI: 1.13–5.01; $P = 0.023$; $I^2 = 0.0\%$, $P_{\text{heterogeneity}} = 0.476$) (**Supplementary Figure 6**; **Table 3**).

Diagnostic Odds Ratio

The summary DOR in WBMRI for detecting bone metastases of PCa is 44.93 (95% CI: 14.44–139.80; $I^2 = 47.2\%$,

TABLE 1 | Characteristics of the studies included.

References	Country	Study design	Base of analysis	Standard reference	Type of PET/CT	PSA, Median (range), ng/ml	Age, y	WBMRI				Control (PET/CT)			
								TP	TN	FP	FN	TP	TN	FP	FN
Dyrberg et al. (27)	Denmark	PD	Patient	Determined as a panel diagnosis by three imaging specialists	^{11}C-Choline-PET/CT	30 (5–1,000)	75 ± 9	16	29	6	4	20	35	0	0
Jambor et al. (25)	Finland	PD	Patient	Consensus based on all imaging modalities, follow-up data, and laboratory results	F-NaF PET/CT	/	/	8	18	1	0	7	19	1	0
Mosavi et al. (24)	Sweden	PD	Patient	Consensus based on all imaging modalities, follow-up data	F-NaF PET/CT	14 (1.3–950)	67 (57–80)	4	10	2	0	4	7	5	0
Wieder et al. (26)	Germany	PD	Lesion	Clinical follow-up and histopathology	^{11}C-Choline-PET/CT	29.9 (1.0–670)	68 (54–80)	55	356	51	15	65	380	6	5
Eschmann et al. (23)	Germany	RD	Lesion	Consensus based on all imaging modalities, follow-up data, and laboratory results	Ga-PSMA-PET/CT	5.4 (0.15–200)	64.1 (51–79)	39	59	0	5	41	59	0	3

WBMRI, whole-body magnetic resonance imaging; PTC/CT, positron emission tomography/computed tomography; TP, true positive; TN, true negative; FP, false positive, FN, false negative; PD, prospective study; RD, retrospective study.

TABLE 2 | Quality evaluation of the included studies using the QUADAS-2 tool.

		References				
		Eschmann et al. (23)	**Mosavi et al. (24)**	**Jambor et al. (25)**	**Wieder et al. (26)**	**Dyrberg et al. (27)**
Patient selection	Was a consecutive or random sample of patients enrolled?	Y	Y	Y	Y	Y
	Was a case-control design avoided?	N	N	N	N	Y
	Did the study avoid inappropriate exclusions?	N	N	N	N	N
Index test(s)	Were the index test results interpreted without knowledge of the results of the reference standard?	Y	Y	Y	Y	U
	If a threshold was used, was it prespecified?	N	N	N	N	N
Reference standard	Is the reference standard likely to correctly classify the target condition?	Y	Y	Y	Y	N
	Were the reference standard results interpreted without knowledge of the results of the index test?	U	U	U	U	U
Flow and timing	Was there an appropriate interval between index test(s) and reference standard?	Y	Y	Y	Y	U
	Did all patients receive a reference standard?	Y	Y	Y	Y	U
	Did patients receive the same reference standard?	Y	Y	Y	Y	U
	Were all patients included in the analysis?	Y	Y	Y	Y	Y

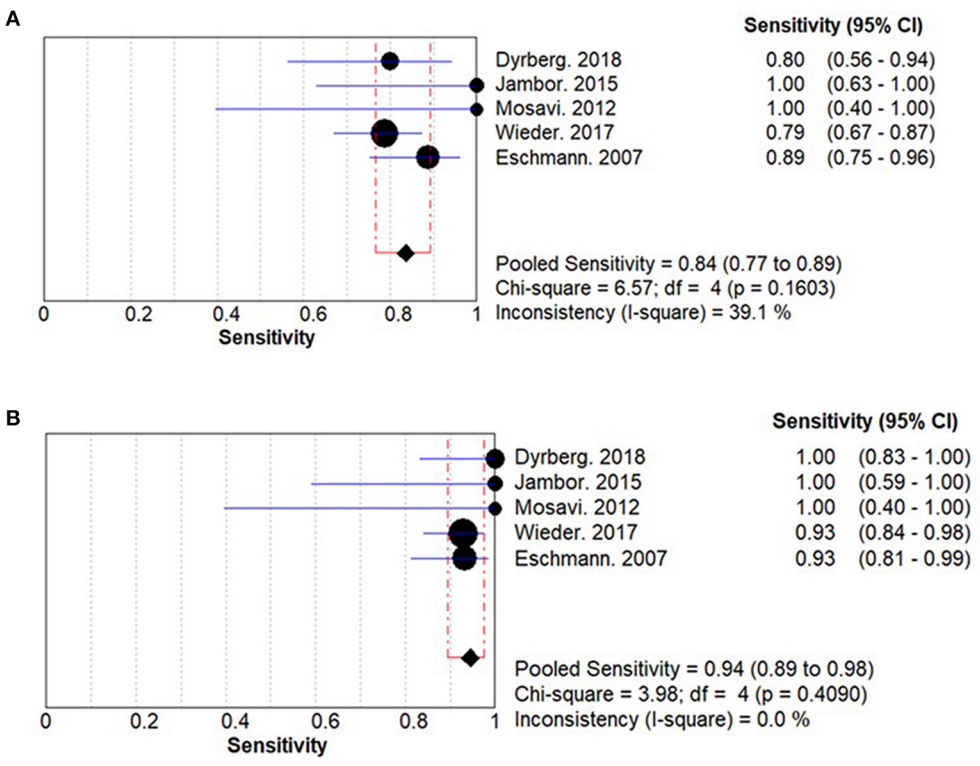

FIGURE 2 | Summary results for sensitivity for whole-body magnetic resonance imaging (WBMRI) **(A)** and positron emission tomography/computed tomography (PET/CT) **(B)**.

TABLE 3 | Relative risk ratios between WBMRI and PET/CT for sensitivity, specificity, PLR, NLR, and DOR.

Outcomes	*N*	Relative risk ratio (95% CI)	*P*	I^2 (%)	*P* for heterogeneity
Sensitivity	5	0.896 (0.813, 0.987)	0.025	0	0.686
Specificity	5	0.939 (0.855, 1.031)	0.184	78.8	0.001
PLR	5	0.416 (0.078, 1.031)	0.305	76.1	0.002
NLR	5	2.378 (1.127, 5.014)	0.023	0	0.476
DOR	5	0.130 (0.015, 1.108)	0.062	46.8	0.111

PLR, positive likelihood ratio; NLR, negative likelihood ratio; DOR, diagnostic odds ratio.

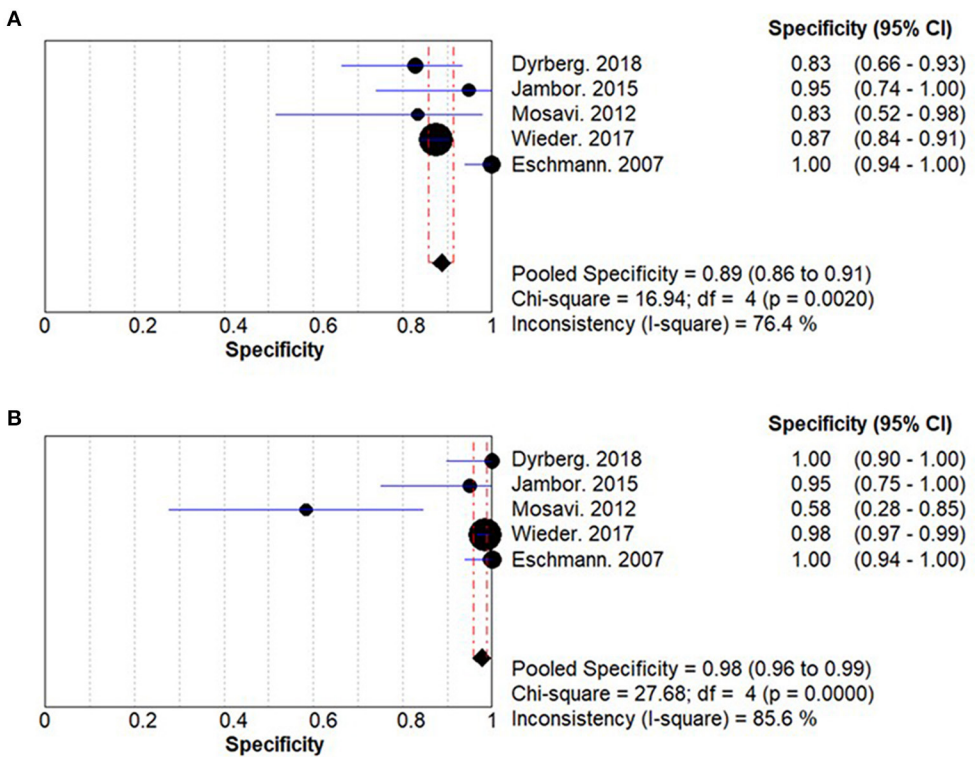

FIGURE 3 | Summary results for specificity in whole-body magnetic resonance imaging (WBMRI) **(A)** and positron emission tomography/computed tomography (PET/CT) **(B)**.

$P_{heterogeneity}$ = 0.108) (**Supplementary Figure 7**). The DOR of PET/CT is 402.92 (95% CI: 70.93–2288.91; I^2 = 51.3%, $P_{heterogeneity}$ = 0.084) (**Supplementary Figure 7**). WBMRI has a similar a DOR compared with PET/CT (ratio between WBMRI and PET/CT: 0.13; 95% CI: 0.02–1.11; P = 0.062; I^2 = 46.8%, $P_{heterogeneity}$ = 0.111) (**Supplementary Figure 8**).

ROC Analysis

The summary AUC for WBMRI is 0.88 (standard error: 0.032) and 0.98 (standard error: 0.013) for PET/CT for diagnosing bone metastases in PCa (**Supplementary Figure 9**).

Discussion

A recent meta-analysis revealed no difference between WBMRI and PET/CT in non-small cell lung cancer (17), but no such study is available for PCa. Therefore, this meta-analysis aims to compare WBMRI and PET/CT for bone metastasis detection in patients with PCa. The results show that PET/CT presents a higher sensitivity and NLR for bone metastasis detection from PCa, whereas no differences are found for specificity and PLR, compared with WBMRI.

A previous meta-analysis of four studies that compared WBMRI and PET/CT for the detection of metastases from lung cancer showed that there are no differences in the diagnostic yield of WBMRI and PET/CT for the detection of the M status of lung cancer (17). A meta-analysis of MRI, choline-PET/CT, bone SPECT, and bone scintigraphy for the detection of bone metastasis from PCa showed that on a per-patient basis, MRI was better than choline-PET/CT and scintigraphy, while on a per-lesion basis, choline-PET/CT was better than bone SPECT and scintigraphy (14). That meta-analysis did not consider the N stage. Similar results were also suggested by a review by Pesapane et al. (28) in breast cancer. Importantly, that review suggested that WMBRI could be more sensitive than PET/CT

for visceral metastases (28–30) and small hepatic and brain metastases (28, 31, 32), but WBMRI could be associated with more false-positives that PET/CT for bone metastases because bone marrow edema caused by benign lesions can appear as metastases on the apparent diffusion coefficient (ADC) map (28). A review highlighted that modern PET/CT protocols have a better diagnostic value than MRI for the detection of PCa metastases but that MRI still has a role to play (33). Since the present meta-analyses only examined bone metastases, this edema from benign lesions might explain, at least in part, why WBMRI fared less well than PET/CT. Nevertheless, other studies in patients with breast cancer reported a similar diagnostic value of WBMRI compared with ^{19}F-FDG PET/CT for bone metastases (34), highlighting that the DWI maps must not be read alone but in combination with the morphological changes (28). Gutzeit et al. (35) reported better performance of WBMRI compared with PET/CT for skeletal metastases in PCa and breast cancer, while the SKELETA trial (25) reported equivalent diagnostic value for bone metastases from PCa. Those conflicting results can be due to the differences in imaging protocols, magnet strength, and radiologist experience among the different centers. Nevertheless, both WBMRI and PET/CT have been shown to be better than CT and bone scan in terms of sensitivity and specificity for bone metastases (36).

The results of this meta-analysis must be considered in light of its limitations. In one study (25), besides PCa, the authors also included patients with breast cancer for comparing the detection of bone metastases; for this meta-analysis, the data pertaining to PCa had to be extracted. Of the five included studies, the analyses are patient-based in three studies and lesion-based in two. The cancer stage for inclusion varied among studies. Among the five studies, three different PET/CT modalities were used. Several studies did not report the true/false positive/negative, and those numbers had to be estimated based on the reported information, such as sensitivity, specificity, PLR, NLR, and the total number of cases, using the Revman software. Regarding stratification based on the risk group, as the risk level of the included patients was not specifically defined in the included studies, and as the number of studies was small, any results in terms of the stratification of risk groups would probably not lead to firm conclusions. This study had heterogeneity, which could be due to different patient risk levels among the included studies and variations in guidelines and country-level practice.

In conclusion, PET/CT presents a higher sensitivity and NLR for the detection of bone metastases from PCa, whereas no differences are found regarding specificity and PLR compared with WBMRI. Although this meta-analysis suggests a possibly better diagnostic performance of PET/CT in the detection of bone metastases in patients with PCa compared with WBMRI, compared with PET/CT, WBMRI is less expensive, more available, less time-consuming, and radiation-free. Further high-quality studies comparing the diagnostic performance of various imaging modalities and optimizing the WBMRI protocols are still needed to improve metastasis early detection in patients with PCa in clinical practice. In addition, novel prostate-specific membrane antigen-based imaging modalities are being developed, further improving the detection of PCa metastases (37). Those modalities will have to be examined in the future.

DATA AVAILABILITY STATEMENT

The original contributions presented in the study are included in the article/**Supplementary Material**, further inquiries can be directed to the corresponding author/s.

AUTHOR CONTRIBUTIONS

YZ carried out the studies, participated in collecting data, and drafted the manuscript. YZ and ML performed the statistical analysis and participated in its design. GZ reviewed and helped to draft the manuscript. XZ provided data analysis and a lot of advice to interpretation to the results, which ensure the high quality of this paper. All authors read and approved the final manuscript.

SUPPLEMENTARY MATERIAL

The Supplementary Material for this article can be found online at: https://www.frontiersin.org/articles/10.3389/fonc.2021.633833/full#supplementary-material

REFERENCES

1. Graham J, Kirkbride P, Cann K, Hasler E, Prettyjohns M. Prostate cancer: summary of updated NICE guidance. *BMJ*. (2014) 348:f7524. doi: 10.1136/bmj.f7524
2. Bray F, Ferlay J, Soerjomataram I, Siegel RL, Torre LA, Jemal A. Global cancer statistics 2018: GLOBOCAN estimates of incidence and mortality worldwide for 36 cancers in 185 countries. *CA Cancer J Clin*. (2018) 68:394–424. doi: 10.3322/caac.21492
3. Berruti A, Dogliotti L, Bitossi R, Fasolis G, Gorzegno G, Bellina M, et al. Incidence of skeletal complications in patients with bone metastatic prostate cancer and hormone refractory disease: predictive role of bone resorption and formation markers evaluated at baseline. *J Urol*. (2000) 164:1248–53. doi: 10.1016/S0022-5347(05)67149-2
4. Bubendorf L, Schöpfer A, Wagner U, Sauter G, Moch H, Willi N, et al. Metastatic patterns of prostate cancer: an autopsy study of 1,589 patients. *Hum Pathol*. (2000) 31:578–83. doi: 10.1053/hp.2000.6698
5. Pasoglou V, Michoux N, Van Damme J, Van Nieuwenhove S, Halut M, Triqueneaux P, et al. Pattern of metastatic deposit in recurrent prostate cancer: a whole-body MRI-based assessment of lesion distribution and effect of primary treatment. *World J Urol*. (2019) 37:2585–95. doi: 10.1007/s00345-019-02700-2
6. Sawicki LM, Kirchner J, Buddensieck C, Antke C, Ullrich T, Schimmöller L, et al. Prospective comparison of whole-body MRI and (68)Ga-PSMA PET/CT for the detection of biochemical recurrence of prostate cancer after radical prostatectomy. *Eur J Nucl Med Mol Imaging*. (2019) 46:1542–50. doi: 10.1007/s00259-019-04308-5
7. Liu D, Kuai Y, Zhu R, Zhou C, Tao Y, Han W, et al. Prognosis of prostate cancer and bone metastasis pattern of patients: a SEER-based study and a local hospital based study from China. *Sci Rep*. (2020) 10:9104. doi: 10.1038/s41598-020-64073-6
8. Mottet, N., Bastian, P. J., Bellmunt, J., R.C.N., v.d,.B., Bolla, M., et al. (2014). *European Association of Urology (EAU). Guidelines on Prostate Cancer*. Arnhem: European Association of Urology

9. Adeleke S, Latifoltojar A, Sidhu H, Galazi M, Shah TT, Clemente J, et al. Localising occult prostate cancer metastasis with advanced imaging techniques (LOCATE trial): a prospective cohort, observational diagnostic accuracy trial investigating whole-body magnetic resonance imaging in radio-recurrent prostate cancer. *BMC Med Imaging*. (2019) 19:90. doi: 10.1186/s12880-019-0380-y
10. Sonni I, Minamimoto R, Baratto L, Iagaru A. Response to: letter to the editors: re: simultaneous PET/MRI in the evaluation of breast and prostate cancer using combined Na[(18)F]F and [(18)F]FDG: a focus on skeletal lesions. *Mol Imaging Biol*. (2020) 22:221–2. doi: 10.1007/s11307-020-01471-2
11. Sartor O, Eisenberger M, Kattan MW, Tombal B, Lecouvet F. Unmet needs in the prediction and detection of metastases in prostate cancer. *Oncologist*. (2013) 18:549–57. doi: 10.1634/theoncologist.2013-0027
12. *NCCN Clinical Practice Guidelines in oncology (NCCN Guidelines). Prostate Cancer. Version 2.2020.* (2020). Fort Washington: National Comprehensive Cancer Network.
13. Lecouvet FE, El Mouedden J, Collette L, Coche E, Danse E, Jamar F, et al. Can whole-body magnetic resonance imaging with diffusion-weighted imaging replace Tc 99m bone scanning and computed tomography for single-step detection of metastases in patients with high-risk prostate cancer? *Eur Urol*. (2012) 62:68–75. doi: 10.1016/j.eururo.2012.02.020
14. Shen G, Deng H, Hu S, Jia Z. Comparison of choline-PET/CT, MRI, SPECT, and bone scintigraphy in the diagnosis of bone metastases in patients with prostate cancer: a meta-analysis. *Skeletal Radiol*. (2014) 43:1503–13. doi: 10.1007/s00256-014-1903-9
15. von Eyben FE, Kairemo K. Meta-analysis of (11)C-choline and (18)F-choline PET/CT for management of patients with prostate cancer. *Nucl Med Commun*. (2014) 35:221–30. doi: 10.1097/mnm.0000000000000040
16. Beheshti M, Vali R, Waldenberger P, Fitz F, Nader M, Hammer J, et al. The use of F-18 choline PET in the assessment of bone metastases in prostate cancer: correlation with morphological changes on CT. *Mol Imaging Biol*. (2009) 11:446–54. doi: 10.1007/s11307-009-0217-0
17. Machado Medeiros T, Altmayer S, Watte G, Zanon M, Basso Dias A, Henz Concatto N, et al. 18F-FDG PET/CT and whole-body MRI diagnostic performance in M staging for non-small cell lung cancer: a systematic review and meta-analysis. *Eur Radiol*. (2020) 30:3641–9. doi: 10.1007/s00330-020-06703-1
18. Selçuk AA. A Guide for Systematic Reviews: PRISMA. *Turk Arch Otorhinolaryngol*. (2019) 57:57–8. doi: 10.5152/tao.2019.4058
19. Aslam S, Emmanuel P. Formulating a researchable question: A critical step for facilitating good clinical research. *Indian J Sex Transm Dis AIDS*. (2010) 31:47–50. doi: 10.4103/0253-7184.69003
20. Whiting PF, Rutjes AW, Westwood ME, Mallett S, Deeks JJ, Reitsma JB, et al. QUADAS-2: a revised tool for the quality assessment of diagnostic accuracy studies. *Ann Intern Med*. (2011) 155:529–36. doi: 10.7326/0003-4819-155-8-201110180-00009
21. Sterne JA, Hernan MA, Reeves BC, Savovic J, Berkman ND, Viswanathan M, et al. ROBINS-I: a tool for assessing risk of bias in non-randomised studies of interventions. *BMJ*. (2016) 355:i4919. doi: 10.1136/bmj.i4919
22. Higgins JPT, Thomas J, Chandler J, Cumpston M, Li T, Page M, et al. *Cochrane Handbook for Systematic Reviews of Interventions version 6.0 (updated July 2019)*. London: Cochrane Collaboration (2019).
23. Eschmann SM, Pfannenberg AC, Rieger A, Aschoff P, Müller M, Paulsen F, et al. Comparison of 11C-choline-PET/CT and whole body-MRI for staging of prostate cancer. *Nuklearmedizin*. (2007) 46:161–168; quiz N147-168. doi: 10.1160/nukmed-0075
24. Mosavi F, Johansson S, Sandberg DT, Turesson I, Sörensen J, Ahlström H. Whole-body diffusion-weighted MRI compared with (18)F-NaF PET/CT for detection of bone metastases in patients with high-risk prostate carcinoma. *AJR Am J Roentgenol*. (2012) 199:1114–20. doi: 10.2214/ajr.11.8351
25. Jambor I, Kuisma A, Ramadan S, Huovinen R, Sandell M, Kajander S, et al. Prospective evaluation of planar bone scintigraphy, SPECT, SPECT/CT, 18F-NaF PET/CT and whole body 1.5T MRI, including DWI, for the detection of bone metastases in high risk breast and prostate cancer patients: SKELETA clinical trial. *Acta Oncol*. (2016) 55:59–67. doi: 10.3109/0284186x.2015.1027411
26. Wieder H, Beer AJ, Holzapfel K, Henninger M, Maurer T, Schwarzenboeck S, et al. 11C-choline PET/CT and whole-body MRI including diffusion-weighted imaging for patients with recurrent prostate cancer. *Oncotarget*. (2017) 8:66516–27. doi: 10.18632/oncotarget.16227
27. Dyrberg E, Hendel HW, Huynh THV, Klausen TW, Løgager VB, Madsen C, et al. (68)Ga-PSMA-PET/CT in comparison with (18)F-fluoride-PET/CT and whole-body MRI for the detection of bone metastases in patients with prostate cancer: a prospective diagnostic accuracy study. *Eur Radiol*. (2019) 29:1221–30. doi: 10.1007/s00330-018-5682-x
28. Pesapane F, Downey K, Rotili A, Cassano E, Koh DM. Imaging diagnosis of metastatic breast cancer. *Insights Imaging*. (2020) 11:79. doi: 10.1186/s13244-020-00885-4
29. Steinborn MM, Heuck AF, Tiling R, Bruegel M, Gauger L, Reiser MF. Whole-body bone marrow MRI in patients with metastatic disease to the skeletal system. *J Comput Assist Tomogr*. (1999) 23:123–9. doi: 10.1097/00004728-199901000-00026
30. Engelhard K, Hollenbach HP, Wohlfart K, von Imhoff E, Fellner FA. Comparison of whole-body MRI with automatic moving table technique and bone scintigraphy for screening for bone metastases in patients with breast cancer. *Eur Radiol*. (2004) 14:99–105. doi: 10.1007/s00330-003-1968-7
31. Schmidt GP, Baur-Melnyk A, Haug A, Heinemann V, Bauerfeind I, Reiser MF, et al. Comprehensive imaging of tumor recurrence in breast cancer patients using whole-body MRI at 1.5 and 3 T compared to FDG-PET-CT. *Eur J Radiol*. (2008) 65:47–58. doi: 10.1016/j.ejrad.2007.10.021
32. Michaels AY, Keraliya AR, Tirumani SH, Shinagare AB, Ramaiya NH. Systemic treatment in breast cancer: a primer for radiologists. *Insights Imaging*. (2016) 7:131–44. doi: 10.1007/s13244-015-0447-4
33. Turpin A, Girard E, Baillet C, Pasquier D, Olivier J, Villers A, et al. Imaging for metastasis in prostate cancer: a review of the literature. *Front Oncol*. (2020) 10:55. doi: 10.3389/fonc.2020.00055
34. Heusner TA, Kuemmel S, Koeninger A, Hamami ME, Hahn S, Quinsten A, et al. Diagnostic value of diffusion-weighted magnetic resonance imaging (DWI) compared to FDG PET/CT for whole-body breast cancer staging. *Eur J Nucl Med Mol Imaging*. (2010) 37:1077–86. doi: 10.1007/s00259-010-1399-z
35. Gutzeit A, Doert A, Froehlich JM, Eckhardt BP, Meili A, Scherr P, et al. Comparison of diffusion-weighted whole body MRI and skeletal scintigraphy for the detection of bone metastases in patients with prostate or breast carcinoma. *Skeletal Radiol*. (2010) 39:333–43. doi: 10.1007/s00256-009-0789-4
36. Yang HL, Liu T, Wang XM, Xu Y, Deng SM. Diagnosis of bone metastases: a meta-analysis comparing 8FDG PET, CT, MRI and bone scintigraphy. *Eur Radiol*. (2011) 21:2604–17. doi: 10.1007/s00330-011-2221-4
37. Anttinen M, Ettala O, Malaspina S, Jambor I, Sandell M, Kajander S, et al. A prospective comparison of (18)F-prostate-specific membrane antigen-1007 positron emission tomography computed tomography, whole-body 1.5 T magnetic resonance imaging with diffusion-weighted imaging, and single-photon emission computed tomography/computed tomography with traditional imaging in primary distant metastasis staging of prostate cancer (PROSTAGE). *Eur Urol Oncol*. (2020). 2020:S2588-9311(20)30090-0. doi: 10.1016/j.euo.2020.06.012
38. Gauthé M, Aveline C, Lecouvet F, Michaud L, Rousseau C, Tassart M, et al. Impact of sodium (18)F-fluoride PET/CT, (18)F-fluorocholine PET/CT and whole-body diffusion-weighted MRI on the management of patients with prostate cancer suspicious for metastasis: a prospective multicentre study. *World J Urol*. (2019) 37:1587–95. doi: 10.1007/s00345-018-2547-5

Conflict of Interest: The authors declare that the research was conducted in the absence of any commercial or financial relationships that could be construed as a potential conflict of interest.

frontiers | Frontiers in Oncology

TYPE Original Research
PUBLISHED 01 December 2022
DOI 10.3389/fonc.2022.1025355

OPEN ACCESS

EDITED BY
Shomik Sengupta,
Eastern Health Clinical School,
Monash University, Australia

REVIEWED BY
Jianbo Li,
Case Western Reserve University,
United States
Kazumi Kamoi,
Saiseikai Shigaken Hospital, Japan

*CORRESPONDENCE
Christian Wetterauer
christian.wetterauer@usb.ch

†These authors have contributed equally to this work and share first authorship

SPECIALTY SECTION
This article was submitted to Genitourinary Oncology, a section of the journal Frontiers in Oncology

RECEIVED 22 August 2022
ACCEPTED 14 November 2022
PUBLISHED 01 December 2022

CITATION
Walter M, Trotsenko P, Breit H-C, Keller N, Meyer A, Winkel DJ, Seifert HH and Wetterauer C (2022) Safety profile of robotic-assisted transperineal MRI-US-fusion guided biopsy of the prostate. *Front. Oncol.* 12:1025355. doi: 10.3389/fonc.2022.1025355

Safety profile of robotic-assisted transperineal MRI-US-fusion guided biopsy of the prostate

Manuel Walter[1†], Pawel Trotsenko[1†], Hanns-Christian Breit[2], Nicola Keller[3], Anja Meyer[1], David Jean Winkel[2], Hans Helge Seifert[1] and Christian Wetterauer[1,3,4*]

[1]Department of Urology, University Hospital Basel, Basel, Switzerland, [2]Department of Radiology, University Hospital Basel, Basel, Switzerland, [3]University of Basel, Basel, Switzerland, [4]Department of Medicine, Faculty of Medicine and Dentistry, Danube Private University, Krems, Austria

Introduction: Robotic-assisted transperineal MRI-US-fusion guided biopsy of the prostate is a novel and highly accurate procedure. The aim of this study was to evaluate the MonaLisa prostate biopsy system in terms of safety, tolerability, and patient-related outcomes.

Methods: This prospective study included 228 patients, who had undergone Robotic-assisted transperineal MRI-US-fusion guided biopsy of the prostate at the University Hospital Basel between January 2020 and June 2022. Peri-operative side effects, functional outcomes and patient satisfaction were assessed.

Results: Mean pain score on the day of biopsy was 1.3 points on VAS, which remained constant on the day after biopsy. Overall, 32 of 228 patients (14%) developed grade I complications according to Clavien-Dindo classification. No higher-grade complications occurred. Gross haematuria, hematospermia and acute urinary retention occurred in 145/228 (63.6%), 98/228 (43%) and 32/228 (14%) patients, respectively. One patient (0.4%) developed urinary tract infection.

Conclusions: Robotic-assisted transperineal MRI-US-fusion guided biopsy of the prostate performed under general anesthesia is a safe and well tolerated procedure. This technique allows to omit perioperative prophylaxis and at the same time minimizes the risk of infectious complications. We attribute the favorable risk profile and tolerability to the minimal invasive approach *via* two entry points.

KEYWORDS

biopsy, prostate, robotic-assisted, safety, transperineal

Introduction

Prostate cancer (PCa) is the second most common malignant disease in men worldwide (1) Suspicion for PCa is based on pathological digital rectal examination (DRE), prostate specific antigen (PSA) or magnetic resonance image (MRI) findings and indicates, as standard of care, a biopsy of the prostate (PB_x) for histopathological verification (2). PB_x represents one of the most common urological procedures, with more than 1 million interventions performed in Europe and the United States every year (3). PB_x can be performed *via* a transrectal (TR) or transperineal (TP) route, each approach being associated with specific benefits and limitations. TR offers practicability in the in-office setup due to feasibility under local anesthesia reflected by the majority of PB_x being performed *via* the TR approach in the US (93.1 – 99.2%) (4). However, punction of the prostate through the rectum ampulla is associated with a significant risk for infectious complications (5). The incidence for infectious complications after TR-PB_x ranges between 5 and 7% with a hospitalization rate of about 2% (2, 3). Rising rates of fluorchinolone-resistance organisms, which could be found in up to 30% of rectal swab cultures prior to TR-PB_x, possibly aggravate the situation (2). With the TP approach infectious complications are significantly lower, even negligible (2, 6, 7). Technological advances in diagnostics of PCa, like the implementation of multiparametric MRI (mpMRI) and MRI-targeted PB_x have increased the detection rate of significant PCa, simultaneously decreasing the detection rate of clinical insignificant PCa (8). Newly available robotic-assisted biopsy systems like MonaLisa combine the robotic precision with the preferable transperineal approach. Furthermore, this system allows for a minimal-invasive and gentle sampling requiring only two puncture sites and thus promising lower complication rates and patient tolerability. The robotic-assisted MRI-TRUS-fusion allows for highly precise biopsies with maximal reproducibility, while safely sparing the neurovascular bundle. So far there are no prospective reports on patient related outcomes in terms of tolerability and complications after robotic-assisted transperineal MRI-US-fusion guided biopsy of the prostate (RA-TP-PB_x). An upcoming PB_x bearing uncertainty regarding a suspected malignant disease as well as the interventional risks, poses a physical and psychological burden for patients. Therefore, the ideal biopsy technique is as painless as possible and combines low complication rates with upmost diagnostic precision. The aim of this study was to evaluate the MonaLisa prostate biopsy system in terms of safety, tolerability, and patient-related outcomes.

Abbreviations: 5-ARI, 5-alpha-reductase inhibitor; AC, anticoagulation; AIDS, acquired immune deficiency syndrome; AUR, acute urinary retention; BC, biopsy cores; DRE, digital rectal examination; ICIQ, International Consultation on Incontinence Questionnaire – Urinary Incontinence; IPSS, International Prostate Symptom Score; i.v., intravenous; INF, histology-proven inflammation; LUTS, lower urinary tract symptoms; mpMRI, multiparametric MRI; MRI, magnetic resonance image; MUD, male urinary disfunction; MMUD, medication for male urinary dysfunction; NIH-CPSI, National Institutes of Health - Chronic Prostatitis Symptom Index; PB_x, biopsy of the prostate; PCa, Prostate cancer; p.o., per os; PSA, prostate specific antigen; PV, prostate volume; QoL, quality of life; RA-TP-PB_x, Robotic-assisted transperineal MRI-US-fusion guided biopsy of the prostate; SD, standard deviation; TP, transperineal; TP-PB_x, transperineal biopsy of the prostate; TR, transrectal; TR-PB_x, transrectal biopsy of the prostate; TRUS, transrectal ultrasound; UTI, urinary tract infections; VAS, visual analog scale.

Materials and methods

This prospective study analyses the safety profile and functional results of 228 patients, who had undergone RA-TP-PB_x at the University Hospital Basel between January 2020 and June 2022. Indication for biopsy resulted from suspicious DRE, elevated PSA values or suspicious lesions in mpMRI. Imaging was performed in all patients prior to biopsy, suspicious lesions were classified according to PI-RADS v2.1. The study was approved by the local ethics committee (ID 2020-01381) and was performed in accordance with the Declaration of Helsinki. All patients provided written informed consent. Side effects, clinical, functional, histological, and demographic data were collected and assessed. In addition, medication for male urinary dysfunction, type of anticoagulation and immunodeficiency, including diabetes mellitus type 2, immunosuppressants or acquired immune deficiency syndrome (AIDS), were recorded.

Biopsy technique

A 3D model of the prostate, including suspicious lesions, was generated by a skilled team of radiologists (DJW, PB) and RA-TP-PBx was performed with an iSR'obot™ MonaLisa device (Biobot©) (Figure 1) by one experienced surgeon (CW). Anticoagulation with factor Xa inhibitors and phenprocoumon was discontinued and bridged with low-molecular-weight heparin according to the individual risk of a thromboembolic event. Therapy with acetylsalicylic acid was continued and was used to bridge patients under therapy with clopidogrel. Standardized, anti-infective prophylaxis was administered to the first 60 (26.3%) patients. After the initial implementation phase of the new biopsy technique anti-infective prophylaxis was omitted if not indicated by positive findings in preoperative urine culture. After RA-TP-PB_x no transurethral catheter was used by default. A detailed description of our procedure has already been published previously (9).

Analysis and statistical methods

Validated questionnaires, including "International Prostate Symptom Score" (IPSS) with quality of life (QoL), "International Consultation on Incontinence Questionnaire – Urinary Incontinence" (ICIQ), and "National Institutes of Health - Chronic Prostatitis Symptom Index" (NIH-CPSI) were used to assess functional outcome before and about one week after biopsy. Additionally, the occurrence of side-effects including acute urinary retention (AUR), gross hematuria, hematospermia, pain according to visual analog scale for pain (VAS, 1 – 10 points), urinary tract infections (UTI), local complications and patient satisfaction were collected and analyzed.

Database was created using Excel (Microsoft©), statistical analyses were performed with SPSS Statistics 24.0 (IBM©). The Chi-squared and Fisher`s exact tests were used to compare nominal data. For determination of significant differences among the normally distributed data the Student`s t test (dependent/independent) was applied. Logistic regression was used for binary classification, i.e. to estimate the posterior probability of a binary response based on a list of independent predictor variables. This probability is described by a generalized linear model. Odd`s ratio was performed for risk assessment. All tests were performed at a two-sided significance level of $\alpha = 0.05$.

Results

Transperineal robotic-assisted biopsy of the prostate was successfully performed in 228 men with suspicious mpMRI-lesions and/or PSA-constellation. Mean (range) age, PSA, and prostate volume (PV) were 64.9 years (46 – 84), 11.8 ng/ml (0.2 - 561) and 48.4 ml (9 – 310), respectively. Detailed patient baseline characteristics are summarized in Table 1. At the time of biopsy, 63/228 (27.6%) patients took regular medication for male urinary dysfunction. 59/228 (25.9%) took anticoagulant medication, of which 38 patients had biopsy under ongoing antiplatelet therapy. 38/228 (16.7%) patients presented a form of immunodeficiency as stated in the methods. Mean pain score on the day of biopsy was 1.3 points on VAS, which remained constant on the day after biopsy (1.2 points). Overall, 32 of 228 patients (14%) developed grade I complications according to Clavien-Dindo classification. No higher-grade complications occurred. The most common side-effect observed after biopsy was gross haematuria 145/228 (63.6%), which was self-limiting and none of these patients required treatment. 59/145 (25.9%) patients reported gross haematuria duration of more than 3 days. Hematospermia occurred in 98/228 (43%) patients. Anticoagulant therapy, continued antiplatelet medication, PV (≥ 40 ml), biopsy proven inflammation or number of biopsy cores (≥ 25) had no significant influence on occurrence of haematuria/-spermia. Acute urinary retention (AUR) occurred in 32/228 (14%) patients. Patients who developed AUR had a significant higher baseline IPSS-Score (13.2 vs. 10; p 0.02), a bigger prostate volume (61.4 vs. 46 ml; p 0.008) and more biopsy cores taken (29 vs. 25; p 0.009). However, number of biopsy cores (≥ 25), PV (≥ 40 ml) and medication for male urinary dysfunction couldn`t be identified as individual risk factors for the occurrence of AUR. IPSS ≥ 8 (moderate/severe symptoms) and biopsy proven inflammation showed only a tendential association

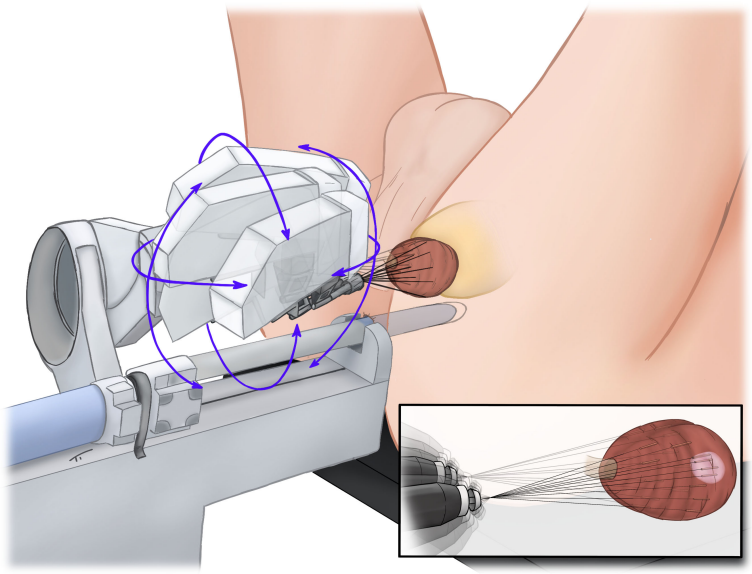

FIGURE 1
Robotic-assisted transperineal MRI-TRUS-fusion guided biopsy of the prostate.

TABLE 1 Baseline characteristics.

Parameter	Patients (n)	Mean ± SD (range)
Age (years)	228	64.9 ± 7.6 (46 – 84)
Prostate volume (cm^3)	228	48.4 ± 30.1 (9 – 310)
Serum PSA (ng/ml)	226	11.8 ± 39.1 (0.2 – 561)
Number of biopsy cores (total)	228	25.6 ± 8.2 (5 – 51)
IPSS	216	10.5 ± 7.2 (0 – 34)
ICIQ	210	1.2 ± 2.6 (0 – 14)
QoL	217	1.6 ± 1.5 (0 – 5)
NIH-CPSI (total)	173	7.8 ± 6.4 (0 – 40)
NIH-CPSI (pain)	173	1.7 ± 3 (0 – 21)
NIH-CPSI (micturition)	173	2.8 ± 2.2 (0 – 10)
NIH-CPSI (Quality of life)	173	3.5 ± 2.9 (0 – 12)
	Patients (n)	**%**
Suspicious DRE	36	15.8
Under "Active surveillance"	31	13.6
Previous biopsy	66	28.9
Immunodeficiency	38	16.7
Medication for MUD	63	27.6
Anticoagulation	59	25.9
Perioperative antibiotic prophylaxis/therapy	76	33.3

SD, standard deviation; PSA, prostate-specific antigen; IPSS, international prostate symptom score; ICIQ, international consultation on incontinence questionnaire; QoL, quality of life; NIH-CPSI, chronic prostatitis symptom index; DRE, digital rectal examination; MUD, male urinary dysfunction.

to an increased risk of AUR (OR = 2.49 and 2.29, respectively). Using multivariate multiple regression, only for AUR a significant overall model ($p = 0.04$) was demonstrated, with none of the predictors providing a clear prediction. Significant influence was shown for IPSS ≥ 8 on "Change of IPSS", although this result is considered random with regard to the insignificant overall model. No statistically significant change of functional scores (IPSS, QoL and ICIQ) occurred in our cohort shortly after biopsy. One patient (0.4%) developed urinary tract infection (UTI). 66/228 (28.9%) had undergone prostate biopsy priorly. 48/66 (84.2%) of these patients favored transperineal robotic-assisted biopsy over all other methods and rated transperineal robotic-assisted biopsy as the most pleasant biopsy approach. Regarding local conditions, haematoma at puncture, local skin infection and bleeding from puncture site occurred in 8/228 (3.5%), 0/228 (0%) and 10/228 (4.4%), respectively. Detailed data for functional outcome and side-effects are summarized in Table 2. Notably, no patients with immunodeficiency developed any infectious complications.

Sub-group-analysis for the functional outcome and side effects and subgroup specifications are summarized in Table 3 and Supplementary Table 1, respectively.

Discussion

To the best of our knowledge, this is the first prospective study to evaluate safety, tolerability, side effects, and functional outcome of transperineal robotic-assisted prostate biopsy. Transrectal ultrasound-guided biopsy of the prostate still is used as the standard approach for obtaining representative samples for identification and classification of PCa (10). However, the current EAU Guidelines 2022 clearly favor the perineal access route, due to the lower risk of infectious complications (1). Our study reports the outcomes of robotic-assisted perineal biopsy, that requires only two puncture sites. The applied sampling strategy provides histologic evaluation of the entire gland including suspicious lesions (9). Overall, 14% of our patients developed grade I complications according to Clavien-Dindo classification. The superior tolerability of the RA-TP-PB_x is highlighted by the mean value of 1.3 points on VAS for pain on the day of and 1.2 points on the days after biopsy. TP-PB_x performed under general anesthesia also displays a favorable pain profile (VAS 1.3) as compared to TP-PB_x (VAS 2) and TR-PB_x (VAS 2) in local anesthesia (11). Furthermore, most patients (84.2%) of our cohort having undergone conventional non-robotic biopsy, preferred RA-TP-PB_x. Although, feasibility of the TP-PBx in local anesthesia was shown in various studies (6, 12), general anesthesia is recommended in RA-TP-PB_x in order to enable maximum diagnostic accuracy. Hematuria and hematospermia were identified as most common side effects. Rates of occurrence were comparable to other studies reporting sides effects of TP-PB_x and TR-PB_x (13). Notably, none of our patients developed significant gross hematuria requiring bladder irrigation. A

TABLE 2 Functional outcomes and side effects.

Parameter	Mean ± SD (range) Before biopsy	Mean ± SD (range) After biopsy	p – value*
IPSS	10.5 ± 7.2 (0 – 34)	11 ± 7.4 (1 – 34)	0.23
ICIQ	1.2 ± 2.6 (0 – 14)	1.6 ± 2.8 (0 – 13)	0.12
QoL	1.6 ± 1.5 (0 – 5)	1.7 ± 1.5 (0 – 5)	0.44
Parameter	**Mean ± SD (range)**		**p – value#**
Pain on the day of biopsy	1.3 ± 1.9 (0 – 9)		0.68
Pain on following day	1.2 ± 1.9 (0 – 10)		
Change of IPSS[1]	0.4 ± 5.2 [(-) 31 – (+) 22]		–
Change of ICIQ[1]	0.3 ± 2.3 [(-) 13 – (+) 8]		–
Change of QoL[1]	0.1 ± 1.4 [(-) 5 – (+) 5]		–
Parameter	**Total (n)**		**%**
Acute urinary retention	32		14
Gross hematuria	145		63.6
Duration of hematuria (1 day)	34		14.9
Duration of hematuria (2-3 days)	51		22.4
Duration of hematuria (>3 days)	59		25.9
Hematospermia	98		43
Urinary tract Infection	1		0.4
Perineal bleeding	10		4.4
Perineal hematoma	8		3.5
Skin infection	0		0
Histology-proven Inflammation	73		32
Negative biopsy	95		40
Positive biopsy	133		60

SD, standard deviation; IPSS, international prostate symptom score; ICIQ, international consultation on incontinence questionnaire; QoL, quality of life.
[1]change of functional parameters (-) decrease of score after biopsy, (+) increase of score after biopsy.
*p – value determined by a dependent Student`s t test.
#p – value determined by an independent Student`s t test.

further advantage of the TP-PB_x is the absence of hematochezia or rectal bleeding, which is described with an incidence of up to 45% in transrectal biopsy (3). In our cohort, the rate of AUR after RA-TP-PB_x was 14%, which is comparable to the study of Pepe et al. with 11.1% on saturation TP-PB_x and > 24 cores taken (14), yet higher than in studies with lower number of biopsy cores taken (10–18) with rates of AUR ranging from 1.4% to 6.7% (15, 16). Even though the number of biopsy cores is considered a risk factor for AUR (14), the number of cores (≥25) had no significant impact on the risk of appearance of an AUR in our cohort applying a target saturation approach (9). Using multivariate multiple regression, an significant overall model ($p = 0.04$) for AUR was shown, with none of the predictors providing a clear prediction. RA-TP-PB_x allows for complete diagnostic coverage of the prostate *via* only two puncture sites. This sterile and minimally invasive approach resulted in the occurrence of only one UTI (0.4%) requiring intravenous antibiotic treatment. Notably, this patient had received antibiotic treatment with oral cephalosporine according to resistency profile, however the duration of pre-treatment (single dose) turned out to be insufficient given the histopathology also revealed acute inflammation. The rate of UTI is comparable to other studies reporting rates of UTI after TP-PBx between 0 – 0.7% (15–17). In contrast, TR- PB_x is associated with higher rates of infectious complications ranging between 2 - 5% despite antibiotic prophylaxis (11, 18, 19). In line with the study of Günzel et al. (11), omission of standard perioperative antibiotic prophylaxis in TP- PB_x did not result in a significant increase of infections. Notably, none of the immunodeficient patients developed infectious complications indicating that the sterile and minimally invasive biopsy technique enables to safely omit perioperative antibiotic prophylaxis even in patients at special risk for the development of infectious complications. Requiring no antibiotic prophylaxis helps to reduce the risk of antibiotic related complications and the development of drug resistant bacteria. Our results corroborate the findings from other groups (20). However, single center data, limited patient number and non-randomized trial design without a control group represent limitations of this study. Further studies are required to confirm our results. Nevertheless, this work indicates the superior safety profile of robotic assisted transperineal prostate biopsy as

10.3389/fonc.2022.1025355

TABLE 3 Functional outcome and side-effects - Subgroup analysis.

Parameter	MMUDyes/no	ACyes/no	BC<25/≥25	INFyes/no	PV<40/≥40	IPSS<8/≥8	MMR
			p – value*				
Acute urinary retention	0.63	0.19	0.33	0.06	0.57	0.06	0.04
Gross hematuria	0.7	0.97	0.45	0.3	0.69	0.3	0.75
Hematospermia	0.5	0.17	0.45	0.45	0.55	0.03	0.17
Perineal hematoma	0.18	0.55	0.59	0.45	0.97	0.92	0.71
Change of IPSS[1]	0.55	0.75	0.72	0.28	0.52	0.01	0.09
Change of ICIQ[1]	0.73	0.58	0.32	0.85	0.75	0.19	0.75
Parameter	**Complication**		**n**		**Mean ± SD (range)**		**p –value#**
PV	AUR no		192		46 ± 24.1 (9 – 217)		0.009
	AUR yes		31		61.4 ± 52.2 (27.5 – 310)		
Number of biopsy cores	AUR no		196		25 ± 7.9 (5 – 46)		0.009
	AUR yes		32		29 ± 9.2 (5 – 51)		
IPSS (before biopsy)	AUR no		185		10 ± 7.1 (0 – 32)		0.02
	AUR yes		30		13.2 ± 7.6 (3 – 34)		
PV - Pain on day of biopsy	No pain		103		44.6 ± 17.8 (18 – 88)		0.4
	> 0 points		107		47.1 ± 24.5 (9 – 173)		
PV - Pain on following day	No pain		111		45.5 ± 20.3 (9 – 120)		0.8
	> 0 points		99		46.4 ± 22.9 (14 – 173)		
BC - Pain on day of biopsy	No pain		104		26.6 ± 7.9 (5 – 51)		0.25
	> 0 points		108		24.5 ± 8.4 (5 – 41)		
BC - Pain on following day	No pain		112		26.3 ± 8.1 (5 – 51)		0.56
	> 0 points		100		24.7 ± 8.3 (6 – 41)		

NIH-CPSI, chronic prostatitis symptom index; INF, histology-proven inflammation; MMUD, medication for male urinary dysfunction; AC, anticoagulation; BC, biopsy cores; PV, prostate volume; IPSS, international prostate symptom score; MMR, multivariate multiple regression (overall model); ICIQ, international consultation on incontinence questionnaire; SD, standard deviation; AUR, acute urinary retention.

*p – value determined using multivariate multiple regression.

#p – value determined by an independent Student`s t test.

[1]change of functional parameters (-) decrease of score after biopsy, (+) increase of score after biopsy.

compared to a transrectal approach. We assume that the minimally invasive biopsy technique *via* only two entry points diminished local tissue trauma and subsequently reduced the risk for infectious complications.

Data availability statement

The raw data supporting the conclusions of this article will be made available by the authors, without undue reservation.

Ethics statement

The studies involving human participants were reviewed and approved by Ethikkommission Nordwest- und Zentralschweiz. The patients/participants provided their written informed consent to participate in this study.

Author contributions

All authors have conjointly designed the study, and MW, PT, and CW interpreted the data and drafted the manuscript. AM supported data collection and patient care. All authors designed and critically revised the manuscript for important intellectual content. MW, PT, and CW were involved in the statistical analysis. All authors contributed to the article and approved the submitted version.

Conflict of interest

Author CW was supported by grants from Siemens Healthineers and Uromed.

The remaining authors declare that the research was conducted in the absence of any commercial or financial relationships that could be construed as a potential conflict of interest.

Publisher's note

Supplementary material

The Supplementary Material for this article can be found online at: https://www.frontiersin.org/articles/10.3389/fonc.2022.1025355/full#supplementary-material

SUPPLEMENTARY TABLE 1
Subgroups specifications.

References

1. Mottet N, Bellmunt J, Bolla M, Briers E, Cumberbatch MG, De Santis M, et al. EAU-ESTRO-SIOG guidelines on prostate cancer. part 1: Screening, diagnosis, and local treatment with curative intent. *Eur Urol* (2017) 71(4):618–29. doi: 10.1016/j.eururo.2016.08.003

2. Borghesi M, Ahmed H, Nam R, Schaeffer E, Schiavina R, Taneja S, et al. Complications after systematic, random, and image-guided prostate biopsy. *Eur Urol* (2017) 71(3):353–65. doi: 10.1016/j.eururo.2016.08.004

3. Loeb S, Vellekoop A, Ahmed HU, Catto J, Emberton M, Nam R, et al. Systematic review of complications of prostate biopsy. *Eur Urol* (2013) 64(6):876–92. doi: 10.1016/j.eururo.2013.05.049

4. Liu W, Patil D, Howard DH, Moore RH, Wang H, Sanda MG, et al. Adoption of prebiopsy magnetic resonance imaging for men undergoing prostate biopsy in the united states. *Urology* (2018) 117:57–63. doi: 10.1016/j.urology.2018.04.007

5. Shigemura K, Fujisawa M. Prevention and management of infectious complications in prostate biopsy: A review. *Int J Urol Off J Jpn Urol Assoc* (2021) 28(7):714–9. doi: 10.1111/iju.14572

6. Wetterauer C, Shahin O, Federer-Gsponer JR, Keller N, Wyler S, Seifert HH, et al. Feasibility of freehand MRI/US cognitive fusion transperineal biopsy of the prostate in local anaesthesia as in-office procedure-experience with 400 patients. *Prostate Cancer Prostatic Dis* (2020) 23(3):429–34. doi: 10.1038/s41391-019-0201-y

7. Symons JL, Huo A, Yuen CL, Haynes AM, Matthews J, Sutherland RL, et al. Outcomes of transperineal template-guided prostate biopsy in 409 patients. *BJU Int* (2013) 112(5):585–93. doi: 10.1111/j.1464-410X.2012.11657.x

8. Kasivisvanathan V, Rannikko AS, Borghi M, Panebianco V, Mynderse LA, Vaarala MH, et al. MRI-Targeted or standard biopsy for prostate-cancer diagnosis. *N Engl J Med* (2018) 378(19):1767–77. doi: 10.1056/NEJMoa1801993

9. Wetterauer C, Trotsenko P, Matthias MO, Breit C, Keller N, Meyer A, et al. Diagnostic accuracy and clinical implications of robotic assisted MRI-US fusion guided target saturation biopsy of the prostate. *Sci Rep* (2021) 11(1):20250. doi: 10.1038/s41598-021-99854-0

10. Lee MS, Moon MH, Kim CK, Park SY, Choi MH, Jung SI. Guidelines for transrectal ultrasonography-guided prostate biopsy: Korean society of urogenital radiology consensus statement for patient preparation, standard technique, and biopsy-related pain management. *Korean J Radiol* (2020) 21(4):422–30. doi: 10.3348/kjr.2019.0576

11. Günzel K, Heinrich S, Schlegel J, Ri C, Schostak M, Magheli A, et al. [Initial results of perineal MRI/ultrasound fusion biopsies under local anesthesia without standard perioperative antibiotic prophylaxis]. *Urol Ausg A.* (2020) 59(10):1225–30. doi: 10.1007/s00120-020-01164-2

12. Thurtle D, Starling L, Leonard K, Stone T, Gnanapragasam VJ. Improving the safety and tolerability of local anaesthetic outpatient transperineal prostate biopsies: A pilot study of the CAMbridge PROstate biopsy (CAMPROBE) method. *J Clin Urol* (2018) 11(3):192–9. doi: 10.1177/2051415818762683

13. Wegelin O, Exterkate L, van der Leest M, Kelder JC, Bosch JLHR, Barentsz JO, et al. Complications and adverse events of three magnetic resonance imaging-based target biopsy techniques in the diagnosis of prostate cancer among men with prior negative biopsies: Results from the FUTURE trial, a multicentre randomised controlled trial. *Eur Urol Oncol* (2019) 2(6):617–24. doi: 10.1016/j.euo.2019.08.007

14. Pepe P, Aragona F. Prostate biopsy: results and advantages of the transperineal approach–twenty-year experience of a single center. *World J Urol* (2014) 32(2):373–7. doi: 10.1007/s00345-013-1108-1

15. Stefanova V, Buckley R, Flax S, Spevack L, Hajek D, Tunis A, et al. Transperineal prostate biopsies using local anesthesia: Experience with 1,287 patients. prostate cancer detection rate, complications and patient tolerability. *J Urol* (2019) 201(6):1121–6. doi: 10.1097/JU.0000000000000156

16. Pepe P, Aragona F. Morbidity after transperineal prostate biopsy in 3000 patients undergoing 12 vs 18 vs more than 24 needle cores. *Urology* (2013) 81(6):1142–6. doi: 10.1016/j.urology.2013.02.019

17. Grummet JP, Weerakoon M, Huang S, Lawrentschuk N, Frydenberg M, Moon DA, et al. Sepsis and 'superbugs': should we favour the transperineal over the transrectal approach for prostate biopsy? *BJU Int* (2014) 114(3):384–8. doi: 10.1111/bju.12536

18. Wagenlehner FME, van Oostrum E, Tenke P, Tandogdu Z, Çek M, Grabe M, et al. Infective complications after prostate biopsy: outcome of the global prevalence study of infections in urology (GPIU) 2010 and 2011, a prospective multinational multicentre prostate biopsy study. *Eur Urol* (2013) 63(3):521–7. doi: 10.1016/j.eururo.2012.06.003

19. Batura D, Gopal Rao G. The national burden of infections after prostate biopsy in England and Wales: a wake-up call for better prevention. *J Antimicrob Chemother* (2013) 68(2):247–9. doi: 10.1093/jac/dks401

20. Sigle A, Suarez-Ibarrola R, Pudimat M, Michaelis J, Jilg CA, Miernik A, et al. Safety and side effects of transperineal prostate biopsy without antibiotic prophylaxis. *Urol Oncol* (2021) 39(11):782.e1–5. doi: 10.1016/j.urolonc.2021.02.016

frontiers | Frontiers in Oncology

TYPE Original Research
PUBLISHED 18 May 2023
DOI 10.3389/fonc.2023.1185057

OPEN ACCESS

EDITED BY
Fabio Grizzi,
Humanitas Research Hospital, Italy

REVIEWED BY
Kaifa Tang,
Guizhou University of Traditional Chinese Medicine, China
Martina Maggi,
Sapienza University of Rome, Italy

*CORRESPONDENCE
Yuhua H
sdfyy_hyh@163.com

RECEIVED 21 March 2023
ACCEPTED 09 May 2023
PUBLISHED 18 May 2023

CITATION
D W, L G, T Z, W X, L Y, Z X, Z W, L G and H Y (2023) Study of iron metabolism based on T2* mapping sequences in PI-RADS 3 prostate lesions.
Front. Oncol. 13:1185057.
doi: 10.3389/fonc.2023.1185057

Study of iron metabolism based on T2* mapping sequences in PI-RADS 3 prostate lesions

Wenhao D[1], Guangzheng L[2], Zhen T[1], Xuedong W[1], Yonggang L[2], Xuefeng Z[1], Weijie Z[1], Gang L[1] and Yuhua H[1]*

[1]Department of Urology, The First Affiliated Hospital of Soochow University, Suzhou, China, [2]Department of Radiology, The First Affiliated Hospital of Soochow University, Suzhou, China

Introduction: Prostate cancer is one of the most common malignant tumors in Chinese men, which is rich in iron metabolic activity and is closely related to all stages of prostate cancer progression. Since the current diagnostic methods are insufficient, we aimed to evaluate the value of quantitative T2 star values from the T2* mapping sequences in multiparametric magnetic resonance imaging (mpMRI) in the diagnosis and grading of PI-RADS 3 prostate cancer (PCa).

Methods: We prospectively enrolled patients with PCa or benign prostatic hyperplasia (BPH) admitted to our hospital from January 2021 to November 2022. Imaging indicators, including the T2* value and apparent diffusion coefficient (ADC) value, were collected, and enzyme-linked immunosorbent assays (ELISAs) were used to measure the levels of proteins involved in iron metabolism in the patients. ROC curves were drawn to explore whether the T2* value could be used for the diagnosis and grading of PCa.

Results: We found that three iron metabolism indexes, ferritin, hepcidin, and the ferric ion (Fe), and the T2* value were significantly different between the PCa group and BPH group and between the low International Society of Urology Pathology (ISUP) group (ISUP ≤ 2) and the high ISUP group (ISUP>2). Additionally, there was a significant correlation between the levels of these three indicators and the T2* value. Further ROC analysis showed that the levels of iron metabolism-related indexes and T2* values performed well in diagnosing and grading PCa.

Discussion: The T2* value has good value in detecting and predicting the grade of prostate cancer and can reflect the iron metabolism of the tumor, which could provide a foundation for the diagnosis and grading of PCa in the future.

KEYWORDS

prostate cancer, PI-RADS, iron mentalism, multiparametric magnetic resonance imaging, diagnosis

1 Introduction

Prostate cancer (PCa) is one of the most common malignancies in male and the second leading cause of cancer-related death in adult men worldwide; in China, PCa ranks ninth in the incidence of male malignancies (1). According to CA-A CANCER JOURNAL FOR CLINICIANS 's forecast, there will be 288,300 new cases of PCa in the United States in 2023, and 34,700 patients will die of prostate cancer2200 (2). Nearly 30% of new cancer cases are PCa. More importantly, despite the continuous progress of prostate diagnostic technology, the incidence of PCa in China is increasing yearly, and the proportion of advanced prostate cancer is significantly higher than that in other countries. This may be due to the limitations of screening and the high rate of missed diagnosis. Many patients are elderly, and because of the subtle nature of PCa symptoms, they are diagnosed for the first time because of frequent urination and other lower urinary tract symptoms (LUTS). Therefore, the accurate screening of PCa in patients with benign prostatic hyperplasia is the most important method to improve the detection rate of PCa.

To date, the diagnosis of PCa mainly depends on two methods: the measurement of serum total prostate-specific antigen (TPSA) levels and multiparametric magnetic resonance imaging (mpMRI). In recent years, noninvasive methods, such as PSA measurements, have been developed for evaluating preoperative PCa lesions, and the diagnostic value of these methods for determining progression and prognosis has been evaluated. Although TPSA assays have high sensitivity, their low specificity has led to the overuse of prostate biopsy. Therefore, improving the efficiency of PCa diagnosis and avoiding unnecessary invasive examinations are pivotal components of the diagnosis and treatment of PCa. mpMRI of the prostate is currently another important component of noninvasive PCa diagnosis. mpMRI is not burdened by the economic costs associated with the surgical injury caused by prostate biopsy or false-positive results and can be comprehensively performed before surgery to assess the location, boundaries, and environment of the tumor. The apparent diffusion coefficient (ADC) value has also been discussed with regard to its relation to the pathological stage and prognosis of PCa (3). PI-RADS is currently one of the most widely used scoring criteria for PCa. It is used to evaluate the likelihood of focal prostate nodules to be PCa by scoring T2 and diffusion-weighted imaging (DWI) sequences. According to the difference in high and low signals and clarity, the PI-RADS divides the prostate score into five grades, of which the third grade represents possible PCa. Although patients with third grade tumors exhibit clear qualitative criteria, there are subjective differences to a certain extent, the requirements for the center are higher, and different radiologists may have different opinions. Moreover, some PCa lesions with 2- or 4-point characteristics are often included in the 3-point category, in which there are a large number of incorrect scores. In addition, there is still a debate about whether lesions with PI-RADS3 scores need invasive puncture. According to studies, the positive rate of PCa puncture with PI-RADS3 patients is only 20%, which greatly affects the detection of PCa. Previous studies have assessed the prevalence of PCa in PI-RADS3 lesions and found that PI-RADS scores do not provide accurate guidance for clinical management (with or without biopsies), and the rate of missed diagnosis is the main problem at present. For patients with PI-RADS3, the ambiguous PI-RADS score does not represent a better prognosis than the higher PI-RADS grade. Although the ADC value can help to judge the malignancy of malignant prostate tumors to some extent, it has obvious limitations. Some PI-RADS3 patients often have a very poor International Society of Urology Pathology (ISUP) grade, which seriously affects their survival and prognosis. Therefore, the two existing noninvasive examination items cannot provide effective guidance on the PI-RADS score, and the diagnosis of PI-RADS3 score of PCa is still in the exploratory stage (4–6). So far, many tools, such as biomarkers, associated with mpMRI have aimed to solved this particular problem, such as SelectMDx (7), 4Kscore, ExosomeDx™ (8) and PCA3 (9). These biomarkers can improve the specificity of PCa by combining with mpMRI, and have a significant improvement compared with traditional TPSA or prostate-specific antigen density (PSAD).

With the in-depth study of iron metabolism, increasing evidence has shown a correlation between iron metabolism and the occurrence and progression of malignant tumors (10). Iron is one of the basic nutrients needed by cancer cells. When tumor cells are in an iron-rich environment, the growth and invasion of cancer cells are significantly faster than those in an iron-deficient environment. However, too much iron can cause another problem: oxidative damage to cancer cells. When cancer cells are exposed to too much iron, iron promotes another phenomenon by activating oxidative damage: iron death, a mechanism that damages the structure of cancer cells. However, cancer cells form protective mechanisms against oxidative damage and iron death, which are different in all types of cancers and have similar mechanisms in PCa. In cancer cells, the activity of antioxidant enzymes is increased, so cancer cells do not immediately undergo the killing caused by fast-acting iron in the iron-rich environment, so a very large amount of iron is needed to cause the death of cancer cells. Cancer cells use iron for important biochemical reactions, such as DNA synthesis, mitochondrial metabolism, angiogenesis and metastatic cell proliferation. In PCa, iron is also very important for the occurrence and development of tumors. Like other tumors, the growth of PCa cells requires sufficient iron, which can activate enzymes that control the transcriptional activity of androgen receptor (AR) in PCa, which is an important initiating factor. Moreover, iron can reactivate the activity of enzymes in cancer cells, thereby increasing energy production and extracellular matrix degradation. Recent studies have confirmed that the content of iron in PCa cells is increased, while in normal cells near PCa cells, iron levels are lower (11). Many kinds of iron metabolism molecules have been shown to promote or inhibit the progression of PCa. For patients with PI-RADS3 prostate disease whose imaging results are unclear, whether the difference in iron metabolism can help to improve the detection rate of PI-RADS3 is a direction that needs attention to guide clinical diagnosis and treatment from a microscopic point of view.

Here, we introduce a less-used MR sequence in urology, since the unclear anatomical division, difficulty in parameter adjustment, small prostate volume and so on. The T2* mapping sequence was

initially used to assess iron deposition in the heart and spleen (12). In the context of liver surgery, the T2* mapping sequence can be used to quantitatively determine liver iron deposition and iron overload based on the difference in T2 relaxation time and has better accuracy than liver biopsy (13). MRI signal decay is affected by the iron content of the tissue; the higher the iron content, the faster the signal decay. In turn, the T2* value represents the iron content as represented by the R2* relaxation rate (14). In the field of PCa, whether the T2* mapping sequence can increase the detection rate of PCa from a new perspective by predicting iron metabolism in patients with PI-RADS3 is unknown. In summary, the assessment of PI-RADS3 seems to have become a key challenge, and a large number of patients with PCa that cannot be diagnosed by TPSA or mpMRI based on T2+DWI sequences are included in this category. This limitation greatly affects the detection rate and prognosis of these patients, and a new method needs to be introduced to address this problem. In the field of urology, whether T2* mapping can be used to evaluate prostatic iron deposition to help diagnose prostate malignant tumors and even evaluate prognosis remains unknown. Therefore, the aim of this study was to prospectively evaluate the role of quantitative measurement of intratumoral iron deposition based on T2* mapping sequence as a noninvasive biomarker of iron metabolism in PCa with PI-RADS 3.

2 Materials and methods

2.1 Participants

This prospective study was approved by the Medical Ethics Committee of the First Affiliated Hospital of Soochow University (Suzhou, China; 2021; No. 133). Written informed consent was obtained from all the patients. Patients were included from January 2021 to November 2022. Patients hospitalized in the First Affiliated Hospital of Soochow University diagnosed with prostate diseases were prospectively subjected to mpMRI before prostate biopsy. The sequence included T2, DWI, ADC and T2* mapping. Serum samples were also collected. Two radiologists rescored all patients based on PI-RADS and included patients with PI-RADS3 in this study. Then, retrospective collection of data regarding the clinical indicators of patients in this study, including TPSA levels, prostate volume, pathological grade and others, was performed. The inclusion criteria were as follows: (1) MRI of the prostate, including T2-weighted imaging (T2WI), DWI, and T2* mapping-weighted imaging and surgery- (laparoscopic radical prostatectomy or transurethral resection of prostate) and postoperative pathology-confirmed PI-RADS 3 PCa or benign prostatic hyperplasia (BPH); (2) MRI examination at our hospital less than six weeks after prostate surgery; and (3) The lack of acute hepatitis or blood diseases affecting iron metabolism. Exclusion criteria were as follows: (1) treatment for PCa before surgery, such as endocrine therapy or radiotherapy; (2) other diseases affecting iron metabolism except PCa; and (3) film reading hampered by MRI artifacts. Based on the primary criteria, our study included 90 patients, including 56 with PCa and 34 with BPH. Ninety-three patients were excluded because of their incorrect PI-RADS score, three patients were excluded because they had received endocrine therapy, one patient was excluded due to an MRI artifact, and one patient was excluded due to reclassification of the PI-RADS score. In accordance with the PCa grading system, patients were divided into five categories. Grades assigned by the ISUP to patients 1, 2, 3, 4, and 5 were 4, 18, 17, 4, and 13, respectively. The PRISMA flow chart was shown in Figure 1.

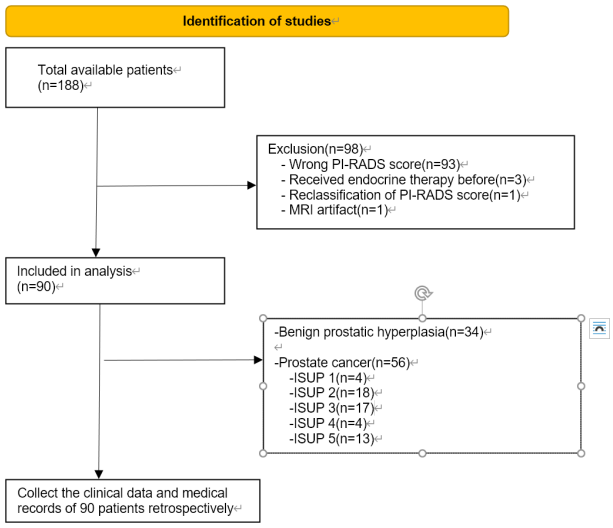

FIGURE 1
PRISMA flow diagram of patients involved and order of the processes.

2.2 Serum and tissue samples

Preoperative blood was collected from the two groups of patients. Serum and erythrocytes were rapidly and carefully separated by centrifugation at 3000 rpm for 10 minutes. The expression levels of ferritin and hepcidin in serum were measured by enzyme-linked immunosorbent assay (ELISA). After the prostate tissue was acquired after laparoscopic radical prostatectomy or transurethral resection of prostate, the specimens were then mashed with an appropriate amount of normal saline. The supernatant was collected by centrifugation at 3000 rpm for 10 minutes, and the tissue homogenate was detected by ELISA. The process was carried out in strict accordance with the kit instructions.

2.3 MRI protocol

Examinations were performed by using a 3.0 T clinical MR scanner (Skyra; Siemens Medical, Germany) with a dedicated 16-channel body-phased array coil. All images of 90 patients were assessed by 2 physicians respectively based on the PI-RADS score. Through the former study and following practice (15), an axial fast spin echo T2-weighted sequence was performed with the following parameters: repetition time/echo time (TR/TE) 7590/104 ms, slice

number 25, slice thickness 3 mm, intersection gap 0 mm, field of view (FOV) 200 mm, voxel size 0.5*0.5*3 and flip angle 120°. T2* relaxation time maps were obtained using a multiecho fast field sequence. The parameters used were as follows: TR 265 ms, TE 4.92, 7.38, 9.84, 12.30, and 14.76 ms, slice number 30, slice thickness 3 mm, intersection gap 0.6 mm, FOV 380 mm, voxel size 1.5*1.5*3 and flip angle 50°.

2.4 PI-RADS score

The images obtained from the mpMRI scans were transferred to the Picture Archiving and Communication System (PACS), and the scores were rescored according to the PI-RADS V2.0 by 2 physicians with 10 years of experience in prostate MR diagnosis. The raters knew the patient's baseline data but were blinded to the pathology results.

2.5 Correlation of the T2* value

The slice that showed the greatest extent of the lesion area was selected on the PACS, and the region of interest (ROI) was set. For multiple suspected tumor sites, the one with lowest T2* value was eventually selected for delineating the ROI. Considering the difficulty of sampling, we generally select an area of 1cm*1cm-sized circular area as the ROI. For tumors with too large lesions, we use the area with the lowest T2* value. Each measurement was repeated 3 times, and the average value was taken. After prostatectomy, each prostate pathology image was divided into 5 mm thick slices. Using the corresponding positions on the MR images, experienced pathologists manually marked six points on the prostate pathology images—the basal section, the apex, the peripheral zone, the central gland, the tip and the urinary tract—which were aligned with the corresponding parts on the MRI images. Symbols were used to identify various distinct morphological characteristics and then used to align the images with the step-section slices. For patients with BPH, the prostate was also corresponded to the six positions as described above, and the average value of the 1cm*1cm circular area of the transitional zone of hyperplasia is taken.

2.6 Data analyses

All data were tested with SPSS 22.0 software (IBM, Armonk, NY, USA). According to the normality test, the baseline data do not fit a normal distribution, and are presented as medians (interquartile range), and group comparisons were made using nonparametric tests. Spearman correlation was used for correlation analysis. Taking the pathological results as the gold standard, the ROC curve was drawn. The difference was considered statistically significant at $p<0.05$, and applied to all evaluations.

3 Results

3.1 Patient characteristics

The pathological findings of 90 patients were included in this prospective study, including 34 patients with BPH and 56 patients with PCa. To explore differences in patient clinical data, we compared the TPSA, ratio of free to total PSA (F/TPSA), prostate volume, apparent diffusion coefficient (ADC) value, T2* value, ferritin, hepcidin, and Fe between the BPH and Pica groups. The results showed that the differences for all indicators between the two groups were statistically significant (all $p<0.05$; Table 1). The PCa group had higher TPSA, ferritin, hepcidin, and Fe levels than the BPH group, while the FTPSA, ADC value, T2* value, and prostate volume were lower than those of the BPH group.

Considering that active monitoring (AS) can be selected for ISUP 1 and some ISUP 2 lesions, to avoid unnecessary repeated puncture and radical surgery, we further divided PCa patients into ISUP ≤ 2 and ISUP > 2 (Table 2). No statistically significant differences in TPSA or prostate volume were found between the two groups ($p=0.09$ and $p=0.151$, respectively). The rest of the indicators were significantly different.

TABLE 1 Patient clinical data [medians (interquartile range)].

Characteristic	Pca	BPH	P
Patient(n)	56	34	–
TPSA(ng ml^{-1})	15.85 (8.31,25.77)	8 (4.86,12.45)	<0.001
F/TPSA	0.12 (0.08,0.15)	0.15 (0.12,0.22)	0.019
Prostate volume(cm^3)	34.85 (28.3,51.59)	59.08 (38.45,73.96)	0.001
ADC(*10^{-3} mm^2/s)	0.695 (0.629,0.768)	0.756 (0.696,0.865)	0.02
T2*(ms)	42.02 (29.76,47)	54.34 (47.46,57.68)	<0.001
Ferritin(ng ml^{-1})	98.03 (82.92,113.69)	84.03 (78.05,92.49)	0.001
Hepcidin(ng ml^{-1})	114.12 (97.34,126.51)	100.74 (94.73,109.85)	0.008
Fe(μmol ml^{-1})	31.78 (27.27,36.07)	25.11 (22.52,30.03)	<0.001

TPSA, Total prostate-specific antigen; F/TPSA, Ratio of free to total PSA; ADC, Apparent diffusion coefficient; Fe, Ferric ion.

TABLE 2 PCa Patient clinical data [medians (interquartile range)].

Characteristic	ISUP ≤ 2	ISUP>2	P
Patient(n)	22	34	–
tPSA(ng ml^{-1})	14.67 (6.58,22.42)	17.34 (11.37,32.87)	0.09
F/TPSA	0.14 (0.12,0.19)	0.1 (0.08,0.14)	0.017
Prostate volume(cm^3)	43.95 (34.02,52.96)	32.41 (25.35,49.49)	0.151
ADC(*10^{-3} mm^2/s)	0.760 (0.684,0.877)	0.671 (0.619,0.729)	0.004
T2*(ms)	47.03 (43.46,49)	34.57 (28.13,42.1)	<0.001
Ferritin(ng ml^{-1})	88.51 (73.13,98.56)	109.08 (93.5,116.87)	0.002
Hepcidin(ng ml^{-1})	105.73 (77.68,115.32)	117.16 (105.21,132.06)	0.012
Fe(μmol ml^{-1})	28.1 (23.56,32.05)	33.42 (29.51,37.53)	0.001
Nerve invasion(n)	14 (63.6%)	25 (73.5%)	0.889
Magin invasion(n)	8 (36.4%)	13 (38.2%)	0.436

TPSA, Total prostate-specific antigen; F/TPSA, Ratio of free to total PSA; ADC, Apparent diffusion coefficient; Fe, Ferric ion.

3.2 Correlation of BPH patient indicators with TPSA and T2* values

Next, we analyzed the correlation between the levels of serum markers and prostate volume and TPSA levels or T2* value, and the results showed that in BPH patients, the TPSA level was correlated with the prostate volume ($p<0.001$; Table 3), while no correlations were observed between the remaining markers and either TPSA or the T2* value (both $P > 0.05$).

3.3 Correlation of PCa patient indicators with ISUP and T2* values

Next, we further analyzed the correlation between PCa patient indicators and ISUP grade and T2* value, and the results showed that TPSA, ADC value, ferritin, hepcidin, and Fe were all correlated with ISUP grade and T2* value. It is worth noting that the correlation coefficients of the T2* value, ferritin, hepcidin, and Fe with ISUP were -0.661, 0.52, 0.411, and 0.535, respectively (all $p< 0.01$; Table 4). Both the T2* mapping sequence and iron-related indexes better predicted the ISUP grade of PCa patients and performed well in evaluating the prognosis of patients. In addition, a correlation between the T2* value and ferritin, hepcidin, and Fe was observed (Table 4).

3.4 T2* value in diagnosing PCa

Then, we investigated the diagnostic value of the T2* value for PCa, as shown in Figure 2A. The ROC curve showed that the T2* value performed well in distinguishing PCa and BPH (AUC=0.865, $p<0.001$), while the TPSA, ADC value, ferritin, hepcidin, and Fe had AUCs of 0.746, 0.647, 0.704, 0.667, and 0.748, respectively (Figure 2B). This finding suggests that TPSA, ferritin and Fe also have good performance in the diagnosis of PCa.

TABLE 3 Associations between various parameters and TPSA or the T2* value in BPH.

Characteristic	TPSA		F/TPSA		Prostate volume		Ferritin		Hepcidin		Fe	
	r	p	r	p	r	p	r	p	r	p	r	p
T2* value	-0.222	0.206	0.159	0.243	-0.099	0.577	0.075	0.673	0.062	0.726	-0.33	0.057
TPSA	–	–	-0.202	0.134	0.695	<0.001	0.041	0.817	0.127	0.475	0.111	0.531

TPSA, Total prostate-specific antigen; ADC, Apparent diffusion coefficient; Fe, Ferric ion.

TABLE 4 Associations between indicators and ISUP grade or T2* value in PCa.

Characteristic	TPSA		T2* Value		ADC Value		Ferritin		Hepcidin		Fe	
	r	p	r	p	r	p	r	p	r	p	r	p
ISUP	0.349	0.008	-0.661	<0.001	-0.432	0.001	0.52	<0.001	0.411	0.002	0.535	<0.001
T2* Value	-0.386	0.003	–	–	0.482	<0.001	-0.441	0.001	-0.324	0.015	-0.541	<0.001

TPSA, Total prostate-specific antigen; ADC, Apparent diffusion coefficient; Fe, Ferric ion; ISUP, International Society of Urology Pathology.

10.3389/fonc.2023.1185057

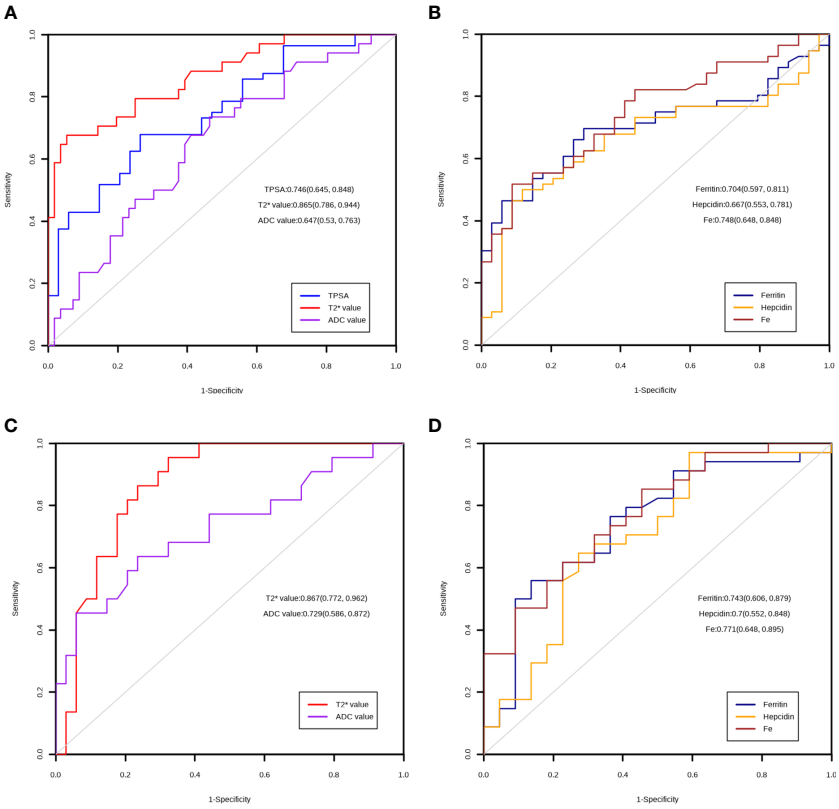

FIGURE 2
ROC curve of the markers. **(A)** Diagnostic utility of TPSA, T2* value and ADC value in the PCA and BPH group. **(B)** Diagnostic utility of ferritin, hepcidin and Fe in the PCA and BPH group. **(C)** Diagnostic utility of T2* value and ADC value in the low ISUP and high ISUP group. **(D)** Diagnostic utility of ferritin, hepcidin and Fe in the low ISUP and high ISUP group.

3.5 The T2* value predicts ISUP grade in PCa patients

Finally, we explored the role of the T2* value in discriminating between PCa patients with ISUP ≤2 and >2. The ROC analysis results showed that the T2* value could significantly differentiate between the grades of PCa (AUC=0.867, p<0.001); the AUCs of the other markers are shown in Figures 2C, D.

4 Discussion

Prostate cancer morbidity and mortality are rising in Asia, with current diagnoses mainly relying on PSA, digital rectal exam (DRE) and mpMRI, as as reported above, posing a new challenge to PCa diagnosis. The focus of the diagnosis of PCa is to differentiate it from BPH, which is associated with symptoms that often mask the existence of PCa. With the advancement of MRI technology, mpMRI has become an effective modality for the noninvasive diagnosis of PCa. The existing routine sequence and the general qualitative PI-RADS scoring model are gradually becoming inadequate for meeting current requirements. Whether needle biopsy should be performed for a PI-RADS score of 3 and the positive rate of needle biopsy were not satisfactory. A 2016 multicenter prospective study showed that the detection rates of PCa were 13%, 31%, and 71% for lesions with a PI-RADS score greater than or equal to 3, respectively (16); other studies have made similar arguments (17–19). Interestingly, a study showed that for PI-RADS3 patients, dividing them into low-risk and high-risk groups according to the 0.5 ml threshold of lesion volume may help physicians make clinical decisions, but there is no large-scale central study to confirm this, and studies are mostly limited to the T1-2 clinical stage (20). Therefore, for PCa patients with PI-RADS 3, the lower detection rate of conventional MR sequences affects the diagnosis of early-stage PCa or clinically significant PCa. In the classic T2+DWI sequence, patients with PI-RADS 3 mostly showed heterogeneous low signals on T2 sequences and isointensity or mild hyperintensity on high b-value DWI sequences. In a previous study, the sensitivity of the T2 sequence + DWI sequence was significantly higher than that of the T2 sequence alone (81% vs. 54%, p<0.01), and the specificity of the T2 sequence + DWI sequence and T2 sequence alone was basically the same (21). DWI reveals obvious differences in the ADC values of patients with PCa and BPH, but there is a large overlap. Consequently, the ADC value alone is not recommended for the differential diagnosis of prostate diseases (22, 23). Models incorporating the qualitative ADC value and qualitative PI-RADS score have improved diagnostic efficiency over the PI-RADS score alone (24). At present, the detection rate of the conventional T2 sequence + DWI sequence is affected by the disease characteristics of the population, the quality of MR imaging, the experience of the reader, and the accuracy of prostate biopsy.

Angiogenesis and tumor metastasis are closely related to cellular iron metabolism. It has been proven that reducing intracellular iron metabolism inhibits tumor cell growth in both hormone-dependent and hormone-resistant cells (25). As a key factor in iron metabolism, hepcidin plays a crucial role, as it regulates the ferritin receptor on the cell membrane, preventing iron from leaving the cell. Subsequently, there is an increase in free iron production in tumor cells, which increases tumor cell invasiveness and promotes tumor cell growth. In this study, a higher level of serum hepcidin was found in the PCa group. In addition, the serum hepcidin levels were correlated with the ISUP grade. Elevated ferritin levels have been reported in other tumors (26–28), and in urine, ferritin heavy and light chains were confirmed to be different between the PCa and BPH groups. However, the effects of serum ferritin on PCa stage, progression, and prognosis need further experimental verification. In our study, the serum ferritin level was positively correlated with ISUP grade. Compared with systemic iron metabolism, local total Fe in prostate tissue can better reflect the significance of iron metabolism in PCa due to the presence of many confounding factors. At present, most studies have collected data on the trace iron in blood, and there are few studies on Fe in tissues. However, many experiments have confirmed that the iron content of PCa cells increases, and there is often iron overload (25). In this study, Fe level was positively correlated with ISUP grade and negatively correlated with T2* value; that is, the T2* value could reflect local iron metabolism in the prostate to a certain extent. In conclusion, for the first time, we identified the differences in iron metabolism in patients with PI-RADS 3. Although they had similar imaging findings, there were significant differences in iron metabolism in patients. The findings represent a considerable difference in iron metabolism that can be assessed during the diagnosis of PCa. The results showed that the levels of three indexes of iron metabolism were positively correlated with ISUP, suggesting that under similar imaging conditions, the degree of active iron metabolism in the tumor represents the prognosis of patients with PCa to some extent. It is interesting to note that there is also a significant negative correlation between the T2* value and the levels of three indicators of iron metabolism in patients with PCa, of which Fe concentration is the most significant, which means that the T2* value is similar to the prediction of liver iron deposition in the field of urology.

We assessed iron metabolism in prostate disorders using the T2* mapping sequence in mpMRI. We found that the T2* value was lower in the PCa group than in BPH group ($p<0.001$). In the PCa group, the T2* value was negatively correlated with ISUP grade, and patients with ISUP>2 tended to have a lower T2* value. Compared to the traditional ADC value, the TPSA and T2* values had better performance in distinguishing PCa and BPH and in distinguishing ISUP ≤ 2 and ISUP>2 (AUC=0.865 and 0.867, respectively). As a traditional PCa diagnostic index, TPSA still has good performance in diagnosing PCa (AUC=0.746), but there was no significant difference within the PCa group ($p=0.08$). The ADC value is used as a quantitative indicator; however, in identifying PCa, the diagnostic performance was not as good as TPSA or the T2* value (AUC=0.647), but it was able to achieve greater diagnostic performance within the PCa group (AUC=0.729), which is consistent with previous papers showing that the ADC value can be used to predict PCa staging, grading and prognosis (29, 30).

To verify whether the T2* value can represent iron metabolism, we added three iron metabolism-related indicators, hepcidin, ferritin, and Fe, to our study and found that the levels were significantly different between PCa and BPH ($p<0.01$). Notably, within the PCa group, the three metrics were still significantly different between the ISUP groups ($p=0.002$, 0.012, 0.001, respectively). In further ROC curve analysis, Ferritin (AUC=0.704), Hepcidin (AUC=0.667) and Fe (AUC=0.748) showed good performance in the diagnosis of prostate cancer. When considering the risk stratification of prostate cancer, the diagnostic efficiency of the Ferritin (AUC=0.743), Hepcidin (AUC=0.7) and Fe (AUC=0.771) is further improved, suggesting that even in patients with prostate cancer, different progression often has different iron metabolism. In the PCa group, the three indexes were all negatively correlated with the T2* value, indicating that the T2* mapping sequence could reflect iron metabolism in PCa to a certain extent and reflect the progression of the disease.

Through this study, we hope to drive the adoption of radiomics and metabonomics in the management of current PI-RADS3 patients. From a radiological standpoint, it might increase the overall diagnostic efficiency; on the other hand, it might allow us to rule out unnecessary biopsies from a clinical perspective, avoiding the risk of possible complications in selected patients.

Inevitably, this article has some limitations. First, the sample size was relatively small, and it is necessary to conduct a multicenter, prospective, large-scale study to confirm the current conclusions. Second, the article lacks prognostic follow-up data, and whether the T2* value can be used as a prognostic indicator remains to be explored. Finally, although the accuracy of sampling was adequate, there are still uncontrollable corresponding errors, and it is necessary to wait for better sampling methods.

5 Conclusion

In conclusion, the validation of tissue extraction and metabolic analysis based on T2* Mapping sequence could provide a practical basis for non-invasive preoperative evaluation of patients with prostate malignancies using this technology, and could provide the possibility to discover potential iron metabolism-related therapeutic targets in the future.

Data availability statement

The raw data supporting the conclusions of this article will be made available by the authors, without undue reservation.

Ethics statement

The studies involving human participants were reviewed and approved by the Medical Ethics Committee of the First Affiliated Hospital of Soochow University (Suzhou, China; 2021; No. 133). The patients/participants provided their written informed consent to participate in this study.

Author contributions

WD analyzed data and wrote the manuscript. YH and XZ developed the project. XW, WZ and GL edited the manuscript. GZL and YL performed MRI examinations. All authors contributed to the article and approved the submitted version.

Funding

This work was supported by grants from the 2018 16th Science and Technology Development Plan of Suzhou, Suzhou, China (No. SS201863).

Conflict of interest

The authors declare that the research was conducted in the absence of any commercial or financial relationships that could be construed as a potential conflict of interest.

Publisher's note

References

1. Kasivisvanathan V, Rannikko AS, Borghi M, Panebianco V, Mynderse LA, Vaarala MH, et al. MRI-Targeted or standard biopsy for prostate-cancer diagnosis. *N Engl J Med* (2018) 378(19):1767–77. doi: 10.1056/NEJMoa1801993

2. Siegel RL, Miller KD, Wagle NS, Jemal A. Cancer statistics, 2023. *CA: A Cancer J Clin* (2023) 73(1):17–48. doi: 10.3322/caac.21763

3. Boschheidgen M, Schimmöller L, Arsov C, Ziayee F, Morawitz J, Valentin B, et al. MRI Grading for the prediction of prostate cancer aggressiveness. *Eur Radiol* (2022) 32 (4):2351–9. doi: 10.1007/s00330-021-08332-8

4. Schoots IG. MRI In early prostate cancer detection: how to manage indeterminate or equivocal PI-RADS 3 lesions? *Trans Androl Urol* (2018) 7(1):70–82. doi: 10.21037/tau.2017.12.31

5. Mazzone E, Stabile A, Pellegrino F, Basile G, Cignoli D, Cirulli GO, et al. Positive predictive value of prostate imaging reporting and data system version 2 for the detection of clinically significant prostate cancer: a systematic review and meta-analysis. *Eur Urol Oncol* (2021) 4(5):697–713. doi: 10.1016/j.euo.2020.12.004

6. Woźnicki P, Westhoff N, Huber T, Riffel P, Froelich MF, Gresser E, et al. Multiparametric MRI for prostate cancer characterization: combined use of radiomics model with PI-RADS and clinical parameters. *Cancers (Basel)* (2020) 12(7):1767. doi: 10.3390/cancers12071767

7. Busetto GM, Del Giudice F, Maggi M, De Marco F, Porreca A, Sperduti I, et al. Prospective assessment of two-gene urinary test with multiparametric magnetic resonance imaging of the prostate for men undergoing primary prostate biopsy. *World J Urol* (2021) 39(6):1869–77. doi: 10.1007/s00345-020-03359-w

8. de la Calle CM, Fasulo V, Cowan JE, Lonergan PE, Maggi M, Gadzinski AJ, et al. Clinical utility of 4Kscore(®), ExosomeDx™ and magnetic resonance imaging for the early detection of high grade prostate cancer. *J Urol* (2021) 205(2):452–60. doi: 10.1097/JU.0000000000001361

9. De Luca S, Passera R, Cattaneo G, Manfredi M, Mele F, Fiori C, et al. High prostate cancer gene 3 (PCA3) scores are associated with elevated prostate imaging reporting and data system (PI-RADS) grade and biopsy Gleason score, at magnetic resonance imaging/ultrasonography fusion software-based targeted prostate biopsy after a previous negative standard biopsy. *BJU Int* (2016) 118(5):723–30. doi: 10.1111/bju.13504

10. Torti SV, Torti FM. Iron and cancer: more ore to be mined. *Nat Rev Cancer* (2013) 13(5):342–55. doi: 10.1038/nrc3495

11. Tesfay L, Clausen KA, Kim JW, Hegde P, Wang X, Miller LD, et al. Hepcidin regulation in prostate and its disruption in prostate cancer. *Cancer Res* (2015) 75 (11):2254–63. doi: 10.1158/0008-5472.CAN-14-2465

12. Papakonstantinou O, Alexopoulou E, Economopoulos N, Benekos O, Kattamis A, Kostaridou S, et al. Assessment of iron distribution between liver, spleen, pancreas, bone marrow, and myocardium by means of R2 relaxometry with MRI in patients with beta-thalassemia major. *J Magn Reson Imaging* (2009) 29(4):853–9. doi: 10.1002/jmri.21707

13. Henninger B, Kremser C, Rauch S, Eder R, Zoller H, Finkenstedt A, et al. Evaluation of MR imaging with T1 and T2* mapping for the determination of hepatic iron overload. *Eur Radiol* (2012) 22(11):2478–86. doi: 10.1007/s00330-012-2506-2

14. Henninger B, Zoller H, Kannengiesser S, Zhong X, Jaschke W, Kremser C. 3D multiecho Dixon for the evaluation of hepatic iron and fat in a clinical setting. *J Magn Reson Imaging* (2017) 46(3):793–800. doi: 10.1002/jmri.25630

15. Tian Z, Li YG, Li GZ, Huang ZH, Dai WH, Wei XD, et al. A correlative study of iron metabolism based on q-Dixon MRI in benign prostatic hyperplasia and prostate cancer. *Asian J Androl* (2022) 24(6):671–4. doi: 10.4103/aja2021116

16. Hansen NL, Barrett T, Kesch C, Pepdjonovic L, Bonekamp D, O'Sullivan R, et al. Multicentre evaluation of magnetic resonance imaging supported transperineal prostate biopsy in biopsy-naïve men with suspicion of prostate cancer. *BJU Int* (2018) 122(1):40–9. doi: 10.1111/bju.14049

17. Pokorny MR, de Rooij M, Duncan E, Schröder FH, Parkinson R, Barentsz JO, et al. Prospective study of diagnostic accuracy comparing prostate cancer detection by transrectal ultrasound-guided biopsy versus magnetic resonance (MR) imaging with subsequent MR-guided biopsy in men without previous prostate biopsies. *Eur Urol* (2014) 66(1):22–9. doi: 10.1016/j.eururo.2014.03.002

18. Thompson J, Lawrentschuk N, Frydenberg M, Thompson L, Stricker P. The role of magnetic resonance imaging in the diagnosis and management of prostate cancer. *BJU Int* (2013) 112(Suppl 2):6–20. doi: 10.1111/bju.12381

19. Liddell H, Jyoti R, Haxhimolla HZ. Mp-MRI prostate characterised PIRADS 3 lesions are associated with a low risk of clinically significant prostate cancer - a retrospective review of 92 biopsied PIRADS 3 lesions. *Curr Urol* (2015) 8(2):96–100. doi: 10.1159/000365697

20. Scialpi M, Martorana E, Aisa MC, Rondoni V, D'Andrea A, Bianchi G. Score 3 prostate lesions: a gray zone for PI-RADS v2. *Turk J Urol* (2017) 43(3):237–40. doi: 10.5152/tud.2017.01058

21. Haider MA, van der Kwast TH, Tanguay J, Evans AJ, Hashmi A-T, Lockwood G, et al. Combined T2-weighted and diffusion-weighted MRI for localization of prostate cancer. *AJR Am J Roentgenol* (2007) 189(2):323–8. doi: 10.2214/AJR.07.2211

22. Yu AC, Badve C, Ponsky LE, Pahwa S, Dastmalchian S, Rogers M, et al. Development of a combined MR fingerprinting and diffusion examination for prostate cancer. *Radiology* (2017) 283(3):729–38. doi: 10.1148/radiol.2017161599

23. Pickles M, Gibbs P, Sreenivas M, Turnbull L. Diffusion-weighted imaging of normal and malignant prostate tissue at 3.0T. *J Magn Reson Imaging* (2006) 23(2):130–4. doi: 10.1002/jmri.20477

24. Moraes MO, Roman DHH, Copetti J, de S Santos F, Agra A, Noronha JAP, et al. Effects of the addition of quantitative apparent diffusion coefficient data on the diagnostic performance of the PI-RADS v2 scoring system to detect clinically significant prostate cancer. *World J Urol* (2020) 38(4):981–91. doi: 10.1007/s00345-019-02827-2

25. Bordini J, Morisi F, Elia AR, Santambrogio P, Pagani A, Cucchiara V, et al. Iron induces cell death and strengthens the efficacy of antiandrogen therapy in prostate cancer models. *Clin Cancer Res* (2020) 26(23):6387–98. doi: 10.1158/1078-0432.CCR-20-3182

26. Zhuge X, Zhou H, Chen L, Chen H, Chen X, Guo C. The association between serum ferritin levels and malignant intraductal papillary mucinous neoplasms. *BMC Cancer* (2021) 21(1):1253. doi: 10.1186/s12885-021-08986-z

27. Miyamoto Y, Nakano S, Ihira H, Yamaji T, Katagiri R, Sawada N, et al. Association of plasma iron status with subsequent risk of total and site-specific cancer: a Large case-cohort study within JPHC study. *Cancer Prev Res (Philadelphia Pa)* (2022) 15(10):669–78. doi: 10.1158/1940-6207.CAPR-22-0151

28. Finianos A, Matar CF, Taher A. Hepatocellular carcinoma in β-thalassemia patients: review of the literature with molecular insight into liver carcinogenesis. *Int J Mol Sci* (2018) 19(12):4070. doi: 10.3390/ijms19124070

29. Gündoğdu E, Emekli E, Kebapçı M. Evaluation of relationships between the final Gleason score, PI-RADS v2 score, ADC value, PSA level, and tumor diameter in patients that underwent radical prostatectomy due to prostate cancer. *Radiol Med* (2020) 125(9):827–37. doi: 10.1007/s11547-020-01183-1

30. Yamamoto S, Yoshida S, Ishii C, Takahara T, Arita Y, Fukushima H, et al. Metastatic diffusion volume based on apparent diffusion coefficient as a prognostic factor in castration-resistant prostate cancer. *J Magn Reson Imaging* (2021) 54(2):401–8. doi: 10.1002/jmri.27596

frontiers | Frontiers in Oncology

TYPE Review
PUBLISHED 05 June 2023
DOI 10.3389/fonc.2023.1178430

OPEN ACCESS

EDITED BY
Daniel N. Costa,
University of Texas Southwestern Medical Center, United States

REVIEWED BY
Octavian Sabin Tataru,
George Emil Palade University of Medicine, Pharmacy, Sciences and Technology of Târgu Mureş, Romania
Iulia Andras,
Iuliu Haţieganu University of Medicine and Pharmacy, Romania

*CORRESPONDENCE
Benedetta Renzetti
benedetta.renzetti@studio.unibo.it

†These authors have contributed equally to this work and share first authorship

RECEIVED 02 March 2023
ACCEPTED 22 May 2023
PUBLISHED 05 June 2023

CITATION
Gaudiano C, Renzetti B, De Fino C, Corcioni B, Ciccarese F, Bianchi L, Schiavina R, Droghetti M, Giunchi F, Brunocilla E and Fiorentino M (2023) Multiparametric magnetic resonance imaging for the differential diagnosis between granulomatous prostatitis and prostate cancer: a literature review to an intriguing diagnostic challenge. *Front. Oncol.* 13:1178430. doi: 10.3389/fonc.2023.1178430

Multiparametric magnetic resonance imaging for the differential diagnosis between granulomatous prostatitis and prostate cancer: a literature review to an intriguing diagnostic challenge

Caterina Gaudiano[1†], Benedetta Renzetti[2*†], Cristina De Fino[2], Beniamino Corcioni[1], Federica Ciccarese[1], Lorenzo Bianchi[2,3], Riccardo Schiavina[2,3], Matteo Droghetti[2,3], Francesca Giunchi[4], Eugenio Brunocilla[2,3] and Michelangelo Fiorentino[5]

[1]Department of Radiology, IRCCS Azienda Ospedaliero-Universitaria di Bologna, Bologna, Italy, [2]Department of Medical and Surgical Sciences (DIMEC), University of Bologna, Bologna, Italy, [3]Division of Urology, IRCCS Azienda Ospedaliero-Universitaria di Bologna, Bologna, Italy, [4]Department of Pathology, IRCCS Azienda Ospedaliero-Universitaria di Bologna, Bologna, Italy, [5]Department of Medical and Surgical Sciences, University of Bologna, Bologna, Italy

Multiparametric magnetic resonance imaging (mpMRI) is currently the most effective diagnostic tool for detecting prostate cancer (PCa) and evaluating adenocarcinoma-mimicking lesions of the prostate gland, among which granulomatous prostatitis (GP) represents the most interesting diagnostic challenge. GP consists of a heterogeneous group of chronic inflammatory lesions that can be differentiated into four types: idiopathic, infective, iatrogenic, and associated with systemic granulomatous disease. The incidence of GP is growing due to the increase in endourological surgical interventions and the adoption of intravesical instillation of Bacillus Calmette-Guerin in patients with non-muscle invasive bladder cancer; therefore, the difficulty lies in identifying specific features of GP on mpMRI to avoid the use of transrectal prostate biopsy as much as possible.

KEYWORDS

prostate cancer, granulomatous prostatitis, non-specific granulomatous prostatitis, granulomatous prostatitis induced by BCG, multiparametric magnetic resonance imaging, PI-RADS score

1 Introduction

There has recently been increasing interest in the diagnostic impact of multiparametric magnetic resonance imaging (mpMRI), which has become crucial for detecting prostate cancer (PCa) in both the peripheral and transition zones (PZ and TZ) and evaluating adenocarcinoma-mimicking lesions of the prostate gland, before planning a transrectal ultrasound (TRUS)/MRI fusion targeted biopsy (1).

As a matter of fact, a valid assessment of suspicious areas in mpMRI is a determinant for avoiding biopsy in patients without target lesions, for averting errors of overdiagnosis related to random biopsies, and for differentiating tumor-like lesions from PCa, which can be monitored in a periodic follow-up (2, 3).

Of the adenocarcinoma-mimicking lesions of the prostate gland, granulomatous prostatitis (GP) usually has the same clinical appearance as PCa, with obstructive and/or irritative symptoms, a diffuse or focal enlargement of the gland at digital rectal examination, and increasing levels of prostate-specific antigen (PSA) (4).

GP comprises a heterogeneous group of chronic inflammatory lesions of often unknown etiology and pathogenesis usually occurring in the PZ (5), which are relatively rare, accounting for 3.3% of all benign conditions of the gland (6), and are the best tumor mimickers.

Nevertheless, the incidence of GP is growing due to the increase of endourological surgical interventions and the adoption of intravesical instillation of Bacillus Calmette-Guerin (BCG) in patients with non-muscle invasive bladder cancer (NMIBC) (6, 7).

The GP is classified into four types, based on etiopathogenetic entities (Table 1) and the corresponding histopathological findings (Table 2), which we will analyze in detail.

Regarding the mpMRI features of GP, large series studies are not available due to the rarity of the disease; therefore, in the literature, mainly case reports and small case series are reported. Nevertheless, in this paper, we intend to illustrate both the most common and the least frequent features of the various types of GP on mpMRI, through a narrative literature review, in order to highlight any radiological criteria for the differential diagnosis between this inflammatory condition and PCa and avoid as much as possible the use of TRUS prostate biopsy. Particularly, we want to focus on evaluating the GP features on the multiparametric study protocol, including T2-weighted (T2w), diffusion-weighted imaging (DWI) with apparent diffusion coefficient (ADC) map, and dynamic contrast-enhanced (DCE) sequences.

2 Materials and methods

This literature review was conducted by searching on PubMed the following keywords: “granulomatous prostatitis” AND “MRI” OR “mpMRI” OR “multiparametric magnetic resonance imaging” OR “magnetic resonance imaging” and including articles published from 2002 to 2022.

The bibliographic search produced 46 results.

After a reading of the titles and abstracts, articles that did not focus on the characteristics of GP on mpMRI were eliminated, the 30 remaining articles were read thoroughly, and, after the elimination of repetitive, irrelevant, and unrelated articles, 15 publications remained (Figure 1).

The selected articles were the ones focused on the peculiar characteristics, and other main variants, of the different types of GP on mpMRI, in the perspective of the differential diagnosis with PCa.

We have attempted to include a variety of articles to ensure a comprehensive and exhaustive assessment of the various forms of GP, selecting the articles focused on mpMRI appearance with a preference for case series rather than case reports.

We prioritized papers with a protocol study adhering as much as possible to the Prostate Imaging Reporting and Data System (PI-RADS) guidelines, including high-resolution T2w in the axial, sagittal, and coronal planes; T1w in the axial plane; and multi-b values and high-b value DWI, with the corresponding ADC map and DCE sequences.

In an article (8), it was specified that, being a retrospective analysis, the imaging parameters were not standardized; thus, 5, 4, and 1 of the 10 patients underwent a spin-echo T1w, gradient-echo T1w, and unenhanced T1w, respectively, while the other sequences were the same. For the same reason, in another article (9), the images after infusion of gadolinium were not available.

Table 3 shows the detailed description of the technical equipment used by each author group.

In all the articles, it was emphasized that the confirmatory diagnosis was histopathological through a target or random sub

TABLE 1 Etiological classification of granulomatous prostatitis.

Idiopathic	• Typical non-specific granulomatous prostatitis • Xanthogranulomatous prostatitis
Infective	• After Bacillus Calmette-Guerin vesical instillations • Bacterial (Tuberculosis, Brucellosis, Syphilis) • Fungal (Coccidiidiomycosis, Cryptococcosis, Blastomycosis, Histoplasmosis, Paracoccidioidomycosis) • Parasitic (Schistosomiasis, Echinococcosis, Enterobiasis) • Viral (Herpes simplex virus)
Iatrogenic	• Post-surgical (TURP) • Actinic
Associated with other rare systemic granulomatous diseases	• Sarcoidosis, rheumatoid arthritis • Wegener’s granulomatosis • Polyarteritis nodosa, Churg–Strauss syndrome

TURP, transurethral resection of the prostate.

TABLE 2 Histopathological features of granulomatous prostatitis types.

GP types	Histopathological features
Idiopathic	• Non-caseous granulomas with a periglandular distribution, consisting of epithelioid cells, neutrophils, histiocytes, lymphocytes, and desquamated cells. Dilated ducts are usually observed • In the xanthogranulomatous subtype, focal accumulations of cholesterol-laden histiocytes are usually seen in the prostate
Infective	• Confluent foci of well-formed caseous granulomas with Langhan's-type giant cell, surrounded by epithelioid histiocytes • In BCG-related GP, caseating or noncaseating granulomas are also seen, although acid-fast bacilli are variably present; Ziehl–Neelsen stain can be useful in obtaining a final diagnosis
Iatrogenic	• Dense inflammation of the prostatic stroma, usually with the presence of rheumatoid-like nodules consisting of palisading histiocytes with foci of fibrinoid necrosis
Associated with other rare systemic granulomatous diseases	• Depending on the primary granulomatous disease

GP, granulomatous prostatitis; BCG, Bacillus Calmette-Guerin.

head prostate biopsy, even if a central pathological review was not specified.

In five articles (8, 9, 12, 15, 18), it has been underlined that mpMRI imaging wax interpreted by two radiologists with many years of post-training experience (from a minimum of 3 years to a maximum of 18 years), and in another article (14), it has been emphasized that diagnostic mpMRI studies were subjected to radiological evaluation at a multidisciplinary conference on prostate imaging.

The findings obtained in the articles are summarized in Table 4 and described in detail in the following sections.

2.1 Multiparametric MRI features and histopathological correlation

Based on histopathological findings and underlying etiology, the GP is classified into four types:

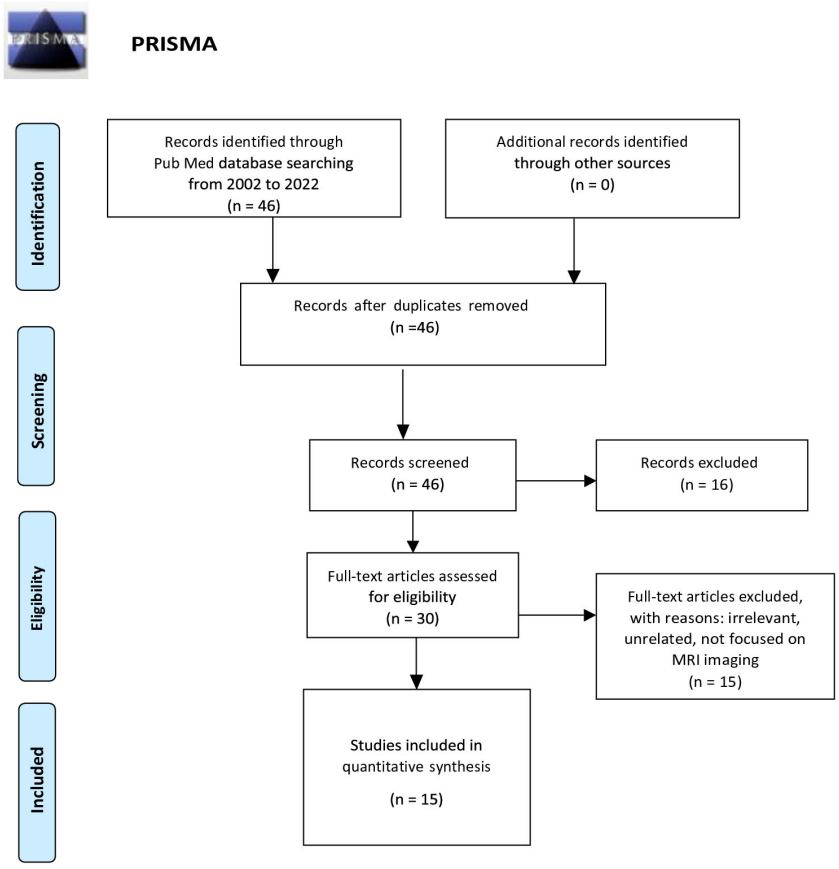

FIGURE 1
Preferred reporting items for systematic reviews and meta-analyses (PRISMA) flow diagram.

TABLE 3 Detailed description of the technical equipment used by each author group.

Authors	Scanner	Endorectal coil	Study protocol	PI-RADS score
Kitzing YX et al. (4)	3 T	No	T2, T1, multi b-DWI, ADC maps and DCE	≥3
Bertelli E et al. (5)	1.5 T	No	T2, T1, multi b-DWI, ADC maps and DCE	≥3
Crocetto F et al. (6)	Not reported	Not reported	Not reported	≥3
Suzuki T et al. (8)	1.5 T	No	T2, T1, multi b-DWI, ADC maps (no DCE)	Not reported
Wang Z et al. (9)	3 T	No	T2, T1, multi b-DWI, ADC maps (no DCE)	Not reported
Cheng Y et al. (10)	Not reported	Not reported	T2, T1, multi b-DWI, ADC maps, and DCE	Not reported
Lee SM et al. (11)	1.5 T	No	T2, T1, multi b-DWI, ADC maps, and DCE	≥3
Gottlieb et al. (12)	3 T	No	T2, T1, multi b-DWI, ADC maps, and DCE	≥3
Bour L et al. (13)	1.5 T	Yes (4/5 patients)	T2, T1, multi b-DWI, ADC maps, and DCE	Not reported
Rais-Bahrami S et al. (14)	3 T	No	T2, T1, multi b-DWI, ADC maps, and DCE	≥3
Kawada H et al. (15)	1.5 T	No	T2, T1, multi b-DWI, ADC maps, and DCE	Not reported
Han C et al. (16)	Not reported	No	T2, T1, multi b-DWI, ADC maps, and DCE	≥3
Suditu N et al. (17)	Recommended 3 T	Recommended	T2, T1, multi b-DWI, ADC maps, and DCE	Not reported
Lee S et al. (18)	3 T	No	T2, T1, multi b-DWI, ADC maps, and DCE	≥3 (except type C=1)
De Luca L et al. (19)	3 T	No	T2, T1, multi b-DWI, ADC maps, and DCE	≥3

PI-RADS, Prostate Imaging Reporting and Data System; DWI, diffusion-weighted imaging; ADC, apparent diffusion coefficient; DCE, dynamic contrast enhanced.

1. Idiopathic (non-specific and non-necrotic)
2. Infective (specific, non-necrotic or necrotic)
3. Iatrogenic (post-surgical)
4. Associated with systemic granulomatous disease (4)

2.1.1 Idiopathic granulomatous prostatitis

Non-specific granulomatous prostatitis (NSGP) represents the most common type among GP, accounting for approximately 60%–77.7% (6).

The etiology of NSGP is unknown, but some studies have hypothesized an autoimmune reaction to cell debris, secretion spilling, and bacterial toxins into the stroma, resulting in blockage of the ducts and reflux of urine (10).

Histologically, NSGP is characterized by histiocytoid granulomas with clusters of macrophages, intermingled with multinucleated giant cell, lymphocytes, plasma cells, and neutrophils. The multinucleated giant cells might be absent (6) (Table 2).

According to the literature, the typical pattern at the mpMRI shows a tumor-like appearance with hypointensity on T2w, hyperintensity on DWI, and low ADC values (6, 11–13) (Table 4; Figures 2–4).

In particular, on T2w, all lesions have lower signal intensity (SI) when compared to femoral head bone and demonstrate higher SI when compared with the obturator muscle (11).

On DWI, all lesions have higher signal intensity than the residual normal PZ (8). Many authors have demonstrated that the values of ADC in GP are lower than in high-grade PCa (5, 11, 13); thus, some authors have proposed using a nomogram that utilizes ADC values threshold to distinguish NSGP from PCa (14).

On DCE, almost all the lesions showed a moderate hyperenhancement after the administration of gadolinium-based contrast agent (5, 11, 13). However, in some patients with NSGP, DCE showed high and early enhancement followed by early wash-out (5), which is the typical pattern of PCa (15), while others highlighted a mild or scarce enhancement (5) (Table 4).

Some authors proposed that moderate hyperenhancement together with low ADC value may suggest the diagnosis of GP rather than PCa (13).

Some cases of diffuse GP may present with hyperintensity on T1w (16).

Morphologically, these lesions are nodular and circumscribed, with a diameter < 1.5 cm (12) (Figure 2) or between 1 and 3.5 cm (5) (Figure 3), usually confined to the PZ; more rarely can NSGP affect the whole PZ (Figure 4) or both the PZ and TZ; the involvement of only the TZ is an exception (5, 12) (Table 4).

Although it is infrequent, some cases in the literature report the presence of bulging and/or irregularity of the glandular capsule in NSGP while extra-capsular extension is usually absent (11, 12).

The xanthogranulomatous prostatitis (XGP) is a very rare subtype of NSGP and very few cases are reported in the literature. The distinctive histological feature is the presence of lipid-laden macrophages called “foamy histiocyte” in the inflammatory cell infiltrate.

The mpMRI showed isointensity on T1w, hypointensity on T2w, marked hyperintensity on DWI, low signal on ADC map, and hyperenhancement on DCE. Unlike NSGP, XGP has a patchy or diffuse involvement of the PZ with disappearance of the normal

10.3389/fonc.2023.1178430

TABLE 4 Multiparametric MRI features of the various types of granulomatous prostatitis.

Non-specific granulomatous prostatitis (NSGP)			
Sequences	Typical pattern	Less frequent patterns	Subtype: Xantogranulomatous prostatitis
T2w	Hypointense circumscribed nodule in the PZ Diameter < 1.5 cm	Hypointense nodule Diameter between 1 and 3.5 cm Both the PZ and TZ The involvement of only the TZ is an exception	Hypointensity with patchy or diffuse involvement of the PZ associated with disappearance of the normal demarcation between PZ and TZ
DWI	Hyperintensity	Hyperintensity	Hyperintensity
ADC map	Low ADC value	Low ADC value	Low ADC value
DCE	Moderate hyperenhancement	High and early enhancement followed by early wash-out	Diffuse hyperenhancement
Specific granulomatous prostatitis (infective and iatrogenic)			
Sequences	**Diffuse pattern**	**Nodular pattern**	**Cystic pattern**
T2w	Diffuse, heterogeneous, non-circumscribed, hypointensity of the PZ Frequent extension in the TZ Presence of capsular bulging	Solid nodule, polygonal in shape, markedly hypointense Diameter > 1.5 cm	Hyperintense nodule with peripheral hypointensity Central necrosis (caseation)
DWI	Hyperintensity	Hyperintensity	Hyperintensity
ADC map	Low ADC value	Low ADC value	Low ADC value
DCE	Moderate or marked enhancement	Contrast enhancement inhomogeneous, early, and prolonged	Early and prolonged peripheral rim enhancement with avascular core ("ring enhancement pattern")
Associated with systemic granulomatous disease			
Sequences			
T2w	Hypointensity		
DWI	Hyperintensity		
ADC map	Low ADC value		
DCE	Diffuse contrast enhancement		

DWI, diffusion-weighted imaging; ADC, apparent diffusion coefficient; DCE, dynamic contrast enhanced; PZ, peripheral zone; TZ, transition zone.

demarcation between PZ and TZ while the prostate capsule is always preserved (10) (Table 4).

2.1.2 Infective granulomatous prostatitis and iatrogenic (post-surgical) granulomatous prostatitis

The cases reported in literature of infective GP are caused by some infectious agents such as virus-like herpes zoster, fungi like *Cryptococcus*, and bacteria like *Mycobacterium tuberculosis* and *Treponema pallidum* (4, 16) (Table 1).

The histological features are usually characterized by granulomas with epithelioid and multinucleated giant cell infiltration with caseous necrosis (4) (Table 2).

Among the iatrogenic causes are as follows: transurethral resection of the prostate (TURP) or the bladder (TURB), prostate biopsy, and open adenomectomy (6) (Table 1).

The most common etiology of specific GP is caused by a later complication of intravesical instillation of BCG; the BCG immunotherapy, given after TURB, is the most effective adjuvant treatment for intermediate and high-grade NMIBC (9).

Some studies proved that 75%–100% of the patients who undergo BCG instillations develop specific GP (17).

The appearance of tubercular GP is variable (16); in fact, three patterns can be identified: diffuse, nodular, and cystic (8).

The most common type is the diffuse pattern in which there is a heterogeneous, non-circumscribed, diffused involvement of the PZ with frequent extension in the TZ and the presence of capsular bulging, without invasion of peri-prostatic tissue (8, 12).

On mpMRI, diffuse pattern of non-necrotic GP shows low T2 signal intensity, similar to SI of bone marrow but lower than the SI of the normal PZ (8) (Table 4).

These lesions, typical of the acute phase, are associated with diffuse restriction on DWI, moderate or marked enhancement on DCE (4), and a decreased signal on the ADC map images (12); these features make them difficult to distinguish from cancer (Table 4).

The nodular pattern is characterized by the presence of solid nodules, polygonal in shape (8) and measuring > 1.5 cm (12), with marked hypointensity of signal in T2w sequences and isointensity of signal on T1w sequences if compared with obturator muscle (8) (Table 4).

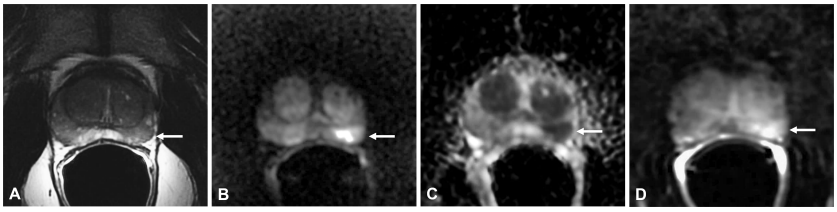

FIGURE 2
Non-specific granulomatous prostatitis in a 56-year-old patient with a PSA value of 6 ng/ml. The axial T2-weighted sequence shows a hypointense nodule in the left mid-peripheral zone (PZ) (arrow in **A**) with high hyperintensity on the DWI image (arrow in **B**), marked hypointensity on the ADC map (arrow in **C**), and high contrast enhancement on the DCE image (arrow in **D**).

All nodular lesions show higher signal intensity on DWI, because DWI reflects the cell density increased by the presence of lymphocytes during acute inflammation (8), and lower SI on ADC when compared to the normal PZ (9) (Table 4).

If there are no necrotic areas, the contrast enhancement is inhomogeneous, early and prolonged (5, 9).

The cystic pattern with mural nodules is caused by central caseous necrosis that manifests with the tubercular granuloma (16). Therefore, in necrotic GP, central necrosis (caseation) is hyperintense on T2w sequences, with marked signal restriction on high b-value DWI, low ADC value, and total lack of contrast enhancement (4, 6), while mural nodules show hypointensity on T2w sequences with contrast enhancement on DCE imaging (8) (Table 4; Figures 5, 6).

Thus, on DCE sequences, these lesions have a typical enhancement behavior characterized by an early and prolonged peripheral rim enhancement with avascular core due to caseous necrosis, already described as "ring enhancement" (5, 15, 16) (Figures 5, 6).

Recently, Lee et al. (18) focused on the multiphase contrast enhancement pattern of BCG-induced GP lesions in a cohort of 24 patients. They found three typical patterns of vascularity based on sequential changes and histological findings: pattern A demonstrated diffuse enhancement, pattern B demonstrated lesions with ring enhancement, and pattern C demonstrated poor rim enhancement. Types A and B are regarded as acute stages, which show diffusion restriction on DWI and intense enhancement, and the difference is, respectively, the absence and presence of a well-defined poorly enhancing area in types A and B; type C is a chronic lesion showing poor enhancement and a low signal intensity on high b-value DWI.

2.1.3 Associated with systemic granulomatous disease

Some articles in the literature report a suspected correlation between GP and systemic disease such as psoriasis, sarcoidosis, rheumatoid arthritis, Wegener's granulomatosis, polyarteritis nodosa, and Churg–Strauss syndrome (Table 1). The histopathological features depend on the primary granulomatous disease (Table 2).

Usually, it is a nodular lesion that can involve both the peripheral and transition zones with a capsular irregularity. mpMRI shows a low signal intensity on T2w, a significant signal restriction on DWI with low ADC and a diffuse contrast enhancement on DCE (Table 4).

It is interesting to note that there could be a link between GP and systemic granulomatous diseases, because these conditions are characterized by an abnormal response of the immune system that could play a direct role in their pathogenesis (19).

3 Discussion and conclusion

GP is a relatively rare chronic inflammatory disease of the prostate (5), which represents approximately 3.3% of all benign conditions of the gland (6), whose incidence is increasing due to the growth of endourological surgical interventions and the adoption of intravesical instillation of BCG in patients with NMIBC (6).

Despite being a benign condition, GP represents one of the main adenocarcinoma-mimicking lesions and in most cases produces PI-RADS ≥ 3 findings at mpMRI, placing a high suspicion of PCa. In a cohort of 105 biopsied PI-RADS 5 lesions, Pepe et al. found six (5.7%) GP, with five non-specific GP and one specific GP secondary to prostatic *M. tuberculosis* (20).

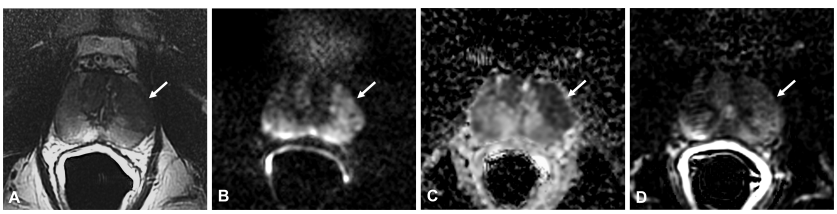

FIGURE 3
Non-specific granulomatous prostatitis in a 47-year-old patient with a PSA value of 9.81 ng/ml. The axial T2-weighted sequence shows a large hypointense area in the anterior left peripheral zone (PZ) with bulging of the glandular capsule (arrow in **A**) with diffuse hyperintensity on the DWI image (arrow in **B**), marked hypointensity on the ADC map (arrow in **C**), and diffuse mild enhancement on the DCE image (arrow in **D**).

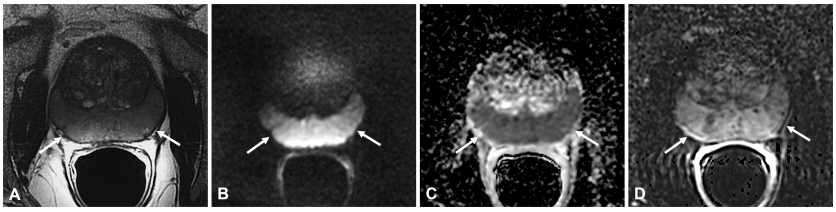

FIGURE 4
Non-specific granulomatous prostatitis in a 66-year-old patient with a PSA value of 15.92 ng/ml. The axial T2-weighted sequence shows diffuse hypointensity and thickening of the peripheral zone (PZ) with preservation of the glandular capsule and pseudocapsule (arrows in **A**). The entire PZ appears diffusely hyperintense on the DWI image (arrows in **B**) and markedly hypointense on the ADC map (arrows in **C**) with diffuse high contrast enhancement on the DCE image (arrow in **D**).

In this article, we have tried to identify the peculiar characteristics of the GP at mpMRI, through a narrative review of the literature, with the aim of improving the differential diagnosis with adenocarcinoma and avoid the use of prostate biopsy as much as possible.

NSGP, including XGP, is a very rare inflammatory condition and radiological reports at mpMRI are too few. According to the literature, we have seen that the typical pattern of NSGP at the mpMRI shows nodular lesions, confined to the PZ, with a tumor-like appearance (6, 11–13). Although DCE images are not specific, moderate or scarce hyperenhancement together with a very low ADC value may suggest the diagnosis of GP rather than PCa (13); therefore, in these cases, and in agreement with the referring urologist, a wait-and-see attitude could be proposed with a re-evaluation on mpMRI after a few months to value the possible self-resolution of the inflammatory picture (19). However, in cases where DCE images showed high and early enhancement followed by early wash-out (5), there is the presence of bulging and/or irregularity of the glandular capsule, or there are no clear parameters to differentiate NSGP from PCa, the use of biopsy is mandatory.

In most cases, NSGP resolves spontaneously without treatments with normalization of PSA level (19); however, careful follow-up is required after this diagnosis in order to exclude the coexistence of an occult PCa.

Nowadays, intravesical BCG instillation is widely used as a treatment for non-muscle invasive bladder cancer after transurethral resection though the immune system activation and the induction of inflammatory response (21). The intraprostatic reflux of contaminated urines from urethra can cause the BCG-induced GP and it usually involves the PZ because of the obtuse angle between the PZ and the urethra (18).

The BCG-induced GP can present variable appearances, probably based on the different stages of the disease. At a certain stage of the development of the disease, some cavitated nodules with a characteristic cystic pattern appear. This pattern consists of hyperintensity on T2 sequences, with marked hyperintensity on high b-value DWI and low ADC value; on DCE sequences, there is a typical enhancement behavior characterized by an early and prolonged peripheral rim enhancement with avascular core. Kawada et al. (15) first analyzed the multiphase contrast enhancement pattern of BCG-induced GP lesions on gadolinium-enhanced MR images showing this characteristic appearance defined “ring enhancement”. The histological analysis confirmed

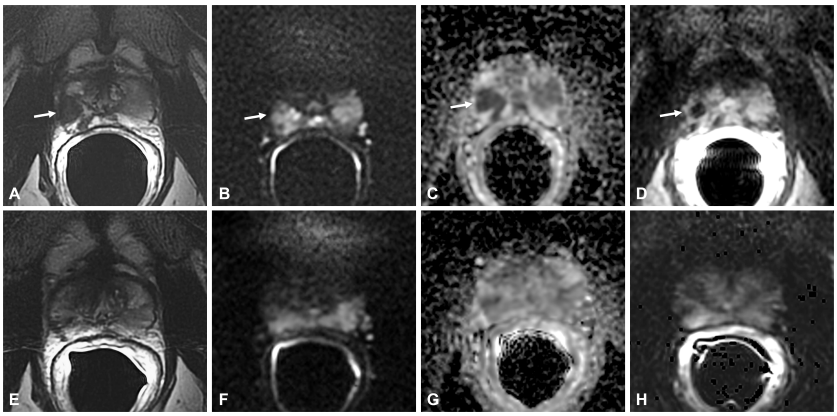

FIGURE 5
Bacillus Calmette-Guérin-induced granulomatous prostatitis in a 58-year-old patient with a PSA value of 1.17 ng/ml. The first mpMRI at diagnosis showed diffuse alteration of the peripheral zone (PZ) with a hypointense nodule in the right middle lobe in the T2-weighted sequence (arrow in **A**) with hyperintensity on the DWI image (arrow in **B**), marked hypointensity on the ADC map (arrow in **C**), and typical “ring enhancement” on the DCE image (arrow in **D**). The corresponding sequences of the 5-month mpMRI follow-up **(E–H)** showed almost complete resolution of the aforementioned findings.

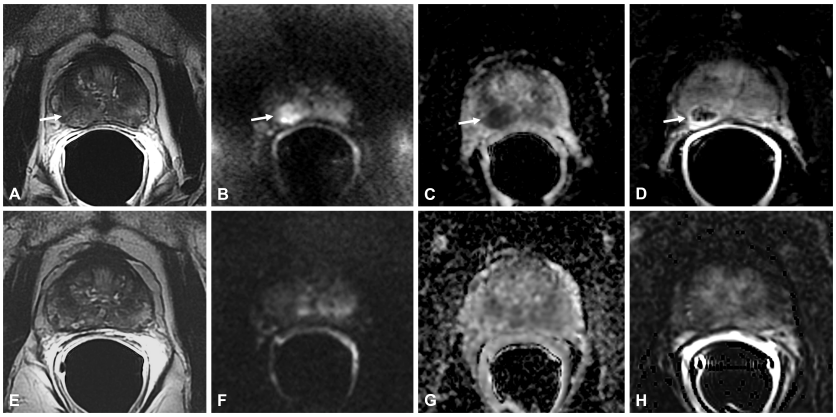

FIGURE 6
Bacillus Calmette-Guérin-induced granulomatous prostatitis in a 53-year-old patient with a PSA value of 5 ng/ml. The first mpMRI at diagnosis showed diffuse alteration of the peripheral zone (PZ) with an inhomogeneous hypointense nodule in the right middle lobe in the T2-weighted sequence (arrow in **A**) with hyperintensity on the DWI image (arrow in **B**), marked hypointensity on the ADC map (arrow in **C**), and typical "ring enhancement" on the DCE image (arrow in **D**). The corresponding sequences of the 7-month mpMRI follow-up **(E–H)** showed complete resolution of the aforementioned findings.

the correspondence between the granulomatous tissue with central caseation necrosis and the ring enhancement area. The authors concluded that this appearance could be considered characteristic of the BCG-induced GP and could be useful to differentiate it from PCa. More recently, Lee et al. (18) attempted to differentiate PCa from BCG-induced GP on the basis of the multiphase contrast enhancement pattern. During the acute phase of the disease, the diffuse enhancement pattern, also called pattern A, prevails and the diagnosis of PCa is more challenging; thus, follow-up or a biopsy is needed. A possible differentiation with PCa can be made in the presence of lesions with ring enhancement, in pattern B, or chronic lesions, in pattern C.

Recognizing the key role of the DCE sequence is fundamental for obtaining the proper identification of caseating granulomas as their high values in DWI sequence could lead to an incorrect diagnosis; this observation highlights the limits of the biparametric MRI protocol in the evaluation of this pathology and suggests the need for the multiparametric MRI protocol in patients with recent intravesical BCG instillation.

Furthermore, a mpMRI follow-up of prostatic lesions, as an alternative to a biopsy, is suggested in patients with suspicious lesions and a history of vesical instillation of BCG for bladder carcinoma as these granulomas can decrease in size, thus suggesting an antitubercular therapy, when required (9). As in the study of Lee et al. (18), the date interval for follow-up after the first diagnosis varied considerably in our study, thus denying a correlation between duration and stage of the disease. No further and precise indications can be extracted from the literature regarding this.

Finally, the present study outlined the limits of the correct assignment of the PI-RADS score in evaluating the radiological findings of benign inflammatory conditions, the proper classification of which can be obtained from its complete clinical context. Therefore, the need to integrate the PI-RADS system in the evaluation of specific benign conditions such as inflammatory diseases can be argued.

The main limitation of the present study is the lack of large series studies on this topic, owing to the rarity of the disease. In fact, mainly case reports and small case series are reported in the literature; thus, a detailed statistical analysis has not been possible.

As a result of the review of the literature, we can conclude that mpMRI of the prostate may play a key role in differentiating BCG-induced GP from adenocarcinoma of the prostate on the basis of the correct evaluation of the typical "ring enhancement" of the prostate lesions on the multiphase contrast-enhanced MRI, in the presence of specific clinical context; an mpMRI follow-up of prostatic lesions can be safely carried out. Conversely, the correct diagnosis of other cases of non-necrotic GP (including NSGP, XGP, and diffuse or nodular BCG-induced GP) is not possible on the basis of the mpMRI features, even when considering the PSA values; a targeted biopsy remains the mandatory approach.

Author contributions

CG conceived, guided, and revised the manuscript. BR reviewed the literature and wrote the original draft of the project. CF, BC, and FC contributed to the literature review and description of MRI features. LB, RS, MD, and FG provided experience in clinical and surgical parts. EB and MF helped in histopathological review. All authors contributed to the article and approved the submitted version.

Funding

The work reported in this publication was funded by the Italian Ministry of Health, RC-2022-2773479.

Conflict of interest

The authors declare that the research was conducted in the absence of any commercial or financial relationships that could be construed as a potential conflict of interest.

Publisher's note

References

1. Gaudiano C, Rustici A, Corcioni B, Ciccarese F, Bianchi L, Schiavina R, et al. PI-RADS version 2.1 for the evaluation of transition zone lesions: a practical guide for radiologists. *Br J Radiol* (2022) 95(1131):20210916. doi: 10.1259/bjr.20210916

2. Ahmed HU, El-Shater Bosaily A, Brown LC, Gabe R, Kaplan R, Parmar MK, et al. PROMIS study group. Diagnostic accuracy of multi-parametric MRI and TRUS biopsy in prostate cancer (PROMIS): a paired validating confirmatory study. *Lancet* (2017) 389(10071):815–22. doi: 10.1016/S0140-6736(16)32401-1

3. Kasivisvanathan V, Rannikko AS, Borghi M, Panebianco V, Mynderse LA, Vaarala MH, et al. PRECISION Study Group Collaborators. MRI-Targeted or standard biopsy for prostate-cancer diagnosis. *N Engl J Med* (2018) 378(19):1767–77. doi: 10.1056/NEJMoa1801993

4. Kitzing YX, Prando A, Varol C, Karczmar GS, Maclean F, Oto A. Benign conditions that mimic prostate carcinoma: MR imaging features with histopathologic correlation. *Radiographics* (2016) 36(1):162–75. doi: 10.1148/rg.2016150030

5. Bertelli E, Zantonelli G, Cinelli A, Pastacaldi S, Agostini S, Neri E, et al. Granulomatous prostatitis, the great mimicker of prostate cancer: can multiparametric MRI features help in this challenging differential diagnosis? *Diagnostics (Basel)* (2022) 12(10):2302. doi: 10.3390/diagnostics12102302

6. Crocetto F, Barone B, De Luca L, Creta M. Granulomatous prostatitis: a challenging differential diagnosis to take into consideration. *Future Oncol* (2020) 16 (13):805–6. doi: 10.2217/fon-2020-0185

7. Pavlica P, Barozzi L, Bartolone A, Gaudiano C, Menchi M, Veneziano S. Nonspecific granulomatous prostatitis. *Ultraschall Med* (2005) 26(3):203–8. doi: 10.1055/s-2005-858072

8. Suzuki T, Takeuchi M, Naiki T, Kawai N, Kohri K, Hara M, et al. MRI Findings of granulomatous prostatitis developing after intravesical bacillus calmette-guérin therapy. *Clin Radiol* (2013) 68(6):595–9. doi: 10.1016/j.crad.2012.12.005

9. Wang Z, Han C, Xu Y, Yu X, Kang W, Xiang Y, et al. The role of prostate-specific antigen and multiparametric magnetic resonance imaging in the diagnosis of granulomatous prostatitis induced by intravesical bacillus calmette-guérin vaccine therapy in patients with nonmuscle invasive bladder cancer. *J Cancer Res Ther* (2021) 17(3):625–9. doi: 10.4103/jcrt.JCRT_1684_20

10. Cheng Y, Zhang X, Ji Q, Shen W. Xanthogranulomatous prostatitis: multiparametric MRI appearances. *Clin Imaging* (2014) 38(5):755–7. doi: 10.1016/j.clinimag.2014.03.008

11. Lee SM, Wolfe K, Acher P, Liyanage SH. Multiparametric MRI appearances of primary granulomatous prostatitis. *Br J Radiol* (2019) 92(1098):20180075. doi: 10.1259/bjr.20180075

12. Gottlieb J, Princenthal R, Cohen MI. Multi-parametric MRI findings of granulomatous prostatitis developing after intravesical bacillus calmette-guérin therapy. *Abdom Radiol (NY)* (2017) 42(7):1963–7. doi: 10.1007/s00261-017-1081-z

13. Bour L, Schull A, Delongchamps NB, Beuvon F, Muradyan N, Legmann P, et al. Multiparametric MRI features of granulomatous prostatitis and tubercular prostate abscess. *Diagn Interv Imaging* (2013) 94(1):84–90. doi: 10.1016/j.diii.2012.09.001

14. Rais-Bahrami S, Nix JW, Turkbey B, Pietryga JA, Sanyal R, Thomas JV, et al. Clinical and multiparametric MRI signatures of granulomatous prostatitis. *Abdom Radiol (NY)* (2017) 42(7):1956–62. doi: 10.1007/s00261-017-1080-0

15. Kawada H, Kanematsu M, Goshima S, Kondo H, Watanabe H, Noda Y, et al. Multiphase contrast-enhanced magnetic resonance imaging features of bacillus calmette-guérin-induced granulomatous prostatitis in five patients. *Korean J Radiol* (2015) 16(2):342–8. doi: 10.3348/kjr.2015.16.2.342

16. Han C, Zhu L, Liu X, Ma S, Liu Y, Wang X. Differential diagnosis of uncommon prostate diseases: combining mpMRI and clinical information. *Insights Imaging* (2021) 12(1):79. doi: 10.1186/s13244-021-01024-3

17. Suditu N, Negru D. Bacillus calmette-guérin therapy-associated granulomatous prostatitis mimicking prostate cancer on MRI: a case report and literature review. *Mol Clin Oncol* (2015) 3(1):249–51. doi: 10.3892/mco.2014.422

18. Lee S, Oh YT, Kim HM, Jung DC, Hong H. Imaging patterns of bacillus calmette-Guérin-Related granulomatous prostatitis based on multiparametric MRI. *Korean J Radiol* (2022) 23(1):60–7. doi: 10.3348/kjr.2020.1369

19. De Luca L, Crocetto F, Barone B, Creta M, Pesce S, Aveta A, et al. Granulomatous prostatitis mimicking prostate cancer in a patient with psoriatic arthritis: a case report. *Future Sci OA* (2020) 6(7):FSO591. doi: 10.2144/fsoa-2020-0031

20. Pepe P, Pennisi M. Negative biopsy histology in men with PI-RADS score 5 in daily clinical practice: incidence of granulomatous prostatitis. *Clin Genitourin Cancer* (2020) 18(6):e684–7. doi: 10.1016/j.clgc.2020.04.001

21. Morales A, Eidinger D, Bruce AW. Intracavitary bacillus calmette-guerin in the treatment of superficial bladder tumors. *J Urol* (2017) 197:S142–5. doi: 10.1016/j.juro.2016.10.101

frontiers | Frontiers in Oncology

TYPE Systematic Review
PUBLISHED 14 August 2023
DOI 10.3389/fonc.2023.1216894

OPEN ACCESS

EDITED BY
Fabio Grizzi,
Humanitas Research Hospital, Italy

REVIEWED BY
Matteo Droghetti,
University of Bologna, Italy
Giuseppe Carlo Iorio,
University of Turin, Italy

*CORRESPONDENCE
Zhongxi Zhang
zhzhxi@126.com

RECEIVED 04 May 2023
ACCEPTED 24 July 2023
PUBLISHED 14 August 2023

CITATION
Huang R, Li Y, Wu H, Liu B, Zhang X and Zhang Z (2023) ^{68}Ga-PSMA-11 PET/CT versus ^{68}Ga-PSMA-11 PET/MRI for the detection of biochemically recurrent prostate cancer: a systematic review and meta-analysis.
Front. Oncol. 13:1216894.
doi: 10.3389/fonc.2023.1216894

^{68}Ga-PSMA-11 PET/CT versus ^{68}Ga-PSMA-11 PET/MRI for the detection of biochemically recurrent prostate cancer: a systematic review and meta-analysis

Ruizhe Huang, Yizhen Li, Haowen Wu, Boyi Liu, Xuanjun Zhang and Zhongxi Zhang*

The First Clinical College, Changsha Medical University, Changsha, China

Purpose: Our aim was to conduct a meta-analysis and systematic review in order to compare the diagnostic efficacy of ^{68}Ga-PSMA-11 PET/CT and ^{68}Ga-PSMA-11 PET/MRI in patients with biochemically recurrent after radical prostatectomy and biochemically recurrent prostate cancers (BCR) after hybrid RT and RP.

Methods: Up until February 2023, we searched PubMed, Embase, and Web of Science for pertinent papers. Studies examining the utility of ^{68}Ga-PSMA-11 PET/CT or PET/MRI as a screening tool for biochemically recurrent prostate cancer were included. To measure heterogeneity, we employed the I^2 statistic. In cases of substantial heterogeneity (I^2 > 50%), we used the random effect model to produce a forest plot. In other cases, we utilized the fixed model. Furthermore, we assessed the quality of the studies included using the Quality Assessment of Diagnostic Performance Studies (QUADAS-2) method.

Results: In total, 37 studies involving 8409 patients were examined. For ^{68}Ga-PSMA-11 PET/CT and ^{68}Ga-PSMA-11 PET/MRI, the combined total detection rate was 0.70 (95% CI: 0.65-0.75) and 0.71 (95% CI:0.67-0.75), respectively. ^{68}Ga-PSMA-11 PET/CT and ^{68}Ga-PSMA-11 PET/MRI did not substantially differ in terms of the overall detection rate for BCR *(P = 0.58)*. The detection rate was unaffected by the PSA values *(all P > 0.05)*.

Conclusion: The diagnostic efficacy of ^{68}Ga-PSMA-11 PET/CT appears to be equivalent to that of ^{68}Ga-PSMA-11 PET/MRI in detecting biochemically recurrent prostate cancer. Nonetheless, it should be noted that not all studies have used pathological biopsies as the gold standard. Therefore, additional larger prospective studies are needed to address this issue.

Systematic review registration: identifier CRD42023410039.

KEYWORDS

PET/CT, PET/MRI, prostate cancer, biochemically recurrence, meta-analysis

1 Introduction

One of the most prevalent diseases in the world, prostate cancer (PCa) has an annual incidence increase of 3% from 2014 to 2019 (1). Radiation therapy and radical surgery are the two most frequently used treatments for prostate cancer. A rise in prostate-specific antigen (PSA) levels following treatment, however, is a sign that over 30% of people may still experience disease recurrence (2, 3). In clinical practice, biochemical recurrence (BCR) of PCa is fairly typical. BCR is defined as an absolute rise in PSA level of 2 ng/ml over the lowest post-treatment PSA level following radiation therapy (RT) or a serum PSA level exceeding a threshold of 0.2 ng/ml twice after radical prostatectomy (RP) (4).

Imaging techniques are advised for individuals with biochemical recurrence who have serum prostate-specific antigen levels greater than 10 ng/mL or PSA doubling times shorter than 6 months (5). However, the ability of these traditional imaging techniques to diagnose aggressive lesions, bone involvement, and nodal metastases is restricted. It is essential to discover more sophisticated imaging techniques to detect the metastasis of the early BCR in order to increase diagnostic precision and select an appropriate treatment strategy.

EANM/SNMMI guidelines recently provided updated guidance and standards for the indication, acquisition, and interpretation of PSMA PET/CT for prostate cancer imaging (Fendler et al.). Currently, several guidelines highlight the superior accuracy of PSMA-ligand PET for staging primary disease (EAU, ESMO, NCCN) or consider additional value (ASCO) in this setting. PSMA-ligand PET/CT evaluation of BCR/BCP is recommended in documents produced by the EAU, ASCO, and NCCN (Fendler et al.). Moreover, evidence is growing in terms of PSMA-guided treatments, particularly metastases-directed therapy (Ceci et al., Rovera et al., Fendler et al., Phillips et al.) (6–9).

A type II membrane glycoprotein with 750 amino acids, prostate-specific membrane antigen(PSMA), is highly produced in prostate cancer cells (10). As a result, PSMA is thought to be a good candidate for PCa PET scanning. There are several radiopharmaceuticals that target PSMA, including ^{68}Ga-PSMA-11, 18F-DCFPyL, and 18F-PSMA-1007 (11, 12).

Gallium-68 (^{68}Ga)-labeled prostate-specific membrane antigen (PSMA-11), a new PET radiopharmaceutical, has recently gained attention as a promising imaging tool for the identification of recurrent prostate cancer. In patients with rising PSA levels, ^{68}Ga-PSMA-11 PET has demonstrated great sensitivity and specificity for the detection of recurrent prostate cancer. However, uncertainty persists over the ideal imaging mode for ^{68}Ga-PSMA-11 PET.

Despite systematic reviews or meta-analyses have evaluated the diagnostic efficacy of ^{68}Ga-PSMA-11PET/CT and PET/MRI in earlier study, the amount of included article is insufficient (10, 13). This meta-analysis will enable more detailed and objective comparison of the diagnostic performance of ^{68}Ga-PSMA-11 PET/CT and ^{68}Ga-PSMA-11PET/MRI in detecting biochemical recurrent prostate. Our aim was to conduct a meta-analysis and systematic review in order to compare the diagnostic efficacy of ^{68}Ga-PSMA-11 PET/CT and ^{68}Ga-PSMA-11 PET/MRI in patients with biochemically recurrent prostate cancer in patient-based analysis.

2 Manuscript formatting

2.1 Material and methods

This article was written according to Preferred Reporting Items for a Systematic Review and Meta-analysis of Diagnostic Test Accuracy (PRISMA-DTA) guidelines. Moreover, our registration number is CRD42023410039.

2.1.1 Search strategy

The search strategy described below was used to perform a thorough search of the PubMed, Embase, and Web of Science databases until February 2023. (1) PET MRI OR PET MR OR positron emission tomography/magnetic resonance imaging OR PET CT OR positron emission tomography OR positron emission tomography/computed tomography; (2) regeneration OR recurrent OR relapse OR recrudescence; (3) prostate cancers OR prostate neoplasm OR prostate tumor OR prostatic tumor. For the reference list, we also go through the search and consider articles that may meet the inclusion criteria.

2.1.2 Inclusion and exclusion criteria

Only study that fulfilled all of the following requirements were included: (1) articles evaluating the diagnostic performance of ^{68}Ga-PSMA-11 PET/CT or ^{68}Ga-PSMA-11 PET/MRI for biochemically recurrent prostate cancer in patient-based analysis; (2) number of patients ≥ 10; (3) retrospective or prospective studies; (4) English articles. The exclusion criteria were: (1) Irrelevant topic; (2) duplicated articles; (3) case reports, abstract, letters, review, or meta-analysis; (4) The full-text versions of the selected articles were screen to see if they fulfilled the inclusion criteria after the titles and abstracts of the articles were assessed in accordance with the inclusion and exclusion criteria. Disagreements among the researchers were resolved by consensus.

2.2 Quality assessment and data extraction

Two researchers separately evaluated the included studies' quality using the Quality Assessment of Diagnostic Performance Studies (QUADAS-2) method. The applicability and bias risk of each study was assessed. Regarding bias risk and applicability, each study was given a rating of high, low, or unclear. A third reviewer was involved to resolve any possible conflicts. For the study, RevMan (version 5.4) was employed.

Two researchers independently extracted data for each of the included articles. The information that was extracted included the following: (1) the author, year of publication; (2) study characteristics, such as country, study design, analysis, and reference standard; (3) patient characteristics, such as number of patients, clinical indication, mean/median age, chemotherapy

before PET; (4) technical characteristics, such as imaging test types, scanner modality, ligand dose, and time from injection to acquisition. When not explicitly mentioned, data were manually extracted from the literature, tables, and figures. We emailed the respective authors for more information when the paper lacked the information. Two researchers reached an accord to resolve their disagreements.

2.2.1 Data synthesis and statistical analysis

Heterogeneity was assessed using the I^2 statistic. A forest plot was constructed in the random-effect model if the significant heterogeneity was observed (I^2 > 50%), otherwise, the fixed model would be applied. All of them used DerSimonian and Laird method. Proportions were transformed with the Freeman-Tukey double inverse sine transformation, and confidence intervals were calculated using the Jackson method. For the presence of heterogeneity (I^2>50%), we used meta-regression and sensitivity analysis to find out the source of heterogeneity.

Publication bias was evaluated using Egger's test. A statistically significant P value was two-tailed and with the threshold of 0.05. Statistical analyses were performed in R software environment for statistical computing and graphics version 4.2.2

2.3 Results

2.3.1 Literature search and study selection

After removing 2757 duplicate studies from the primary search, 3016 studies were identified out of the 5773 articles that were initially found. Based on the study's title or abstract, 1465 papers were disqualified. A total of 1496 investigations were collectively omitted from case reports, abstracts, letters, reviews, or meta-analyses. There were still 55 studies for full-text screening, and another 18 were disqualified due to the following reasons: non-English studies (n = 3); cannot extract positivity rate data (n = 7); and different radiotracers (n = 8). 37 studies that satisfied the criteria for the meta-analysis were finally included, including 25 articles for ^{68}Ga-PSMA-11 PET/CT (14–38) and 13 articles for ^{68}Ga-PSMA-11 PET/MRI (4, 26, 39–49). One of the studies included not only ^{68}Ga-PSMA-11 PET/CT but also ^{68}Ga-PSMA-11 PET/MRI. Figure 1 illustrates the PRISMA flow chart of the study selection procedure.

2.3.2 Study description and quality assessment study description and quality assessment

The study and patient characteristics from the 37 studies covering 8409 patients were listed in Table 1. Tables 2, 3 showed the technical the parts. Additionally, using the Quality Assessment of Diagnostic Accuracy Studies (QUADAS-2) tool, a quality assessment of the relevant studies was conducted. The quality evaluation chart reveals that flow and timing are the key areas where there is a high risk of bias (Figure 2). This is due to the fact that most studies did not analyze all of the enrolled patients, which caused this issue. Overall, the risk of bias of the included articles was satisfactory.

2.3.3 Diagnostic performance of ^{68}Ga-PSMA-11 PET/CT and PET/MRI for biochemically recurrent prostate cancer

In comparison to ^{68}Ga-PSMA-11 PET/CT, which had a positivity rate of 0.70 (95% CI: 0.65-0.75), ^{68}Ga-PSMA-11 PET/MRI had a positivity rate of 0.71 (95% CI: 0.67-0.75). The analysis included 8409 patients from 37 studies. There was no statistically significant difference in the overall detection rate between ^{68}Ga-PSMA-11 PET/CT and ^{68}Ga-PSMA-11 PET/MRI (*P=0.58)* (Figure 3).

Regarding the pooled overall detection rate of ^{68}Ga-PSMA-11 PET/CT and ^{68}Ga-PSMA-11 PET/MRI for BCR, the I^2 was 93% and 81%, respectively. For ^{68}Ga-PSMA-11 PET/CT, the subgroup analysis and meta-regression analysis showed that the data analysis (qualitative vs. quantitative) was the possible cause of heterogeneity, while the study design (The number of patients: Greater than 56 vs. less than or equal to 56) was identified as the potential cause of heterogeneity for the ^{68}Ga-PSMA-11 PET/MRI studies Tables 4, 5. There were no potential sources of heterogeneity found by the sensitivity analysis. The result revealed only slight variations in the data, with values ranging from 0.70 to 0.74 for the ^{68}Ga-PSMA-11 PET/MRI and from 0.69 to 0.71 for the ^{68}Ga-PSMA-11 PET/CT. Overall, the detection rates remained consistent and stable after sensitivity analysis. (Supplementary Tables 1, 2).

According to the funnel plot and Egger's test, both the ^{68}Ga-PSMA-11 PET/CT *(P = 0.39)* and the ^{68}Ga-PSMA-11 PET/MRI *(P = 0.28)* showed no sign of publication bias (Supplementary Tables 1 and 2).

2.3.4 BCR positivity rate for ^{68}Ga-PSMA-11 PET/CT and ^{68}Ga-PSMA-11 PET/MRI according to the different PSA subgroups

For ^{68}Ga-PSMA-11 PET/CT and ^{68}Ga-PSMA-11 PET/MRI, the detection rates were 0.47 (95% CI: 0.42-0.51) and 0.45 (95% CI: 0.24-0.67) for PSA levels <0.5 ng/ml, and when PSA levels were > 0.5 ng/ml, the detection rates were 0.77 (95% CI: 0.72-0.82) and 0.90 (95% CI: 0.79-0.98); Detection rates at PSA levels <0.2 ng/ml were 0.42 (95% CI: 0.36-0.47) and 0.13 (95% CI: 0.00-0.51); For PSA levels 0.2-0.5 ng/ml, the detection rates were 0.51 (95% CI: 0.41-0.62) and 0.46 (95% CI: 0.23-0.69); For PSA levels 0.5-1.0 ng/mL, detection rates were 0.63 (95% CI: 0.55-0.71) and 0.73 (95% CI: 0.45-0.95); For PSA values 1.0-2.0 ng/mL, the detection rates were 0.76 (95% CI: 0.69-0.82) and 0.63 (95% CI: 0.30-0.92); the detection rates for PSA levels > 2.0 ng/ml were 0.90 (95% CI: 0.85-0.93) and 0.89 (95% CI: 0.77-0.98). The only significant difference ^{68}Ga-PSMA-11 PET/CT and ^{68}Ga-PSMA-11 PET/MRI was at PSA levels > 0.5 ng/ml *(P=0.04)* (Figures 4–10).

2.4 Discussion

According to previous studies, PET/MRI with PSMA imaging agent has a slightly higher diagnostic performance than PET/CT for local recurrence and lymph node recurrence (10, 44, 46, 49). However, according to Huo et al. and Glemser et al., there is no

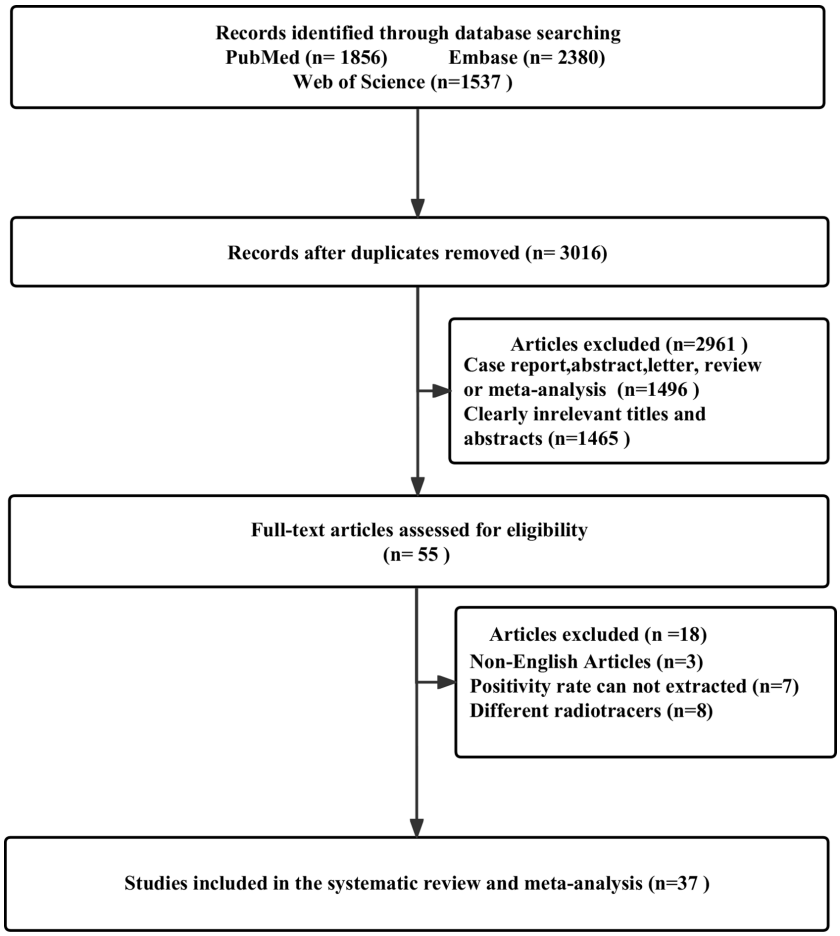

FIGURE 1
The flow chart for the PRISMA study selection procedure.

TABLE 1 Characteristics of the studies and patients.

Author	Year	Types of imaging tests	Study characteristics					Patient characteristics	
			Country	Study design	Analysis	No. of patients	PSA level prior to PET (ng/ml)	Mean/ Median age	Previous treatment
Gühne et al.	2022	PET/CT	Germany	Retro	PB	83	Median = 1.3	Median = 70	Mixed
Duan et al. (15)	2022	PET/CT	USA	Pro	PB	58	NA	NA	Mixed
Uprimny et al. (16)	2021	PET/CT	Austria	Retro	PB	440	NA	NA	Mixed
Lengana et al. (17)	2021	PET/CT	South Africa	Pro	PB	21	Mean = 2.6	Mean = 68.6	Mixed
Plaza López et al. (18)	2021	PET/CT	Spain	Retro	PB	14	Mean = 1.8	Mean = 71.1	Mixed
Yuminaga et al. (19)	2021	PET/CT	Australia	Pro	PB	384	Median = 0.5	Median = 69.5	RP
Tseng et al. (20)	2021	PET/CT	China	Pro	PB	34	Median = 0.5	Median = 67	RP
Strauss et al. (21)	2021	PET/CT	Germany	Retro	PB	142	Median = 2.3	NA	RP

(Continued)

TABLE 1 Continued

Author	Year	Types of imaging tests	Study characteristics					Patient characteristics	
			Country	Study design	Analysis	No. of patients	PSA level prior to PET (ng/ml)	Mean/ Median age	Previous treatment
Ribeiro et al. (22)	2021	PET/CT	Brazil	Retro	PB	57	NA	Median = 69	NA
Morawitz et al. (23)	2021	PET/CT	Germany	Retro	PB	36	Median = 1.5	Median = 71	RP
Lawal et al. (24)	2021	PET/CT	South Africa	Retro	PB	247	Median = 2.7	Mean = 65.7	Mixed
Kroenke et al. (25)	2021	PET/CT	Germany	Retro	PB	127	Median = 0.7	Median = 69.0	RP
Jentjens et al.	2021	PET/CT	Belgium	Pro	PB	34	Median = 0.8	Median = 67.5	Mixed
Fourquet et al. (27)	2021	PET/CT	France	Retro	PB	294	NA	Mean = 68.0	RP
Dadgar et al. (28)	2021	PET/CT	Iran	Retro	PB	19	Median = 1.7	Median = 72.0	Mixed
Cerci et al.	2021	PET/CT	Brazil	Pro	PB	1004	Mean = 1.6	Mean = 67.3	Mixed
Carvalho et al. (30)	2021	PET/CT	Portugal	Pro	PB	70	NA	NA	Mixed
Afshar-Oromieh et al. (31)	2021	PET/CT	Germany	Retro	PB	2533	NA	Median = 68	RP
Abghari-Gerst et al.	2021	PET/CT	USA	Pro	PB	1539	median:7	Mean = 67.3	Mixed
Seniaray et al. (33)	2020	PET/CT	India	Retro	PB	170	NA	NA	Mixed
Regula et al. (34)	2020	PET/CT	Sweden	Pro	PB	30	Median = 5	Median = 70	Mixed
Rauscher et al. (35)	2020	PET/CT	Germany	Retro	PB	102	Median = 0.9	Median = 69	RP
Radzina et al. (36)	2020	PET/CT	Latvia	Pro	PB	32	Median = 1.1	Mean = 63	Mixed
Miksch et al. (37)	2020	PET/CT	Germany	Retro	PB	116	Mean = 0.2	Mean = 67.6	RP
Huits et al. (38)	2020	PET/CT	Netherlands	Retro	PB	100	Median = 0.5	Mean = 65	RP
Glemser et al. (47)	2022	PET/MRI	Germany	Retro	PB	53	median:1.6	mean:67.7	mixed
Afshar et al.	2013	PET/MRI	Germany	Pro	PB	20	median:2.62	mean:69.6	mixed
Grubmüller et al.	2017	PET/MRI	Austria	Retro	PB	71	median:1.04	NA	RP
Guberina et al.	2019	PET/MRI	Germany	Retro	PB	93	median:1.64	NA	RP
Mai et al.	2021	PET/MRI	Belgium	Pro	PB	20	median:0.79	mean:67.5	mixed
Joshi et al. (43)	2020	PET/MRI	Australia	Pro	PB	21	median:0.69	median:68	mixed
T. Lake et al. (41)	2017	PET/MRI	USA	Pro	PB	55	mean:7.9	mean:68.3	mixed
Kranzbühler et al.	2019	PET/MRI	Switzerland	Retro	PB	66	median:0.23	NA	mixed
Lütje et al. (40)	2017	PET/MRI	Germany	Retro	PB	25	mean3.9	mean:70.5	RP

(Continued)

TABLE 1 Continued

Author	Year	Types of imaging tests	Study characteristics					Patient characteristics	
			Country	Study design	Analysis	No. of patients	PSA level prior to PET (ng/ml)	Mean/ Median age	Previous treatment
Mapelli et al. (39)	2022	PET/MRI	Italy	Pro	PB	35	mean:1.88	mean:70	mixed
Martinez et al. (4)	2022	PET/MRI	USA	Pro	PB	109	mean:5.56	mean:69	mixed
Alonso et al. (48)	2018	PET/MRI	India	Pro	PB	36	median:3.3	mean:64.7	mixed
Freitag et al. (49)	2017	PET/MRI	Germany	Retro	PB	119	median:1.70	NA	RP

PB, patient-based; Pro, prospective; Retro, retrospective; NA, not available.

significant difference between the overall detection rates of the two imaging modalities (13, 47). Thus controversy remains regarding the diagnostic performance of both imaging modalities for biochemical recurrent prostate cancer. The aim of this study was to quantitatively compare the diagnostic performance of the two diagnostic modalities for biochemical recurrent prostate cancer.

In the present study, the capability of two imaging modalities to identify BCR was comprehensively reviewed and assessed. The detection rates in patient-based analysis for ^{68}Ga-PSMA-11 PET/CT and ^{68}Ga-PSMA-11 PET/MRI were 0.70 (95% Cl: 0.65; 0.75) and 0.73 (95% Cl: 0.64; 0.81) accordingly. Between these two imaging modalities, there was no significant difference *(P=0.58)*. A significant difference between these two imaging modalities for PSA levels aspect only existed when PSA was higher than 0.5, according to the study *(P=0.04)* (Figure 7).

PET/MRI provides metabolic, anatomical, and functional information in a single modality by combining the strengths of PET and MRI. While MRI offers precise anatomical and functional information through techniques like perfusion and diffusion-weighted imaging, PSMA-11 PET provides metabolic information by detecting PSMA expression in prostate cancer cells. With the use of this extensive information, clinicians can make a more thorough evaluation of the kind and severity of prostate cancer. PET/MRI detection rates may be superior to PET/CT for PSA levels higher than 0.5 due to the fact that PET/MRI provides more precise and detailed anatomical data, particularly in terms of soft tissue contrast (48). In order to more precisely localize probable tumor lesions, PSMA-11 PET/MRI can provide detailed anatomical information on the prostate region, including its shape, location, and size (36).

TABLE 2 Technical aspects of included ^{68}Ga-PSMA-11 PET/MRI studies.

Author	Year	Scanner Modality(PET/MRI)	Ligand dose	Time from injection to acquisition	Image analysis
Glemser et al. (47)	2022	NA	71-287MBq	170min for PET/MRI	quantitative
Afshar et al.	2013	Siemens Biograph	76-259 MBq	90min for PET/MRI	quantitative
Grubmüller et al.	2017	Siemens Biograph Mmr	NA	NA	qualitative
Guberina et al.	2019	Siemens Biograph Mmr	66–167 MBq	167min for PET/MRI	quantitative
Mai et al.	2021	GE Healthcare	NA	NA	quantitative
Joshi et al. (43)	2020	NA	150MBq	45-60min for PET/MRI	quantitative
T. Lake et al. (41)	2017	GE SIGNA PET/MR	201.5 ± 52.9 MBq	65min for PET/MRI	qualitative
Kranzbühler et al.	2019	GE SIGNA PET/MR	130 ± 16 MBq	NA	quantitative
Lütje et al. (40)	2017	Siemens Healthcare	118 ± 23 MBq	175 ± 45 min for PET/MRI	quantitative
Mapelli et al. (39)	2022	SIGNA PET/MRI	129-288MBq	60min for PET/MRI	quantitative
Martinez et al. (4)	2022	Siemens Biograph mMR	148MBq	90min for PET/MRI	quantitative
Alonso et al. (48)	2018	GE Discovery	2.0 MBq/kg	NA	quantitative
Freitag et al. (49)	2017	Siemens Biograph mMR	202 ± 69 MBq	70min for PET/MRI	quantitative

TABLE 3 Technical aspects of included ^{68}Ga-PSMA-11 PET/CT studies.

Author	Year	Scanner Modality(PET/CT)	Ligand dose	Time from injection to acquisition	Image analysis
Gühne et al.	2022	Siemens Healthineers	243.2 ± 35.8MBq	71min for PET/CT	quantitative
Duan et al. (15)	2022	GE Healthcare	146.5 ± 16.7MBq	86.8 ± 11.5min for PET/CT	quantitative
Uprimny et al. (16)	2021	GE Healthcare	95.0–216.0 MBq	67min for PET/CT	quantitative
Lengana et al. (17)	2021	Siemens Biograph 40	NA	60min for PET/CT	qualitative
Plaza López et al. (18)	2021	GE HealthCare	2.2 MBq/kg	60min for PET/CT	qualitative
Yuminaga et al. (19)	2021	Philips GEMINI TOF	150-300 MBq	50-70min for PET/CT	qualitative
Tseng et al. (20)	2021	Siemens Healthineers	88.4-182.8 MBq	60min for PET/CT	qualitative
Strauss et al. (21)	2021	Siemens Biograph	193.6 ± 62.87MBq	80-90min for PET/CT	quantitative
Ribeiro et al. (22)	2021	Philips Health	NA	60min for PET/CT	qualitative
Morawitz et al. (23)	2021	Siemens Healthineers	182 ± 45 MBq	NA	quantitative
Lawal et al. (24)	2021	Siemens Medical Solution	2MBq/kg	60min for PET/CT	qualitative
Kroenke et al. (25)	2021	Siemens Medical Solutions	51-248 MBq	42-116min for PET/CT	quantitative
Jentjens et al.	2021	Siemens Healthineers	1.8MBq/kg	60min for PET/CT	quantitative
Fourquet et al. (27)	2021	Philips Medical Systems	1.2MBq/kg	60-90min for PET/CT	quantitative
Dadgar et al. (28)	2021	Siemens	126-187 MBq	60min for PET/CT	quantitative
Cerci et al.	2021	NA	2MBq/kg	60-90min for PET/CT	qualitative
Carvalho et al. (30)	2021	Siemens Biography	2MBq/kg	60min for PET/CT	quantitative
Afshar-Oromieh et al. (31)	2021	NA	52–480 MBq	NA	quantitative
Seniaray et al. (33)	2020	NA	132–222 MBq	45 ± 15min for PET/CT	qualitative
Regula et al. (34)	2020	GE Healthcare	1.3–2.9 MBq/kg	60-78min for PET/CT	quantitative
Rauscher et al. (35)	2020	Biograph-Mct	94–232 MBq	41-85min for PET/CT	quantitative
Radzina et al. (36)	2020	Gemini TF64	1.8-2.2 MBq/kg	51-81min for PET/CT	quantitative
Miksch et al. (37)	2020	Siemens Biograph-Mct	162.7 ± 22.3 MBq	64.4 ± 12.2min for PET/CT	qualitative
Huits et al. (38)	2020	Philips Ingenuity	2.0 MBq/kg	60min for PET/CT	qualitative
Abghari-Gerst et al.	2021	GE Discovery	NA	61min for PET/CT	quantitative

In addition, compared to PET/CT, PET/MRI often has lower radiation doses, which may be advantageous for younger patients or those who need numerous follow-up exams, lowering the risk of radiation exposure. It's important to remember that clinical practices may vary between different medical facilities, even though PSMA-11 PET/MRI may be advantageous when PSA is greater than 0.5. It is important to stress that this is only an observation or trend and does not always mean that PSMA-11 PET/MRI is always preferable than PSMA-11 PET/CT.

Compared to previous meta-analyses (13), the current meta-study found that ^{68}Ga-PSMA-11 PET CT and ^{68}Ga-PSM A-11 PET-MRI had similar results in terms of diagnostic performance and detection rates for the detection of biochemically recurrent prostate cancer. This shows that for the same detection performance, PET/CT is more cost-effective. These findings are consistent with previous meta-analyses. The main disadvantage of the previous meta-analysis is the small sample size, while the main advantage of the meta-analysis in this article is the large sample size(including 37 studies). However, due to the recent development of ^{68}Ga-PSMA-11 PET/MRI, there is limited study in this field and a scarcity of comparable evidence available. Future head-to-head studies that systematically assesses both modalities might produce novel findings.

The findings of the meta-analysis contrasting ^{68}Ga-PSMA-11 PET/CT and ^{68}Ga-PSMA-11 PET/MRI for the identification of biochemically recurring prostate cancer can have significant repercussions for future study in the field as well as for policy and practice. To make the best use of various imaging modalities in clinical practice, these findings can inspire future study paths, help decision-making, and enhance patient management. The diagnosis of PSMA-PET has a significant impact on the management of recurrent patients, allowing clinicians to select better treatment options to treat them, such as the treatment of recurrent M1a

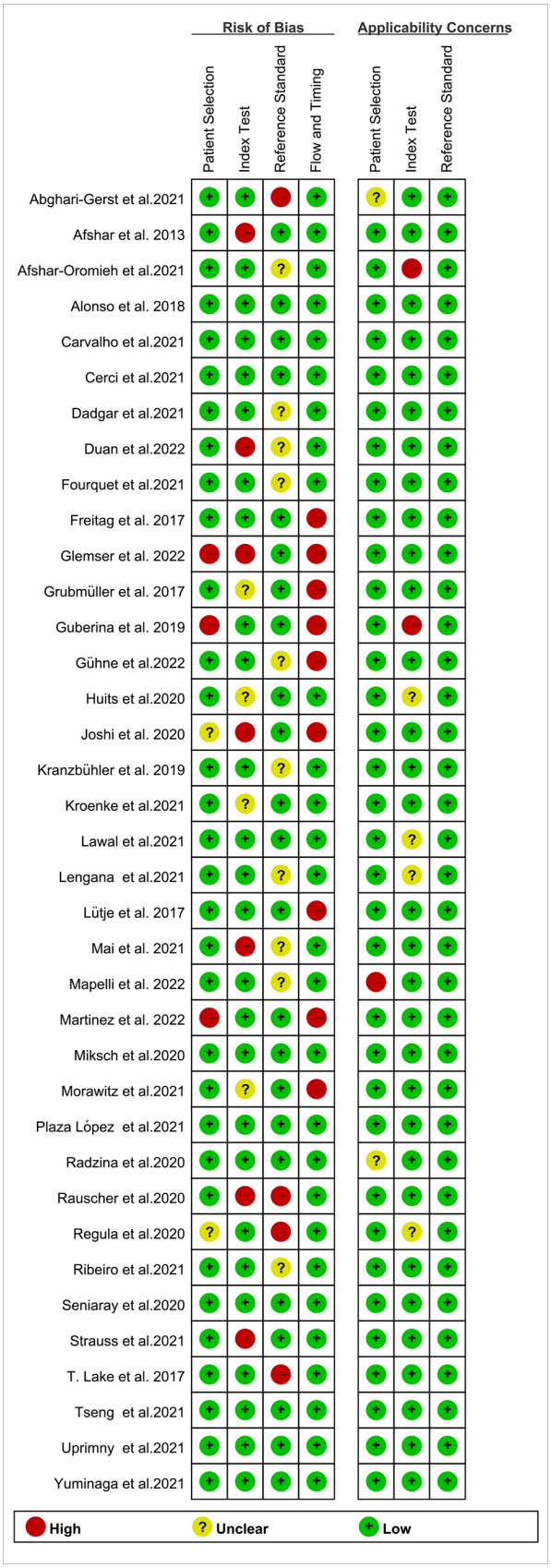

FIGURE 2
Graph of risk of bias and applicability of all eligible studies based on QUADAS-2 tool.

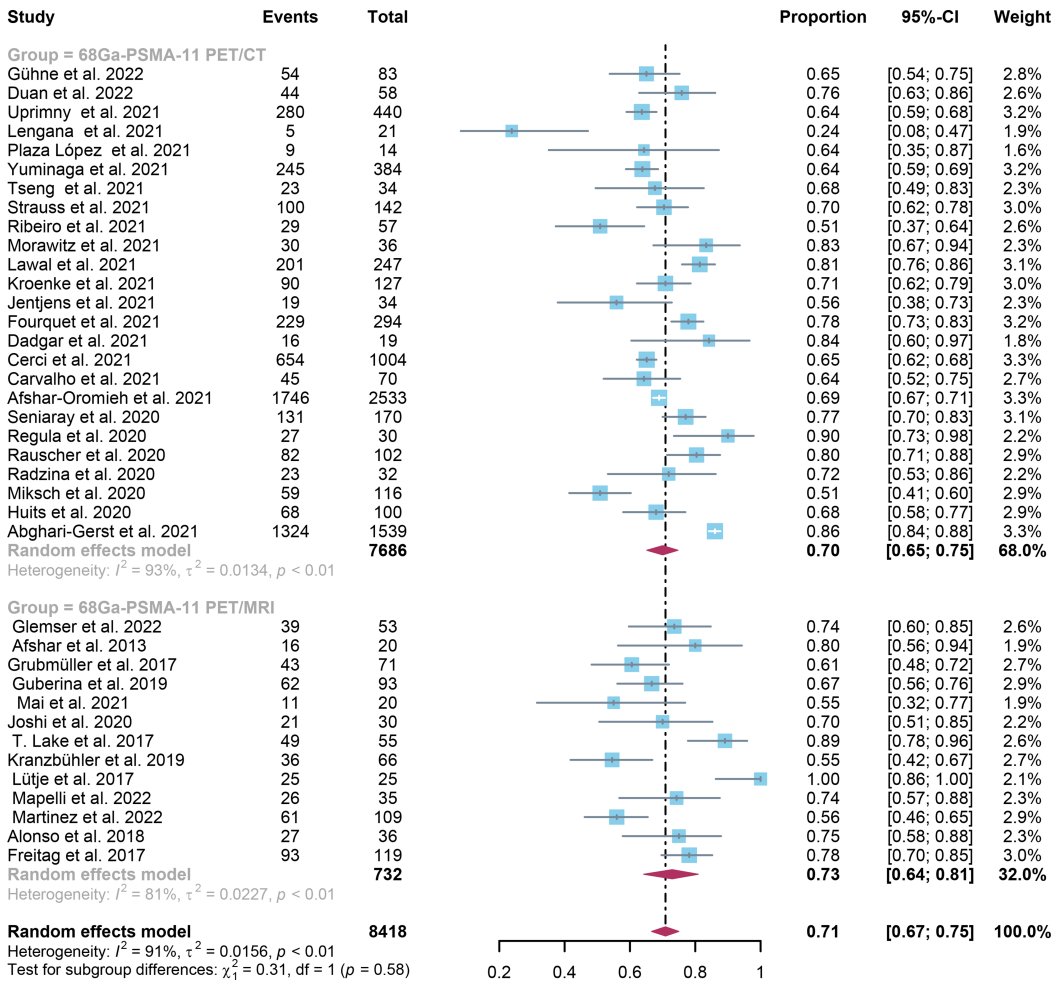

FIGURE 3
^{68}Ga-PSMA-11 PET/CT and ^{68}Ga-PSMA-11 PET/MRI forest plots for biochemically recurrent prostate cancer. In each study, positive results were represented by squares, and the 95% confidence interval was shown by horizontal bars.

TABLE 4 Subgroup analysis and meta-regression analysis of diagnostic performance of ^{68}Ga-PSMA-11 PET/MRI.

Covariate/Subgroup	Studies, n	Positivity rate (95%CI)	P-value
Study design			0.82
Prospective	7	0.74(0.58-0.88)	
Retrospective	6	0.72(0.61-0.82)	
Treatment			0.35
RP	4	0.73(0.64-0.81)	
Mixed	9	0.70(0.61-0.78)	
The number of patients			0.03
>56	5	0.64(0.55-0.73)	
≤56	8	0.79(0.68-0.89)	
Image analysis			0.72
Qualitative	2	0.73(0.64-0.81)	
Quantitative	11	0.72(0.63-0.81)	

TABLE 5 Subgroup analysis and meta-regression analysis of diagnostic performance of ^{68}Ga-PSMA-11 PET/CT.

Covariate/Subgroup	Studies, n	Positivity rate (95%CI)	P-value
Study design			0.66
Prospective	10	0.70(0.65-0.75)	
Retrospective	15	0.71(0.66-0.76)	
Treatment			0.90
RP	10	0.71(0.66-0.75)	
Mixed	14	0.71(0.63-0.78)	
The number of patients			0.93
>307	20	0.70(0.64-0.76)	
≤307	5	0.70(0.61-0.79)	
Image analysis			0.03
Qualitative	10	0.70(0.65-0.75)	
Quantitative	15	0.74(0.69-0.79)	

8.7 Positivity analysis of overall detection rate for ^{68}Ga-PSMA-11 PET/MRI		
8.8	8.9 ^{68}Ga-PSMA-11 PET/MRI	
	8.10 Positivity rate (95% CI)	8.11 I^2
8.12 Omitting Glemser et al.	8.13 0.73 [0.63,0.82]	8.14 82.40%
8.15 Omitting Afshar et al.	8.16 0.72 [0.63,0.81]	8.17 82.30%
8.18 Omitting Grubmüller et al.	8.19 0.74 [0.65, 0.82]	8.20 81.50%
8.21 Omitting Guberina et al.	8.22 0.74 [0.64, 0.82]	8.23 82.30%
8.24 Omitting Mai et al.	8.25 0.74 [0.65,0.82]	8.26 81.90%
8.27 Omitting Joshi et al.	8.28 0.73 [0.64,0.82]	8.29 82.50%
8.30 Omitting T. Lake et al.	8.31 0.71 [0.62, 0.79]	8.32 78.10%
8.33 Omitting Kranzbühler et al.	8.34 0.74 [0.66,0.82]	8.35 80.00%
8.36 Omitting Lütje et al.	8.37 0.70 [0.63, 0.76]	8.38 71.60%
8.39 Omitting Mapelli et al.	8.40 0.73 [0.63, 0.82]	8.41 82.40%
8.42 Omitting Martinez et al.	8.43 0.74 [0.66, 0.83]	8.44 78.60%
8.45 Omitting Alonso et al.	8.46 0.73 [0.63, 0.81]	8.47 82.40%
8.48 Omitting Freitag et al.	8.49 0.72 [0.63, 0.81]	8.50 81.20%

prostate cancer, the MDT approach of targeting PSMA-positive lesions according to the pattern of recurrence (sLND, SBRT, combination of sLND and SBRT). Based on the PSMA-PET method, these treatments were chosen (50–53).

Both ^{68}Ga-PSMA-11 PET/CT and ^{68}Ga-PSMA-11 PET/MRI demonstrated high heterogeneity in terms of overall detection rates. In an attempt to find out the source of this heterogeneity, we conducted sensitivity analysis and meta-regression. Our findings showed that for PET/CT, the primary cause of heterogeneity was image analysis *(P=0.03)*. On the other hand, for PET/MRI, the primary cause of heterogeneity appeared to be the number of patients involved in the studies *(P=0.03)*. The sensitivity analysis did not identify any potential sources of heterogeneity.

It is also important to note the limitations of our meta-analysis. First of all, the gold standard for pathology was not available for all of the patients. Secondly, many of the included studies were retrospective studies, further lager prospective studies are needed. Finally, the included study used various protocols, such as different methods for administering contrast agents, different contrast procedures, and varied standards for interpretation, which may cause heterogeneity.

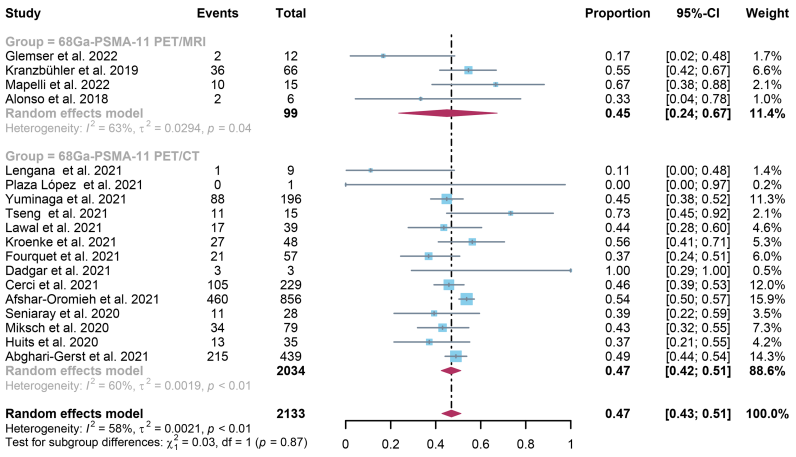

FIGURE 4
Forest plot of ^{68}Ga-PSMA-11 PET/CT and ^{68}Ga-PSMA-11 PET/MRI detection rates in patients with PSA<0.5.

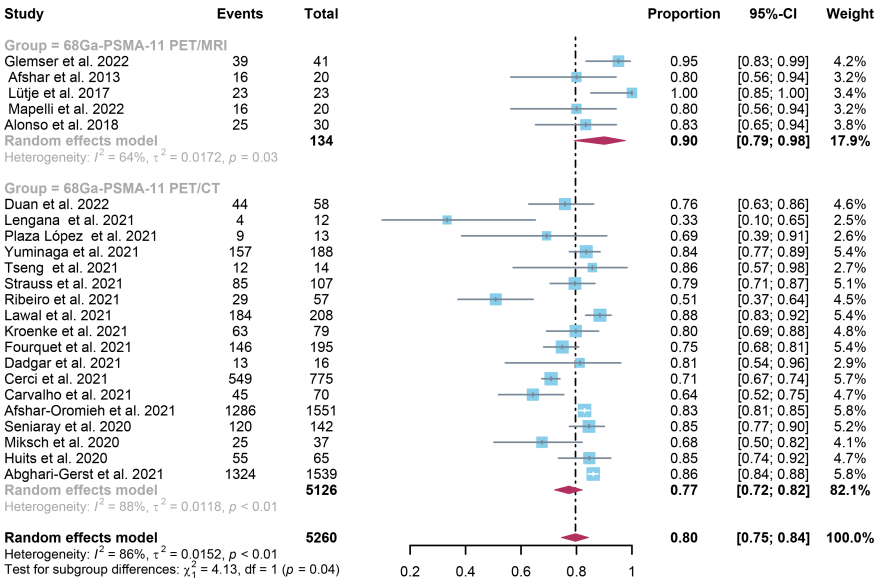

FIGURE 5
Forest plot of ^{68}Ga-PSMA-11 PET/CT and ^{68}Ga-PSMA-11 PET/MRI detection rates in patients with PSA>0.5.

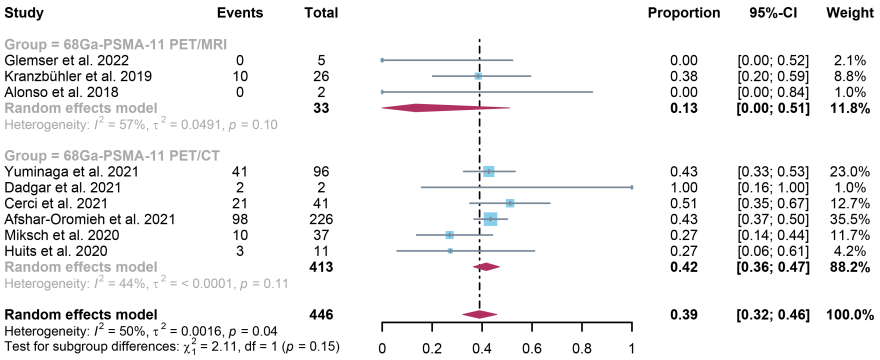

FIGURE 6
Forest plot of ^{68}Ga-PSMA-11 PET/CT and ^{68}Ga-PSMA-11 PET/MRI detection rates in patients with PSA≤ 0.2.

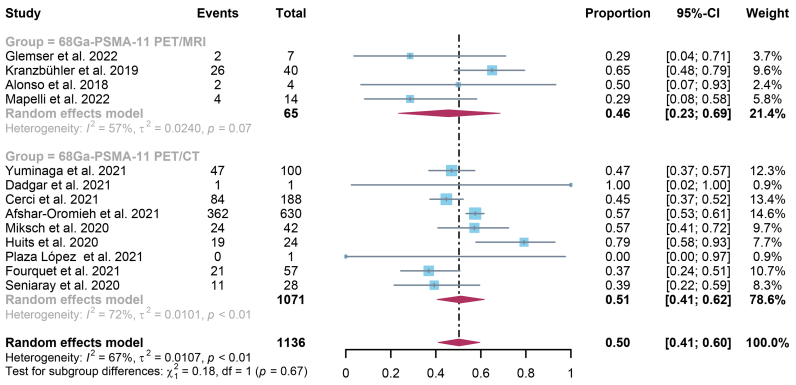

FIGURE 7
Forest plot of ^{68}Ga-PSMA-11 PET/CT and ^{68}Ga-PSMA-11 PET/MRI detection rates in patients with 0.2<PSA<0.5.

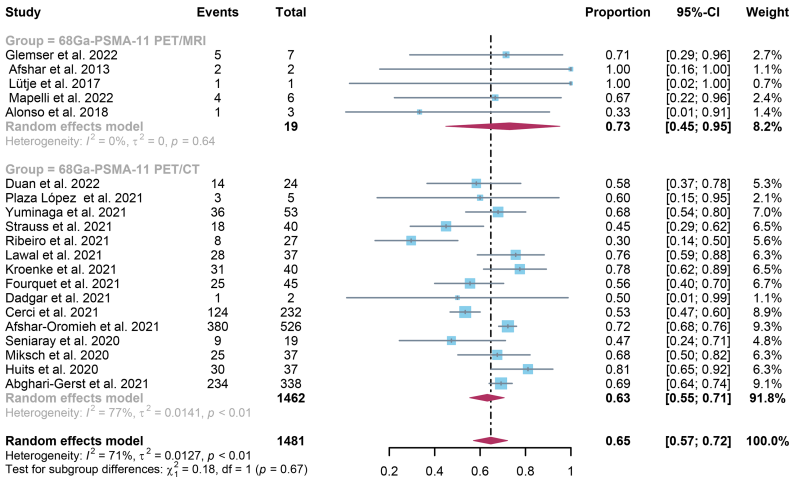

FIGURE 8
Forest plot of ^{68}Ga-PSMA-11 PET/CT and ^{68}Ga-PSMA-11 PET/MRI detection rates in patients with 0.5≤PSA<1.0.

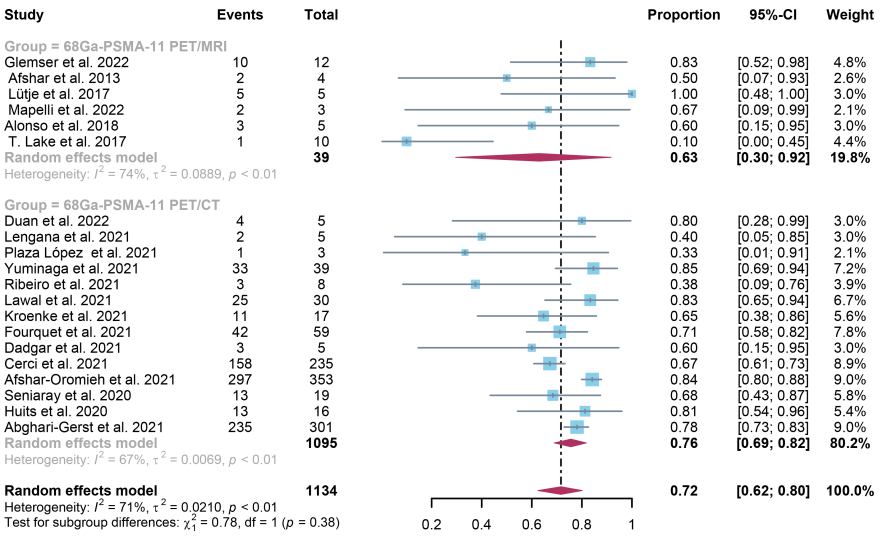

FIGURE 9
Forest plot of ^{68}Ga-PSMA-11 PET/CT and ^{68}Ga-PSMA-11 PET/MRI detection rates in patients with 1.0≤PSA<2.0.

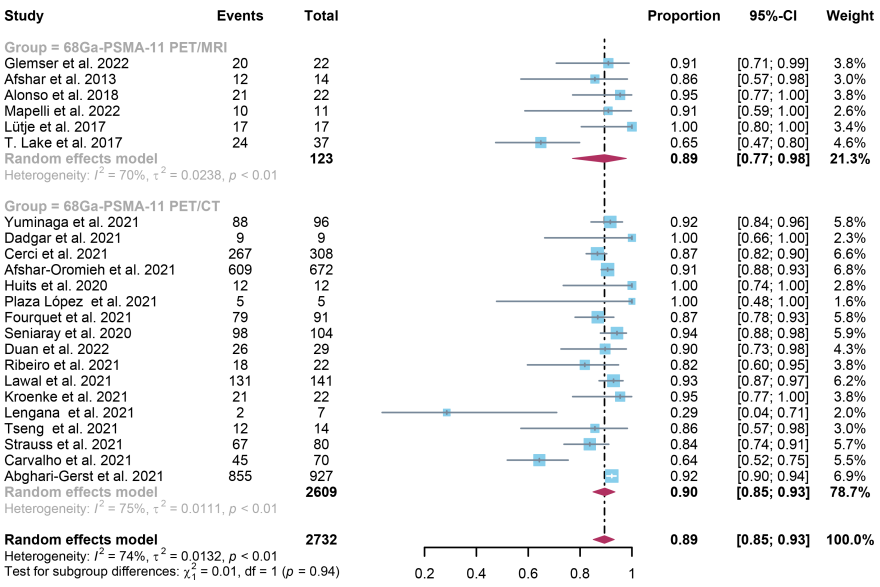

FIGURE 10
Forest plot of ^{68}Ga-PSMA-11 PET/CT and ^{68}Ga-PSMA-11 PET/MRI detection rates in patients with PSA≥2.0.

2.5 Conclusion

The diagnostic efficacy of ^{68}Ga-PSMA-11 PET/CT appears to be equivalent to that of ^{68}Ga-PSMA-11 PET/MRI in detecting biochemically recurrent prostate cancer. Nonetheless, it should be noted that not all studies have used pathological biopsies as the gold standard. Therefore, additional larger head-to-head prospective studies are needed to address this issue.

Data availability statement

The original contributions presented in the study are included in the article/Supplementary Material. Further inquiries can be directed to the corresponding author.

Author contributions

The study was conceptualized and designed by RH and ZZ, and it was verified using information gathered and examined by YL, HW, BL, and XZ. The manuscript was written by RH. The article's submission was reviewed and approved by all of the writers.

Conflict of interest

The authors declare that the research was conducted in the absence of any commercial or financial relationships that could be construed as a potential conflict of interest.

Publisher's note

All claims expressed in this article are solely those of the authors and do not necessarily represent those of their affiliated organizations, or those of the publisher, the editors and the reviewers. Any product that may be evaluated in this article, or claim that may be made by its manufacturer, is not guaranteed or endorsed by the publisher.

Supplementary material

The Supplementary Material for this article can be found online at: https://www.frontiersin.org/articles/10.3389/fonc.2023.1216894/full#supplementary-material

References

1. Siegel RL, Miller KD, Wagle NS, Jemal A. Cancer statistics, 2023. *CA Cancer J Clin* (2023) 73(1):17–48. doi: 10.3322/caac.21763

2. Cary KC, Punnen S, Odisho AY, Litwin MS, Saigal CS, Cooperberg MR. Nationally representative trends and geographic variation in treatment of localized prostate cancer: the urologic diseases in America project. *Prostate Cancer Prostatic Dis* (2015) 18(2):149–54. doi: 10.1038/pcan.2015.3

3. Han M, Partin AW, Pound CR, Epstein JI, Walsh PC. Long-term biochemical disease-free and cancer-specific survival following anatomic radical retropubic prostatectomy. The 15-year Johns Hopkins experience. *Urol Clin North Am* (2001) 28(3):555–65. doi: 10.1016/s0094-0143(05)70163-4

4. Martinez J, Subramanian K, Margolis D, O'Dwyer E, Osborne J, Jhanwar Y, et al. 68ga-Psma-Hbed-Cc Pet/Mri is superior to multiparametric magnetic resonance

imaging in men with biochemical recurrent prostate cancer: a prospective single-institutional study. *Transl Oncol* (2022) 15(1):101242. doi: 10.1016/j.tranon.2021.101242

5. Cornford P, Bellmunt J, Bolla M, Briers E, De Santis M, Gross T, et al. Eau-Estro-Siog guidelines on prostate cancer. Part II: treatment of relapsing, metastatic, and castration-resistant prostate cancer. *Eur Urol* (2017) 71(4):630–42. doi: 10.1016/j.eururo.2016.08.002

6. Phillips R, Shi WY, Deek M, Radwan N, Lim SJ, Antonarakis ES, et al. Outcomes of observation vs stereotactic ablative radiation for oligometastatic prostate cancer: the Oriole phase 2 randomized clinical trial. *JAMA Oncol* (2020) 6(5):650–9. doi: 10.1001/jamaoncol.2020.0147

7. Ceci F, Rovera G, Iorio GC, Guarneri A, Chiofalo V, Passera R, et al. Event-Free Survival after (68) ga-Psma-11 Pet/Ct in Recurrent Hormone-Sensitive Prostate Cancer (Hspc) Patients Eligible for Salvage Therapy. *Eur J Nucl Med Mol Imaging* (2022) 49(9):3257–68. doi: 10.1007/s00259-022-05741-9

8. Fendler WP, Eiber M, Beheshti M, BOmanji J, Calais J, Ceci F, et al. Psma Pet/Ct: joint Eanm procedure guideline/Snmmi procedure standard for prostate cancer imaging 2.0. *Eur J Nucl Med Mol Imaging* (2023) 50(5):1466–86. doi: 10.1007/s00259-022-06089-w

9. Rovera G, Grimaldi S, Dall'Armellina S, Passera R, Oderda M, Iorio GC, et al. Predictors of bone metastases at (68)Ga-Psma-11 Pet/Ct in hormone-sensitive prostate cancer (Hspc) patients with early biochemical recurrence or persistence. *Diagnostics (Basel)* (2022) 12(6):1309. doi: 10.3390/diagnostics12061309

10. Liu FY, Sheng TW, Tseng JR, Yu KJ, Tsui KH, Pang ST, et al. Prostate-specific membrane antigen (Psma) fusion imaging in prostate cancer: Pet-Ct vs Pet-Mri. *Br J Radiol* (2022) 95(1131):20210728. doi: 10.1259/bjr.20210728

11. Sun J, Lin Y, Wei X, Ouyang J, Huang Y, Ling Z. Performance of 18f-Dcfpyl Pet/Ct imaging in early detection of biochemically recurrent prostate cancer: a systematic review and meta-analysis. *Front Oncol* (2021) 11:649171. doi: 10.3389/fonc.2021.649171

12. Kesch C, Vinsensia M, Radtke JP, Schlemmer HP, Heller M, Ellert E, et al. Intraindividual comparison of (18)F-Psma-1007 Pet/Ct, multiparametric Mri, and radical prostatectomy specimens in patients with primary prostate cancer: a retrospective, proof-of-concept study. *J Nucl Med* (2017) 58(11):1805–10. doi: 10.2967/jnumed.116.189233

13. Huo H, Shen S, He D, Liu B, Yang F. Head-to-head comparison of (68)Ga-Psma-11 Pet/Ct and (68)Ga-Psma-11 Pet/Mri in the detection of biochemical recurrence of prostate cancer: summary of head-to-head comparison studies. *Prostate Cancer Prostatic Dis* (2023) 26(1):16–24. doi: 10.1038/s41391-022-00581-y

14. Gühne F, Radke S, Winkens T, Kühnel C, Greiser J, Seifert P, et al. Differences in distribution and detection rate of the [(68)Ga]Ga-Psma ligands Psma-617, -I&T and -11-Inter-Individual comparison in patients with biochemical relapse of prostate cancer. *Pharm (Basel)* (2021) 15(1):9. doi: 10.3390/ph15010009

15. Duan H, Baratto L, Hatami N, Liang T, Mari Aparici C, Davidzon GA, et al. (68)Ga-Psma11 Pet/Ct for biochemically recurrent prostate cancer: influence of dual-time and Pmt- vs Sipm-based detectors. *Transl Oncol* (2022) 15(1):101293. doi: 10.1016/j.tranon.2021.101293

16. Uprimny C, Bayerschmidt S, Kroiss AS, Fritz J, Nilica B, Svirydenka H, et al. Early injection of furosemide increases detection rate of local recurrence in prostate cancer patients with biochemical recurrence referred for (68)Ga-Psma-11 Pet/Ct. *J Nucl Med* (2021) 62(11):1550–7. doi: 10.2967/jnumed.120.261866

17. Lengana T, Lawal IO, Rensburg CV, Mokoala KMG, Moshokoa E, Ridgard T, et al. A comparison of the diagnostic performance of (18)F-Psma-1007 and (68)Ga-Psma-11 in the same patients presenting with early biochemical recurrence. *Hell J Nucl Med* (2021) 24(3):178–185. doi: 10.1967/s002449912401

18. Plaza López PJ, Puertas E, Aguiló JJ, Suarez-Piñera M, Domenech B, Mestre-Fusco A, et al. (68)Ga-Psma-11 Pet/Ct in patients with occult biochemical recurrence of prostate carcinoma and negative (18)F-CholinePet/Ct. *Prelim Assess Its Clin Use Actas Urol Esp (Engl Ed)* (2021) 45(5):353–8. doi: 10.1016/j.acuroe.2021.04.008

19. Yuminaga Y, Rothe C, Kam J, Beattie K, Arianayagam M, Bui C, et al. (68)Ga-Psma Pet/Ct versus Ct and bone scan for investigation of Psa failure post radical prostatectomy. *Asian J Urol* (2021) 8(2):170–5. doi: 10.1016/j.ajur.2020.02.001

20. Tseng JR, Yu KJ, Liu FY, Yang LY, Hong JH, Yen TC, et al. Comparison between (68)Ga-Psma-11 Pet/Ct and multiparametric magnetic resonance imaging in patients with biochemically recurrent prostate cancer following robot-assisted radical prostatectomy. *J Formos Med Assoc* (2021) 120:688–96. doi: 10.1016/j.jfma.2020.07.029

21. Strauss DS, Sachpekidis C, Kopka K, Pan L, Haberkorn U, Dimitrakopoulou-Strauss A. Pharmacokinetic studies of [(68) ga]Ga-Psma-11 in patients with biochemical recurrence of prostate cancer: detection, differences in temporal distribution and kinetic modelling by tissue type. *Eur J Nucl Med Mol Imaging* (2021) 48(13):4472–82. doi: 10.1007/s00259-021-05420-1

22. Ribeiro AMB, Lima ENP, de Cássio Zequi S. Evaluation of the clinical use of Pet/Ct with 68ga-Psma for the assessment of biochemical recurrence of low or intermediate-risk prostate cancer. *Urol Oncol: Semin Original Invest* (2021) 39(1):73.e9–73.e18. doi: 10.1016/j.urolonc.2020.07.010

23. Morawitz J, Kirchner J, Lakes J, Bruckmann NM, Mamlins E, Hiester A, et al. Psma Pet/Ct vs. Ct alone in newly diagnosed biochemical recurrence of prostate cancer after radical prostatectomy: comparison of detection rates and therapeutic implications. *Eur J Radiol* (2021) 136:109556. doi: 10.1016/j.ejrad.2021.109556

24. Lawal IO, Lengana T, Popoola GO, Orunmuyi AT, Kgatle MM, Mokoala KMG, et al. Pattern of prostate cancer recurrence assessed by (68)Ga-Psma-11 Pet/Ct in men treated with primary local therapy. *J Clin Med* (2021) 10(17):3883. doi: 10.3390/jcm10173883

25. Kroenke M, Mirzoyan L, Horn T, Peeken JC, Wurzer A, Wester H-J, et al. Matched-pair comparison of 68ga-Psma-11 and 18f-Rhpsma-7 Pet/Ct in patients with primary and biochemical recurrence of prostate cancer: frequency of non–tumor-related uptake and tumor positivity. *J Nucl Med* (2021) 62(8):1082–8. doi: 10.2967/jnumed.120.251447

26. Jentjens S, Mai C, Ahmadi Bidakhvidi N, De Coster L, Mertens N, Koole M, et al. Prospective comparison of simultaneous [(68)Ga]Ga-Psma-11 Pet/Mr versus pet/Ct in patients with biochemically recurrent prostate cancer. *Eur Radiol* (2022) 32(2):901–11. doi: 10.1007/s00330-021-08140-0

27. Fourquet A, Lahmi L, Rusu T, Belkacemi Y, Créhange G, de la Taille A, et al. Restaging the biochemical recurrence of prostate cancer with [(68)Ga]Ga-Psma-11 Pet/Ct: diagnostic performance and impact on patient disease management. *Cancers (Basel)* (2021) 13(7):1594. doi: 10.3390/cancers13071594

28. Dadgar H, Seyedi Vafaee M, Norouzbeigi N, Jafari E, Gholamrezanezhad A, Assadi M. Dual-Phase 68ga-Psma-11 Pet/Ct may increase the rate of detected lesions in prostate cancer patients. *Urologia* (2021) 88(4):355–61. doi: 10.1177/0391560321993544

29. Cerci JJ, Fanti S, Lobato EE, Kunikowska J, Alonso O, Medina S, et al. Diagnostic performance and clinical impact of (68)Ga-Psma-11 Pet/Ct imaging in early relapsed prostate cancer after radical therapy: a prospective multicenter study (Iaea-Psma study). *J Nucl Med* (2022) 63(2):240–7. doi: 10.2967/jnumed.120.261886

30. Carvalho J, Nunes P, Da Silva ET, Silva R, Lima J, Quaresma V, et al. [68ga]Ga-Psma-11 Pet-Ct: local preliminary experience in prostate cancer biochemical recurrence patients. *Arch Ital Urol Androl* (2021) 93(1):21–5. doi: 10.4081/aiua.2021.1.21

31. Afshar-Oromieh A, da Cunha ML, Wagner J, Haberkorn U, Debus N, Weber W, et al. Performance of [(68)Ga]Ga-Psma-11 Pet/Ct in patients with recurrent prostate cancer after prostatectomy-a multi-centre evaluation of 2533 patients. *Eur J Nucl Med Mol Imaging* (2021) 48(9):2925–34. doi: 10.1007/s00259-021-05189-3

32. Abghari-Gerst M, Armstrong WR, Nguyen K, Calais J, Czernin J, Lin D, et al. A comprehensive assessment of (68)Ga-Psma-11 Pet in biochemically recurrent prostate cancer: results from a prospective multicenter study on 2,005 patients. *J Nucl Med* (2022) 63(4):567–72. doi: 10.2967/jnumed.121.262412

33. Seniaray N, Verma R, Khanna S, Belho E, Pruthi A, Mahajan H. Localization and restaging of carcinoma prostate by (68)Gallium prostate-specific membrane antigen positron emission tomography computed tomography in patients with biochemical recurrence. *Indian J Urol* (2020) 36(3):191–9. doi: 10.4103/iju.IJU_275_19

34. Regula N, Kostaras V, Johansson S, Trampal C, Lindström E, Lubberink M, et al. Comparison of (68)Ga-Psma-11 Pet/Ct with (11)C-Acetate Pet/Ct in re-staging of prostate cancer relapse. *Sci Rep* (2020) 10(1):4993. doi: 10.1038/s41598-020-61910-6

35. Rauscher I, Krönke M, König M, Gafita A, Maurer T, Horn T, et al. Matched-pair comparison of (68)Ga-Psma-11 Pet/Ct and (18)F-Psma-1007 Pet/Ct: frequency of pitfalls and detection efficacy in biochemical recurrence after radical prostatectomy. *J Nucl Med* (2020) 61(1):51–7. doi: 10.2967/jnumed.119.229187

36. Radzina M, TIrane M, Roznere L, Zemniece L, Dronka L, Kalnina M, et al. Accuracy of (68)Ga-Psma-11 Pet/Ct and multiparametric Mri for the detection of local tumor and lymph node metastases in early biochemical recurrence of prostate cancer. *Am J Nucl Med Mol Imaging* (2020) 10(2):106–18.

37. Miksch J, Bottke D, Krohn T, Thamm R, Bartkowiak D, Solbach C, et al. Interobserver variability, detection rate, and lesion patterns of (68)Ga-Psma-11-Pet/Ct in early-stage biochemical recurrence of prostate cancer after radical prostatectomy. *Eur J Nucl Med Mol Imaging* (2020) 47(10):2339–47. doi: 10.1007/s00259-020-04718-w

38. Huits TH, Luiting HB, van der Poel HG, Nandurkar R, Donswijk M, Schaake E, et al. Distribution of prostate cancer recurrences on gallium-68 prostate-specific membrane antigen ((68) Ga-Psma) positron-emission/computed tomography after radical prostatectomy with pathological node-positive extended lymph node dissection. *BJU Int* (2020) 125(6):876–83. doi: 10.1111/bju.15052

39. Mapelli P, Ghezzo S, Samanes Gajate AM, Preza E, Palmisano A, Cucchiara V, et al. (68)Ga-Psma and (68)Ga-Dota-Rm2 Pet/Mri in recurrent prostate cancer: diagnostic performance and association with clinical and histopathological data. *Cancers (Basel)* (2022) 14(2):334. doi: 10.3390/cancers14020334

40. Lütje S, Cohnen J, Gomez B, Grüneisen J, Sawicki L, Rübben H, et al. Integrated (68)Ga-Hbed-Cc-Psma-Pet/Mri in patients with suspected recurrent prostate cancer. *Nuklearmedizin* (2017) 56(3):73–81. doi: 10.3413/Nukmed-0850-16-09

41. Lake ST, Greene KL, Westphalen AC, Behr SC, Zagoria R, Small EJ, et al. Optimal Mri sequences for (68)Ga-Psma-11 Pet/Mri in evaluation of biochemically recurrent prostate cancer. *EJNMMI Res* (2017) 7(1):77. doi: 10.1186/s13550-017-0327-7

42. Kranzbühler B, Müller J, Becker AS, Garcia Schüler HI, Muehlematter U, Fankhauser CD, et al. Detection rate and localization of prostate cancer recurrence using (68)Ga-Psma-11 Pet/Mri in patients with low Psa values ≤ 0.5 ng/ml. *J Nucl Med* (2020) 61(2):194–201. doi: 10.2967/jnumed.118.225276

43. Joshi A, Roberts MJ, Perera M, Williams E, Rhee H, Pryor D, et al. The clinical efficacy of Psma Pet/Mri in biochemically recurrent prostate cancer compared with standard of care imaging modalities and confirmatory histopathology: results of a

single-centre, prospective clinical trial. *Clin Exp Metastasis* (2020) 37(4):551–60. doi: 10.1007/s10585-020-10043-1

44. Guberina N, Hetkamp P, Ruebben H, Fendler W, Grueneisen J, Suntharalingam S, et al. Whole-body integrated [(68)Ga]Psma-11-Pet/Mr imaging in patients with recurrent prostate cancer: comparison with whole-body Pet/Ct as the standard of reference. *Mol Imaging Biol* (2020) 22(3):788–96. doi: 10.1007/s11307-019-01424-4

45. Grubmüller B, Baltzer P, D'Andrea D, Korn S, Haug AR, Hacker M, et al. (68) Ga-Psma 11 ligand pet imaging in patients with biochemical recurrence after radical prostatectomy - diagnostic performance and impact on therapeutic decision-making. *Eur J Nucl Med Mol Imaging* (2018) 45(2):235–42. doi: 10.1007/s00259-017-3858-2

46. Afshar-Oromieh A, Haberkorn U, Schlemmer HP, Fenchel M, Eder M, Eisenhut M, et al. Comparison of Pet/Ct and Pet/Mri hybrid systems using a 68ga-labelled Psma ligand for the diagnosis of recurrent prostate cancer: initial experience. *Eur J Nucl Med Mol Imaging* (2014) 41(5):887–97. doi: 10.1007/s00259-013-2660-z

47. Glemser PA, Rotkopf LT, Ziener CH, Beuthien-Baumann B, Weru V, Kopp-Schneider A, et al. Hybrid imaging with [(68)Ga]Psma-11 Pet-Ct and Pet-Mri in biochemically recurrent prostate cancer. *Cancer Imaging* (2022) 22(1):53. doi: 10.1186/s40644-022-00489-9

48. Alonso O, Dos Santos G, García Fontes M, Balter H, Engler H. (68)Ga-Psma and (11)C-Choline comparison using a tri-modality Pet/Ct-Mri (3.0 t) system with a dedicated shuttle. *Eur J Hybrid Imaging* (2018) 2(1):9. doi: 10.1186/s41824-018-0027-1

49. Freitag MT, Radtke JP, Afshar-Oromieh A, Roethke MC, Hadaschik BA, Gleave M, et al. Local recurrence of prostate cancer after radical prostatectomy is at risk to be missed in (68)Ga-Psma-11-Pet of Pet/Ct and Pet/Mri: comparison with Mpmri integrated in simultaneous Pet/Mri. *Eur J Nucl Med Mol Imaging* (2017) 44(5):776–87. doi: 10.1007/s00259-016-3594-z

50. Bianchi L, Ceci F, Balestrazzi E, Costa F, Droghetti M, Piazza P, et al. Psma-pet guided treatment in prostate cancer patients with oligorecurrent progression after previous salvage treatment. *Cancers (Basel)* (2023) 15(7):2027. doi: 10.3390/cancers15072027

51. Bianchi L, Ceci F, Costa F, Balestrazzi E, Droghetti M, Piazza P, et al. The impact of Psma-Pet on oncologic control in prostate cancer patients who experienced Psa persistence or recurrence. *Cancers (Basel)* (2022) 15(1):247. doi: 10.3390/cancers15010247

52. Bravi CA, Droghetti M, Fossati N, Gandaglia G, Suardi N, Mazzone E, et al. Definition and impact on oncologic outcomes of persistently elevated prostate-specific antigen after salvage lymph node dissection for node-only recurrent prostate cancer after radical prostatectomy: clinical implications for multimodal therapy. *Eur Urol Oncol* (2022) 5(3):285–95. doi: 10.1016/j.euo.2021.06.003

53. de Barros HA, van Beurden I, Droghetti M, Wilthagen EA, Özman O, Bergman AM, et al. Role of local and/or metastasis-directed therapy in patients with hormone-sensitive M1a prostate cancer-a systematic review. *Eur Urol Oncol* (2023) 6(1):16–27. doi: 10.1016/j.euo.2022.10.002

frontiers | Frontiers in Oncology

TYPE Original Research
PUBLISHED 24 August 2023
DOI 10.3389/fonc.2023.1220009

OPEN ACCESS

EDITED BY
Fabio Grizzi,
Humanitas Research Hospital, Italy

REVIEWED BY
Chenyang Shen,
University of Texas Southwestern Medical Center, United States
James C. L. Chow,
University of Toronto, Canada

*CORRESPONDENCE
Bendik Skarre Abrahamsen
bendik.s.abrahamsen@ntnu.no

RECEIVED 09 May 2023
ACCEPTED 31 July 2023
PUBLISHED 24 August 2023

CITATION
Abrahamsen BS, Knudtsen IS, Eikenes L, Bathen TF and Elschot M (2023) Pelvic PET/MR attenuation correction in the image space using deep learning. *Front. Oncol.* 13:1220009. doi: 10.3389/fonc.2023.1220009

Pelvic PET/MR attenuation correction in the image space using deep learning

Bendik Skarre Abrahamsen[1*], Ingerid Skjei Knudtsen[1], Live Eikenes[1], Tone Frost Bathen[1,2] and Mattijs Elschot[1,2]

[1]Department of Circulation and Medical Imaging, Norwegian University of Science and Technology, Trondheim, Norway, [2]Department of Radiology and Nuclear Medicine, St. Olavs Hospital, Trondheim University Hospital, Trondheim, Norway

Introduction: The five-class Dixon-based PET/MR attenuation correction (AC) model, which adds bone information to the four-class model by registering major bones from a bone atlas, has been shown to be error-prone. In this study, we introduce a novel method of accounting for bone in pelvic PET/MR AC by directly predicting the errors in the PET image space caused by the lack of bone in four-class Dixon-based attenuation correction.

Methods: A convolutional neural network was trained to predict the four-class AC error map relative to CT-based attenuation correction. Dixon MR images and the four-class attenuation correction μ-map were used as input to the models. CT and PET/MR examinations for 22 patients ([^{18}F]FDG) were used for training and validation, and 17 patients were used for testing (6 [^{18}F]PSMA-1007 and 11 [^{68}Ga]Ga-PSMA-11). A quantitative analysis of PSMA uptake using voxel- and lesion-based error metrics was used to assess performance.

Results: In the voxel-based analysis, the proposed model reduced the median root mean squared percentage error from 12.1% and 8.6% for the four- and five-class Dixon-based AC methods, respectively, to 6.2%. The median absolute percentage error in the maximum standardized uptake value (SUV_{max}) in bone lesions improved from 20.0% and 7.0% for four- and five-class Dixon-based AC methods to 3.8%.

Conclusion: The proposed method reduces the voxel-based error and SUV_{max} errors in bone lesions when compared to the four- and five-class Dixon-based AC models.

KEYWORDS

PET/MR, attenuation correction, deep learning, prostate cancer, artificial intelligence frontiers, MRAC, pseudo-CT

Abbreviations: AC, attenuation correction; LAC, linear attenuation coefficient; MAE, mean absolute error; MAPE, mean absolute percentage error; PET_{4C}, PET images reconstructed using four-class Dixon-based μ-map; PET_{5C}, PET images reconstructed using five-class Dixon-based μ-map with bone registered from bone atlas; PET_{MR+CT}, PET images reconstructed using four-class Dixon-based μ-map with bone information from CT; PET_{cor}, reconstructed PET_{4C} corrected using the proposed method; PI, postinjection time; RMSPE, root-mean-squared percentage error

1 Introduction

The advent of prostate-specific membrane antigen (PSMA) tracers has led to the increasing adoption of PET as the modality of choice in diagnosing recurrent prostate cancer (1). For this patient group, [^{68}Ga]GaPSMA-11 PET/MR has been shown to have similar diagnostic performance to [^{68}Ga]Ga-PSMA-11 PET/CT in nodal and osseous metastasis (2–4) and superior performance in the detection of local recurrences due to the higher soft-tissue contrast provided by MR (2, 5). However, attenuation correction (AC), which is the most important correction required for quantitatively accurate PET imaging, remains a challenge in PET/MR imaging (6–8).

For PET/CT, the contrast of the CT images is dependent on the electron density of the imaged tissue, which in turn is related to the linear attenuation coefficient (LAC) of the PET photons (6, 9). A piecewise linear transformation of the CT Hounsfield units can be used to estimate the LAC at the PET photon energy of 511 keV (10). This approach is widely accepted as AC for PET/CT in clinical practice (6, 11). Since the signal in MR comes from proton densities and tissue relaxation times, no such straightforward relationship between the MR intensity values and LAC at the PET photon energy exists (6, 9, 11).

In current clinical practice, whole-body PET/MR AC is typically derived from Dixon MR sequences. These sequences are time-efficient to acquire and are available in all commercially available clinical PET/MR scanners (12). In four-class Dixon-based AC, Dixon MR images are segmented into four components: fat, lung, soft tissue, and background air, and each component is subsequently assigned a respective predefined LAC (13). Bone, although highly attenuating, is not accounted for in this four-class attenuation correction model. Disregarding the bone can lead to an underestimation of the standardized uptake values in and near the bone. For the pelvic region in particular, errors as large as 30% have been found in the most impacted bone lesions (14). In the staging of prostate cancer recurrence after definitive therapy, bone lesions are also fairly common and can be expected in more than 20% of the cases (15). In restaging after salvage radiotherapy, bone lesions are even more common and are observed in as many as 45% of cases (16).

The short $T2^*$ relaxation times and low proton density of cortical bone cause the MR signal to decay quickly in bone tissue (17) and make bone hard to distinguish from air in conventional MR images. Thus, in the four-class Dixon-based AC model, bone is classified as soft tissue. To tackle this issue, Paulus et al. (18) proposed the five-class Dixon-based AC model. This model is an atlas-based approach for whole-body PET AC based on individual registration of the major bones (skull, femur, hips, and spine, including sacrum) from a bone atlas consisting of paired Dixon MR images and bone masks. However, this method is prone to registration errors and misses bones entirely in some cases (19, 20). In a recent retrospective study of 200 patients, it was advised not to use this form of AC for PSMA PET/MR without great caution and thorough inspection of the resulting μ-maps (20).

Several deep learning-based approaches have also been suggested to improve AC in PET/MR. These approaches can broadly be categorized into those that only use the Dixon images (7, 21), those that require other MR sequences than the standard Dixon images (22–25), and approaches that only use the PET data (26). A different way to categorize these approaches is by whether their goal is to create a pseudo-CT image or a μ-map (21–23, 25, 27) or to directly correct or predict the corrected PET image itself (26).

An obvious limitation of the acquisition of additional MR sequences for AC purposes is that it requires additional scan time. Approaches that rely on the PET data itself as input data, either for μ-map prediction or for direct prediction of the corrected PET image itself, are dependent on the tracer for which the model is trained. These models are thus not directly applicable to multiple tracers without retraining the model.

We introduce a novel, deep learning-based approach to improving AC in pelvic PET/MR acquisitions. The proposed method aims to directly correct the errors in the PET images caused by bones not being included in the four-class AC model rather than predicting new μ-maps. For this purpose, a voxel-wise correction map is predicted by a convolutional neural network using Dixon MR and the four-class μ-map as input. The predicted correction map can subsequently be applied as a postprocessing step directly in the PET image space to correct PET images reconstructed with the four-class μ-map without re-reconstruction of the images. Additionally, the proposed model requires no additional sequences beyond the standard Dixon MR images and does not require retraining to be used with multiple tracers. In this work, we evaluated the quantitative impact of the proposed method on PSMA uptake in the pelvic region of patients suspected of recurrence of prostate cancer.

2 Materials and methods

2.1 Patient selection and data acquisition

This study included 49 patients who underwent same-day PET/CT and PET/MR procedures following a single tracer injection. The included cohort consisted of male patients with suspicion of lymphoma and lung cancer scanned with [^{18}F]FDG (FDG), which was used for training and validation of the proposed model. A separate cohort with patients suspected of recurrence of prostate cancer after radical treatment scanned with [^{68}Ga]Ga-PSMA-11 or [^{18}F]PSMA-1007 was used as the test set. The PET acquisitions included one to five bed positions, where data were acquired for 5–10 min per bed. Patients with sphincter pumps and metal implants were excluded, as were those with imperfect coregistration between MR and CT.

PET and MR images were acquired on a 3T Biograph mMR PET/MR scanner (Siemens Healthineers, Erlangen, Germany, updates MR B20P and MR E11). A standard Dixon sequence was acquired for attenuation correction purposes. The scan parameters and resolution of the Dixon series varied within the dataset. The parameters of the Dixon series are summarized in Table 1.

TABLE 1 Scan parameters for the different Dixon series contained in the dataset.

Dixon series	Spacing (mm)	TR (ms)	TE_1 (ms)	TE_2 (ms)
1	2.1 × 2.1 × 3.0	3.8	1.2	1.2
2	1.3 × 1.3 × 3.0	3.8	1.2	2.5
3	2.1 × 2.1 × 2.6	3.8	1.2	2.5
4	2.6 × 2.6 × 3.1	3.6	1.2	2.5

The enumeration of the series is arbitrary. The flip angle was 10° for all variations.

Low-dose CT images were acquired at a Biograph64 PET/CT scanner (Siemens Healthineers, Erlangen, Germany) using adaptive exposure control (tube voltage: 120 kV, peak and tube current median: 34.8, range: 17–52, slice thickness: 3 mm, matrix: 512 × 512, and pixel spacing: 1.5 mm × 1.5 mm). The CT images were acquired arms-up as opposed to the MR images. The PET images from the PET/CT examination were not used in this study.

2.2 μ-Map generation

To generate the reference standard μ-map, the CT images were first registered to the Dixon MR images with the Elastix registration toolbox (28, 29) using a composite registration scheme consisting of a rigid and a deformable stage (Supplementary Section 1). To obtain an accurate registration between CT and MR, arms were masked out from the MR images and corresponding four-class μ-maps. After the registration, the CT Hounsfield unit values were scaled to their corresponding LAC at 511 keV according to parameters by Burger et al. (10).

Due to the difficulty of attaining perfect coregistration in soft tissue and bone simultaneously, only the bone information was transferred into the Dixon four-class μ-map from the scanner console to generate the reference standard μ-map image as opposed to using a scaled registered CT directly. Bone information was defined as all voxels within the CT image with a LAC of >0.1 cm^{-1}. This approach is similar to Bradshaw et al. (25), who also used MR-based AC for the soft tissue classes and coregistered bone information from CT images to form the reference standard μ-map. The CT-to-MR coregistration of each case was closely examined, and only images found to perform well upon visual inspection were kept in the dataset. The bone information was only inserted in a mask covering the pelvic region, which was defined as all slices from approximately the upper thighs to approximately vertebrae L2 of the lumbar spine.

2.3 PET reconstruction

PET reconstructions were performed using the Siemens proprietary offline PET reconstruction tools (E7tools, Siemens Healthineers, Erlangen, Germany) or at the scanner console with the following reconstruction settings: ordinary Poisson ordered-subset expectation-maximization algorithm with three iterations, 21 subsets, and a 4-mm Gaussian postreconstruction filter with resolution modeling included in the reconstruction (PSF). The PET volumes were reconstructed with a 344 × 344 matrix with an in-plane resolution of 2.1 mm × 2.1 mm and a slice thickness of 2.0 mm. Absolute scaling (30) was used for scatter correction in patients imaged with [^{68}Ga]Ga-PSMA-11, and relative scaling was used for [^{18}F]PSMA-1007 images and FDG images (31).

2.4 Correction method

A deep convolutional neural network was trained to predict the correction map between the PET images reconstructed using the reference standard μ-map, referred to as PET_{CT+MR}, and the PET images reconstructed using the Dixon-based four-class μ-map, PET_{4C}. The correction map was calculated as shown in Eq (1) For more details, see Supplementary Section 2.

$$\text{Correction map} = \frac{PET_{4C} - PET_{CT+MR}}{PET_{4C}} \quad (1)$$

The correction map was only estimated within the mask covering the pelvic region. Dixon in-phase, Dixon out-of-phase, and the four-class Dixon-based μ-map were used as inputs to the network. The images were resampled to the PET image space and min–max scaled to intensities in the range [0,1]. A threshold intensity mask was used to set intensity values outside the body contour to zero.

An overview of the network architecture is given in Figure 1. The network consisted of a nine-block ResNet (33) architecture inspired by Johnson et al. (32) and Wang et al. (35). The network was trained using *L2* loss and an Adam optimizer (36) for 100 epochs with a linearly decaying learning rate starting from epoch 50. The code for training the network and the hyperparameters used in the final model is available on github (https://github.com/ntnu-mr-cancer/PETMR-4CMRAC-Correction-maps).

Results for additional tested network architectures can be found in Supplementary Section 3. The output of the network is a predicted correction map, which is used to correct the PET_{4C} images by solving Eq (1). for PET_{CT+MR}. The resulting corrected PET image will be referred to as PET_{cor}. An overview of the methods from image acquisition to corrected PET images is given in Figure 2.

2.5 Analysis and statistics

Voxel- and lesion-based analysis was performed to assess the performance of the method. For the voxel-based analysis, only

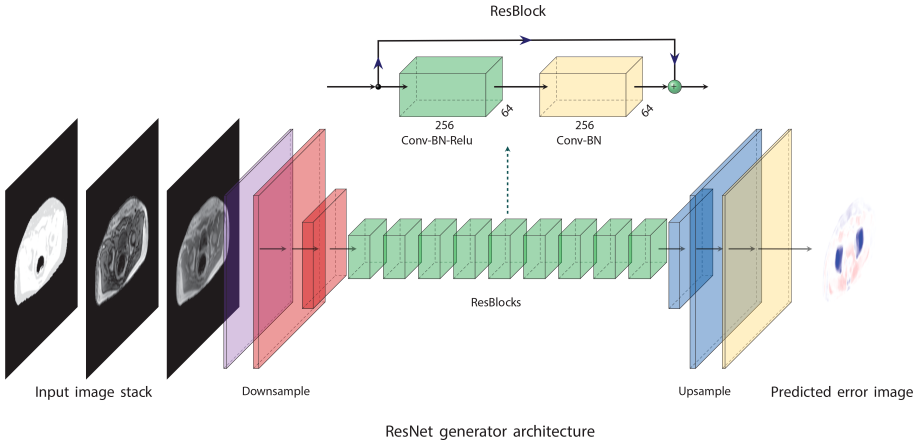

FIGURE 1
The network architecture is based on ideas proposed by Johnson et al. (32). It consists of nine residual blocks (33) (ResBlocks) between a convolutional front-end and a transposed convolutional back-end. The convolutional front-end downsamples the images to one-fourth of their original resolution, and the transpose convolutional back-end upsamples the images to their original resolution. The figure was made using PlotNeuralNet (34).

voxels within the pelvic mask that had an activity concentration of > 300 Bq ml^{-1} were used in the calculation. The relative error image (RE_x), defined as shown in Eq. (2),ResNet generator architecture

$$RE_x = \frac{I_x - I_{GS}}{I_{GS}} \tag{2}$$

Where I is the image intensity, GS represents the reference standard PET image PET_{CT+MR}, and x is either PET image that is compared to the PET_{CT+MR} (i.e., PET_{cor} or PET_{4C}). RE_x was used as a basis to calculate the mean absolute percentage error (MAPE) and root-mean-squared percentage error (RMSPE) that were used as quantitative metrics in the voxel-based analysis. MAPE and RMSPE were defined as shown in Eq. (3)

$$\begin{aligned} MAPE &= \frac{1}{n_{mask}} \sum_{i \in mask} ||RE_x|| \\ RMSPE &= \sqrt{\mu_{RE_x}^2 + \sigma_{RE_x}^2}, \end{aligned} \tag{3}$$

Where μ_{REx} and σ_{REx} are the mean and standard deviation, RE_x and n_{mask} are the number of voxels within the mask that satisfy the activity concentration threshold. It is understood that the summation in the definition of MAPE and the summations performed in calculating μ_{REx} and σ_{REx} in RMSPE are performed only over n_{mask}.

To assess lesion performance, lesions were extracted from radiology reports. The lesion performance was measured as the relative error and MAPE of the maximum standardized uptake values (SUV_{max}) of the corresponding lesions between the PET images.

All presented values are given as medians with ranges in brackets unless otherwise mentioned. A two-sided Wilcoxon signed-rank test was performed to assess whether there were any differences between RMSPE values of the PET_{cor} image and PET images reconstructed using four- and five-class Dixon-based AC (PET_{4C} and PET_{5C}) in the test set. A test of difference was also made for each of the tracers in the test set separately. Benjamini–Hochberg correction was used to correct the p-value for multiple comparisons where applicable (37). A Mann–Whitney U test was used to compare differences between the RMSPE of [^{68}Ga]Ga-PSMA-11 and [^{18}F]PSMA-1007 images. No statistical tests were performed for the lesion-based analysis due to the limited number of samples. A difference was considered significant if $p < 0.05$ was achieved.

3 Results

From the 49 included patients, two patients were removed from the dataset due to severe artifacts in the PET images and eight were removed due to suboptimal coregistration between CT and MR. This resulted in a training set consisting of 18 patients scanned with FDG, a validation set of four patients scanned with FDG, and a test set consisting of 17 patients scanned with [^{68}Ga]Ga-PSMA-11 or [^{18}F]PSMA-1007. An overview of the dataset is presented in Table 2, and a flow diagram of patient inclusion can be found in the Supplementary Material (S1). From radiology reports of patients in the test set, 16 soft tissue lesions and four bone lesions were extracted.

Training the convolutional neural network took approximately 4 h on a single NVIDIA GeForce GTX 1080 Ti. An example of a corrected PET image can be seen in Figure 3. The corrected PET images were found to closely resemble the reference standard PET_{CT+MR} images.

The voxel-based RMSPE and MAPE were 12.1% [8.6%, 15.4%] and 6.2% [4.0%, 10.3%], respectively, for the PET_{4C} images and 8.6% [5.3%, 11.5%] and 3.5% [2.3%, 5.1%], respectively, for the PET_{5C} images. In the PET_{cor} images, the RMSPE was 6.2% [4.1%, 8.6%] and the MAPE was 3.3% [2.3%, 4.6%]. The error in PET_{cor} is thus approximately reduced by half compared to the PET_{4C} images. A significant difference was found between the RMSPE of the PET_{cor} images and the PET_{4C} images ($p < 0.0001$) and between PET_{cor} images and the PET_{5C} images ($p < 0.0001$). A significant difference

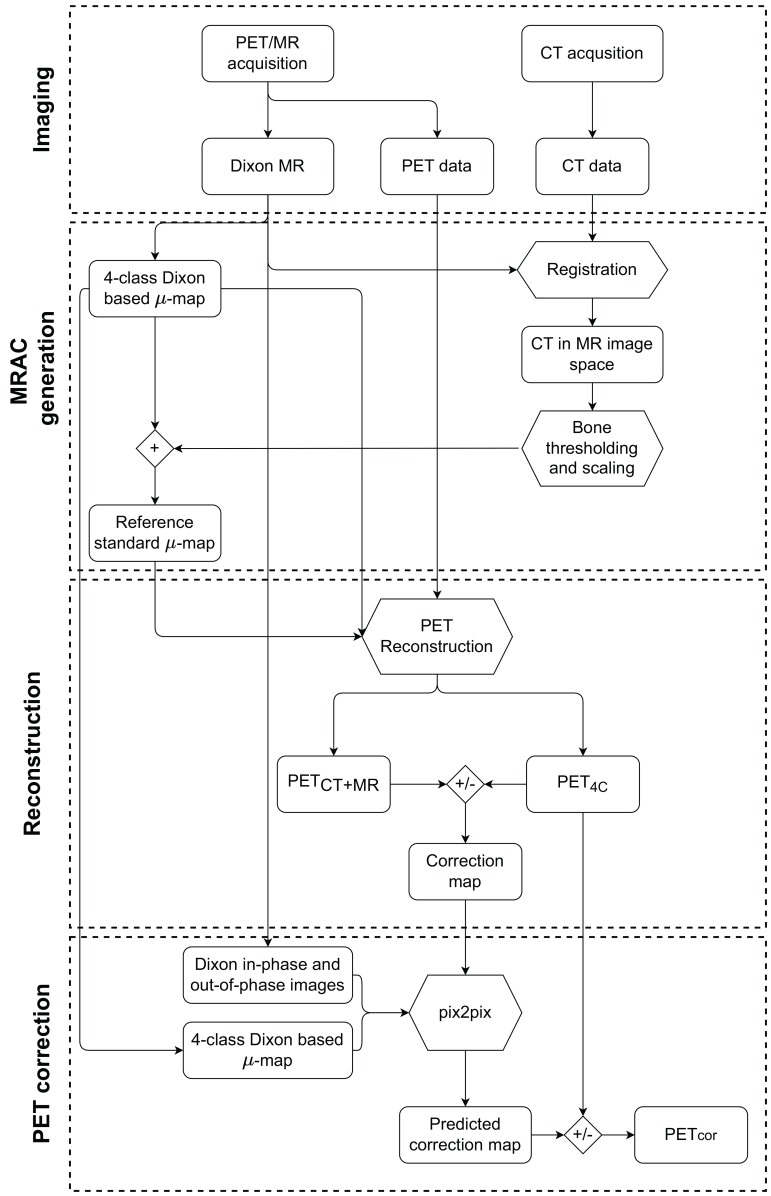

FIGURE 2
Graphical overview of the methodology from acquisition to generation of the corrected PET image (PET_{cor}). The node labeled + refers to overwriting linear attenuation coefficients (LAC) in the four-class Dixon-based μ-map with CT bone information scaled to LAC at 511 keV. The nodes labeled +/-represent the creation of the correction map as specified in Eq (1), and the application of the correction map to PET reconstructed with the four-class Dixon-based μ-map (PET_{4C}). PET_{MR+CT} is PET reconstructed using reference standard μ-map, which is obtained by using a four-class Dixon-based μ-map for soft tissue and bone information from a co-registered CT image.

TABLE 2 Summary statistics for included patients.

Fold	Train	Val	Test	Test
Tracer	FDG (n = 18)	FDG (n = 4)	18F-PSMA (n = 6)	68Ga-PSMA (n = 11)
PI (min)	98 [88–157]	116 [90–168]	136 [116–165]	58 [48–105]
Weight (kg)	88 [71–120]	82 [73–92]	78 [62–86]	85 [74–103]
Dose (MBq)	352 [280–478]	328 [290–368]	200 [153–218]	149 [133–157]

Data is given as median values with ranges in brackets. Fold specifies which part of the data was used for training (Train), validation (Val) and testing (Test) of the model. PI = time between tracer injection and image acquisition.

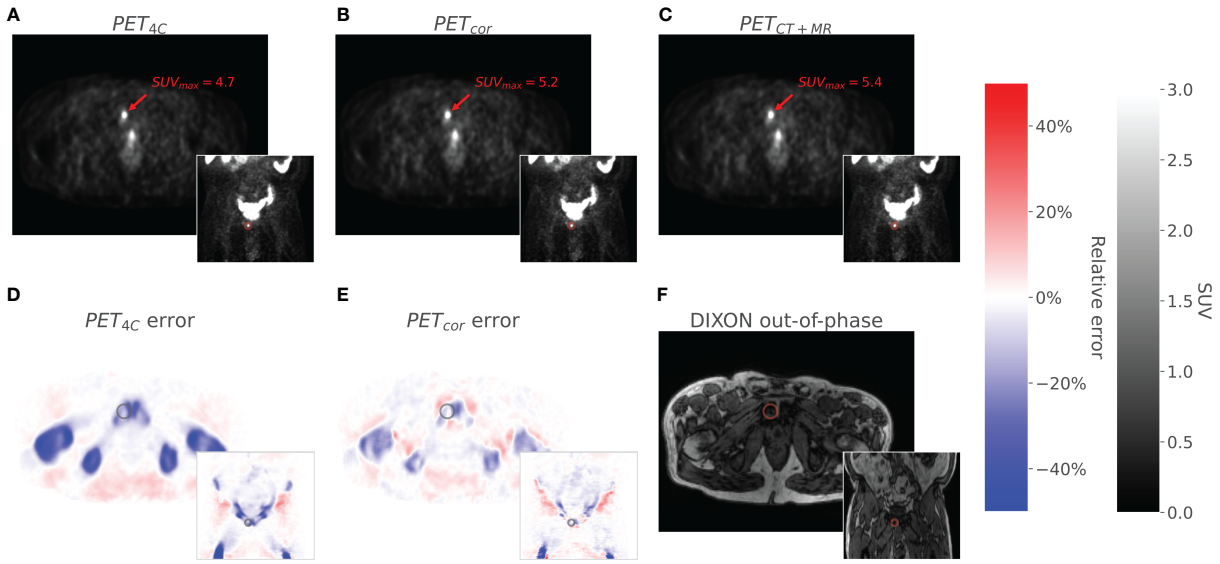

FIGURE 3
The figure shows axial and coronal images of PET_{4C} **(A)**, PET_{cor} **(B)**, and PET_{CT} **(C)**. The PET_{4C} error **(D)** is the relative error image between the PET_{4C} image and PET_{MR+CT}, and the PET_{cor} error **(E)** is the relative error image between PET_{cor} and PET_{MR+CT}. Values outside the body contour in the relative error images are set to zero. The Dixon out-of-phase image is given as an anatomical correlate **(F)**. A lesion located in the *os pubis* is highlighted in all images.

was also found between the RMSPE values for [^{68}Ga]Ga-PSMA-11 and [^{18}F]PSMA-1007 patients individually between PET_{cor} and both PET_{4C} and PET_{5C}, as shown in Figure 4. No significant difference was found when comparing the RMSPE of PET_{cor} between patients acquired with [^{68}Ga]Ga-PSMA-11 and [^{18}F]PSMA-1007.

The lesion performance is summarized in Table 3 and Figure 5. Performance in soft tissue lesions improved marginally from a MAPE of 2.9% [0.8%, 6.5%] in PET_{4C} to 2.2% [0.1%, 8.1%] for PET_{cor}. For bone lesions, we observed more than a fivefold decrease in MAPE from 20.0% [12.0%, 30.4%] in PET_{4C} to 3.8% [1.0%, 9.2%] in PET_{cor}. PET_{5C}, in comparison to the proposed model, had lower MAPE in soft tissue lesions and higher MAPE in bone lesions.

We observed a decrease in performance with increasing postinjection time (PI) in the test set. In a simple linear regression model, a significant linear trend ($p < 0.05$, $r^2 = 0.30$) was found between the voxel-based RMSPE measurements and the PI time (see Supplementary Section 5 for further details).

4 Discussion

In this study, we propose a novel attenuation correction method that seeks to directly correct for the errors obtained by not including bone when using the conventional four-class Dixon-based AC. We

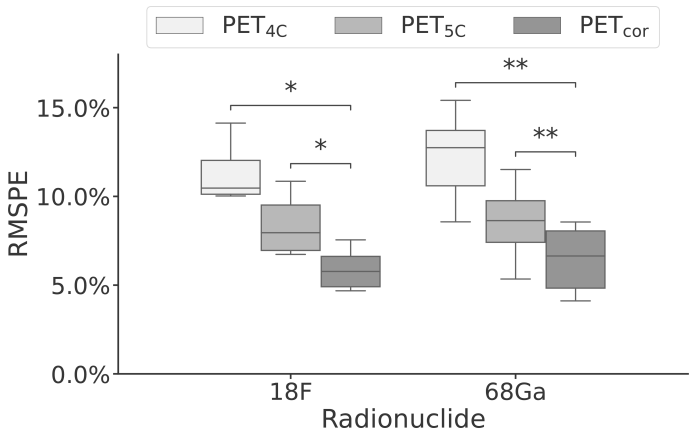

FIGURE 4
Box-and-whisker plot of the root mean squared percentage error performance stratified by radionuclide for PET reconstructed using four- and five-class Dixon-based attenuation correction (PET_{4C} and PET_{5C}) and the proposed model (PET_{cor}). The central line within each box is the median. The box edges extend from the 25th to the 75th percentile. Values were considered outliers if they were more than 1.5 times the interquartile ranges of the box edges. The whiskers extend to the most extreme nonoutlier value in the data. *$p < 0.05$; **$p < 0.01$.

TABLE 3 Lesion performance of PET images reconstructed using four- and five-class Dixon-based μ-maps (PET_{4C} and PET_{5C}) and PET corrected using the proposed model (PET_{cor}) relative to the reference standard.

	Type	Bone (n = 4)	Soft tissue (n = 16)
Model	Error		
4-class	Absolute percentage error	20.0% [12.0%, 30.4%]	2.9% [0.8%, 6.5%]
	Relative error	−20.0% [−30.4%, − 12.0%]	−2.7% [−6.5%, 6.4%]
5-class	Absolute percentage error	7.0% [2.1%, 23.7%]	0.9% [0.0%, 2.6%]
	Relative error	−7.0% [−23.7%, −2.1%]	−0.5% [−2.6%, 2.5%]
Corrected	Absolute percentage error	3.8% [1.0%, 9.2%]	2.2% [0.1%, 8.1%]
	Relative error	1.3% [−6.0%, 9.2%]	−1.9% [−8.1%, 4.4%]

Statistics are given as medians, with ranges in brackets.

show that the model reduces quantification errors in a voxel-based analysis and in bone lesions compared to four- and five-class Dixon-based methods. For soft tissue lesions, the performance remains similar to that of the four-class Dixon-based AC model.

Our method can be directly applied as a correction filter in the image space to PET_{4C} images without the need for additional reconstruction or the acquisition of additional MR sequences. It can thus also be used to correct PET_{4C} images retrospectively, as long as Dixon MR images are available. This distinguishes it from other models that seek to improve pseudo-CT generation. The model also only relies on Dixon MR images, which are fast to acquire. Furthermore, like the models that predict pseudo-CT images from MR series (21–23, 25, 27), but unlike the models that predict the pseudo-CT images or AC and scatter-corrected PET directly from non-attenuation corrected PET (26, 38, 39), the predicted correction maps are not tracer-dependent.

We observed that the proposed method is robust to variations in tracer type and scatter correction method. The training and validation sets consisted of FDG images, whereas the test set consisted of [^{68}Ga]Ga-PSMA11 and [^{18}F]PSMA-1007 images. Since there were no [^{68}Ga]Ga-PSMA-11 images in the training data, the model had only seen images reconstructed using relative scaling during scatter correction in training. Nevertheless, no differences in performance were seen between [^{68}Ga]Ga-PSMA-11 and [^{18}F]PSMA-1007 patients in the test set.

A decrease in performance was seen with increasing PI. This trend can be explained by the higher number of counts acquired at lower PI, making the correction map that the model tries to predict less noisy. All patients had PET/MR and PET/CT acquisition performed on the same day. For around half of the patients in the test set, the PET/CT images were acquired at what was considered the optimal PI for the given tracer, and the PET/MR images were acquired once the PET/CT examination was finished. If all PET/MR had been acquired closer to the recommended PI, we would expect to see a slight increase in performance.

Multiple other methods have been suggested for improving PET/MR attenuation correction in the pelvic region (7, 22, 23, 25, 27). Bradshaw et al. (25) proposed a model based on the Deep Medic CNN architecture (40). In this model, T2 and T1 Lava Flex images were used for the prediction of pseudo-CT images, resulting in an RMSPE of 4.9% in the reconstructed PET image. Leynes et al. (23) used Dixon-based images and zero-echo-time images as input

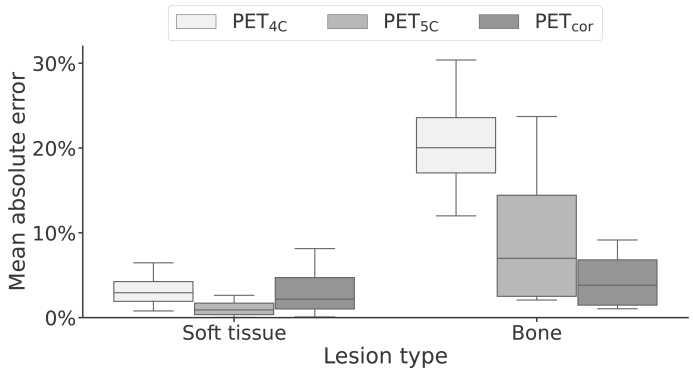

FIGURE 5
Box-and-whisker plot of the mean absolute error of soft-tissue and bone lesions for PET reconstructed using four- and five-class Dixon-based attenuation correction (PET_{4C} and PET_{5C}) and the proposed model (PET_{cor}). The central line within each box is the median. The box edges extend from the 25th to the 75th percentile. Values were considered outliers if they were more than 1.5 times the interquartile ranges of the box edges. The whiskers extend to the most extreme nonoutlier value in the data.

to a deep learning model based on the UNET architecture to generate μ-maps. The resulting PET reconstruction had an RMSPE of 2.85%. Similar to Bradshaw et al. (25), Torrado-Carvajal et al. (7) used a UNET-like architecture to create a pseudo-CT image using solely Dixon MR images as input. Their approach resulted in an absolute mean relative change of 1.83%.

A different family of models is composed of models that use non-attenuation corrected PET images as input and either the pseudo-CT (41) or the attenuation and scatter-corrected PET as output (26, 38). Though good performance can be obtained with these models, they are tracer-dependent and would likely need to be retrained for optimal performance with each new tracer. In addition, the models proposed in the literature (26, 38, 41) have only been trained and validated on PET/CT data so far, and their performance is yet to be assessed using data acquired on the PET/MR system.

Though many methods have been proposed, it is difficult to directly compare their performance. As pointed out by Lee (42), there is substantial heterogeneity in the choice of PET reconstruction parameters and performance metrics. There is also no reference dataset that can be used to benchmark the performance of different models. What is considered gold standard AC also varies between studies. In this study, we directly estimate the error of not including bones in the four-class Dixon-based μ-maps. The most common is to use registered CT images translated to LAC at 511 keV as the gold standard μ-map. This does, however, rely on a close-to-perfect coregistration between CT and MR images, which can be difficult to obtain in practice (25, 43, 44). We adopted a method similar to Bradshaw et al. (25) in which soft-tissue classes and air in the μ-map are derived from the MR images, and bone and osseous tissues are derived from the CT images.

A primary limitation of this study is the limited number of patients. The training set consisted of only 18 patients, and the test set consisted of 17 patients. Since the model was trained using a 2D network, this still constituted a considerable number of images, but we do not expect that the limited training set was able to capture all the expected interpatient variability. The number of lesions was also limited. In bone, where the model had the largest impact in our testing, only four lesions were found.

The current method is also limited to pelvic imaging only. Adapting to a different clinical application would require retraining of the model. Additionally, in the current work, only a limited subset of reconstruction parameters was used, and we did not evaluate the robustness of the method toward changes in reconstruction parameters. However, since the method is trained to predict correction maps for the PET images directly, we suspect the model to be subject to similar variability between reconstruction parameters as SUV_{max} measurements themselves (45, 46). Lastly, the model is only tested on a specific patient cohort consisting of elderly male patients. Consequently, the model must be evaluated on a larger and more diverse patient cohort before implementation in clinical practice is justified.

5 Conclusion

Direct correction of four-class Dixon-based AC PET in the image space is a viable method for improving AC of pelvic PSMA PET/MR imaging. The method is tracer-independent, requires only the Dixon MR series and the four-class Dixon-based μ-map, and can be retrospectively applied to PET data without the need for re-reconstruction. It gives superior performance to the four- and five-class Dixon-based AC in a voxel-based RMSPE analysis and for quantification of bone lesion uptake.

Data availability statement

The datasets presented in this article are not readily available because The data are not publicly available because they contain information that could compromise research participant privacy/consent. Requests to access the datasets should be directed to bendik.s.abrahamsen@ntnu.no.

Ethics statement

The studies involving humans were approved by Regional Committee for Medical and Health Research Ethics Mid Norway (FDG data: identifier REK2014/1289 and PSMA data: identifier REK2020/83009). The studies were conducted in accordance with the local legislation and institutional requirements. The participants provided their written informed consent to participate in this study.

Author contributions

All authors contributed to the study conception and design. The data collection of the FDG lymphoma and lung cancer dataset was performed by LE. Data collection of the [18F]PSMA-1007 and [68Ga]Ga-PSMA-11 images was performed by IK and BA. Analysis and interpretation of data was performed by ME, TB and BA. The first draft of the manuscript was written by BA and all authors commented on previous versions of the manuscript. All authors read and approved the final manuscript.

Funding

This work was supported by Norwegian Cancer Society and Prostatakreft-foreningen (Grant Number 215951), the Liaison Committee between the Central Norway Regional Health Authority and the Norwegian University of Science and Technology (Grant Numbers 90265300) and 180N – Norwegian Nuclear Medicine Consortium.

Conflict of interest

The authors declare that the research was conducted in the absence of any commercial or financial relationships that could be construed as a potential conflict of interest.

Publisher's note

All claims expressed in this article are solely those of the authors and do not necessarily represent those of their affiliated organizations, or those of the publisher, the editors and the reviewers. Any product that may be evaluated in this article, or claim that may be made by its manufacturer, is not guaranteed or endorsed by the publisher.

Supplementary material

The Supplementary Material for this article can be found online at: https://www.frontiersin.org/articles/10.3389/fonc.2023.1220009/full#supplementary-material

References

1. Fanti S, Goffin K, Hadaschik BA, Herrmann K, Maurer T, MacLennan S, et al. Consensus statements on PSMA PET/CT response assessment criteria in prostate cancer. *Eur J Nucl Med Mol Imaging* (2021) 48:469–76. doi: 10.1007/s00259-020-04934-4

2. Guberina N, Hetkamp P, Ruebben H, Fendler W, Grueneisen J, Suntharalingam S, et al. Whole-body integrated [68Ga]PSMA-11-PET/MR imaging in patients with recurrent prostate cancer: Comparison with whole-body PET/CT as the standard of reference. *Mol Imaging Biol* (2019) 22:788–96. doi: 10.1007/s11307-019-01424-4

3. Jentjens S, Mai C, Ahmadi Bidakhvidi N, De Coster L, Mertens N, Koole M, et al. Prospective comparison of simultaneous [68Ga]Ga-PSMA-11 PET/MR versus PET/CT in patients with biochemically recurrent prostate cancer. *Eur Radiol* (2022) 32:901–11. doi: 10.1007/s00330-021-08140-0

4. Freitag MT, Radtke JP, Hadaschik BA, Kopp-Schneider A, Eder M, Kopka K, et al. Comparison of hybrid 68Ga-PSMA PET/MRI and 68Ga-PSMA PET/CT in the evaluation of lymph node and bone metastases of prostate cancer. *Eur J Nucl Med Mol Imaging* (2016) 43:70–83. doi: 10.1007/s00259-015-3206-3

5. Freitag MT, Radtke JP, Afshar-Oromieh A, Roethke MC, Hadaschick BA, Gleave M, et al. Local recurrence of prostate cancer after radical prostatectomy is at risk to be missed in 68Ga-PSMA-11-PET of PET/CT and PET/MRI: comparison with mpMRI integrated in simultaneous PET/MRI. *Eur J Nucl Med Mol Imaging* (2017) 44:776–87. doi: 10.1007/s00259-016-3594-z

6. Chen Y, An H. Attenuation correction of PET/MR imaging. *Magn Reson Imaging Clin N Am* (2017) 25:245–55. doi: 10.1016/j.mric.2016.12.001

7. Torrado-Carvajal A, Vera-Olmos J, Izquierdo-Garcia D, Catalano OA, Morales MA, Margolin J, et al. Dixon-VIBE deep learning (DIVIDE) pseudo-CT synthesis for pelvis PET/MR attenuation correction. *J Nucl Med* (2019) 60:429–35. doi: 10.2967/jnumed.118.209288

8. Ringheim A, Campos Neto GdC, Martins KM, Vitor T, da Cunha ML, Baroni RH. Reproducibility of standardized uptake values of same-day randomized 68Ga-PSMA-11 PET/CT and PET/MR scans in recurrent prostate cancer patients. *Ann Nucl Med* (2018) 32:523–31. doi: 10.1007/s12149-018-1275-7

9. Mehranian A, Arabi H, Zaidi H. Vision 20/20: Magnetic resonance imaging-guided attenuation correction in PET/MRI: Challenges, solutions, and opportunities: PET/MRI, quantification, attenuation map, attenuation correction, tracer uptake. *Med Phys* (2016) 43:1130–55. doi: 10.1118/1.4941014

10. Burger C, Goerres G, Schoenes S, Buck A, Lonn A, von Schulthess G. PET attenuation coefficients from CT images: experimental evaluation of the transformation of CT into PET 511-keV attenuation coefficients. *Eur J Nucl Med* (2002) 29:922–7. doi: 10.1007/s00259-002-0796-3

11. Catana C. Attenuation correction for human PET/MRI studies. *Phys Med Biol* (2020) 65(23):TR02. doi: 10.1088/1361-6560/abb0f8

12. Iagaru A, Hope T, Veit-Haibach P. *PET/MRI in oncology. 1 edn*. Cham, Switzerland: Springer International Publishing (2018). doi: 10.1007/978-3-319-68517-5

13. Martinez-Moller A, Souvatzoglou M, Delso G, Bundschuh RA, Chefd'hotel C, Ziegler SI, et al. Tissue classification as a potential approach for attenuation correction in whole-body PET/MRI: Evaluation 13 with PET/CT data. *J Nucl Med* (2009) 50:520–6. doi: 10.2967/jnumed.108.054726

14. Samarin A, Burger C, Wollenweber SD, Crook DW, Burger IA, Schmid DT, et al. PET/MR imaging of bone lesions – implications for PET quantification from imperfect attenuation correction. *Eur J Nucl Med Mol Imaging* (2012) 39:1154–60. doi: 10.1007/s00259-012-2113-0

15. Perera M, Papa N, Roberts M, Williams M, Udovicich C, Vela I, et al. Gallium-68 prostate-specific membrane antigen positron emission tomography in advanced prostate cancer—updated diagnostic utility, sensitivity, specificity, and distribution of prostate-specific membrane antigen-avid lesions: A systematic review and meta-analysis. *Eur Urol* (2020) 77:403–17. doi: 10.1016/j.eururo.2019.01.049

16. Zamboglou C, Strouthos I, Sahlmann J, Farolfi A, Serani F, Medici F, et al. Metastasis-free survival and patterns of distant metastatic disease after PSMA-PET-guided salvage radiotherapy in recurrent or persistent prostate cancer after prostatectomy. *Int J Radiat. Oncol Biol Phys* (2022) 113(5):1015–24. doi: 10.1016/j.ijrobp.2022.04.048

17. Du J, Carl M, Bydder M, Takahashi A, Chung CB, Bydder GM. Qualitative and quantitative ultrashort echo time (UTE) imaging of cortical bone. *J Magn Reson* (2010) 207:304–11. doi: 10.1016/j.jmr.2010.09.013

18. Paulus DH, Quick HH, Geppert C, Fenchel M, Zhan Y, Hermosillo G, et al. Whole-body PET/MR imaging: Quantitative evaluation of a novel model-based MR attenuation correction method including bone. *J Nucl Med* (2015) 56:1061–6. doi: 10.2967/jnumed.115.156000

19. Elschot M, Selnæs KM, Johansen H, Krüger-Stokke B, Bertilsson H, Bathen TF. The effect of including bone in dixon-based attenuation correction for 18f-fluciclovine PET/MRI of prostate cancer. *J Nucl Med* (2018) 59:1913–7. doi: 10.2967/jnumed.118.208868

20. Bogdanovic B, Gafita A, Schachoff S, Eiber M, Cabello J, Weber WA, et al. Almost 10 years of PET/MR attenuation correction: the effect on lesion quantification with PSMA: clinical evaluation on 200 prostate cancer patients. *Eur J Nucl Med Mol Imaging* (2020) 48:543–53. doi: 10.1007/s00259-020-04957-x

21. Pozaruk A, Pawar K, Li S, Carey A, Cheng J, Sudarshan VP, et al. Augmented deep learning model for improved quantitative accuracy of MR-based PET attenuation correction in PSMA PET-MRI prostate imaging. *Eur J Nucl Med Mol Imaging* (2020) 48:9–20. doi: 10.1007/s00259-020-04816-9

22. Leynes AP, Yang J, Shanbhag DD, Kaushik SS, Seo Y, Hope TA, et al. Hybrid ZTE/dixon MR-based attenuation correction for quantitative uptake estimation of pelvic lesions in PET/MRI. *Med Phys* (2017) 44:902–13. doi: 10.1002/mp.12122

23. Leynes AP, Yang J, Wiesinger F, Kaushik SS, Shanbhag DD, Seo Y, et al. Zero-echo-time and dixon deep pseudo-CT (ZeDD CT): Direct generation of pseudo-CT images for pelvic PET/MRI attenuation correction using deep convolutional neural networks with multiparametric MRI. *J Nucl Med* (2018) 59:852–8. doi: 10.2967/jnumed.117.198051

24. Qian P, Zheng J, Zheng Q, Liu Y, Wang T, Al Helo R, et al. Transforming UTE-mDixon MR abdomenpelvis images into CT by jointly leveraging prior knowledge and partial supervision. *IEEE/ACM Trans Comput Biol Bioinform* (2021) 18:70–82. doi: 10.1109/TCBB.2020.2979841

25. Bradshaw TJ, Zhao G, Jang H, Liu F, McMillan AB. Feasibility of deep learning–based PET/MR attenuation correction in the pelvis using only diagnostic MR images. *Tomography* (2018) 4:138–47. doi: 10.18383/j.tom.2018.00016

26. Mostafapour S, Gholamiankhah F, Dadgar H, Arabi H, Zaidi H. Feasibility of deep learning-guided attenuation and scatter correction of whole-body 68Ga-PSMA PET studies in the image domain. *Clin Nucl Med* (2021) 46:609–15. doi: 10.1097/RLU.0000000000003585

27. Qian P, Chen Y, Kuo J-W, Zhang Y-D, Jiang Y, Zhao K, et al. mDixon-based synthetic CT generation for PET attenuation correction on abdomen and pelvis jointly using transfer fuzzy clustering and active learning-based classification. *IEEE Trans Med Imaging* (2020) 39:819–32. doi: 10.1109/TMI.2019.2935916

28. Klein S, Staring M, Murphy K, Viergever MA, Pluim JPW. elastix: A toolbox for intensity-based medical image registration. *IEEE Trans Med Imaging* (2010) 29:196–205. doi: 10.1109/TMI.2009.2035616

29. Shamonin DP, Bron EE, Lelieveldt BPF, Smits M, Klein S, Staring M. Fast parallel image registration on CPU and GPU for diagnostic classification of alzheimer's disease. *Front Neuroinform* (2014) 7:50. doi: 10.3389/fninf.2013.00050

30. Heußer T, Mann P, Rank CM, Schäfer M, Dimitrakopoulou-Strauss A, Schlemmer HP, et al. Investigation of the halo-artifact in 68Ga-PSMA-11-PET/MRI. *PLOS. ONE* (2017) 12:e0183329. doi: 10.1371/journal.pone.0183329

31. Ollinger JM. Model-based scatter correction for fully 3d PET. *Phys Med Biol* (1996) 41:153–76. doi: 10.1088/0031-9155/41/1/012

32. Johnson J, Alahi A, Fei-Fei L. Perceptual losses for real-time style transfer and super-resolution. In: Leibe B, Matas J, Sebe N, Welling M, editors. *Computer vision – ECCV 2016*, vol. 9906. Cham, Switzerland: Springer International Publishing (2016). p. 694–711. doi: 10.1007/978-3-319-46475-643

33. He K, Zhang X, Ren S, Sun J. Deep residual learning for image recognition. *Proc IEEE Conf Comput Vision Pattern Recognition (CVPR)* (2016), 770–8. doi: 10.1109/CVPR.2016.90

34. Iqbal H. *Harisiqbal88/plotneuralnet v1.0.0.* (2018). doi: 10.5281/zenodo.2526396

35. Wang TC, Liu M-Y, Zhu J-Y, Tao A, Kautz J, Catanzaro B. High-resolution image synthesis and semantic manipulation with conditional gans. *Proc IEEE Conf Comput Vision Pattern Recognition (CVPR)* (2018), 8798–807. doi: 10.1109/CVPR.2018.00917

36. Kingma DP, Ba J. Adam: A method for stochastic optimization. *arXiv preprint arXiv:1412.6980* (2014).

37. Benjamini Y, Hochberg Y. Controlling the false discovery rate: A practical and powerful approach to multiple testing. *J R Stat Soc Ser B Stat Methodol* (1995) 57:289–300. doi: 10.1111/j.2517-6161.1995.tb02031.x

38. Shiri I, Arabi H, Geramifar P, Hajianfar G, Ghafarian P, Rahmim A, et al. Deep-JASC: joint attenuation and scatter correction in whole-body 18f-FDG PET using a deep residual network. *Eur J Nucl Med Mol Imaging* (2020) 47:2533–48. doi: 10.1007/s00259-020-04852-5

39. Dong X, Lei Y, Wang T, Higgins K, Liu T, Curran WJ, et al. Deep learning-based attenuation correction in the absence of structural information for whole-body positron emission tomography imaging. *Phys Med Biol* (2020) 65:055011. doi: 10.1088/1361-6560/ab652c

40. Kamnitsas K, Ledig C, Newcombe VFJ, Simpson JP, Kane AD, Menon DK, et al. Efficient multi-scale 3d CNN with fully connected CRF for accurate brain lesion segmentation. *Med Image Anal* (2017) 36:61–78. doi: 10.1016/j.media.2016.10.004

41. Dong X, Wang T, Lei Y, Higgins K, Liu T, Curran WJ, et al. Synthetic CT generation from nonattenuation corrected PET images for whole-body PET imaging. *Phys Med Biol* (2019) 64:215016. doi: 10.1088/1361-6560/ab4eb7

42. Lee J. A review of deep-learning-based approaches for attenuation correction in positron emission tomography. *IEEE Trans radiat. plasma Med Sci* (2021) 5(2):160–184. doi: 10.1109/TRPMS.2020.3009269

43. Lee MS, Cho JY, Kim SY, Cheon GJ, Moon MH, et al. Diagnostic value of integrated PET/MRI for detection and localization of prostate cancer: Comparative study of multiparametric MRI and PET/CT. *J Magn Reson* (2017) 45:597–609. doi: 10.1002/jmri.25384

44. Akbarzadeh A, Gutierrez D, Baskin A, Ay MR, Ahmadian A, Riahi Alam N, et al. Evaluation of whole-body MR to CT deformable image registration. *J Appl Clin Med Phys* (2013) 14:238–53. doi: 10.1120/jacmp.v14i4.4163

45. Adams MC, Turkington TG, Wilson JM, Wong TZ. A systematic review of the factors affecting accuracy of SUV measurements. *AJR Am J Roentgenol* (2010) 195:310–20. doi: 10.2214/AJR.10.4923

46. Brendle C, Kupferschläger J, Nikolaou K, la Fougère C, Gatidis S, Pfannenberg C. Is?the standard uptake value (SUV) appropriate for quantification in clinical PET imaging? - variability induced by different SUV measurements and varying reconstruction methods. *Eur J Radiol* (2015) 84:158–62. doi: 10.1016/j.ejrad.2014.10.018

frontiers | Frontiers in Oncology

TYPE Original Research
PUBLISHED 11 September 2023
DOI 10.3389/fonc.2023.1193370

OPEN ACCESS

EDITED BY
Fabio Grizzi,
Humanitas Research Hospital, Italy

REVIEWED BY
Manuela Andrea Hoffmann,
Federal Ministry of Defence, Germany
Shady Saikali,
AdventHealth, United States

*CORRESPONDENCE
Zhiyi Lin
9129219@qq.com
Wenxin Chen
wenxinchzt@aliyun.com

†These authors have contributed equally to this work

RECEIVED 03 April 2023
ACCEPTED 31 July 2023
PUBLISHED 11 September 2023

CITATION
Zhang Y, Shi Y, Ye L, Li T, Wei Y, Lin Z and Chen W (2023) Improving diagnostic efficacy of primary prostate cancer with combined ^{99m}Tc-PSMA SPECT/CT and multiparametric-MRI and quantitative parameters. *Front. Oncol.* 13:1193370. doi: 10.3389/fonc.2023.1193370

Improving diagnostic efficacy of primary prostate cancer with combined ^{99m}Tc-PSMA SPECT/CT and multiparametric-MRI and quantitative parameters

Yu Zhang[1,2,3†], Yuanying Shi[1†], Liefu Ye[4,5], Tao Li[4,5], Yongbao Wei[4,5], Zhiyi Lin[1,2,3*] and Wenxin Chen[1,2,3*]

[1]Department of Nuclear Medicine, Shengli Clinical Medical College of Fujian Medical University, Fuzhou, China, [2]Department of Nuclear Medicine, Fujian Provincial Hospital, Fuzhou, China, [3]Department of Nuclear Medicine, Fujian Research Institute of Nuclear Medicine, Fuzhou, China, [4]Department of Urology, Shengli Clinical Medical College of Fujian Medical University, Fuzhou, China, [5]Department of Urology, Fujian Provincial Hospital, Fuzhou, China

Purpose: This prospective study aimed to evaluate the difference between ^{99m}Tc-PSMA single-photon emission computed tomography (SPECT)/CT and multiparametric magnetic resonance imaging (mpMRI) in the detection of primary prostate cancer (PCa).

Materials and methods: Fifty-six men with suspected PCa between October 2019 and November 2022 were prospectively enrolled in this study. The median age of the patients was 70 years (range, 29-87 years). Patients were divided into high-(Gleason score>7, n=31), medium- (Gleason score=7, n=6) and low-risk groups (Gleason score < 7, n=6). All patients underwent ^{99m}Tc-PSMA SPECT/CT and mpMRI at an average interval of 3 days (range, 1-7 days). The maximum standardized uptake value (SUV_{max}), the minimum apparent diffusion coefficient (ADC_{min}), and their ratio (SUV_{max}/ADC_{min}) were used as imaging parameters to distinguish benign from malignant prostatic lesions.

Results: Of the 56 patients, 12 were pathologically diagnosed with a benign disease, and 44 were diagnosed with PCa. ^{99m}Tc-PSMA SPECT/CT and mpMRI showed no significant difference in the detection of primary PCa (kappa =0.401, *P*=0.002), with sensitivities of 97.7% (43/44) and 90.9% (40/44), specificities of 75.0% (9/12) and 75.0% (9/12), and AUC of 97.4% and 95.1%, respectively. The AUC of SUV_{max}/ADC_{min} was better than those of SUV_{max} or ADC_{min} alone. When SUV_{max}/ADC_{min} in the prostatic lesion was $>7.0\times10^3$, the lesion was more likely to be malignant. When SUV_{max}/ADC_{min} in the prostatic lesion is $>27.0\times10^3$, the PCa patient may have lymph node and bone metastases. SUV_{max} was positively correlated with the Gleason score (*r*=0.61, P=0.008), whereas ADC_{min} was negatively correlated with the Gleason score (*r*=-0.35, *P*=0.023). SUV_{max}/ADC_{min} was positively correlated with the Gleason score (*r*=0.59, *P*=0.023).

SUV_{max}/ADC_{min} was the main predictor of the high-risk group, with an optimal cut-off value of 15.0×10^3.

Conclusions: The combination of ^{99m}Tc-PSMA SPECT/CT and mpMRI can improve the diagnostic efficacy for PCa compared with either modality alone; SUV_{max}/ADC_{min} is a valuable differential diagnostic imaging parameter.

KEYWORDS

prostate-specific membrane antigen, magnetic resonance imaging, prostate cancer, single-photon emission computed tomography, technetium radioisotopes

Introduction

Prostate cancer (PCa) is one of the most common malignancies in men (1). Early diagnosis and accurate grading of PCa are of great significance for formulating therapeutic strategies and improving prognosis (2). Multiparametric magnetic resonance imaging (mpMRI) is a well-established tool for the appraisal of primary PCa and has shown high affectability (3, 4). Prostate biopsy remains the gold standard for PCa diagnosis. In addition to providing evidence for diagnosis, the pathological results can also provide the classification and grouping information of PCa. Ultrasound-guided puncture biopsy still has a high false-negative rate of 20-25%, and there are complications such as bleeding, infection, pain, and urinary retention (3). Therefore, it is important to explore a noninvasive preoperative diagnosis method for PCa to improve puncture accuracy and avoid unnecessary biopsy. Current strategies used to locally stage PCa and recognize the exact location of disease foci depend on the results of systematic or targeted biopsies and mpMRI. However, mpMRI has limited specificity (4–6). Although targeted mpMRI biopsies have significantly improved the identification of clinical PCa, there is still over a 30% chance of missing primary PCa in men (7). Therefore, additional complementary methods are required to better characterize and identify primary PCa.

Prostate-specific membrane antigen (PSMA) is a type II transmembrane protein that is overexpressed on the surface of 90% of PCa cells. Its expression positively correlates with the degree of malignancy (8). Published studies have demonstrated the superiority of ^{68}Ga/^{18}F-PSMA PET/CT or PET/MR in the detection of primary PCa. However, PET/CT or PET/MR is not widely available in less developed countries, and far fewer institutions have PET/CT or PET/MR devices than SPECT/CT devices. The limited production of ^{68}Ga from ^{68}Ge-^{68}Ga generator and ^{18}F from cyclotron, combined with the relatively short half-life of ^{68}Ga (67.71 min) and ^{18}F (109.8min), results in the need for multiple rounds of production per day to maintain patient use, limiting the number of patient tests per day. Although clinical SPECT system sensitivity and resolution are not as good as those of PET, the recent combination of SPECT and CT and the ability to quantify tissue radioactivity concentration in absolute units have resulted in a significant improvement in imaging quality. ^{99m}Tc, available from ^{99}Mo-^{99m}Tc generators, is a nuclide routinely used in SPECT imaging, has good physical properties (half-life is 361.2 min), and is inexpensive and widely available. Thus, ^{99m}Tc-based PSMA ligands are a cost-effective clinical alternative. Our previous study showed that ^{99m}Tc-labelled PSMA molecular probe (^{99m}Tc-HYNIC-Glu-Urea-A, herein referred to as ^{99m}Tc-PSMA) single-photon emission computed tomography (SPECT)/CT can display bone metastases of PCa with high sensitivity and specificity (9), with only a small amount of radiation uptake in the intestinal tract and no significant radiation uptake in other major organs (10). However, to our knowledge, ^{99m}Tc-PSMA SPECT/CT has rarely been reported for the diagnosis of primary PCa. In recent years, with the development of imaging technology, mpMRI including functional sequences such as diffusion weighted imaging(DWI) had been widely used in the diagnosis and preoperative localization of PCa (5). The ADC_{min} from DWI reflects the degree of diffusion of water molecules in the tumor tissue. SUV_{max} represents PSMA expression associated with the biological characteristics of tumors. Our study aimed to evaluate the difference between ^{99m}Tc-PSMA SPECT/CT and mpMRI for the detection of primary PCa.

Materials and methods

Ethical approval

This study was approved by the ethics committee of Fujian Provincial Hospital (reference number, K2019-10-017) and conducted in compliance with the principles of the Declaration of Helsinki. Furthermore, informed consent was obtained from all participants and/or their legal guardians.

Sample size calculation

We conducted a prospective head-to-head observational study to analyze the diagnostic efficacy between ^{99m}Tc-PSMA SPECT/CT and mpMRI in treatment-naive PCa. In this study, the sensitivity and specificity of ^{99m}Tc-PSMA SPECT/CT and mpMRI in the diagnosis of PCa were assumed to be greater than 50% (H_0 = 50%). Referring to similar published literature on ^{68}Ga-

PSMA PET/CT and mpMRI (11), a sensitivity and specificity value of 80% was assumed. PASS 11 software (Power Analysis and Sample Size, NCSS, LLC) was used to estimate the required sample size. Assuming α=0.05 (unilateral), β=0.1, and a 1:1 ratio between the groups, the calculations indicated that at least 46 patients needed to be included in the study. Consequently, 56 individuals were enrolled in this study.

Patient selection

Fifty-six men were enrolled in this study between October 2019 and November 2022. The inclusion criteria were as follows (2): ① digital rectal examination touching the prostate nodules; ② transrectal ultrasound suspected PCa; ③ PSA>10 ng/mL or progressive PSA increase (12); ④ no treatment administered before the scan; and ⑤ complete medical records, control data, and clinical follow-up results. The exclusion criteria were as follows: ① the presence of severe syndromes that were difficult to manage; ② active or upcoming participation in other clinical drug trials; ③ lack of regular review or follow-up results; ④ a second primary tumor, and ⑤ inability to obtain relevant contrast imaging and clinical data. All eligible patients underwent ^{99m}Tc-PSMA SPECT/CT and mpMRI at an average interval of 3 days (1–7 days). None of the patients received antineoplastic therapy between the two scans. After both scans were completed, a transrectal needle prostate biopsy was performed. The patient characteristics are presented in Table 1.

TABLE 1 Patient characteristics.

Patient characteristic	Value
No. of patients	56
Age (years), median (IQR)	70 (29-87)
serum PSA(ng/mL), median (IQR)	14.8 (5.1-710.0)
PI-RADS score, n (%)	
1-2	8 (14.3%)
3	5 (8.9%)
4-5	43 (76.8%)
Pathological features of the specimen	
benign nodules, n (%)	12 (21.4%)
adenocarcinoma, n (%)	43 (76.8%)
neuroendocrine carcinoma, n (%)	1 (1.8%)
Gleason score	
<7 (low risk), n (%)	6 (14.0%)
=7 (intermediate risk), n (%)	6 (14.0%)
>7 (high risk), n (%)	31 (72.0%)
IUSP GG	
1-3 (low-grade), n (%)	12 (28.0%)
≥4 (high-grade), n (%)	31 (72.0%)
Prostatectomy	
Yes, n (%)	23 (41.1%)
No, n (%)	33 (58.9%)

IQR, interquartile range; IUSP GG, International Society of Urological Pathology Grade Group; PSA, prostate specific antigen; PI-RADS, prostate imaging reporting and data system.

^{99m}Tc-PSMA SPECT/CT acquisition protocol

The PSMA lyophilized kit (HYNIC-PSMA) (patent number, Zl202010878750.4) was provided by the Shanghai Engineering Research Centre of Molecular Imaging Probes. The synthesis procedure has been reported previously (9). The radiochemical purity was>95%. All patients were injected intravenously with a dose of 0.74 GBq (20 mCi) ^{99m}Tc-PSMA. Whole-body planar imaging and regional (neck-pelvic) SPECT/CT were performed 2 h after injection using a Discovery NM/CT 670Pro (GE, USA) with low-energy, high-resolution collimators. The image acquisition protocol was as follows: planar imaging: peak energy 140 keV (^{99m}Tc) and scan velocity 15 cm/min in a 256×1025 matrix. Regional SPECT/CT: camera matrix size 128×128, zoom 1.0, rotation 360°, and 30 s/frame for 60 frames. Low-dose CT (130 keV; 60 mA) was used.

mpMRI acquisition protocol

mpMRI was performed with a high-field system (Magnetom Prisma 3.0T, Siemens, The Germany) using a standardized protocol with pelvic external phased-array coils. The sequences included: transverse T1-weighted imaging (T1WI) (repetition time [TR] =500ms, echo time [TE]=12ms, field-of-view [FOV]=20 cm×20 cm, matrix=320×256); T2-weighted imaging (T2WI) (TR=5800ms, TE=106ms, FOV=20 cm×20 cm, matrix=320×256); fat-suppression spectral presaturation attenuated inversion recovery-T2WI (TR=5800ms, TE=97ms, FOV=20 cm×20 cm, matrix=320×240), and diffusion weighted imaging (DWI) (TR=5100ms, TE=64ms, FOV=20 cm×20 cm, matrix=114×114, b=50s/mm^2, 600 s/mm^2, 1500 s/mm^2, 3000 s/mm^2). The section thickness of each sequence was 3.5 mm.

Image analysis

^{99m}Tc-PSMA SPECT/CT and mpMRI images were independently read by two nuclear medicine physicians and two radiologists, respectively. The readers were blinded to the mpMRI and ^{99m}Tc-PSMA SPECT/CT clinical reports and other readers' findings. ^{99m}Tc-PSMA SPECT/CT and mpMRI were performed on a workstation (Xeleris, General Electric, Waukesha, WI) and (syngo.via, Siemens Healthineers, respectively). The locations of lesions on mpMRI and ^{99m}Tc-PSMA SPECT/CT images were compared, and lesions with the same locations on the two scans

were selected as the primary lesion to extract parameters for analysis.

Diagnostic criteria for primary PCa

On mpMRI, combined with the reconstructed apparent diffusion coefficient (ADC) images, a lesion with a prostate imaging reporting and data system (PI-RADS) score > 3 was considered a positive lesion (PCa) (13). The lesions' region of interest (ROI) was delineated, and the lowest ADC (ADC_{min}) was calculated. On SPECT/CT, areas with higher imaging agent uptake than normal prostate tissue after excluding physiological uptake were considered positive lesions (PCa). For imaging-based quantification analysis, Q.Metrix software (Q.Metrix GE Healthcare) was used (14). Acquisition information, including camera sensitivity, activities in full and empty syringes, administration time, and scan time, was input into the system. The volume of interest (VOI) was delineated, and the NM was 0.4. The calculated maximum standardized uptake value (SUV) voxel volume was 3.2×10^{-3} mL. VOI-related quantitative parameters were automatically generated, and SUV_{max} was used for quantitative analysis.

Diagnostic criteria for PCa metastases

On mpMRI, ①lymph node metastases: round, short-axis diameter>8 mm, uneven signals in lymph nodes on T2WI, irregular boundaries, and evident enhancement on dynamic contrast-enhanced (DCE) (15); ② bone metastases: low signal intensity on T1WI and T2WI, limited diffusion on DWI, and early enhancement after contrast agent injection on DEC (16, 17). On SPECT/CT, ①lymph node and bone metastases: uptake than normal tissue(lesion SUV_{max}≥liver SUV_{max}) after excluding lacrimal glands, salivary glands, kidneys, bladder and intestines physiological uptake. The SUV_{max} of all focal SPECT-positive sites was determined based on the ROI basis (17). In the quantification analysis, the size of each SPECT-positive bone and lymph node correlated with the SUV_{max}.

Validation of findings

Prostate needle biopsies were performed in all participants. We used a protocol for transperineal MRI/PSMA-ultrasound fusion targeted and systematic biopsy. In brief, the image-guide (cognitive guidance, MRI/US and PSMA/US) technique was used. Targeted and systematic biopsies were performed in the same session. The number of biopsy cores was as follows: 3-4 cores for targeted biopsy and 10-12 cores for systematic biopsy. If the biopsy results were positive, patients with surgical indications underwent radical prostatectomy, and the pathological results were based on the gross specimen. For patients without surgical indications, pathological results were based on biopsy results. If the needle biopsy results are negative and the clinical symptoms are highly indicative of PCa, the patient's serum PSA value and imaging (mpMRI, ^{99m}Tc-PSMA SPECT/CT) should be followed up for 3-6 months. If the disease does not progress, PCa could be excluded. If the disease progresses, an additional needle biopsy should be performed (12). Not all bone and lymph node lesions showed positive pathological results. Thus, the validated method reported in previous studies was used (9, 17). All patients were followed up for at least 6 months (or until death). Serum PSA levels were reviewed every 3 months for all patients. The subsequent therapeutic schedule options depended on the patient's condition, including radical prostatectomy, local radiation therapy, and chemotherapy. Future imaging modalities were selected according to their respective clinical needs and were not bound by a specific protocol. Patients who met at least one of the following conditions were metastases: ① Response to therapy (hormone therapy and radiation) and subsequent serum PSA decline were confirmed by follow-up examination (MRI, CT, PET, etc.); ② two or more imaging examinations recommended metastases, and ③ PSA≥100 ng/mL, suggesting distant metastases (18).

Statistical analysis

Data analysis was performed using SPSS 19.0 software (statistical product and service solutions, Chicago, Illinois). McNemar's test was used to compare the cancer detection concordance rates between ^{99m}Tc-PSMA SPECT/CT and mpMRI. The Mann-Whitney *U* test was used to compare the differences in quantitative diagnostic parameters among the different groups. Receiver operating characteristic (ROC) analysis was performed to evaluate the sensitivity, specificity, area under the ROC curve (AUC), and a cut-off value of each parameter. The Kruskal-Wallis test was used to compare the differences in quantitative diagnostic parameters among different tumor size groups. The correlation between the Gleason Score and SUV_{max}, ADC_{min}, and SUV_{max}/ADC_{min} was evaluated using Spearman correlation analysis. Logistic regression analysis was used to calculate predictors of the Gleason score. $P<0.05$ was considered statistically significant.

Results

Overall results

Among the 56 participants, 44 (78.5%) were diagnosed with PCa, and 12 (21.5%) with prostate hyperplasia (BPH). A flowchart illustrating the participant inclusion procedure is shown in Figure 1. Among the 44 patients with PCa, one (2%) had neuroendocrine carcinoma, and 43 (98%) had adenocarcinoma. The surgical indications were judged by the urological surgeon according to the clinical status of the patient (2).The 23 patients with PCa diagnosed by puncture underwent robot-assisted laparoscopic radical prostatectomy (RP); postoperative pathology results were consistent with those of puncture in 11 (11/23,47.8%) patients. 12 (12/23,52.2%) patients with PCa experienced pathological upgrading. The Gleason score of patients who underwent surgery

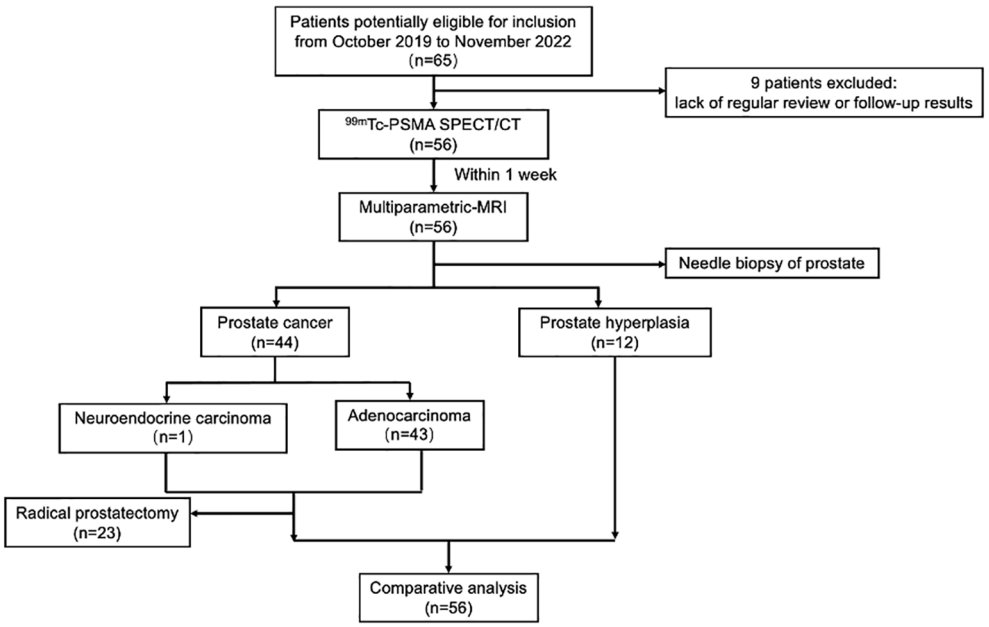

FIGURE 1
Flowchart of participant selection in the study. ^{99m}Tc-PSMA SPECT/CT, ^{99m}Tc-labelled prostate-specific membrane antigen molecular probe single photon emission computed tomography; MRI, magnetic resonance imaging.

was based on the surgical specimen, and the Gleason score of patients who did not undergo surgery was based on the puncture specimen. Among 44 patients with PCa, 23 (52.3%) had metastases.

Sensitivity and specificity analyses

For all 56 patients, the sensitivity of ^{99m}Tc-PSMA SPECT/CT and mpMRI in detecting primary PCa was 97.7% (43/44) and 90.9% (40/44), respectively; the difference was not statistically significant (χ^2 = 0.102, *P*=0.749). Their specificity was 75.0% (9/12) and 75.0% (9/12), respectively, with no statistically significant difference (χ^2 = 1.333, *P*=0.248) (Table 2). ROC curve analysis revealed an accuracy, as measured by AUC, of 97.4% (*95% CI.* 93.7%-100.0%) for ^{99m}Tc-PSMA, 95.1% (95% CI. 88.8%-100.0%) for mpMRI, and 98.2% (*95% CI.* 95.2%-100.0%) for ^{99m}Tc-PSMA +mpMRI (Figure 2).

Differences in quantitative parameters among different groups

The Mann-Whitney *U* test was used to compare differences in quantitative diagnostic parameters among the different groups (Table 2). The SUV_{max}/ADC_{min} of the PCa group was significantly higher than that of the BPH group, and the SUV_{max}/ADC_{min} of the subgroup with metastases was higher than that of the subgroup without metastasis (Table 2). In ^{99m}Tc-PSMA SPECT/CT combined with mpMRI, when the cut-off value for SUV_{max}/ADC_{min} was set at 7.0×10^3, the sensitivity and specificity of SUV_{max}/ADC_{min} in PCa were 93.2% (95%*CI.*85.7%-100.0%) and 100.0% (95% *CI.*100.0%-100.0%), respectively, with a Youden index of 0.932 and an AUC of 0.982 (95% CI. 95.2%-100.0%) (Figure 3). When the cut-off value for SUV_{max}/ADC_{min} was set at 27.0×10^3, the sensitivity and specificity of SUV_{max}/ADC_{min} in PCa with metastases was 76.2% (95%*CI.*58.0%-99.4%) and 73.9% (95%

TABLE 2 ^{99m}Tc-PSMA SPECT/CT and mpMRI in the diagnosis of primary prostate cancer.

Pathological diagnosis	^{99m}Tc-PSMA		mpMRI	
	Positive	Negative	Positive	Negative
Positive (n=44)	43	1	40	4
Negative (n=12)	3	9	3	9
Total	46	10	43	13
PPV	0.935 (95% CI. 0.863-1.000)		0.930 (95% CI. 0.854-0.100)	
NPV	0.900 (95% CI. 0.714-1.000)		0.692 (95% CI. 0.414-0.943)	

CI, confidence interval; PPV, positive predictive value; NPV, negative predictive value; ^{99m}Tc-PSMA SPECT/CT, ^{99m}Tc-labelled prostate-specific membrane antigen molecular probe single photon emission computed tomography; mpMRI, multiparametric magnetic resonance imaging.

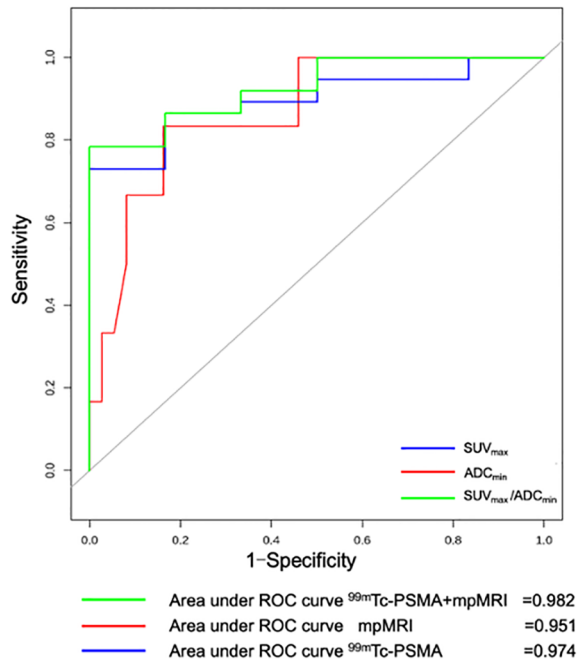

FIGURE 2
Receiver operating curve (ROC) for ^{99m}Tc-PSMA SPECT/CT, mpMRI, and ^{99m}Tc-PSMA SPECT/CT+ mpMRI for detection of primary prostate cancer (n=56). ^{99m}Tc-PSMA SPECT/CT, ^{99m}Tc-labelled prostate-specific membrane antigen molecular probe single photon emission computed tomography; mpMRI, multiparametric magnetic resonance imaging; SUV_{max}, maximum standardized uptake value; ADC_{min}, the minimum apparent diffusion coefficient.

CI.56.0%-91.9%), respectively, with a Youden index=0.501 and AUC=0.760 (*95% CI*. 61.0%-91.0%) (Figure 3A).

Difference between tumor size and quantitative parameters

The 44 prostatic lesions detected were grouped according to their maximum tumor diameter: G1 (7/44, maximum diameter < 1.0 cm), G2 (23/44, maximum diameter: 1.0 cm-3.0 cm), and G3 (14/44, maximum diameter > 3.0 cm). The Kruska–Wallis test was used to compare the differences in quantitative diagnostic parameters among different tumor size groups. There were differences in SUV_{max}/ADC_{min} among the tumor size groups; the larger the tumor size, the larger the SUV_{max}/ADC_{min} value (Figure 4).

Relationship between Gleason score and quantitative parameters

Gleason scoring is unsuitable for treating neuroendocrine PCa (19). Therefore, 43 patients with PCa were enrolled in this cohort study. Spearman correlation analysis was used, and the results revealed that ADC_{min} showed a weak negative correlation with Gleason score (r=-0.35, P=0.023), whereas SUV_{max} (r=0.61, P=0.008) and SUV_{max}/ADC_{min} (r=0.59, P=0.023) showed a moderate positive correlation with Gleason score (Figure 5). Based on the Gleason score, the patients were divided into high-

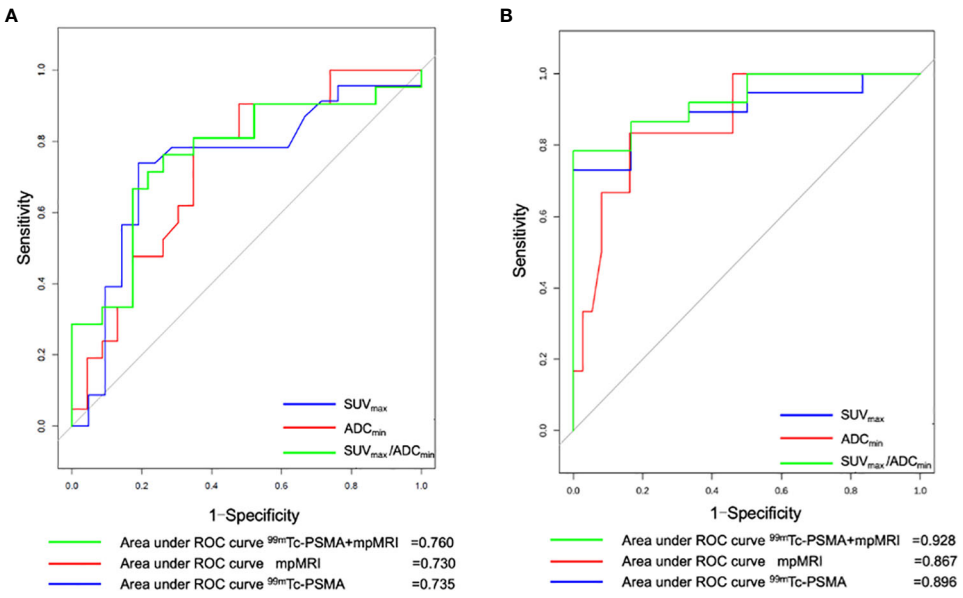

FIGURE 3
Receiver operating curve (ROC) for **(A)**^{99m}Tc-PSMA SPECT/CT, mpMRI, and ^{99m}Tc-PSMA SPECT/CT+ mpMRI for detecting prostate cancer with metastases (n=44) and for **(B)** ^{99m}Tc-PSMA SPECT/CT, mpMRI and ^{99m}Tc-PSMA SPECT/CT+ mpMRI for detection of prostate cancer with Gleason score ≥7 (n=43). ^{99m}Tc-PSMA SPECT/CT, ^{99m}Tc-labelled prostate-specific membrane antigen molecular probe single photon emission computed tomography; mpMRI, multiparametric magnetic resonance imaging; SUV_{max}, maximum standardized uptake value; ADC_{min}, the minimum apparent diffusion coefficient.

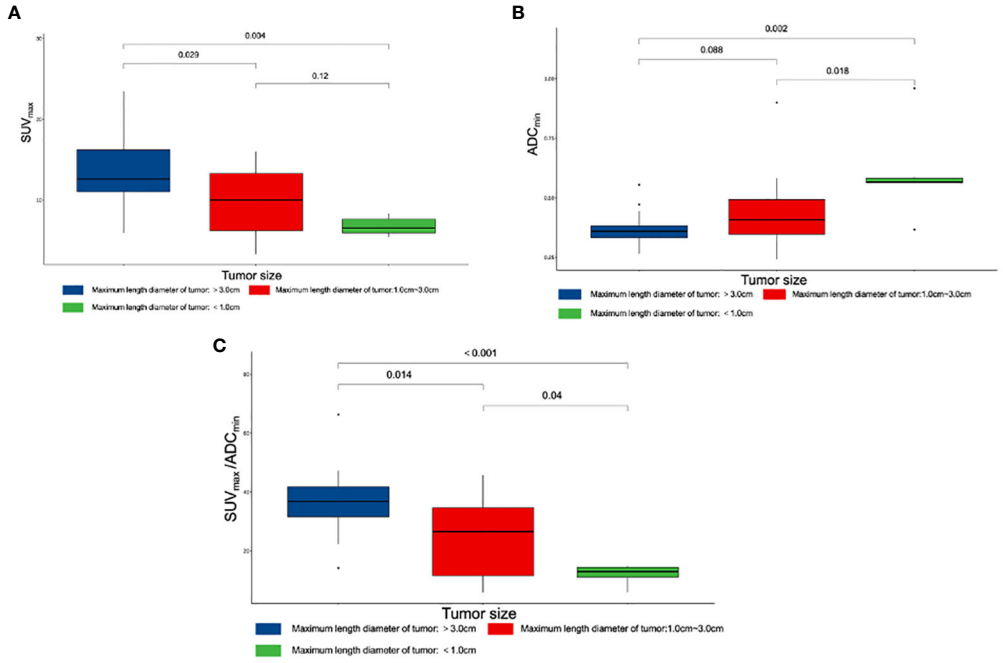

FIGURE 4
Box plot of different parameters and tumor size. **(A)** Differences among SUV_{max} and tumor size. **(B)** Differences among ADC_{min} and tumor size. **(C)** Differences among SUV_{max}/ADC_{min} and tumor size. SUV_{max}, maximum standardized uptake value; ADC_{min}, the minimum apparent diffusion coefficient.

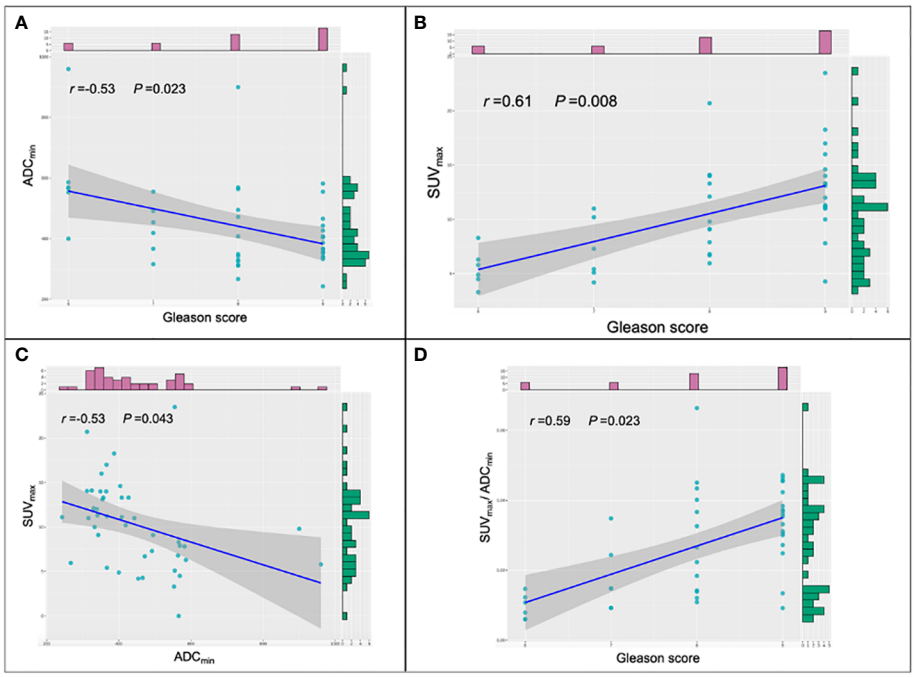

FIGURE 5
Scatter plots of the different parameters and Gleason score. **(A)** Correlations among ADC_{min} and Gleason score in prostate cancer (PCa) lesions. **(B)** Correlations among SUV_{max} and Gleason score in PCa lesions. **(C)** Correlations among SUV_{max} and ADC_{min} in PCa lesions. **(D)** Correlations among SUV_{max}/ADC_{min} and Gleason score in PCa lesions. SUV_{max}, maximum standardized uptake value; ADC_{min}, the minimum apparent diffusion coefficient.

(Gleason score>7, n=31), medium- (Gleason score=7a, n=4;Gleason score=7b, n=2) and low-risk groups (Gleason score < 7, n=6). According to the Mann-Whitney *U* test, there were statistical differences in SUV_{max}, $ADC_{min,}$ and SUV_{max}/ADC_{min} between the high-, medium- and low-risk groups (all $P < 0.05$) (Table 3). With the presence of a high-risk group (yes=1, no=0) as the dependent variable, and age, serum PSA level, and SUV_{max}/ADC_{min} as the independent variables, logistic regression analysis showed that SUV_{max}/ADC_{min} was independently correlated with the presence of a high-risk group; for every 1×10^3 increase in SUV_{max}/ADC_{min}, the detection rate of the high-risk group increased by 55.7% (*OR*=1.557, *P*=0.042). When the cut-off value for SUV_{max}/ADC_{min} was set at 15.0×10^3, the sensitivity and specificity of SUV_{max}/ADC_{min} in the high-risk PCa group were 78.4% (95%*CI*.65.1%-91.6%) and 100.0% (95%*CI*.100.0%-100.0%), respectively, with a Youden index of 0.784 and AUC of 0.928 (*95% CI.* 84.0%-100.0%) (Figure 3B) (Table 4).

Discussion

The labeling method for ^{99m}Tc-HYNIC-Glu-Urea-A(^{99m}Tc-PSMA) is simple and has high radiochemical purity (10). Previous studies have demonstrated the high diagnostic efficacy of ^{99m}Tc-PSMA SPECT/CT in detecting recurrent biochemical lesions after radical prostatectomy and bone metastases of PCa (9, 20). With the introduction of imaging technology, the diagnosis and initial management of localized PCa are increasingly dependent on imaging findings. ^{99m}Tc-PSMA SPECT/CT is predominantly used in the primary PCa staging of regional and distant diseases. However, little is known about the value of ^{99m}Tc-PSMA SPECT/CT for the primary detection of lesions within the prostate. To our knowledge, this is the first comparison between ^{99m}Tc-PSMA SPECT/CT and mpMRI for primary PCa lesions.

In our cohort study, ^{99m}Tc-PSMA SPECT/CT and mpMRI had limited specificity for detecting primary PCa lesions. SUV_{max} and ADC_{min} are important quantitative parameters in SPECT/CT and mpMRI, respectively. Typical PCa foci showed localized high-uptake foci on ^{99m}Tc-PSMA SPECT/CT and low-signal foci on mpMRI ADC maps (Figure 6). Previous studies on PCa detection by PET have shown that there may be a certain degree of correlation between mpMRI and PET parameters in the same PCa lesion; that is, SUV_{max} and ADC_{min} were negatively correlated (21, 22). Therefore, it is essential to study whether combining these two imaging techniques can further improve the diagnostic efficacy of PCa. In our study, SUV_{max} was positively correlated with the Gleason score, while ADC_{min} was negatively correlated. Based on the above results, we combined the two parameters and used the

TABLE 3 Difference between the three diagnostic parameters among different groups.

Group (No. of patients)	^{99m}Tc-PSMA	mpMRI	^{99m}Tc-PSMA+ mpMRI
	SUV_{max}	ADC_{min}	$SUVmax/ADC_{min}$
Prostate hyperplasia (n=12)	0.00 (0.00-0.54) △	0.69 (0.57-0.81)×10^{-3}□	0.00 (0.00-6.51)×10^3▽
Prostate cancer (n=44)	10.60 (0.00-23.48)	0.41 (0.24-0.96)×10^{-3}	26.87 (0.00-663.50)×10^3
Gleason score<7(n=6)	4.90 (0.00-8.30) *	0.57 (0.40-0.96)×10^{-3}#	8.22 (0.00-14.66)×10^3★
Gleason score=7(n=6)	6.360 (4.20-11.00)	0.44 (0.32-0.56)×10^{-3}	14.80 (9.19-34.82)×10^3
Gleason score>7(n=31)	12.00 (4.28-23.48)	0.37 (0.24-0.90)×10^{-3}	33.14 (9.19-66.35)×10^3
Metastases (n=21)	12.00 (0.00-20.70) ▲	0.37 (0.24-0.57)×10^{-3}◆	35.40 (0.00-66.35)×10^3•
No metastasis (n=23)	7.80 (3.30-23.48)	0.49 (0.28-0.96)×10^{-3}	14.77 (5.96-43.38)×10^3

^{99m}Tc-PSMA SPECT/CT, ^{99m}Tc-labelled prostate-specific membrane antigen molecular probe single photon emission computed tomography; mpMRI, multiparametric magnetic resonance imaging.
Comparison of SUV_{max} between groups: △compared to the prostate cancer group, P=0.005; ▲compared with the no metastasis subgroup, P=0.007; * compared between the Gleason score subgroup, P < 0.001.
Comparison of ADC_{min} between groups: □compared to the prostate cancer group, P=0.002; ◆compared with the no metastasis subgroup, P=0.009; # compared between the Gleason score subgroup, P=0.012.
Comparison of SUV_{max}/ADC_{min} between groups: ▽compared to the prostate cancer group, P=0.003; •compared with the no metastasis subgroup, P=0.003; ★ compared between the Gleason score subgroup, P < 0.001.

TABLE 4 Multivariate logistic regression analysis of related factors of Gleason score.

Independent variable	OR value	95% CI for OR value		*P*-value
		Lower	Upper	
Age (years)	0.998	0.864	1.152	0.977
PSA (ng/mL)	1.028	0.977	1.081	0.288
SUV_{max}/ADC_{min} ($\times10^3$)	1.557	1.015	2.388	0.042

CI, confidence interval; OR, odds ratio; PSA, prostate specific antigen, SUV_{max}/ADC_{min}, maximum standardized uptake value/minimum apparent diffusion coefficient.

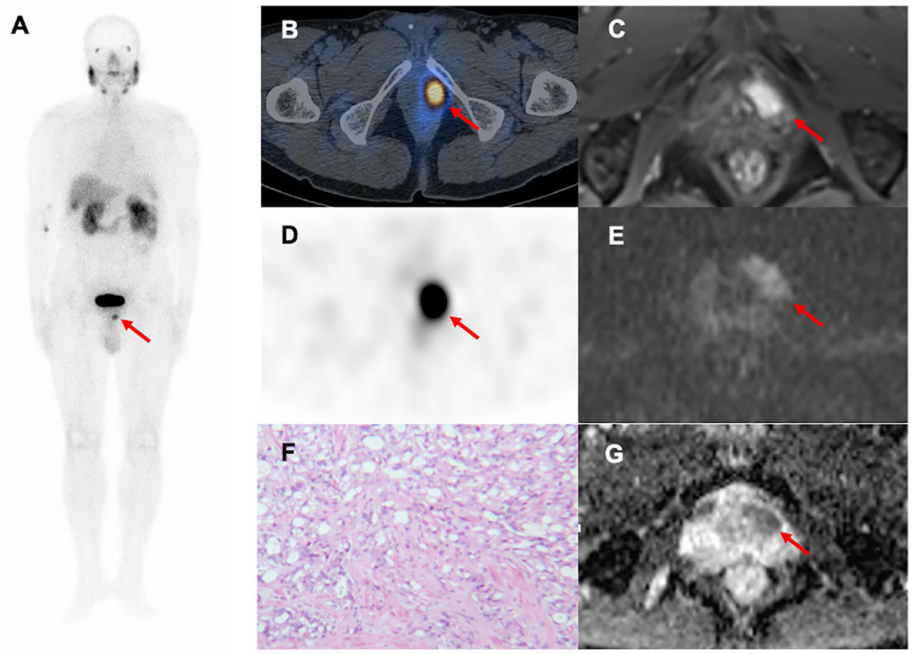

FIGURE 6
A 79-year-old man with progressive dysuria. The PSA level was 15.31 ng/mL at the time of ^{99m}Tc-PSMA SPECT/CT and mpMRI. Whole-body planar ^{99m}Tc-PSMA **(A)** and transverse SPECT/CT **(B, D)** showed foci of increased PSMA uptake in the left-anterior (red arrow, SUV_{max}=13.10, SUV_{max}/ADC_{min}=16.7×10^3). Hypointense signals were shown on apparent diffusion coefficient (ADC) **(G)**, red arrow), and hyperintense signals on diffusion-weighted imaging (DWI) **(E)**, red arrow) in the left transitional band of the prostatic apex. Dynamic contrast-enhanced (DCE) scanning was significantly enhanced **(C)**, red arrow). **(F)** Prostatic lesion was confirmed pathologically as prostate cancer (hematoxylin and eosin (HE) staining, 100×magnification; Gleason score: 4 + 5 = 9). ^{99m}Tc-PSMA SPECT/CT, ^{99m}Tc-labelled prostate-specific membrane antigen molecular probe single photon emission computed tomography; mpMRI, multiparametric magnetic resonance imaging; SUV_{max}, maximum standardized uptake value; ADC_{min}, the minimum apparent diffusion coefficient.

ratio to construct a new parameter (SUV_{max}/ADC_{min}) to obtain a more significant correlation with the Gleason score. The results of this study are consistent with our expectations. SUV_{max}/ADC_{min} was positively correlated with the Gleason score, which was also consistent with previous ^{68}Ga-PSMA PET/CT and mpMRI-related research results (23–25). In addition, Schmidkonz et al. confirmed that SUV_{max} in prostatic lesions could be used to predict primary PCa and lymph node and bone metastases. This may be the higher the uptake of PSMA in prostatic lesions, the higher the malignancy of the lesions, resulting in an increased risk of bone or lymph node metastasis (25). However, approximately 10% of patients with primary PCa have low PSMA expression (26). Some false-negative results were obtained in the clinical setting when SUV_{max} was used separately. The ratio SUV_{max}/ADC_{min} synthesizes the expression of PSMA and the degree of diffusion of water molecules (27). The present study found that the diagnostic efficacy of SUV_{max}/ADC_{min} was better than that of SUV_{max} or ADC_{min} alone. SUV_{max}/ADC_{min} may be used as a predictive parameter for PCa, helping to distinguish benign and malignant lesions of PCa and determine whether there were metastases. The result was also consistent with previous ^{18}F-choline PET/MRI related research (21). Zhang et al. conducted a retrospective ^{68}Ga-PSMA-11 PET/CT analysis of 42 patients with moderate-and high-risk PCa who underwent RP, and found that SUV_{max} in local prostate lesions was significantly higher in the group with pelvic lymph node metastases than in the group without lymph node metastases (28). In our study, the larger the prostatic lesion size, the higher the SUV_{max}/ADC_{min}. When SUV_{max}/ADC_{min} in the prostatic lesion was >7.0×10^3, the lesion was more likely to be malignant. When SUV_{max}/ADC_{min} in the prostatic lesion is >27.0×10^3, the patient with PCa may have lymph node and bone metastases. Hence, we postulated that SUV_{max} combined with ADC_{min} (SUV_{max}/ADC_{min}) might decrease bias and improve diagnostic accuracy.

The prognosis of PCa is closely related to the Gleason score grading system (29). The Gleason score is a critical indicator of the pathological results of prostate biopsy. In the previous study on PSMA, Kasperzyk et al. evaluated the expression of PSMA in PCa tissues by immunohistochemical staining, and found that Gleason score in the group with high PSMA expression was significantly higher than that in the group with low PSMA expression (30). Uprimny et al. retrospectively analyzed the ^{68}Ga-PSMA-11 PET/CT examination data of 90 patients with PCa confirmed by prostate biopsy, and found that SUV_{max} was significantly positively correlated with Gleason score (31).In our study, patients with PCa were divided into high-,medium- and low-risk groups with a Gleason score of 7 as the cut-off value. Our results showed that SUV_{max}/ADC_{min} was the main predictor of the high-risk group, with an optimal cut-off value of 15.0×10^3. This suggests that SUV_{max}/ADC_{min} ratio is a useful imaging parameter for evaluating tumor biology and prognosis, which may significantly impact the selection of therapeutic strategies.

This study had some limitations. Among the 44 patients diagnosed with PCa, 21 did not undergo RP, and gross specimens could not be obtained; only puncture biopsy could be used as the final pathological result. The pathological grading of puncture lesions may differ from actual grading. Furthermore, this was a single-center study with a small sample size, and the conclusions should be verified in a large-scale sample cohort. We did not evaluate the role of SUV_{max}/ADC_{min} in predicting prognosis at follow-up. However, this exploratory study is still valuable as the first clinical quantitative application of ^{99m}Tc-PSMA SPECT/CT combined with mpMRI in PCa lesions. In a future study, we aim to develop a novel analytical approach based on a radiomics quantitative model derived from ^{99m}Tc-PSMA SPECT/CT and mpMRI for noninvasive prediction of intraprostatic lesions in patients with PCa and prognosis.

Conclusion

In this prospective study, our results revealed that combined ^{99m}Tc-PSMA SPECT/CT and mpMRI had a higher diagnostic accuracy for detecting treatment-naive PCa than either modality alone. In addition, SUV_{max}/ADC_{min} is a promising molecular imaging parameter for diagnosing PCa and evaluating its biological behavior.

Data availability statement

The raw data supporting the conclusions of this article will be made available by the authors, without undue reservation.

Ethics statement

The studies involving humans were approved by the ethics committee of Fujian Provincial Hospital. The studies were conducted in accordance with the local legislation and institutional requirements. The participants provided their written informed consent to participate in this study. Written informed consent was obtained from the individual(s) for the publication of any potentially identifiable images or data included in this article.

Author contributions

Conceptualization: WC. Data curation: YZ. Formal analysis: YZ. Investigation: YZ. Methodology: YZ. Project administration: WC and ZL. Resources: WC, TL, YW, and LY. Software: YZ and YS. Supervision: WC and ZL. Validation: WC and ZL. Visualization: YZ and YS. Roles/Writing-original draft: YZ. Writing- review & editing: WC. All authors contributed to the article and approved the submitted version.

Funding

This work was supported by Startup Fund for scientific research, Fujian Medical University (2021QH1282) and Fujian Provincial Department of Finance (MCZ [2021] No. 0917).

Acknowledgments

The authors thank our Urology colleagues, who referred the patients to our SPECT centre, and technical support from Dr. Shaoli Song (from the department of nuclear medicine, Fudan University Shanghai Cancer Center, Shanghai, China).

Conflict of interest

The authors declare that the research was conducted in the absence of any commercial or financial relationships that could be construed as a potential conflict of interest.

Publisher's note

References

1. Miller KD, Nogueira L, Mariotto AB, Rowland JH, Yabroff KR, Alfano CM, et al. Cancer treatment and survivorship statistics, 2019. *CA Cancer J Clin* (2019) 69(5):363–85. doi: 10.3322/caac.21565

2. Schaeffer EM, Srinivas S, Adra N, An Y, Barocas D, Bitting R, et al. NCCN guidelines® Insights: Prostate cancer, version 1.2023. *J Natl Compr Canc Netw* (2022) 20(12):1288–98. doi: 10.6004/jnccn.2022.0063

3. Ahmed HU, El-Shater Bosaily A, Brown LC, Gabe R, Kaplan R, Parmar MK, et al. Diagnostic accuracy of multi-parametric MRI and TRUS biopsy in prostate cancer (PROMIS): a paired validating confirmatory study. *Lancet* (2017) 389(10071):815–22. doi: 10.1016/S0140-6736(16)32401-1

4. von Hardenberg J, Borkowetz A, Siegel F, Kornienko K, Westhoff N, Jordan TB, et al. GESRU academics prostate cancer group in cooperation with the working group of focal and microtherapy of the german society of urology (DGU). Potential candidates for focal therapy in prostate cancer in the era of magnetic resonance imaging-targeted biopsy: A large multicenter cohort study. *Eur Urol Focus* (2021) 7(5):1002–10. doi: 10.1016/j.euf.2020.09.015

5. Maier SE, Wallström J, Langkilde F, Johansson J, Kuczera S, Hugosson J, et al. Prostate cancer diffusion-weighted magnetic resonance imaging: Does the choice of diffusion-weighting level matter? *J Magn Reson Imaging* (2022) 55(3):842–53. doi: 10.1002/jmri.27895

6. Patel HD, Koehne EL, Shea SM, Fang AM, Gorbonos A, Quek ML, et al. Systematic versus Targeted Magnetic Resonance Imaging/Ultrasound Fusion Prostate Biopsy among Men with Visible Lesions. *J Urol* (2022) 207(1):108–17. doi: 10.1097/JU.0000000000002120

7. Johnson DC, Raman SS, Mirak SA, Kwan L, Bajgiran AM, Hsu W, et al. Detection of individual prostate cancer foci via multiparametric magnetic resonance imaging. *Eur Urol* (2019) 75(5):712–20. doi: 10.1016/j.eururo.2018.11.031

8. Krohn T, Verburg FA, Pufe T, Neuhuber W, Vogg A, Heinzel A, et al. [(68)Ga] PSMA-HBED uptake mimicking lymph node metastasis in coeliac ganglia: an important pitfall in clinical practice. *Eur J Nucl Med Mol Imaging* (2015) 42(2):210–4. doi: 10.1007/s00259-014-2915-3

9. Zhang Y, Lin Z, Li T, Wei Y, Yu M, Ye L, et al. Head-to-head comparison of 99mTc-PSMA and 99mTc-MDP SPECT/CT in diagnosing prostate cancer bone metastasis: a prospective, comparative imaging trial. *Sci Rep* (2022) 12(1):15993. doi: 10.1038/s41598-022-20280-x

10. Xu X, Zhang J, Hu S, He S, Bao X, Ma G, et al. 99mTc-labeling and evaluation of a HYNIC modified small-molecular inhibitor of prostate-specific membrane antigen. *Nucl Med Biol* (2017) 48:69–75. doi: 10.1016/j.nucmedbio.2017.01.010

11. Berger I, Annabattula C, Lewis J, Shetty DV, Kam J, Maclean F, et al. 68Ga-PSMA PET/CT vs. mpMRI for locoregional prostate cancer staging: correlation with final histopathology. *Prostate Cancer Prostatic Dis* (2018) 21(2):204–11. doi: 10.1038/s41391-018-0048-7

12. Schaeffer E, Srinivas S, Antonarakis ES, Armstrong AJ, Bekelman JE, Cheng H, et al. NCCN guidelines insights: Prostate cancer, version 1.2021. *J Natl Compr Canc Netw* (2021) 19(2):134–43. doi: 10.6004/jnccn.2021.0008

13. Weinreb JC, Barentsz JO, Choyke PL, Cornud F, Haider MA, Macura KJ, et al. PI-RADS prostate imaging - reporting and data system: 2015, version 2. *Eur Urol* (2016) 69(1):16–40. doi: 10.1016/j.eururo.2015.08.052

14. Dong F, Li L, Bian Y, Li G, Han X, Li M, et al. Standardized uptake value using thyroid quantitative SPECT/CT for the diagnosis and evaluation of graves' Disease: A prospective multicenter study. *BioMed Res Int* (2019) 2019:7589853. doi: 10.1155/2019/7589853

15. Schilham MGM, Zamecnik P, Privé BM, Israël B, Rijpkema M, Scheenen T, et al. Head-to-head comparison of 68Ga-prostate-specific membrane antigen PET/CT and ferumoxtran-10-enhanced MRI for the diagnosis of lymph node metastases in prostate cancer patients. *J Nucl Med* (2021) 62(9):1258–63. doi: 10.2967/jnumed.120.258541

16. Lecouvet FE, El Mouedden J, Collette L, Coche E, Danse E, Jamar F, et al. Can whole-body magnetic resonance imaging with diffusion-weighted imaging replace Tc-99m bone scanning and computed tomography for single-step detection of metastases in patients with high-risk prostate cancer? *Eur Urol* (2012) 62(1):68–75. doi: 10.1016/j.eururo.2012.02.020

17. Freitag MT, Radtke JP, Hadaschik BA, Kopp-Schneider A, Eder M, Kopka K, et al. Comparison of hybrid (68)Ga-PSMA PET/MRI and (68)Ga-PSMA PET/CT in the evaluation of lymph node and bone metastases of prostate cancer. *Eur J Nucl Med Mol Imaging* (2016) 43(1):70–83. doi: 10.1007/s00259-015-3206-3

18. Stattin K, Sandin F, Bratt O, Lambe M.. The Risk of Distant Metastases and Cancer Specific Survival in Men with Serum Prostate Specific Antigen Values above 100 ng/ml. *J Urol* (2015) 194(6):1594–600. doi: 10.1016/j.juro.2015.07.082

19. Swanson GP, Trevathan S, Hammonds KAP, Speights VO, Hermans MR. Gleason score evolution and the effect on prostate cancer outcomes. *Am J Clin Pathol* (2021) 155(5):711–7. doi: 10.1093/ajcp/aqaa130

20. Liu C, Zhu Y, Su H, Xu X, Zhang Y, Ye D, et al. Relationship between PSA kinetics and Tc-99m HYNIC PSMA SPECT/CT detection rates of biochemical recurrence in patients with prostate cancer after radical prostatectomy. *Prostate* (2018) 78(16):1215–21. doi: 10.1002/pros.23696

21. Wetter A, Lipponer C, Nensa F, Heusch P, Rübben H, Schlosser TW, et al. Quantitative evaluation of bone metastases from prostate cancer with simultaneous [18F] choline PET/MRI: combined SUV and ADC analysis. *Ann Nucl Med* (2014) 28(5):405–10. doi: 10.1007/s12149-014-0825-x

22. Rakheja R, Chandarana H, DeMello L, Jackson K, Geppert C, Faul D, et al. Correlation between standardized uptake value and apparent diffusion coefficient of neoplastic lesions evaluated with whole-body simultaneous hybrid PET/MRI. *AJR Am J Roentgenol* (2013) 201(5):1115–9. doi: 10.2214/AJR.13.11304

23. Ergül N, Yilmaz Güneş B, Yücetaş U, Toktaş MG, Çermik TF. 68Ga-PSMA-11 PET/CT in newly diagnosed prostate adenocarcinoma. *Clin Nucl Med* (2018) 43(12):e422–7. doi: 10.1097/RLU.0000000000002289

24. Jena A, Taneja R, Taneja S, Singh A, Kumar V, Agarwal A, et al. Improving diagnosis of primary prostate cancer with combined 68Ga-prostate-specific membrane antigen-HBED-CC simultaneous PET and multiparametric MRI and clinical parameters. *AJR Am J Roentgenol* (2018) 211(6):1246–53. doi: 10.2214/AJR.18.19585

25. Schmidkonz C, Cordes M, Beck M, Goetz TI, Schmidt D, Prante O, et al. SPECT/CT with the PSMA ligand 99mTc-MIP-1404 for whole-body primary staging of patients with prostate cancer. *Clin Nucl Med* (2018) 43(4):225–31. doi: 10.1097/RLU.0000000000001991

26. Eiber M, Weirich G, Holzapfel K, Souvatzoglou M, Haller B, Rauscher I, et al. Simultaneous 68Ga-PSMA HBED-CC PET/MRI improves the localization of primary prostate cancer. *Eur Urol* (2016) 70(5):829–36. doi: 10.1016/j.eururo.2015.12.053

27. Uslu-Beşli L, Bakır B, Asa S, Güner E, Demirdağ Ç, Şahin OE, et al. Correlation of SUVmax and apparent diffusion coefficient values detected by Ga-68 PSMA PET/MRI in primary prostate lesions and their significance in lymph node metastasis: preliminary results of an on-going study. *Mol Imaging Radionucl Ther* (2019) 28:104–11. doi: 10.4274/mirt.galenos.2019.63825

28. Zhang Q, Zang S, Zhang C, Fu Y, Lv X, Zhang Q, et al. Comparison of 68Ga-PSMA-11 PET-CT with mpMRI for preoperative lymph node staging in patients with intermediate to high-risk prostate cancer. *J Transl Med* (2017) 15(1):230. doi: 10.1186/s12967-017-1333-2

29. Fizazi K, Tran N, Fein L, Matsubara N, Rodriguez-Antolin A, Alekseev BY, et al. Abiraterone acetate plus prednisone in patients with newly diagnosed high-risk metastatic castration-sensitive prostate cancer (LATITUDE): final overall survival analysis of a randomised, double-blind, phase 3 trial. *Lancet Oncol* (2019) 20(5):686–700. doi: 10.1016/S1470-2045(19)30082-8

30. Kasperzyk JL, Finn SP, Flavin R, Fiorentino M, Lis R, Hendrickson WK, et al. Prostate-specific membrane antigen protein expression in tumor tissue and risk of lethal prostate cancer. *Cancer Epidemiol Biomarkers Prev* (2013) 22(12):2354–63. doi: 10.1158/1055-9965.EPI-13-0668

31. Uprimny C, Kroiss AS, Decristoforo C, Fritz J, von Guggenberg E, Kendler D, et al. 68Ga-PSMA-11 PET/CT in primary staging of prostate cancer: PSA and Gleason score predict the intensity of tracer accumulation in the primary tumour. *Eur J Nucl Med Mol Imaging* (2017) 44(6):941–9. doi: 10.1007/s00259-017-3631-6

frontiers | Frontiers in Oncology

TYPE Original Research
PUBLISHED 09 November 2023
DOI 10.3389/fonc.2023.1225490

OPEN ACCESS

EDITED BY
Fabio Grizzi,
Humanitas Research Hospital, Italy

REVIEWED BY
Shady Saikali,
AdventHealth, United States
Jeffrey Tuan,
National Cancer Centre Singapore, Singapore

*CORRESPONDENCE
Muhammad Shahid Anwar
shahidanwar786@gachon.ac.kr
Muhammad Faran Majeed
m.faran.majeed@kum.edu.pk

RECEIVED 19 May 2023
ACCEPTED 16 October 2023
PUBLISHED 09 November 2023

CITATION
Mehmood M, Abbasi SH, Aurangzeb K, Majeed MF, Anwar MS and Alhussein M (2023) A classifier model for prostate cancer diagnosis using CNNs and transfer learning with multi-parametric MRI. *Front. Oncol.* 13:1225490. doi: 10.3389/fonc.2023.1225490

A classifier model for prostate cancer diagnosis using CNNs and transfer learning with multi-parametric MRI

Mubashar Mehmood[1], Sadam Hussain Abbasi[2], Khursheed Aurangzeb[3], Muhammad Faran Majeed[2*], Muhammad Shahid Anwar[4*] and Musaed Alhussein[3]

[1]Department of Computer Science, COMSATS Institute of Information Technology, Islamabad, Pakistan, [2]Department of Computer Science, Kohsar University Murree, Punjab, Pakistan, [3]Department of Computer Engineering, College of Computer and Information Sciences, King Saud University, Riyadh, Saudi Arabia, [4]Department of AI and Software, Gachon University, Seongnam, Republic of Korea

Prostate cancer (PCa) is a major global concern, particularly for men, emphasizing the urgency of early detection to reduce mortality. As the second leading cause of cancer-related male deaths worldwide, precise and efficient diagnostic methods are crucial. Due to high and multiresolution MRI in PCa, computer-aided diagnostic (CAD) methods have emerged to assist radiologists in identifying anomalies. However, the rapid advancement of medical technology has led to the adoption of deep learning methods. These techniques enhance diagnostic efficiency, reduce observer variability, and consistently outperform traditional approaches. Resource constraints that can distinguish whether a cancer is aggressive or not is a significant problem in PCa treatment. This study aims to identify PCa using MRI images by combining deep learning and transfer learning (TL). Researchers have explored numerous CNN-based Deep Learning methods for classifying MRI images related to PCa. In this study, we have developed an approach for the classification of PCa using transfer learning on a limited number of images to achieve high performance and help radiologists instantly identify PCa. The proposed methodology adopts the EfficientNet architecture, pre-trained on the ImageNet dataset, and incorporates three branches for feature extraction from different MRI sequences. The extracted features are then combined, significantly enhancing the model's ability to distinguish MRI images accurately. Our model demonstrated remarkable results in classifying prostate cancer, achieving an accuracy rate of 88.89%. Furthermore, comparative results indicate that our approach achieve higher accuracy than both traditional hand-crafted feature techniques and existing deep learning techniques in PCa classification. The proposed methodology can learn more distinctive features in prostate images and correctly identify cancer.

KEYWORDS

transfer learning, convolutional neural network, deep learning, PCA, MRI images

1 Introduction

A major challenge for medical science is cancer, which is the most widespread disease in humans around the globe. Cancer cells exhibit aggressive growth rates, and their precise diagnosis is pivotal to a patient's survival. The most prevalent cancer diagnosed in men worldwide is PCa. Alarming statistics from the American Cancer Society predict approximately 288,300 new PCa cases in the United States by 2023, with an estimated 34,700 fatalities cancer society (1).

The conventional method for PCa classification relies on the Gleason Score (GS), as determined by analyzing biopsy samples. However, this conventional biopsy method has been found to exhibit reduced sensitivity in accurately identifying PCa. Furthermore, the Gleason classification method encounters challenges stemming from variations in interpretation, encompassing discrepancies among different observers (interobserver variability) and inconsistencies within assessments made by the same observer (intraobserver variability). These variations can predominantly be attributed to the heavy reliance on human interpretation within the Gleason classification method ŞCheck that all equations and special characters are displayed correctly.erbănescu et al. (2). Recent advancements in mpMRI have emerged as a pivotal tool for assessing the risk of PCa and improving the grading and classification of PCa Oberlin et al. (3); Bardis et al. (4). High-grade PCa is frequently characterized by the presence of more densely packed structures which can be effectively identified through the utilization of advanced MRI-based machine learning techniques. These approaches enable the detection and assessment of high-grade PCa, thereby enhancing diagnostic precision and treatment planning for patients. This study aims to create an automated method for classifying PCa, aiding radiologists' assessments.

The implementation of quantitative assessments of mpMRI offers radiologists a valuable, noninvasive tool to enhance their clinical decision-making processes. Furthermore, it helps mitigate the discrepancies that can arise due to differences between readers. With the growing interest in the integration of artificial intelligence (AI) with medical practice, empowered by enhanced computational capabilities and the emergence of new AI methodologies, there has been a surge in studies introducing CAD approaches. These systems leverage machine-learning and deep-learning approaches to detect and classify tumors in medical imagery, with a pronounced impact on PCa detection and classification Abbasi et al. (5). This study aims to build an automated PCa classification method, addressing the limitations of traditional GS and improving the diagnostic potential offered by mp-MRI. Early-stage PCa identification is extremely important and beneficial for treatments. Identification of PCa using MRI images improves the rate of early diagnosis and assists in building a Computer Aided Diagnostic (CAD) system Jin et al. (6); Reda et al. (7). A pivotal objective within CAD systems is the development of objective and reproducible metrics for automated analysis Cem Birbiri et al. (8). The continuous refinement of PCa classification techniques holds significant importance, particularly in distinguishing between low and high-grade cancers.

To identify PCa, several approaches have been proposed. Most of them used traditional machine-learning approaches, to classify images and train classifiers Bardis et al. (4); Monni et al. (9); Abbasi et al. (5); Gillies et al. (10); Fehr et al. (11); Vignati et al. (12); Liu et al. (13); Ullah et al. (14); Shahzad et al. (15); Laghari et al. (16); Sobecki et al. (17); Giannini et al. (18); Wang et al. (19); Schelb et al. (20); Wildeboer et al. (21); Wibmer et al. (22). Many of these approaches used features of low radiomics focused on previous clinical reports, which may not fully leverage the entire information within the MRI images Källén et al. (23). Moreover, unsupervised approaches were previously used to acquire features that may contain unnecessary information or may exclude essential clues. Deep learning approaches recently acquired great performance and are widely used in classifying and identification tasks of both medical applications Esteva et al. (24); Albarqouni et al. (25); Yuan and Meng (26) and natural images LeCun et al. (27). They can train classifiers and learn features jointly. Because deep learning techniques have enormous potential and success, the authors use them to classify PCa. Deep learning-based architectures have yielded remarkable results because of their capability to autonomously acquire and represent features Tsehay et al. (28). Compared to conventional approaches, CNN-based models such as Alexnet demonstrated improved performance Kiraly et al. (29). A challenge associated with architectures like this is the substantial data needed for effective training such as in Chen et al. (30). Using transfer learning is an easier way to handle this problem. In order to extract features and identify data from one domain into another, transfer learning employs training experience as a sort of knowledge sharing Le et al. (31). Good performance can be accomplished with small training images by using the transfer learning technique Wildeboer et al. (32); Zhong et al. (33) that applies models of pre-trained images from other datasets. Furthermore, various MRI sequences of PCa present different concerns, and it is important to consider an effective way to incorporate different details. By combining details derived from multi-parametric images, a descriptive representation of PCa may be gained Cem Birbiri et al. (8).

A multi-parametric MRI transfer learning (mp-TL) system to identify PCa is presented in this study. To obtain features from various MRI sequences, the proposed transfer learning model has three branches: ADC and T2w (sagittal, trans-axial). The features extracted from these categories are combined in the model. For this study, we aim to utilize transfer learning techniques leveraging a family of networks of pre-trained EfficientNet models for the classification of prostate images. Compound scaling is used in the recently proposed Efficient-Nets architecture to balance the network's three dimensions (Depth, Height, and Width). The proposed method demonstrates good performance in effectively classifying PCa images, contributing to enhanced diagnosis. The improvement in classifying PCa techniques is necessary to distinguish low and high-grade cancer. There is a need for an efficient deep learning-based architecture that efficiently classifies PCa images. In the proposed methodology, the important step for the classification of MRI images is the pre-processing stage. Pre-processing is used to process the PCa MRI images, and then the classification and feature extraction of PCa images is performed using deep CNN models. The contribution of this study is based on the classification of images and results in comparison with existing approaches. These are a few of this study's major contributions.

- The proposed approach here harnesses transfer learning to jointly analyze multiple MRI sequences, rather than focusing solely on a single MRI sequence. This enables us to extract more discriminative features, leading to a substantial enhancement in PCa classification.
- To demonstrate the model's effectiveness, the authors evaluate the PCa dataset utilizing a diverse range of Efficient-Net Models, encompassing B0, B5, and B7.
- Multi-view ensemble approach is used for classifying multi-parametric MRI images.
- An Efficient-Net model with fine-tuning and an additional Global Average Pooling (GAP) layer at the model's end, serves as a crucial component. This not only extracts vital information but also forwards it to the activation function for further processing.
- The proposed approach's effectiveness is highlighted through extensive experimentation conducted on the PCa dataset.

2 Related work

Numerous studies have been carried out by researchers to predict prostate MRI imaging. The literature on MRI image classification encompasses a range of both deep-learning and machine-learning techniques. There are various PCa MRI datasets that can be used for classification tasks, such as prostatex, ACRIN, and I2CVB. However, accessibility to these datasets is often limited or incomplete for many researchers. In contrast, Prostatex is a publicly accessible dataset specifically intended for research purposes.

For the MRI imaging classification of PCa, Chen et al. (34) suggested a deep-learning method focused on classification. A deep convolutional neural network, such as InceptionV3 and VGG-16 underwent pre-training on the ImageNet dataset. Subsequently, the multi-parametric magnetic resonance imaging dataset was fine-tuned. Xu et al. (35) employed residual networks for the identifying PCa. ResNets have demonstrated a capacity to learn both low-level and high-level features, making them well-suited for detecting subtle and intricate patterns in medical images, which are often indicative of diseases like PCa.Their study showcased the feasibility of training residual networks to acquire features that are valuable for identifying suspicious indicative of PCa.

In this study, Alkadi et al. (36), the authors employ a deep convolutional neural network to segment prostate lesions in T2W MRI images. They introduce a 3D sliding window technique for 3D context while maintaining computational efficiency. The approach distinguishes cancerous and non-cancerous tissues, with comparable results to multi-parametric systems, avoiding intricate alignment steps. This comprehensive study Viswanath et al. (37) assesses the performance of supervised classifiers in a multisite approach for detecting prostate cancer (PCa) extent using T2w MRI. The primary focus is on radiomic features extracted from high-resolution T2 images. The aim is to enhance the accuracy and timeliness of diagnoses in the context of medical imaging, particularly for PCa detection, where early and precise identification is critical for effective treatment.

Authors in this study Muhammad et al. (38) have highlighted the potential of utilizing a combination of multiple parameters, either as individual parameters or integrated multiple parameters within a machine learning framework, to enhance diagnostic capabilities. Their Schelb et al. (20) study highlights the effectiveness of training deep learning models to recognize and segment lesions in T2 and diffusion MRI data, significantly improving the clinical evaluation of MRI data. The UNet model was trained using cross-validation, incorporating split-sample techniques, and subsequently validated using an external test set. Singh et al. (39) suggest the use of deep neural networks for cribriform pattern classification. In this study, the authors introduce an automated image classification system employing deep learning and hand-crafted features to analyze prostate images. The focus is on detecting cribriform patterns, with results demonstrating diagnostic potential.

With notable advancements in computer vision, particularly in target recognition and identification through deep convolutional neural networks, the medical imaging research community is increasingly delving into the exploration of diverse CNN architectures. These architectures offer substantial potential for enhancing the accuracy of cancer detection systems. In this study, Yoo et al. (40) developed and introduced an automated pipeline based on CNN. This pipeline is designed to analyze images on a per-patient basis, aiming to detect clinically relevant PCa.

Bulten et al. (41) reported that the implementation of a semi-automatic labeling system eliminated the need for pathologists to manually annotate the images. A high degree of agreement with the reference norm has been obtained by the established framework. The deep learning method outperformed pathologists in different observation trials. Li et al. (42) clarify that for the diagnosis of disease, histology analysis is also seen as the gold standard. By reducing test time and inter-observer variability, computer-aided diagnostic software can theoretically further optimize existing pathology workflows. Previous cancer grading analyses have predominantly focused on the classification of predefined regions of significance or the handling of extensive volumes of fine-grained annotations.

Using a Genetic Algorithm, Namdar et al. (43) recommended fine-tuning a qualified CNN for enhanced PCa diagnosis, resulting in an improved AUC. Furthermore, Kwon et al. (44) proposed a radiomics-based method for prostate image identification. The purpose was to identify multi-parametric MRI for clinically important PCa. Lay et al. (45) stated because MR imaging has its limitations, researchers suggest a different PCa detection technique that can be most effective. The cancer detection approach trains random ferns on MR sequences in the absence of one or more of these MR sequences and then uses these random ferns to add the MR sequences.

An approach for evaluating the grade for PCa has been suggested in this paper by Abraham and Nair (46). In this method, features are extracted utilizing deep network autoencoders in conjunction with hand-crafted features, subsequently categorized with a softmax classifier. Song et al. (47) have shown that radiologists manually

mark the regions of significance for PCa and measure the scores for each area. The authors developed a model on patch-based DCNN that utilizes a combination of MRI data to distinguish between cancerous and non-cancerous patients of PCa.

According to Lemaitre et al. (48), new magnetic resonance imaging (MRI) approaches have emerged to enhance diagnostic accuracy. However, factors like observer variability and the visibility and complexity of lesions can still impact diagnosis. In this respect, CAD-based applications are designed to support radiologists in their clinical practice. Taking account of all MRI modalities, the authors suggest a CAD method. The goal of this CAD scheme was to detect the prostate position of cancer. Liu et al. (49) stated that for the classification of PCa, deep learning architecture was developed using the 3D multipara-metric MRI data. The Xmas-Net model was used for extracting features in this study. Mehrtash et al. (50) have demonstrated that to better detect PCa Computer-assisted diagnosis of MRI PCa may be used as a method of clinical decision support to help interpretation by radiologists. CNN models are used to detect the probability of a patient being affected or not.Yang et al. (51) provides an integrated method for detecting PCa that can simultaneously image PCa and locate lesions based on characteristics of the deep convolutionary neural network and SVM.

3 Transfer learning

TL is a technique for transferring information across domains Orenstein and Beijbom (52). Deep learning is a challenging and time-intensive process, especially in medical imaging, where a substantial amount of training data is needed to understand certain patterns. To address the challenge of limited data, medical imaging datasets are utilized to fine-tune the weights of deep learning models that were previously trained for different computer vision applications, thus accelerating the training process. The strategy frequently used in various computer vision problems is fine-tuning transfer learning. For classification, the dense layers are well-tuned, while the top layers are frozen. The proposed methodology for classifying prostate images using transfer learning is shown in Figure 1.

4 Materials and methods

The prostate dataset was obtained from the Cancer Imaging Archive Nolan (53). The dataset consists of prostate MRI images which are labeled with the help of radiologists. After performing minor data preprocessing, we carefully selected 221 cases of prostate cancer for our dataset. Our dataset comprised 98 cases of low-grade and 123 cases of high-grade cancer. Every patient included in the study exhibited an initial screening result that raised suspicions regarding prostate cancer. Subsequently, each of these patients underwent a biopsy, from which a GS was determined. These cases are annotated with two-class labels distinguishing between low-grade (GS = 3 + 4, 3 + 3) and high-grade (GS = 4 + 4, 4 + 3, 5 + 3, 3 + 5) cancer. For each case, T2w (sagittal and transaxial) and ADC images were provided to conduct experiments.

In our experimental setup, we adopted a systematic approach to partitioning the dataset to ensure robust training and evaluation of our model. We performed a random selection process, wherein 80% of the dataset was utilized for various purposes, including training and validation, while the remaining 20% of the images were exclusively designated as the test set. Within this 80% portion of the dataset, we further allocated distinct proportions for training

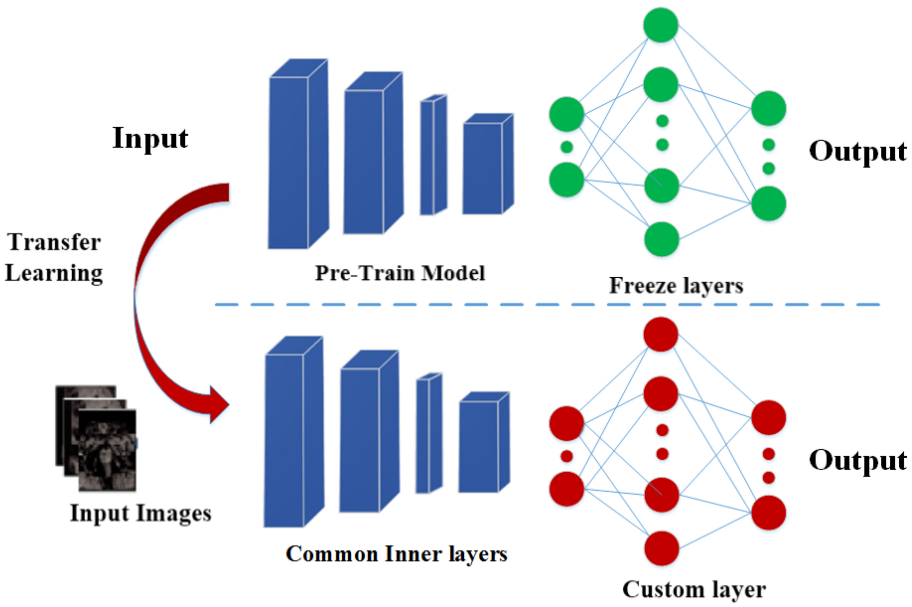

FIGURE 1
The top layers (last) are fine-tuned using TL.

and validation. Approximately 50% of the dataset was allocated for training, which served as the foundation for our transfer learning process. The remaining 30% of this 80% portion was dedicated to the validation set. This set played a pivotal role in monitoring the model's performance during training. By periodically evaluating the model's predictions on this validation subset, we could make informed decisions regarding hyperparameter tuning and model adjustments, ultimately ensuring that our model's generalization capabilities were optimized. Lastly, the 20% of the images that constituted the test set were kept entirely separate from the training and validation data. This segregation ensured that our model was assessed on entirely unseen data, mirroring real-world scenarios where it would be applied to make predictions. The test set served to evaluate the model's performance, providing a reliable measure of its ability to generalize to new and previously unseen data. Through this well-structured data partitioning strategy, we aimed to achieve a robust and thorough assessment of our model's capabilities, while also upholding the principles of fairness, rigor, and transparency in our experimental approach.

4.1 Proposed approach

This study presented a transfer learning model that utilizes multiparametric MRI for the classification of PCa into low-grade and high-grade. In Figure 2, the proposed model is mentioned. To learn features from multiparametric sequences (ADC, T2w), the authors make a transfer learning model with three branches and combine them to gain discriminative descriptors. A significant amount of training data is needed for deep convolution neural networks in medical imaging. When the available data is insufficient, deep CNNs often rely on pre-trained models. These models have been previously trained on extensive datasets, allowing for knowledge transfer, which is a fundamental aspect of TL.

Figure 3 describes the suggested model's workflow. Transfer learning-based multi-parametric MRI model to automatic PCa identification is presented in this study. Various sequences of MRI reveal distinct aspects of PCa. T2-weighted (T2w) and ADC (Apparent Diffusion Coefficient) imaging modalities offer distinct insights, and their integration can significantly enhance the accuracy of PCa classification. To learn features from multi-parametric sequences T2w (sagittal and transaxial) and ADC, the authors make a transfer learning model with three branches of architecture to gain features separately for each modality and then combine them to gain one feature vector. We feed these sequences simultaneously in the network and their concatenation after the convolutional layer. Such a fusion approach allows the learning process to generate effective and discriminating PCa-related characteristics of multiple modalities mutually influenced by each other. To achieve better performance, we fine-tune our model by changing the top layers and defining the last layer classes to two nodes, as we identify PCa as a low-grade and high-grade form of cancer. After optimizing the MPTL methodology, we could perform the task of classifying prostate images. The performance of classifying PCa could be further improved by improving the ability to combine learned features.

4.2 Transfer learning using a single sequence to extract features

Due to the limited availability of prostate cancer data, we have opted for a transfer learning strategy instead of training an entire

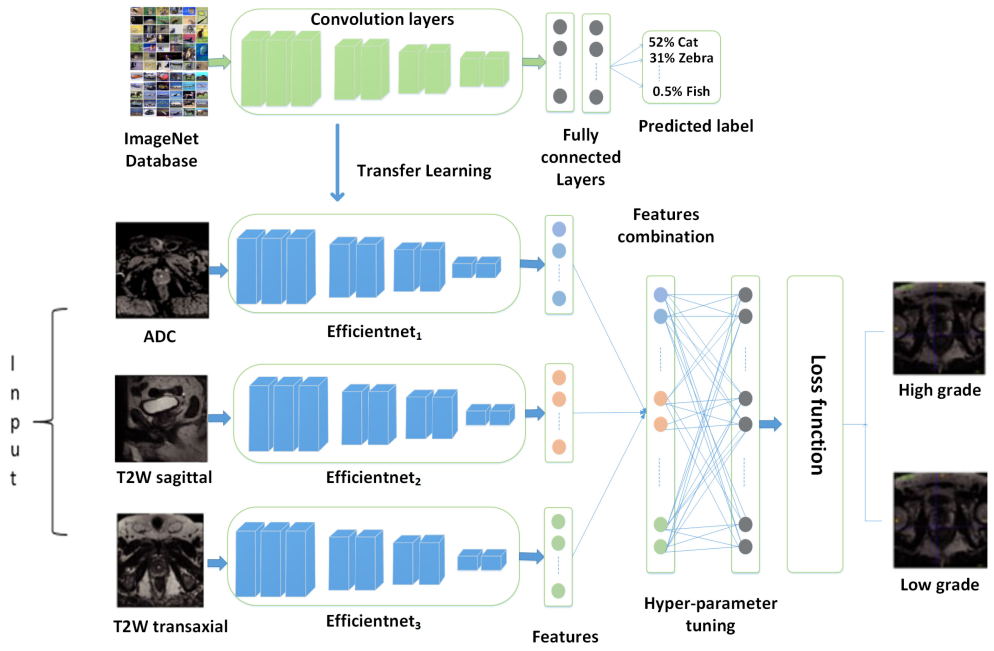

FIGURE 2
Proposed model.

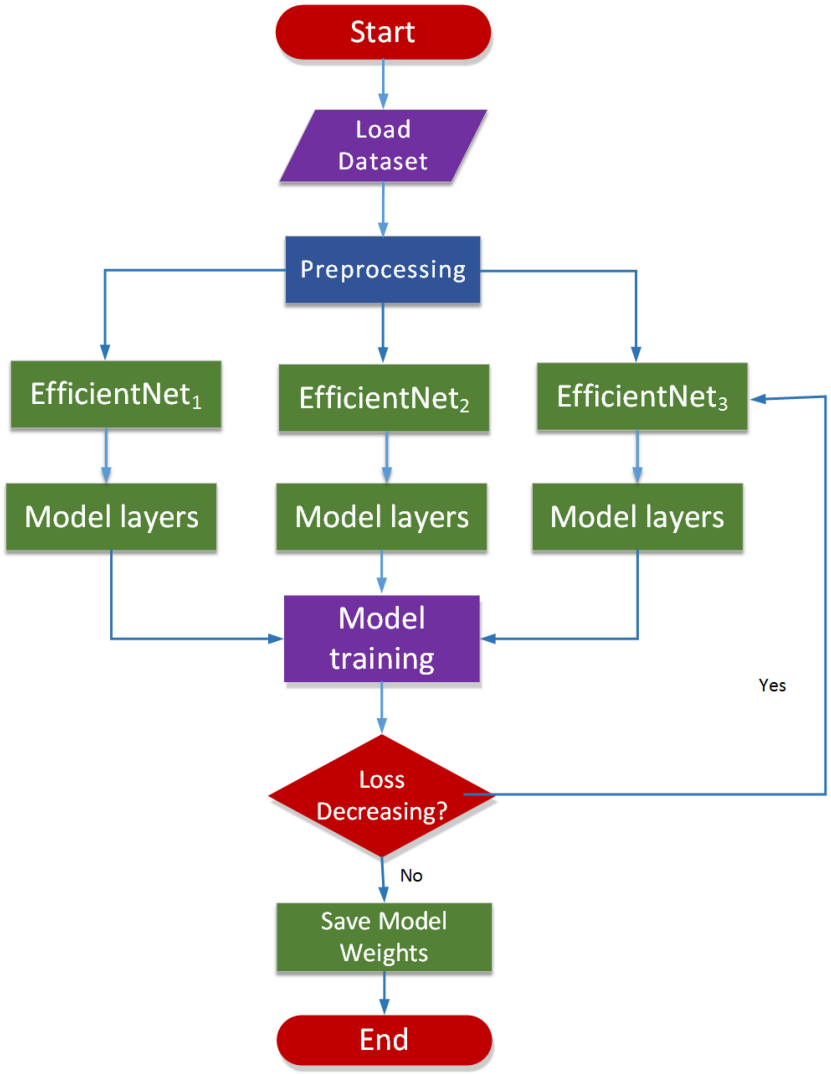

FIGURE 3
Workflow of the proposed model.

deep-learning neural network from the ground up. Specifically, we have harnessed the power of established deep learning architectures like ConvNets, AlexNet, and VGGNet, which have previously been trained on ImageNet datasets and are readily accessible as pre-trained networks. By implementing the EfficientNet architecture across multiple MRI series, we can extract essential features from ADC, T2w sagittal, and T2w transaxial images. This innovative approach allows us to transfer the knowledge acquired from ImageNet and effectively characterize PCa images.

4.3 A multisequence MRI-based feature fusion method

Different MRI modalities of PCa demonstrate different aspects. Various sequences of MRI disclose various PCa kinds. To provide separate and complementary data, T2w and ADC are recorded, and their combination can effectively increase the precision of PCa diagnosis. It is efficient to obtain the simultaneous information from MRI in deep learning method to optimize the relation between different MRIs. We feed these sequences simultaneously in the network and their concatenation after the convolutional layer. Such a fusion approach allows the learning process to generate effective and discriminating PCa-related characteristics of multiple modalities mutually influenced by each other. The performance is seen as the final joint characteristic after fully connected layers.

4.4 Developing a fine-tuned training strategy

In our approach utilizing the Efficient-Net architecture, we took several steps to enhance the classification of PCa into high and low-grade. We integrated fully connected layers into the network and fine-tuned it using our dataset. This fine-tuning process was pivotal in adapting the model to our specific classification task. To boost the

feature extraction capabilities of our model, we introduced custom layers, including global average pooling within the classification layers. This addition helped in capturing more nuanced features from the medical images, which is crucial in accurately classifying cancer. What sets our approach apart is the use of Efficient-Net architectures, which come with distinct advantages. These models are not only faster in classification, being 6.1× faster compared to existing CNN models, but they are also significantly smaller, being 8.4× smaller. Importantly, their compact size doesn't compromise their accuracy. Our Efficient-Net models leveraged TL based on architectures pre-trained on the extensive ImageNet dataset, known for its high accuracy and efficiency. This TL approach allowed us to benefit from the knowledge embedded in these pre-trained models, especially when our own dataset was limited. To further enhance the training process and ensure robustness, we employed data augmentation. This technique plays a crucial role in augmenting the dataset, increasing the diversity of training samples, and consequently, improving the model's ability to generalize to unseen data. It is particularly effective in preventing overfitting, a common challenge in classification tasks. One notable aspect of our strategy is the use of a pre-trained model as a feature extractor. In this approach, the last fully connected layer is removed, and the remaining layers are treated as a fixed feature extractor. This significantly accelerates the training process. In essence, our approach combines the advantages of Efficient-Net architectures, Transfer Learning, data augmentation, and a pre-trained feature extractor to enhance the classification of prostate cancer. Figure 4 provides a visual representation of our model in action, demonstrating its potential in the field of medical image classification. The performance of the baseline Efficient-Net architecture is demonstrated in Figure 5.

4.5 Evaluation metrics

The output of input images is typically evaluated using the evaluation matrices listed below. The confusion matrix can be used to measure these matrices, including accuracy, precision, recall, and F1-score. The confusion matrix has four different types of parameters, where TP denotes a true positive, TN denotes a true negative, FP denotes a false positive, and FN denotes a false negative. as shown in Table 1 and equations are given below.

True Positives: The precise predicted positive values demonstrate that the predicted and the actual class value are both positive.

True Negatives: These are the accurately predicted negative values, showing that both the predicted and the actual class value are negative.

False Positives: When the predicted class is true but the actual class is false.

False Negatives: When the predicted class is no but the actual class is yes.

Accuracy: Accuracy is the most used performance metric, which may be calculated as the ratio of correctly expected observations to all observations. Having high accuracy will lead one to believe that our models outperform.

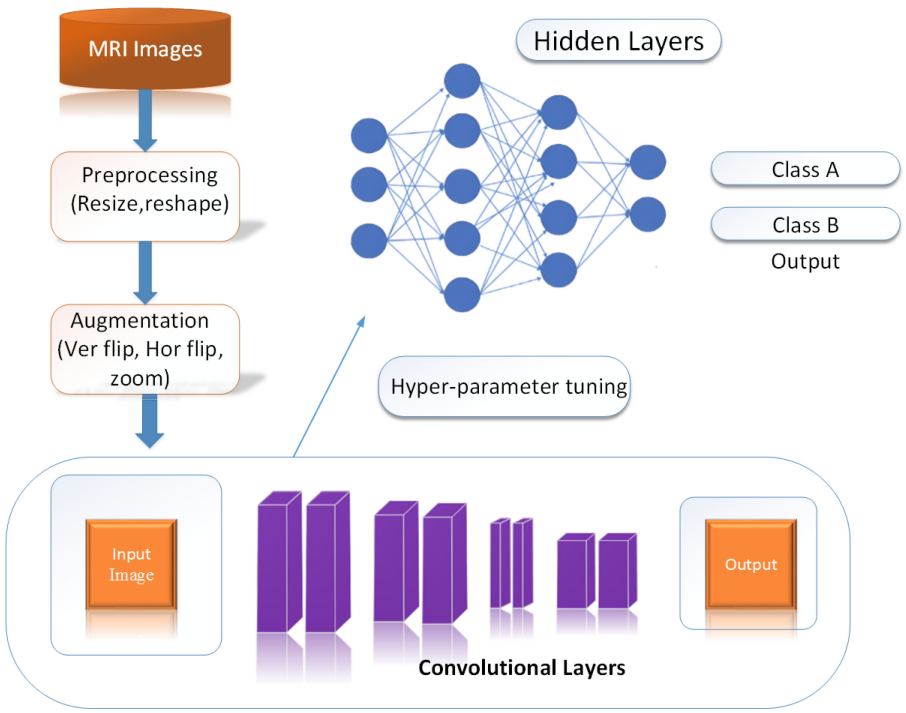

FIGURE 4
Model into work.

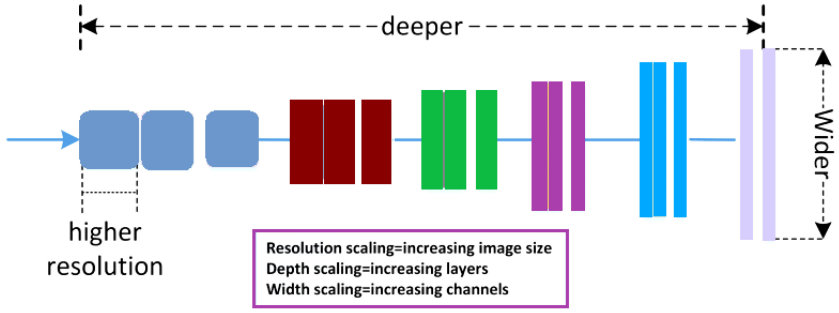

FIGURE 5
Efficient-net baseline model.

$$Accuracy = \frac{TP + TN}{TP + TN + FP + FN} \quad (1)$$

Precision: Precision is the ratio of accurately predicted positive observations to all predicted positive observations.

$$Precision = \frac{TP}{TP + FP} \quad (2)$$

Recall: Recall is defined as the ratio of accurately predicted positive observations to all of the actual class observations.

$$Recall = \frac{TP}{TP + FN} \quad (3)$$

F1 score: The weighted average of recall and accuracy is the Score. This score takes into consideration both false positives and false negatives. Although it is not as easy to immediately understand as accuracy, it is typically more beneficial than precision, especially if we have an uneven class distribution. If false positives and false negatives result in equal losses, accuracy performs better. It is simpler to include both accuracies and recall if the cost of false positives and negatives is significantly different.

$$F1 - Score = \frac{2 \times Precision \ \ xRecall}{Precision + Recall} \quad (4)$$

4.6 Experimental settings

To get generalized results, the authors repeated the experiment several times, looking at different learning and test data

TABLE 1 Literature review regarding PCa classification.

Author(s)	Description of Research	Methodology	Dataset Used	Evaluation Measures
Chenet al. (34)	Use transfer learning for prediction of PCa	InceptionV3, VGG-16	PROSTATEx	AUC, ROC
Xu et al. (35)	Utilize the residual networks for detecting PCa	Res-Net	PROSTATEx	ROC, HoM
Alkadi et al. (36)	Using deep convolutional encoder-decoder for detection	DCNN	I2CVB	Accuracy, DSC, IoU
Kwon et al. (44)	Apply CART and LASSO for detecting PCa	CART, LASSO	PROSTATEx	ROC, AUC
Lay et al. (45)	Apply Random ferns for classifying PCa	Random ferns	PROSTATEx	ROC, AUC
Abraham and Nair (46)	CNN inceptionV3 for feature pooling and selection	CNN, SVM	PROSTATEx	Accuracy, kappa, PPV
Songet al. (47)	Model with patchbased DCNN for PCa	DCNN	PROSTATEx	AUC
Lemaitre et al. (48)	RF classifier for feature learning and classification	RF classifier	I2CVB	AUC
Liu et al. (49)	Xmas-Net model used for extracting features	Xmas-Net	PROSTATEx	ROC, AUC
Mehrtash et al. (50)	Probability of patient being affected or not	CNN	PROSTATEx	ROC
Yanget al. (51)	The model with DCNN, SVM to detect PCa	DCNN, SVM	PROSTATEx	FROC, ROC, LLF, NL

combinations. To increase the robustness of the presented MPTL approach and to reduce overfitting, the authors used the data augmentation technique to increase the size of the training data of different image transformations. Before transferring images as input to the networks, the authors conducted some preprocessing steps. To fit the model, images are resized or reshaped from the original size to 244 × 244 for the family of Efficient-Net models for image classification. The Adam optimizer was used to further train the entire set of pre-trained Efficient-Net models.

The settings utilized to conduct the experiments are as follows.

- Experiment carried out using a Google Colab Pro platform with a GPU T4 P100 and 25 Gigabytes memory.
- Batch size of 16.
- Learning rate from le-1 to le-6 with weight decay of le-4.
- Epochs are set to 150.
- The Adam optimizer was used to further train the whole set of pre-trained Efficient-Net models Perez and Wang (54).

4.7 Experiments and results

We conducted an extensive comparative analysis to evaluate our proposed model alongside eight baseline methods. Initially, we employed a transfer learning model without fine-tuning, utilizing image features directly from ImageNet for experimentation. We then delved into three additional baseline experiments, finetuning single MRI sequences, specifically T2-weighted (T2w) and ADC (Apparent Diffusion Coefficient), for prostate cancer classification. Subsequently, we extended our experiments to three more baseline experiments, employing two MRI parameters as input. The comprehensive classification results for both our method and the eight baseline methods are meticulously detailed in Table 2.

To assess the classification performance of our proposed MPTL model, we carried out a comprehensive evaluation, comparing it with state-of-the-art prostate cancer classification methods, including both deep learning and machine learning-based approaches. These comparisons were conducted using our prostate cancer datasets, and we followed the experiment settings outlined in these reference papers to ensure a fair and equitable assessment. Table 3 meticulously presents the precision, recall, and accuracy metrics achieved by both our approach and the comparative methodologies. It's noteworthy that deep learning-based techniques outperformed methods relying on traditional radiomics features or conventional machine learning approaches. This observation highlights the capability of deep learning-based techniques to capture more distinctive features for the identification of prostate cancer.

Our method performs better at classification than the preceding approaches. This is due to the fact that convergence issues and over-fitting issues with little data on PCa also hinder deep network training. In comparison, the image details in the transfer learning model using Efficient-Net were considered by our MPTL model. Therefore, as compared to previous classification techniques, our technique evaluates more precise parameters for PCa and achieves more efficiency.

This method classified the input image into cancer types with low and high grades. We elaborate on the experimental results performance to distinguish between the aggressive and non-aggressive forms of cancer. The Efficient-Net B7 architecture, which was trained on images of PCa, produces the greatest results. Table 3 shows the results of the proposed methods. In Şerbănescu et al. (2), authors apply the Google-Net approach for the identification of PCa classification for binary classification to distinguish low and high-grade forms of cancer and achieve 60.9 accuracies and performance. In Chen et al. (34) authors apply the VGG-16 approach for the identification of PCa classification for binary classification to distinguish the low and high-grade forms of cancer and achieve 83 accuracies and performance.

In Kwon et al. (44), authors apply the CART approach for the identification of PCa classification for binary classification to distinguish the low and high-grade forms of cancer and achieve 82.0 accuracies and performance. In Le et al. (31), authors apply the ResNet approach for the identification of PCa classification for binary classification to distinguish low and high-grade forms of cancer and achieve 82.09 accuracies and performance. In Muhammad et al. (55), authors apply the inceptionV3 approach for the identification of PCa classification for binary classification to distinguish the low and high-grade forms of cancer and achieve 80.09 accuracies and performance.

TABLE 2 Comparison results of PCa classification.

References	Methods	Accuracy	Precision	Precision	F1-score
Chen et al. Chen et al. (34)	VGG-16	83	82.42	88.23	86.78
Kwon et al. Kwon et al. (44)	CART	82.0	81.84	81.46	79.61
Le et al. Le et al. (31)	ResNet	82.09	82.27	82.88	82.34
Muhammad Muhammad et al. (55)	inceptionV3	80.09	78.95	83.96	81.61
Serbanescu et al. Şerbănescuet al. (2)	GoogleNet	60.9	58.78	59.36	57.89
Present work (MPTL)	EfficientNet-B0	84.44	87.5	84.0	85.71
	EfficientNet-B5	86.67	83.33	90.90	86.95
	EfficientNet-B7	88.89	91.67	88.0	89.47

TABLE 3 Comparison results of PCa MRI.

	Accuracy	Precision	Recall	F1-score
MPTL-B0	84.44	87.5	84.0	85.71
T2w sagittal	71.43	72.13	73.79	72.66
T2w transaxial	73.78	71.43	79.39	75.44
ADC	74.72	73.86	78.30	76.06
ADC and T2w sagittal	81.81	82.97	86.67	84.78
ADC and T2w transaxial	83.33	85.1	83.34	84.20
Sagittal and T2w transaxial	82.21	86.95	83.33	85.10
MPTL-B5	86.67	83.33	90.90	86.95
MPTL-B7	88.89	91.67	88.0	89.47

The comparison results of different methods with multi-parametric modalities are shown in Table 2. The results demonstrate that our proposed approach with a fusion of three modalities performs better results than single modalities and pair of modalities which depicts that our approach performance is better on multiple modalities.

The learning curve for accuracy and loss during training and validation is depicted in Figures 6, 7. Our approach also shows better identification performance compared with the other machine learning approaches with extraction features from a single MRI sequence, showing that the methods based on deep learning will learn more high-level discriminative features. ROC curves of PCa classification are shown in Figure 8. The results demonstrate the performance of the model to identify input images is classified as low and high-grade forms of cancer that are aggressive and non-aggressive forms of cancer.

4.8 Cross dataset validation

To comprehensively evaluate the generalization performance of the proposed Multi-Parameter Transfer Learning (MPTL) model, an extensive experiment was conducted across diverse datasets. The primary objective of this experiment was to showcase the practicality and effectiveness of the MPTL framework in real-world scenarios where data sources may vary significantly.

For this purpose, we strategically leveraged two distinct datasets, both of which are publicly available to ensure transparency and reproducibility in our research. The first dataset, sourced from the Cancer Imaging Archive Nolan (53), is a substantial collection of medical images related to prostate cancer. The second dataset, referred to as I2CVB G. Lemaitre et al. (56), provides an additional set of prostate MRI images for comparative analysis. It's worth noting that these datasets bring a wealth of diversity to the experiment. They exhibit variations in terms of image characteristics such as shapes, angles, sizes, resolutions, and formats. This diversity mirrors the real-world scenario where medical imaging data can originate from various sources and possess inherent dissimilarities. After minor cleaning, our training process was conducted on a robust training set comprising 5096 images from the first dataset. Subsequently, we rigorously assessed the model's performance on an independent test set comprising 1371 images sourced from the I2CVB dataset. This demarcation of

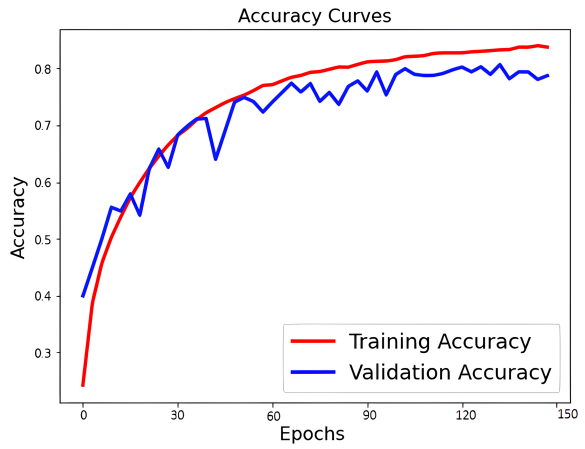

FIGURE 6
Accuracy curves of PCa classification.

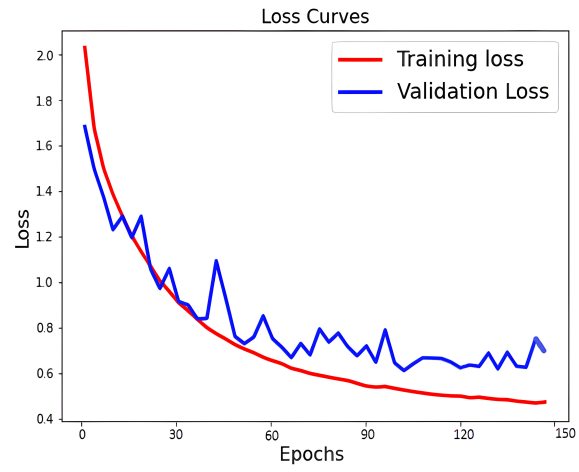

FIGURE 7
Loss curves of PCa classification.

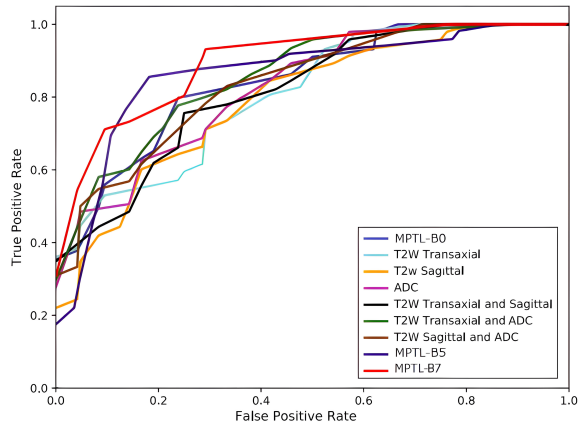

FIGURE 8
ROC curves of PCa.

training and testing datasets enabled us to simulate a real-world scenario where a model is required to adapt and generalize across distinct data sources.

The results obtained in this cross-dataset experiment are highly encouraging. The proposed MPTL framework exhibited remarkable performance, further emphasizing its versatility and effectiveness in handling diverse data sources. Specifically, our model achieved an accuracy rate of 86.65%, indicating its capability to make correct classifications. The precision rate, measuring the model's ability to correctly classify positive cases, stood at an impressive 83.36%. Furthermore, the recall rate, signifying the model's capacity to identify all relevant instances, reached an impressive 89.18%. Lastly, the F1-score, which strikes a balance between precision and recall, demonstrated a robust performance at 86.13%. These outcomes underscore the generalization power of the MPTL framework for the classification of prostate MRI images. The model's consistent and high-quality performance across datasets with diverse characteristics reinforces its potential utility in real-world medical applications, where data heterogeneity is often encountered.

5 Conclusion

In terms of replacing manual cancer assessment by radiologists using MRI images, CAD plays a critical role. There are, however, numerous risks and a high level of complexity involved in this task, along with expert-level opinions. The manual extraction of handcrafted features and subsequent classification not only consumes time but also introduces a higher likelihood of errors. To streamline the assessment process for radiologists and mitigate diagnostic errors, the necessity for an automated decision-making classification model becomes evident. In this paper, we introduce an innovative MPTL model for the automatic classification of PCa. Our model leverages knowledge from ImageNet to aid in the feature learning process from multi-parametric MRI (mp-MRI) sequences. These transferred features are combined to enhance the accuracy of PCa classification. A refined fine-tuning method including global average pooling is further applied to enhance PCa classification. As a result, the learned features exhibit significantly enhanced discriminative capabilities. Through an extensive series of comparative studies, we have highlighted the exceptional performance of our model in direct comparison to the prevailing state-of-the-art cancer classification methods. Our empirical results unequivocally establish the efficacy of our proposed approach in achieving high-precision PCa classification. Our findings highlight the potential benefits of transfer learning techniques from natural images to the medical domain, potentially offering valuable solutions in scenarios where the availability of annotated training datasets is limited for various practical considerations.

Data availability statement

The raw data supporting the conclusions of this article will be made available by the authors, without undue reservation.

Author contributions

Conceptualization, MM, MFM, and SA; methodology, MM, MSA, and MA; software, MM, KA, and MSA; validation, MFM, SA, and KA; formal analysis, MA and MSA; investigation, MSA, and SA; resources, MM, MFM and SA; data curation, KA, MSA, and MFM; writing—original draft preparation, MM, MFM, and SA; writing—review and editing, MSA, MA, KA, and MFM; visualization, MM, MFM, and SA; supervision, MFM and SA; project administration, MA and KA; funding acquisition, MA. All authors contributed to the article and approved the submitted version.

Funding

The author(s) declare financial support was received for the research, authorship, and/or publication of this article. This Research is funded by Researchers Supporting Project Number (RSPD2023R947), King Saud University, Riyadh, Saudi Arabia.

Conflict of interest

The authors declare that the research was conducted in the absence of any commercial or financial relationships that could be construed as a potential conflict of interest.

Publisher's note

References

1. Cancer society, A. *American cancer society*. (2021), Dataset.

2. Şerbănescu M-S, Manea NC, Streba L, Belciug S, Ples¸ea IE, Pirici I, et al. Automated Gleason grading of prostate cancer using transfer learning from general-purpose deep-learning networks. *Romanian J Morphology Embryology* (2020) 61:149. doi: 10.47162/RJME.61.1.17

3. Oberlin DT, Casalino DD, Miller FH, Meeks JJ. Dramatic increase in the utilization of multiparametric magnetic resonance imaging for detection and management of prostate cancer. *Abdominal Radiol* (2017) 42:1255–8. doi: 10.1007/s00261-016-0975-5

4. Bardis MD, Houshyar R, Chang PD, Ushinsky A, Glavis-Bloom J, Chahine C, et al. Applications of artificial intelligence to prostate multiparametric MRI (mpMRI): Current and emerging trends. *Cancers* (2020) 12:1204. doi: 10.3390/cancers12051204

5. Abbasi AA, Hussain L, Awan IA, Abbasi I, Majid A, Nadeem MSA, et al. Detecting prostate cancer using deep learning convolution neural network with transfer learning approach. *Cogn Neurodynamics* (2020) 14:523–33. doi: 10.1007/s11571-020-09587-5

6. Jin J, Zhang L, Leng E, Metzger GJ, Koopmeiners JS. Detection of prostate cancer with multiparametric MRI utilizing the anatomic structure of the prostate. *Stat Med* (2018) 37:3214–29. doi: 10.1002/sim.7810

7. Reda I, Shalaby A, Khalifa F, Elmogy M, Aboulfotouh A, Abou El-Ghar M, et al. Computeraided diagnostic tool for early detection of prostate cancer, in: *2016 IEEE International Conference on Image Processing (ICIP)* (IEEE). (2016) 2668–72.

8. Cem Birbiri U, Hamidinekoo A, Grall A, Malcolm P, Zwiggelaar R. Investigating the performance of generative adversarial networks for prostate tissue detection and segmentation. *J Imaging* (2020) 6:83. doi: 10.3390/jimaging6090083

9. Monni F, Fontanella P, Grasso A, Wiklund P, Ou Y-C, Randazzo M, et al. Magnetic resonance imaging in prostate cancer detection and management: a systematic review. *Minerva urologica e nefrologica= Ital J Urol Nephrol* (2017) 69:567–78. doi: 10.23736/S0393-2249.17.02819-3

10. Gillies RJ, Kinahan PE, Hricak H. Radiomics: images are more than pictures, they are data. *Radiology* (2016) 278:563–77. doi: 10.1148/radiol.2015151169

11. Fehr D, Veeraraghavan H, Wibmer A, Gondo T, Matsumoto K, Vargas HA, et al. Automatic classification of prostate cancer Gleason scores from multiparametric magnetic resonance images. *Proc Natl Acad Sci* (2015) 112:E6265–73. doi: 10.1073/pnas.1505935112

12. Vignati A, Mazzetti S, Giannini V, Russo F, Bollito E, Porpiglia F, et al. Texture features on T2-weighted magnetic resonance imaging: new potential biomarkers for prostate cancer aggressiveness. *Phys Med Biol* (2015) 60:2685. doi: 10.1088/0031-9155/60/7/2685

13. Liu L, Tian Z, Zhang Z, Fei B. Computer-aided detection of prostate cancer with MRI: technology and applications. *Acad Radiol* (2016) 23:1024–46. doi: 10.1016/j.acra.2016.03.010

14. Ullah N, Khan MS, Khan JA, Choi A, Anwar MS. A robust end-to-end deep learning-based approach for effective and reliable BTD using MR images. *Sensors* (2022) 22:7575. doi: 10.3390/s22197575

15. Shahzad M, Tahir MA, Alhussein M, Mobin A, Shams Malick RA, Anwar MS. NeuPD—A neural network-based approach to predict antineoplastic drug response. *Diagnostics* (2023) 13:2043. doi: 10.3390/diagnostics13122043

16. Laghari AA, Sun Y, Alhussein M, Aurangzeb K, Anwar MS, Rashid M. Deep residual-dense network based on bidirectional recurrent neural network for atrial fibrillation detection. *Sci Rep* (2023) 13:15109. doi: 10.1038/s41598-023-40343-x

17. Sobecki P, Życka-Malesa D, Mykhalevych I, Sklinda K, Przelaskowski A. MRI imaging texture features in prostate lesions classification, in: *EMBEC & NBC 2017: Joint Conference of the European Medical and Biological Engineering Conference (EMBEC) and the Nordic-Baltic Conference on Biomedical Engineering and Medical Physics (NBC), Tampere, Finland, June 2017 (Springer)*. (2018) 827–30.

18. Giannini V, Vignati A, Mirasole S, Mazzetti S, Russo F, Stasi M, et al. MR-T2-weighted signal intensity: a new imaging biomarker of prostate cancer aggressiveness. *Comput Methods Biomechanics Biomed Engineering: Imaging Visualization* (2016) 4:130–4. doi: 10.1080/21681163.2014.910476

19. Wang X, Yang W, Weinreb J, Han J, Li Q, Kong X, et al. Searching for prostate cancer by fully automated magnetic resonance imaging classification: deep learning versus non-deep learning. *Sci Rep* (2017) 7:15415. doi: 10.1038/s41598-017-15720-y

20. Schelb P, Kohl S, Radtke JP, Wiesenfarth M, Kickingereder P, Bickelhaupt S, et al. Classification of cancer at prostate MRI: deep learning versus clinical PI-RADS assessment. *Radiology* (2019) 293:607–17. doi: 10.1148/radiol.2019190938

21. Wildeboer RR, van Sloun RJG, Huang P, Wijkstra H, Mischi M. 3-D multi-parametric contrast-enhanced ultrasound for the prediction of prostate cancer. *Ultrasound Med Biol* (2019) 45:2713–24. doi: 10.1016/j.ultrasmedbio.2019.05.017

22. Wibmer A, Hricak H, Gondo T, Matsumoto K, Veeraraghavan H, Fehr D, et al. Haralick texture analysis of prostate MRI: utility for differentiating non-cancerous prostate from prostate cancer and differentiating prostate cancers with different Gleason scores. *Eur Radiol* (2015) 25:2840–50. doi: 10.1007/s00330-015-3701-8

23. Källén H, Molin J, Heyden A, Lundström C, Åström K. Towards grading gleason score using generically trained deep convolutional neural networks, in: *2016 IEEE 13th International Symposium on Biomedical Imaging (ISBI)* (IEEE). (2016) 1163–7.

24. Esteva A, Kuprel B, Novoa RA, Ko J, Swetter SM, Blau HM, et al. Dermatologist-level classification of skin cancer with deep neural networks. *nature* (2017) 542:115–8. doi: 10.1038/nature21056

25. Albarqouni S, Baur C, Achilles F, Belagiannis V, Demirci S, Navab N. Aggnet: deep learning from crowds for mitosis detection in breast cancer histology images. *IEEE Trans Med Imaging* (2016) 35:1313–21. doi: 10.1109/TMI.2016.2528120

26. Yuan Y, Meng MQ-H. Deep learning for polyp recognition in wireless capsule endoscopy images. *Med Phys* (2017) 44:1379–89. doi: 10.1002/mp.12147

27. LeCun Y, Bengio Y, Hinton G. Deep learning. *nature* (2015) 521:436–44. doi: 10.1038/nature14539

28. Tsehay Y, Lay N, Wang X, Kwak JT, Turkbey B, Choyke P, et al. Biopsy-guided learning with deep convolutional neural networks for Prostate Cancer detection on multiparametric MRI, in: *2017 IEEE 14th International Symposium on Biomedical Imaging (ISBI 2017)* (IEEE). (2017) 642–5.

29. Kiraly AP, Nader CA, Tuysuzoglu A, Grimm R, Kiefer B, El-Zehiry N, et al. Deep convolutional encoder-decoders for prostate cancer detection and classification, in: *Medical Image Computing and Computer Assisted Intervention- MICCAI 2017: 20th International Conference, Quebec City, QC, Canada, September 11-13, 2017, Proceedings, Part III 20* (Springer). (2017) 489–97.

30. Chen Q, Xu X, Hu S, Li X, Zou Q, Li Y. A transfer learning approach for classification of clinical significant prostate cancers from mpMRI scans. in: *Medical Imaging 2017: Computer-Aided Diagnosis* (SPIE). (2017) 10134:1154–7.

31. Le MH, Chen J, Wang L, Wang Z, Liu W, Cheng K-TT, et al. Automated diagnosis of prostate cancer in multi-parametric MRI based on multimodal convolutional neural networks. *Phys Med Biol* (2017) 62:6497. doi: 10.1088/1361-6560/aa7731

32. Wildeboer RR, Mannaerts CK, van Sloun RJG, Budäus L, Tilki D, Wijkstra H, et al. Automated multiparametric localization of prostate cancer based on B-mode, shear-wave elastography, and contrast-enhanced ultrasound radiomics. *Eur Radiol* (2020) 30:806–15. doi: 10.1007/s00330-019-06436-w

33. Zhong X, Cao R, Shakeri S, Scalzo F, Lee Y, Enzmann DR, et al. Deep transfer learning-based prostate cancer classification using 3 Tesla multi-parametric MRI. *Abdominal Radiol* (2019) 44:2030–9. doi: 10.1007/s00261-018-1824-5

34. Chen Q, Hu S, Long P, Lu F, Shi Y, Li Y. A transfer learning approach for Malignant prostate lesion detection on multiparametric MRI. *Technol Cancer Res Treat* (2019) 18:1533033819858363. doi: 10.1177/1533033819858363

35. Xu H, Baxter JSH, Akin O, Cantor-Rivera D. Prostate cancer detection using residual networks. *Int J Comput assisted Radiol Surg* (2019) 14:1647–50. doi: 10.1007/s11548-019-01967-5

36. Alkadi R, Taher F, El-Baz A, Werghi N. A deep learning-based approach for the detection and localization of prostate cancer in T2 magnetic resonance images. *J digital Imaging* (2019) 32:793–807. doi: 10.1007/s10278-018-0160-1

37. Viswanath SE, Chirra PV, Yim MC, Rofsky NM, Purysko AS, Rosen MA, et al. Comparing radiomic classifiers and classifier ensembles for detection of peripheral zone prostate tumors on T2-weighted MRI: a multi-site study. *BMC Med Imaging* (2019) 19:1–12. doi: 10.1186/s12880-019-0308-6

38. Muhammad S, Dailey MN, Farooq M, Majeed MF, Ekpanyapong M. Spec-Net and Spec-CGAN: Deep learning models for specularity removal from faces. *Image Vision Computing* (2020) 93:103823. doi: 10.1016/j.imavis.2019.11.001

39. Singh M, Kalaw EM, Jie W, Al-Shabi M, Wong CF, Giron DM, et al. *Cribriform pattern detection in prostate histopathological images using deep learning models*. arXiv preprint arXiv:1910.04030 (2019).

40. Yoo S, Gujrathi I, Haider MA, Khalvati F. Prostate cancer detection using deep convolutional neural networks. *Sci Rep* (2019) 9:1–10. doi: 10.1038/s41598-019-55972-4

41. Bulten W, Pinckaers H, van Boven H, Vink R, de Bel T, van Ginneken B, et al. Automated deep-learning system for Gleason grading of prostate cancer using biopsies: a diagnostic study. *Lancet Oncol* (2020) 21:233–41. doi: 10.1016/S1470-2045(19)30739-9

42. Li J, Li W, Gertych A, Knudsen BS, Speier W, Arnold CW. An attention-based multi-resolution model for prostate whole slide imageclassification and localization. *arXiv preprint arXiv:1905.13208* (2019).

43. Namdar K, Gujrathi I, Haider MA, Khalvati F. Evolution-based fine-tuning of CNNs for prostate cancer detection. *arXiv preprint arXiv:1911.01477* (2019). doi: 10.48550/arXiv.1911.01477

44. Kwon D, Reis IM, Breto AL, Tschudi Y, Gautney N, Zavala-Romero O, et al. Classification of suspicious lesions on prostate multiparametric MRI using machine learning. *J Med Imaging* (2018) 5:034502–2. doi: 10.1117/1.JMI.5.3.034502

45. Lay N, Tsehay Y, Sumathipala Y, Cheng R, Gaur S, Smith C, et al. A decomposable model for the detection of prostate cancer in multi-parametric MRI, in: *Medical Image Computing and Computer Assisted Intervention–MICCAI 2018: 21st International Conference, Granada, Spain, September 16-20, 2018, Proceedings, Part II 11 (Springer)*. (2018) 930–9.

46. Abraham B, Nair MS. Computer-aided classification of prostate cancer grade groups from MRI images using texture features and stacked sparse autoencoder. *Computerized Med Imaging Graphics* (2018) 69:60–8. doi: 10.1016/j.compmedimag.2018.08.006

47. Song Y, Zhang Y-D, Yan X, Liu H, Zhou M, Hu B, et al. Computer-aided diagnosis of prostate cancer using a deep convolutional neural network from multiparametric MRI. *J Magnetic Resonance Imaging* (2018) 48:1570–7. doi: 10.1002/jmri.26047

48. Lemaitre G, Martí R, Rastgoo M, Mériaudeau F. Computer-aided detection for prostate cancer detection based on multi-parametric magnetic resonance imaging, in: *2017 39th Annual International Conference of the IEEE Engineering in Medicine and Biology Society (EMBC) (IEEE)*. (2017) 3138–41.

49. Liu S, Zheng H, Feng Y, Li W. Prostate cancer diagnosis using deep learning with 3D multiparametric MRI. in: *Medical imaging 2017: computer-aided diagnosis* (SPIE). (2017) 10134:581–4. doi: 10.1117/12.2277121

50. Mehrtash A, Sedghi A, Ghafoorian M, Taghipour M, Tempany CM, Wells WM III, et al. Classification of clinical significance of MRI prostate findings using 3D convolutional neural networks. In: *Medical imaging 2017: computer-aided diagnosis* (SPIE). (2017) 10134:589–92. doi: 10.1117/12.2277123

51. Yang X, Liu C, Wang Z, Yang J, Le Min H, Wang L, et al. Co-trained convolutional neural networks for automated detection of prostate cancer in multi-parametric MRI. *Med image Anal* (2017) 42:212–27. doi: 10.1016/j.media.2017.08.006

52. Orenstein EC, Beijbom O. Transfer learning and deep feature extraction for planktonic image data sets, in: *2017 IEEE winter conference on applications of computer vision (WACV) (IEEE)*. (2017) 1082–8.

53. Nolan T. *Spie-aapm-nci prostatex challenges (prostatex)*. (2017), Dataset. doi: 10.7937/K9TCIA.2017.MURS5CL.

54. Perez L, Wang J. The effectiveness of data augmentation in image classification using deep learning. *arXiv preprint arXiv:1712.04621* (2017). doi: 110.3389/fmed.2021.629134

55. Muhammad S, Dailey MN, Sato I, Majeed MF. Handling specularity in intrinsic image decomposition, in: *Image Analysis and Recognition: 15th International Conference, ICIAR 2018, Povoa´ de Varzim, Portugal, June 27–29, 2018, Proceedings 15 (Springer)*. (2018) 107–15.

56. Lemaitre G, Marti R, Meriaudeau F. Computer-aided detection and diagnosis for prostate cancer based on mono and multi-parametric mri: A review. (2015). doi: 10.1016/j.compbiomed.2015.02.009. DatasetJ. F. J. C. V. P. M. W.

frontiers | Frontiers in Oncology

TYPE Original Research
PUBLISHED 23 November 2023
DOI 10.3389/fonc.2023.1247682

OPEN ACCESS

EDITED BY
Fabio Grizzi,
Humanitas Research Hospital, Italy

REVIEWED BY
Baijun Dong,
Shanghai Jiao Tong University, China
Nil Tokgoz,
Gazi University, Türkiye

*CORRESPONDENCE
Tan-Hui Chen
chenth0629@sina.com
Yan-Shun Lin
569091449@qq.com

†These authors share first authorship

RECEIVED 26 June 2023
ACCEPTED 02 October 2023
PUBLISHED 23 November 2023

CITATION
Zhao Y-Y, Xiong M-L, Liu Y-F, Duan L-J, Chen J-L, Xing Z, Lin Y-S and Chen T-H (2023) Magnetic resonance imaging radiomics-based prediction of clinically significant prostate cancer in equivocal PI-RADS 3 lesions in the transitional zone. *Front. Oncol.* 13:1247682. doi: 10.3389/fonc.2023.1247682

Magnetic resonance imaging radiomics-based prediction of clinically significant prostate cancer in equivocal PI-RADS 3 lesions in the transitional zone

Ying-Ying Zhao[1†], Mei-Lian Xiong[2†], Yue-Feng Liu[3], Li-Juan Duan[1], Jia-Li Chen[1], Zhen Xing[2], Yan-Shun Lin[1*] and Tan-Hui Chen[2*]

[1]Department of Radiology, Fuqing City Hospital Affiliated to Fujian Medical University, Fuqing, China, [2]Department of Radiology, The First Affiliated Hospital of Fujian Medical University, Fuzhou, China, [3]Department of Ophthalmology Surgery, Taihe Hospital, Hubei University of Medicine, Shiyan, China

Purpose: This bi-institutional study aimed to establish a robust model for predicting clinically significant prostate cancer (csPCa) (pathological grade group ≥ 2) in PI-RADS 3 lesions in the transition zone by comparing the performance of combination models.

Materials and methods: This study included 243 consecutive men who underwent 3-Tesla magnetic resonance imaging (MRI) and ultrasound-guided transrectal biopsy from January 2020 and April 2022 which is divided into a training cohort of 170 patients and a separate testing cohort of 73 patients. T2WI and DWI images were manually segmented for PI-RADS 3 lesions for the mean ADC and radiomic analysis. Predictive clinical factors were identified using both univariate and multivariate logistic models. The least absolute shrinkage and selection operator (LASSO) regression models were deployed for feature selection and for constructing radiomic signatures. We developed nine models utilizing clinical factors, radiological features, and radiomics, leveraging logistic and XGboost methods. The performances of these models was subsequently compared using Receiver Operating Characteristic (ROC) analysis and the Delong test.

Results: Out of the 243 participants with a median age of 70 years, 30 were diagnosed with csPCa, leaving 213 without a csPCa diagnosis. Prostate-specific antigen density (PSAD) stood out as the only significant clinical factor (odds ratio [OR], 1.068; 95% confidence interval [CI], 1.029–1.115), discovered through the univariate and multivariate logistic models. Seven radiomic features correlated with csPCa prediction. Notably, the XGboost model outperformed eight other models (AUC of the training cohort: 0.949, and validation cohort: 0.913). However, it did not surpass the PSAD+MADC model ($P > 0.05$) in the training and testing cohorts (AUC, 0.949 vs. 0.888 and 0.913 vs. 0.854, respectively).

Conclusion: The machine learning XGboost model presented the best performance in predicting csPCa in PI-RADS 3 lesions within the transitional

zone. However, the addition of radiomic classifiers did not display any significant enhancement over the compound model of clinical and radiological findings. The most exemplary and generalized option for quantitative prostate evaluation was Mean ADC+PSAD.

KEYWORDS

magnetic resonance imaging, prostate cancer, PI-RADS, transitional zone, radiomics

1 Introduction

Prostate cancer is the most common cancer affecting men worldwide (1), with a lifetime risk as high as 37% (2). By 2040, global prostate cancer incidences are projected to rise to nearly 2.3 million new cases and 740 000 deaths (3). Multi-Magnetic resonance imaging (mpMRI) of the prostate, which helps improve the detection, localization, and staging of prostate cancer (PCa), has been established as the de facto standard for the imaging assessment of suspected PCa (4). A large-sample study demonstrated that utilizing MRI for initial screening before biopsy can minimize needless biopsies by approximately half for cases with a PI-RADS score of 3 or higher, and prevent the overdiagnosis of clinically insignificant lesions (5).

The Prostate Imaging Reporting and Data System (PI-RADS) has undergone continuous refinement and updates since its conception, allowing for more standardized assessments of prostate lesions. The most recent iteration, PI-RADSv2.1 revised in 2019, standardizes the terminology, interpretation, and contents of MRI reports (6). Lesions are classified into five categories (1 to 5), based on their anatomical location and MRI signal changes. Higher categories correlate with a higher probability of detecting clinically significant prostate cancer (csPCa). Lesions categorized as PI-RADS 1 and 2 bear an exceedingly low cancer detection rate (CDR) of less than 5% (7, 8) and necessitate only follow-up. In contrast, lesions classified as PI-RADS 4 and 5 have an extremely high CDR (40–80%) (7, 8) calling for further biopsy. However, PI-RADS 3 lesions present a moderate CDR, indicating an ambiguous risk of malignancy.

PI-RADS 3 lesions are frequently identified in patients undergoing MRI examinations, with reported incidences ranging from 22%–32% (9); However, most studies indicate a relatively low detection rate for csPCa, between 2%–22.9% (10, 11). Concurrently, the false negative rate for csPCa is notably high at 16.2% for cases with PI-RADS scores of 3 or higher (5). Current guidelines offer no explicit direction for subsequent treatment of PI-RADS 3 lesions, thereby presenting a dilemma for urologists in deciding between follow-up prostate-specific antigen (PSA) testing and imaging monitoring, or immediate biopsy. It is crucial to selectively submit patients likely to have csPCa to undergo prostate biopsy, maximizing the benefits from the procedure and potential aggressive treatment strategies.

Although the implementation of PI-RADSv2.1 has boosted the precision in identifying csPCa, PI-RADS 3 lesions remain elusive within the "gray zone" of mpMRI evaluations, especially for the transition zone (TZ). Benign prostatic hyperplasia, a common condition in elderly men, creates a degree of organized chaos within the TZ, hampering accurate lesion categorization (12). Recent studies suggest exploiting radiomic features and mean apparent diffusion coefficient (ADC) values to quantitively evaluate MRI enhances diagnostic accuracy for TZ lesions over mere qualitative PI-RADS assessment (13–15). Engel et al. reported that the risk stratification for prostatic TZ lesions could be improved through a quantitative diffusion-weighted imaging (DWI) analysis (4). Another study demonstrated an achievable specificity and sensitivity through downgrading PI-RADS lesions at or above 4 based on mean ADC values or machine learning algorithms (15). Ultimately, radiomics hold potential in algorithmically identifying csPCa in PI-RADS 3 lesions (13–16). A greater balance between biopsy-associated complications, overdiagnosis, and overlooking csPCa diagnosis might be achieved using radiomics prostate MRI. For patients with both PI-RADS 3 and a low risk of csPCa, immediate biopsy can possibly be deferred. However, previous studies of this nature typically involved smaller cohorts from a single institution and lacked distinction between PZ and TZ lesions (17).

Therefore, we hypothesized that the characteristics of detected TZ lesions can be improved through radiomics. This study aimed to assess different algorithm models for risk stratification among patients with PI-RADS 3 in the TZ, using a combination of individual clinical characteristics and radiological data.

2 Materials and methods

2.1 Demographic information and clinical data

This retrospective study included patients from two institutions (The First Affiliated Hospital of Fujian Medical University and Fuqing Hospital). The institutional ethics committee approved this study and waived the requirement for informed consent. Data were retrospectively collected from men who underwent MRI and biopsy examinations between January 2020 and April 2022 according to the following eligibility criteria: (a) men with PI-RADS 3 lesions (v2.1 standard), (b) PI-RADS 3 lesions confirmed by pathology and matched to the MR images in the same region, and (c) ultrasound-guided prostate biopsy or radical surgery performed within 1 month of the MRI examination. The exclusion criteria were: (a) biopsy or a history of treatment (antihormonal therapy, radiation therapy, focal

therapy, or prostatectomy) for prostate cancer prior to the MRI examination, (b) multiple primary cancers or a previous history of cancer, (c) incomplete sequences or severe artefacts on MRI images, and (d) any PI-RADS 4 or 5 lesions. Figure 1 presents the flowchart of the inclusion and exclusion criteria of the study.

The following clinical and laboratory data were collected: age, the most recent serological value of total prostate-specific antigen (tPSA; ng/mL), free prostate-specific antigen (fPSA; ng/mL), fPSA/tPSA (f/t), prostate volume(V), PSA density (total PSA/prostatic volume ratio [PSAD]) during MRI examination and final histopathological analysis, and mean ADC value (mm^2/s). The mean ADC value was calculated in volumes of interest (VOIs), encompassing the entire lesion without exceeding the lesion margins. Table 1 presents the baseline epidemiologic and clinical characteristics, including tumor location, pathological findings, and clinical assessment.

A 12-core systematic biopsy was performed by urologists with three to five years of transrectal ultrasound-guided prostate biopsy experience. Based on biopsy results, the patients were divided into two cohorts: the csPCa and no csPCa (benign and Grade Group 1 [GG1]) groups. The primary endpoint of csPCa was defined as patients with≥GG2 (Gleason 3 + 4) prostate cancer.

2.2 MRI examination

During the study period, prostate MRI was performed at Institution 1 using a 3.0T scanner (Spectra; Siemens Healthineers), whereas it was performed using a 3.0T MRI system (Philips Ingenia, Amsterdam, the Netherlands) at Institution 2. Standard multichannel body coils and integrated spine phased-array coils were used according to the guidelines of the European Society of Urogenital Radiology (18). Appendix Table 1 summarizes the details of the MRI protocols of each institution.

2.3 MRI lesion segmentation

To confirm that the lesions were classified as PI-RADS 3 as per the PI-RADS v2.1 guidelines, the MR images were interpreted by two radiologists (Y. Y. Z. and M. L. X.) with 6 and 10 years of experience in prostate MRI interpretation, respectively, who were blinded to the pathological data. In cases of disagreement, a final consensus was reached by re-reading.

Axial T2-weighted and diffusion-weighted images in DICOM format were downloaded from the picture archiving and communication system (PACS). The MRI index lesions were manually segmented by an investigator (Y. Y. Z.). Given the importance of heterogeneity analysis while avoiding partial volume effects, VOIs encompassing the entire lesion, including bleeding, necrosis, and cystic areas, the urethra, ejaculatory duct, and other normal anatomical structures were drawn on each slice with the lesion. Segmentation was performed under the supervision of another radiologist (T.H.C. with 20 years of experience in prostate MRI), using the dedicated software ITK-SNAP (version 3.8.0 for Win,

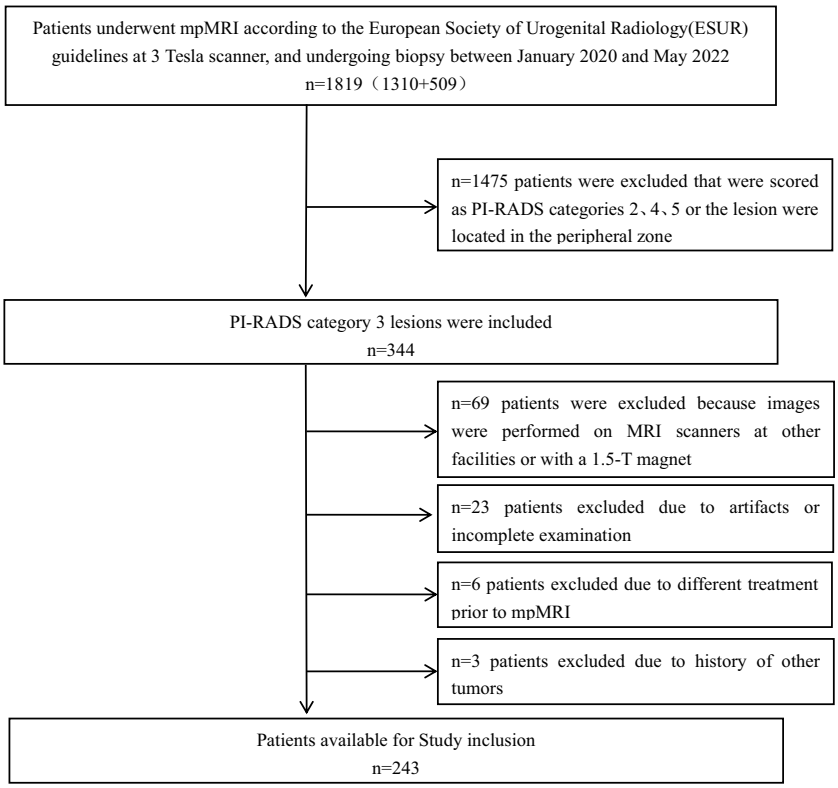

FIGURE 1
Flowchart of the study population.

10.3389/fonc.2023.1247682

TABLE 1 The Characteristics of Demographic and Clinical Data of Patients with PIRADs 3 Lesions on MRI.

	level	Overall	No csPCa	csPCa	*p*
n		(n=243)	(n=213)	(n=30)	
GGG (%)	0	183 (75.3)	183 (85.9)	0 (0.0)	<0.001
	1	30 (12.3)	30 (14.1)	0 (0.0)	
	2	19 (7.8)	0 (0.0)	19 (63.3)	
	3	8 (3.3)	0 (0.0)	8 (26.7)	
	4	3 (1.2)	0 (0.0)	3 (10.0)	
age (median [IQR])		70	70	72	0.026
		[66.00, 75.00]	[65.00, 74.00]	[68.00, 76.00]	
MADC (median [IQR]×10-4)		8.22	8.39	6.98	<0.001
		[7.51, 8.83]	[7.68, 8.91]	[6.43, 7.75]	
MT2WI (median [IQR]×102)		2.85	2.85	2.81	0.742
		[2.52, 3.38]	[2.54, 3.38]	[2.42, 3.53]	
RT2WI (median [IQR])		3.05	3.06	2.98	0.346
		[2.66, 3.40]	[2.66, 3.43]	[2.75, 3.18]	
V (median [IQR])		50	51.94	43.04	0.012
		[35.19, 66.60]	[35.70, 69.18]	[23,68, 52.56]	
PSAD (median [IQR]×10-2)		17.69	16.54	38.34	<0.001
		[10.10, 29.32]	[9.81, 25.38]	[19.19, 53.07]	
tPSA (median [IQR])		8.65	8.38	10.67	0.009
		[5.23, 13.55]	[5.07, 12.30]	[8.17, 19.18]	
fPSA (median [IQR])		1.45	1.42	1.94	0.029
		[0.95, 2.20]	[0.90, 2.14]	[1.35, 2.78]	
f/t (median [IQR])		0.17	0.17	0.13	0.044
		[0.12, 0.22]	[0.14, 0.22]	[0.10, 0.20]	

GGG, Gleason grade group; MADC,mean apparent diffusion coefficient; V, the volume of prostate; PSAD, prostate specific antigen density; tPSA, total prostate specific antigen; fPSA,free prostate specific antigen; f/t,fPSA/tPSA.

http://www.itksnap.org/). In addition, segmentation was also performed separately on axial T2-weighted and ADC images. The background obturator internus in the corresponding or adjacent layers was segmented for reference, excluding the muscle steatosis area while encompassing at least 50 voxels in at least three adjacent sections.

For the intraobserver and interobserver agreement evaluation in manual segmentation, we randomly selected 50 patients, and their ROIs were delineated 1 month later by the same radiologists (Y. Y. Z. and M. L. X.).

2.4 Image postprocessing and analysis

T2-weighted images were normalized by dividing the voxel intensities by the mean value of the background obturator internus tissue. Since ADC is a quantitative measurement, it was not normalized. Radiomic feature calculations were performed using the pyradiomics package of Python 3.7.1. (https://github.com/Radiomics/pyradiomics) (18) according to the analytical steps depicted in Figure 2. Within each VOI, 14 volume and shape features, 198 first-order histogram features, 264 grey-level co-occurrence matrix (GLCM) features, 154 grey-level dependence matrix (GLDM) features, 176 grey-level run length matrix (GLRLM) features, 176 grey-level size zone matrix (GLSZM) features, and 55 neighboring grey tone difference matrix (NGTDM) features were calculated, resulting in 1037 features per VOI. These features were calculated on both the ADC maps and T2-weighted images; thus, a total of 2074 radiomics features were obtained for each lesion.

2.5 Radiomics feature selection and signature building

All patients were randomly stratified into the training and testing cohorts in a 7:3 ratio. The mean ADC was extracted from the

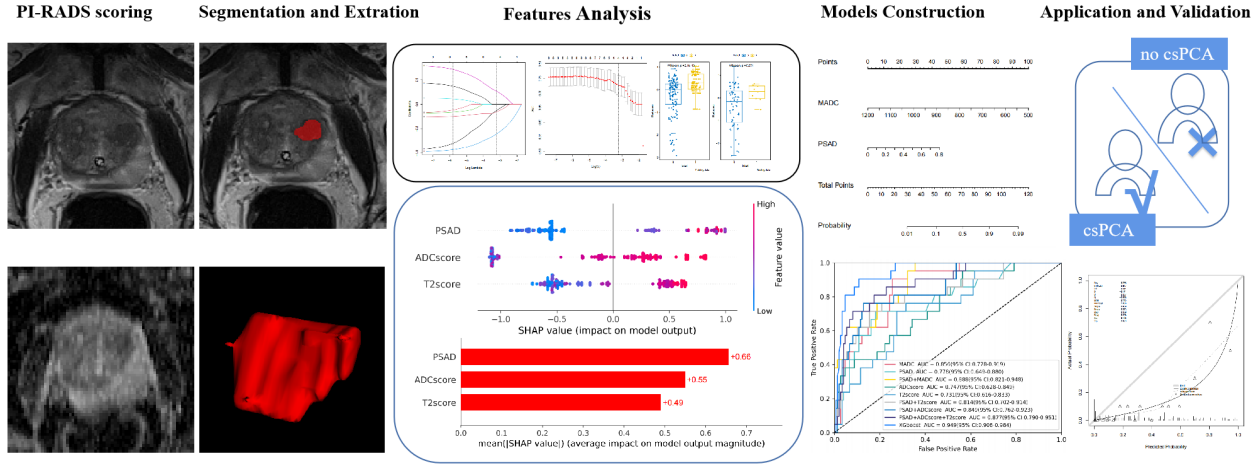

FIGURE 2
Radiomics analysis workflow. Radiomics features were extracted from both T2-weighted images (T2WI) and apparent diffusion coefficient (ADC) maps. The Student's *t*-test or Mann–Whitney U-test and the least absolute shrinkage selection operator were used for feature selection, and the models were constructed based on logistic regression and XGboost methods for predicting clinically significant prostate cancer.

radiomic dataset for separate analyses. Missing data were analyzed using the Random Forest Multiple Interpolation method (R language mice package). The features with ICC < 0.75 were filtered out. Subsequently, upsampling was used to address sample imbalance in the training cohort, and the Student's *t*-test or Mann–Whitney U-test was used for preliminary feature selection, which was determined using the Shapiro–Wilk and Levene's tests. The least absolute shrinkage selection operator (LASSO)-logistic regression model was used to select the predictive features, and the radiomics signature (rad score) was calculated by adding the selected radiomics features, weighted by their respective coefficients. This procedure was performed separately on the T2-weighted and ADC images.

2.6 Creation and verification of model

Multivariate logistic regression analysis was used to identify independent predictive clinical factors. Prediction models were established based on clinical variables (clinical model), radiological features (radiological model), radiomic signatures (radiomics Model), and a combination of clinical variables, radiological features, and radiomics features (logistic regression and XGboost models) to generate a quantitative predictive tool for csPCa diagnosis. Calibration curves were used to evaluate the robustness of the model. Decision curve analysis (DCA) was used to evaluate the net benefit of the model for clinical decision-making at different threshold probabilities.

2.7 Statistical analysis

For demographic data, continuous variables were analyzed using Student's *t*-test or Mann–Whitney U test, as determined by Shapiro–Wilk and Levene's test. Continuous variables with normal distribution were presented as mean ± standard deviation. Continuous variables with non-normal distribution were presented as median (inter-quartile range [IQR]). Categorical variables were analyzed using the chi-square test or Fisher's exact test. Univariate and multivariate logistic regression analyses were used to identify the significant predictors of csPCa. LASSO logistic regression analysis was used for screening the predictive radiomics features. The eXtreme Gradient Boosting (XGboost) model was created with stratified 10-fold cross-validation, and a grid search was performed to identify the optimal hyperparameters for training using the GridSearchCV function in Scikit-learn (estimated by ten-fold cross-validation). The diagnostic performance of different models for the prediction of csPCa was assessed using receiver operating characteristic (ROC) curve analysis and by calculating the accuracy, sensitivity, specificity, and area under the ROC curve (AUC) with 95% CI. The Delong test was used to compare the performance of the different models, regardless of whether they differed significantly. All data analyses were performed using Python (version 4.0.1; https://www.r-project.org) and R (version 3.7.3; https://www.python.org/downloads/) software. All tests were two-sided, with statistical significance set at $P \leq 0.05$.

3 Results

3.1 Demographic information and clinical data

This study included 243 patients (median age, 70 years; IQR, 66–75 years). Prostate biopsy revealed that 213 (87.6%) patients did not have csPCa [183(75.3%) men had no cancer, and 30 (12.3%) had GG1], and 30 (12.3%) patients had csPCa. The detection rate for csPCa was equal to 13.7% (23/168 cases) vs 9.3% (7/75 cases) with PI-RADS 3 lesions diagnosed in the institution 1 vs the institution 2. The median PSA level was 8.65 ng/ml, with a mean prostate volume was 50.0 mL, and the median PSAD was 0.17 ng/mL^2. The patients were randomly allocated

to the training (N = 170) and testing (N = 73) cohorts. Table 1 presents the results of the comparison between the clinical factors of the csPCa and no csPCa groups.

3.2 Radiomics features selection and signature building

Initially, 2074 features were generated from the original T2-weighted and ADC imaging data, and 233 features related to csPCa diagnosis were selected. Highly correlated features were discarded (correlation between two variables > 0.6). Subsequently, the seven most predictive features were selected from the T2-weighted and ADC images using LASSO-logistic regression (Figure 3 and Table 2). The radiomic signature was then calculated by weighting their respective coefficients. The boxplot depicted in Figure 3 presents the differences between the two groups.

3.3 Development and validation of individualized logistic prediction models

Univariable logistic regression analysis of all potential factors identified age (odds ratio [OR], 1.075; 95% confidence interval [CI], 1.006–1.153), V (OR, 0.987; 95% CI, 0.974–0.998), PSAD (OR, 1.07; 95% CI, 1.034–1.113), and MADC (OR, 0.242; 95% CI, 0.126–0.422) as the independent parameters for csPCa prediction. When age, V, PSAD, and MADC were included in the multivariate logistic regression analysis, only PSAD and MADC remained significantly correlated with tumor diagnosis (Table 3). Table 4 presents the eight models built for predicting csPCa using radiomics, a clinical variable, and the MADC values.

3.4 Development of the XGboost prediction model

Clinical factors (PSAD) and radiomic signatures were identified as the predictors most significantly associated with csPCa diagnosis. Therefore, these three features were employed as the input variables, whereas diagnostic efficiency was considered the output variance. The XGboost model hyperparameters were optimized using grid search and ten-fold cross-validation. The other parameters were set to default values. The detailed weights of the trained XGboost with the PSAD, T2 score, and ADC score for predicting csPCa are presented in Figure 4.

3.5 Performance comparisons of models

As shown in Tables 4, 5, and Figure 5, MADC was found to be the best-performing single-parameter model, with an AUC of 0.856 (95% CI, 0.782–0.923), and 0.788 (95% CI, 0.628–0.920) in the training and testing cohorts, respectively (Figure 4 and Table 4). The best combined models were PSAD + MADC (AUC, 0.888 [95% CI, 0.814–0.943], and

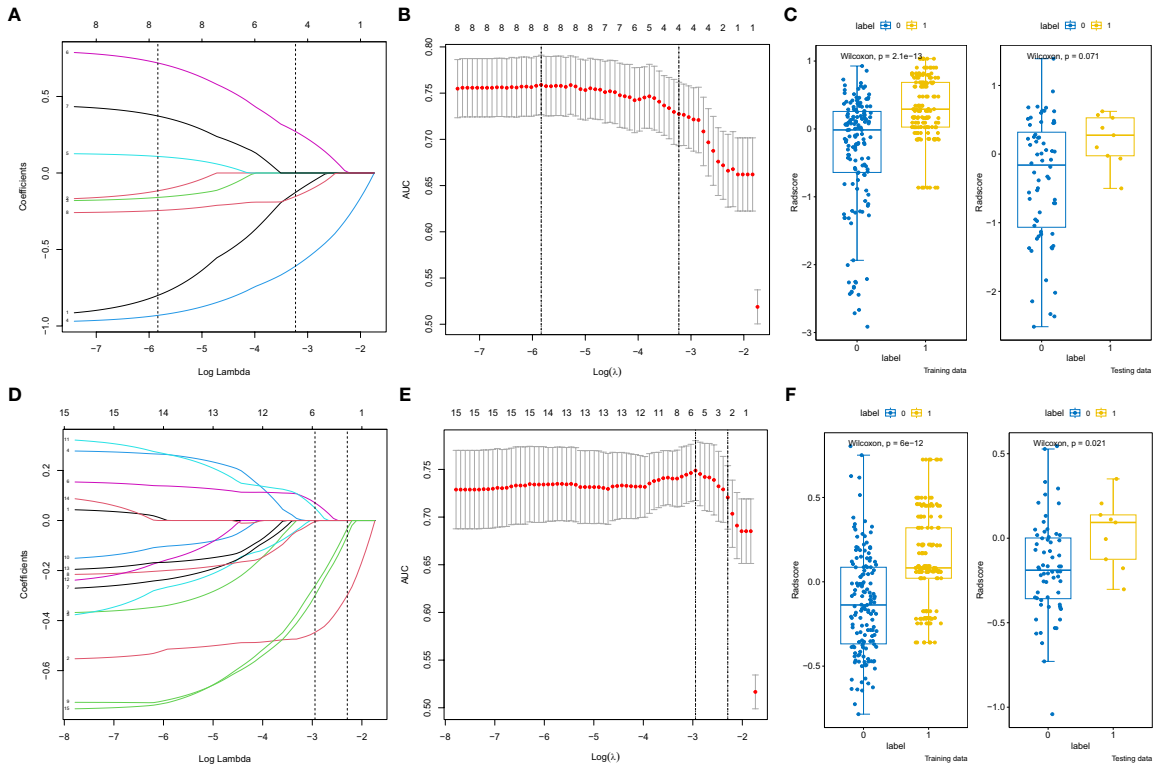

FIGURE 3
Radiomics features selection by the least absolute shrinkage selection operator. **(A, D)** Coefficient profiles of radiomics features of the apparent diffusion coefficient (ADC) and T2-weighted images (T2WI). **(B, E)** The adjustment penalty parameter λ is -3.229 ×10^{-4} and -2.294×10^{-4} for the ADC and T2WI, and seven features were selected according to 10-fold cross-validation. **(C, F)** The boxplot of radscores of the csPCa and No csPCa groups in the training and testing cohorts of the ADC and T2WI.

TABLE 2 The final 7 radiomics features selected from T2WI and ADC.

Features	Coef	OR
ADC.wavelet.HLH_glszm_SizeZoneNonUniformityNormalized	-0.60887	0.543965
ADC.wavelet.LLL_firstorder_10Percentile	-0.15362	0.857601
ADC.exponential_firstorder_Energy	-0.12684	0.880874
ADC.wavelet.HHL_glrlm_LongRunHighGrayLevelEmphasis	0.270977	1.311245
T2WI.original_shape_Sphericity	-0.29877	0.741728
T2WI.wavelet.LHL_glcm_MCC	-0.06151	0.940344
T2WI.wavelet.LLL_gldm_LargeDependenceLowGrayLevelEmphasis	-0.03154	0.968952

0.854 [95% CI, 0.733–0.952] in the training and testing cohorts, respectively) and PSAD + ADC score + T2 score (0.877 [95% CI, 0.791–0.954], and 0.812 [95% CI, 0.684–0.920] in the training and testing cohorts, respectively) (Figure 5 and Table 4). However, they showed no evidence of improvement compared with the MADC model (P =0.162 and P = 0.687 in the training cohorts, respectively, and P =0.303 and P = 0.818 in the testing cohorts, respectively).

The XGboost model demonstrated the highest performance for predicting csPCa, with an AUC of 0.949 (95% CI, 0.904–0.983) and 0.913 (95% CI, 0.816–0.984) in the training and testing cohorts, respectively. Significant differences were observed between the AUCs of the XGboost model and the other five models (PSAD, ADC score, T2 score, PSAD + ADC score, and PSAD + ADC score + T2 score) (Figure 4 and Tables 4, 5). The AUCs of the training cohort were 0.949 vs. 0.778 vs. 0.747 vs. 0.731 vs. 0.849 vs. 0.877. The AUCs of the validation cohort were 0.913 vs. 0.620 vs. 0.688 vs. 0.740 vs. 0.757 vs. 0.812. However, it did not outperform the PSAD+MADC model (AUC, 0.949 vs. 0.888 and 0.913 vs. 0.854, respectively) ($P > 0.05$) in the training and testing cohorts, respectively.

4 Discussion

Precise definition of PI-RADS 3 lesions in the transition zone (TZ) presents a significant challenge due to the atypical imaging features associated with these lesions. This is complicated by the reality that malignant epithelial cells often associated with csPCa are, in this classification, usually distributed sparsely and arranged around the acinar structures. Subsequently, csPCa imaging and benign conditions like hyperplasia, inflammation, and fibrosis can exhibit significant overlap (19). This can result in near imperceptible changes to MRI signal, leading to high rates of interpretation migration and fair inter-observer agreement (20). Furthermore, prostatic hyperplasia in elderly men, predominantly originating in the TZ, is intrinsically heterogeneous and comprises ill-defined tissues, often mistaken for csPCa due to their cellular and vascular nature (12). Currently, there is a shortage of effective means to refine lesion classification, leaving clinical management unclear.

Radiomic analysis provides a non-invasive tool using existing MRI images to obtain data about target organs and tissues. Its strength lies in eliminating subjective interpretation and observer reliance, concurrently analyzing hundreds of imaging features. This allows for a thorough characterization of tumor heterogeneity, reflecting tumor cellularity, proliferation, angiogenesis, hypoxia, and necrosis (21). Guiding classification, risk stratification, and clinical decision-making measures for suspicious lesions form key aspects of its performance duties (16, 22, 23). Consequently, radiomic analysis shows immense potential in distinguishing csPCas from painless or benign cases (22, 23).

Several studies have probed into the function of radiomics in prostate imaging (24–26). Hou et al. evaluated radiomics machine

TABLE 3 Results of univariate and multivariate logistic regression analyses.

Facotrs	Uni_OR	Uni_95%CI	Uni_P	Mul_OR	Mul_95%CI	Mul_*P*
age	1.075	(1.006~1.153)	0.036	1.067	(0.968~1.178)	0.188
T	1.034	(0.99~1.076)	0.117	–	–	–
F	1.276	(0.969~1.654)	0.07	–	–	–
F/T	0.174	(0~1.228)	0.588	–	–	–
V	0.987	(0.974~0.998)	0.035	0.995	(0.981~1.008)	0.506
PSAD	1.07	(1.034~1.113)	<0.001	1.068	(1.029~1.115)	0.001
MT2WI	0.902	(0.525~1.373)	0.666	–	–	–
RT2WI	0.854	(0.356~1.96)	0.715	–	–	–
MADC	0.242	(0.126~0.422)	<0.001	0.231	(0.107~0.437)	<0.001

TABLE 4 The performance of different models in training and testing cohorts for predicting tumor diagnosis in csPCa patients.

	Model	AUC (95% CI)	Accuracy	Sensitivity	Specificity
Training	MADC	0.856 (0.782-0.923)	0.765	0.905	0.745
	PSAD	0.778 (0.661-0.888)	0.806	0.714	0.819
	ADCscore	0.747 (0.640-0.850)	0.5	0.952	0.436
	T2score	0.731 (0.616-0.838)	0.694	0.762	0.685
	PSAD+MADC	0.888 (0.814-0.943)	0.688	1	0.644
	PSAD+T2score	0.814 (0.689-0.913)	0.829	0.714	0.846
	PSAD+ADCscore	0.849 (0.752-0.929)	0.859	0.762	0.872
	PSAD+ADCscore+T2score	0.877 (0.791-0.954)	0.824	0.81	0.826
	XGboost	0.949 (0.904-0.983)	0.894	0.905	0.893
Testing	MADC	0.788 (0.628-0.920)	0.699	0.778	0.688
	PSAD	0.620 (0.371-0.846)	0.795	0.556	0.828
	ADCscore	0.688 (0.540-0.818)	0.548	0.889	0.5
	T2score	0.740 (0.557-0.882)	0.767	0.556	0.797
	PSAD+MADC	0.854 (0.733-0.952)	0.63	0.889	0.594
	PSAD+T2score	0.809 (0.676-0.922)	0.781	0.556	0.812
	PSAD+ADCscore	0.757 (0.627-0.877)	0.74	0.333	0.797
	PSAD+ADCscore+T2score	0.812 (0.684-0.920)	0.822	0.667	0.844
	XGboost	0.913 (0.816-0.984)	0.904	0.889	0.906

MADC, mean ADC; PSAD, PSA density; XGboost, XGboost machine learning model.

learning (ML) models and reported an enhanced risk stratification, superior to subjective radiologist evaluation for identifying csPCa in PI-RADS v2 category 3 lesions, with the AUC of radiomics ML models ranging from 0.87–0.89 (24). In a different study, Li et al. utilized a support vector machine (SVM) classification to stratify the Gleason Score (GS) of prostate cancer in the central gland using mpMRI. This approach showcased exceptional performance, with AUC values oscillating between 0.97 (CI 0.94–0.99) and 0.91 (CI 0.85–0.95) (25). Schelb et al. used a U-Net trained with T2-weighted and diffusion-weighted images, thereby achieving a performance on par with that of PI-RADS assessment (26). These studies collectively attest to the superior performance of radiomics in detecting prostate lesions.

Our study exhibits a classification capability that is, at the very least, comparable to those reported in the literature, thereby reiterating the utility of radiomics in prostate MRI. As reported in Table 4, the XGboost model showed the best performance, with AUC values of 0.949 and 0.913 in the training and testing cohorts, respectively. This indicates the XGboost model's robust capacity to recognize csPCa, indicating that machine learning's potential as an efficient and noninvasive instrument for the prediction of csPCa in PI-RADS 3 lesions. Commonly deployed to address classification issues, XGboost stands as the most accurate model for predicting 1-year survival among non-small cell lung cancer patients diagnosed with bone metastases (27). XGboost can also infer the tissue sources of 10 unique cancer types and outperforms traditional machine learning algorithms (28).

The predictive potential of clinical and radiological biomarkers for diagnosing prostate cancer associated with equivocal PI-RADS 3 lesions undergoing biopsy has been evaluated positively in previous studies (29, 30). For instance, Brancato et al. concluded that the most vital feature for the detection of cancer in PI-RADS 3 lesions was based on ADC maps (31). Our data also supported the use of quantitative ADC measurements for decision-making in PI-RADS 3 lesions, with AUC of 0.856 (0.782–0.923) and 0.788 (0.628–0.920) in the training and testing cohorts, respectively. Efficient at discerning the microenvironment of neoplastic tissues, ADC can identify alterations in compartmental volumes, such as stroma, epithelium, and lumen space, and cellularity (32), It currently serves as best parameter for prostate MRI assessment (4, 33). Moreover, ADC has been consistently proven to be inversely correlated with factors like tumor grade, tumor aggressiveness, and pathological stage (34–36). We compared the performance of the mean ADC with biparametric radiomics to assess whether it had an added value over that of machine learning. The Delong test results revealed superior performance from XGboost models as opposed to the mean ADC model in the training cohorts. However, this superiority was not replicated in the testing cohorts. Moreover, it did not outperform the PSAD+MADC model (AUC, 0.949 vs. 0.888 and 0.913 vs. 0.854, respectively) ($P > 0.05$) in both the training and testing cohorts. Thus, within the context of our study, ADC values remained the most decisive parameter, aligning with previous studies' findings (33, 36). Bonekamp et al. (36) compared the performance of biparametric contrast-free radiomics with that of

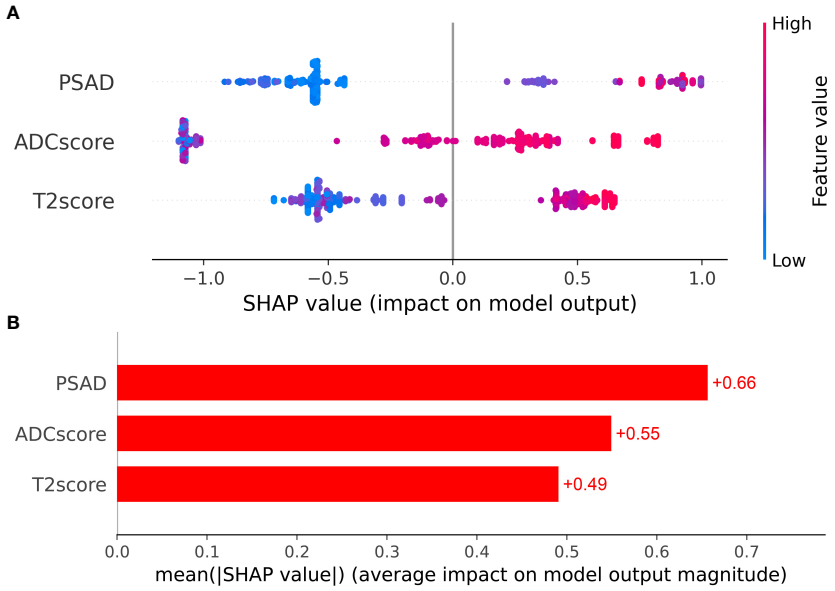

FIGURE 4
(A) The Beeswarm plot depicts the predictive value of each feature for each patient, and **(B)** the bar plot depicts the importance of each feature.

machine learning for detecting csPCa, also concluded that the performance of radiomic machine learning did not exceed that of the mean ADC. This finding is coherent with the results observed in our study.

However, several differences from the present study should be noted. Prior studies did not conduct separate analyses for peripheral zone (PZ) and TZ lesions. Given that the lesion characteristics significantly differ between PZ and TZ, and the primary sequences vary, it is recommended to perform targeted analysis based on lesions in different zones rather than combining them. Second, some studies exploring the intelligent diagnosis of PI-RADS 3 lesions were confined to basic radiomic features (33, 35, 36) and overlooked the additional diagnostic value of clinical indicators. Compared with these similar studies, the present study evaluated clinical features associated with csPCa, encompassing age, tPSA, fPSA, fPSA/tPSA, prostate volume, and PSA density. However, only one of these, specifically PSAD, proved useful for building predictive models.

MRI application as an adjuvant examination rather than a clinical triage tool can pose challenges, considering negative

TABLE 5 The performance comparisons of different models in training and testing cohorts.

Model	MADC	PSAD	PSAD + MADC	ADCscore	T2score	PSAD + T2score	PSAD + ADCscore	PSAD + ADCscore + T2score	XGboost
MADC	/	0.219	0.162	0.099	0.046	0.505	0.909	0.687	0.023
PSAD	0.322	/	0.014	0.674	0.467	0.247	0.019	0.005	0.000
PSAD + MADC	0.303	0.06	/	0.031	0.007	0.132	0.357	0.805	0.075
ADCscore	0.367	0.684	0.078	/	0.857	0.38	0.047	0.018	0.000
T2score	0.653	0.519	0.295	0.534	/	0.049	0.061	0.002	0.000
PSAD + T2score	0.846	0.043	0.513	0.19	0.493	/	0.377	0.022	0.001
PSAD + ADCscore	0.771	0.183	0.146	0.337	0.88	0.304	/	0.18	0.004
PSAD + ADCscore + T2score	0.818	0.158	0.611	0.017	0.34	0.953	0.307	/	0.003
XGboost	0.133	0.038	0.368	0.000	0.008	0.098	0.015	0.018	/

Based on Delong.test, the upper right of the diagonal (yellow) was the P value of model comparisons in the training set, and the down left of the diagonal (blue) was the P value of model comparisons in the testing set.

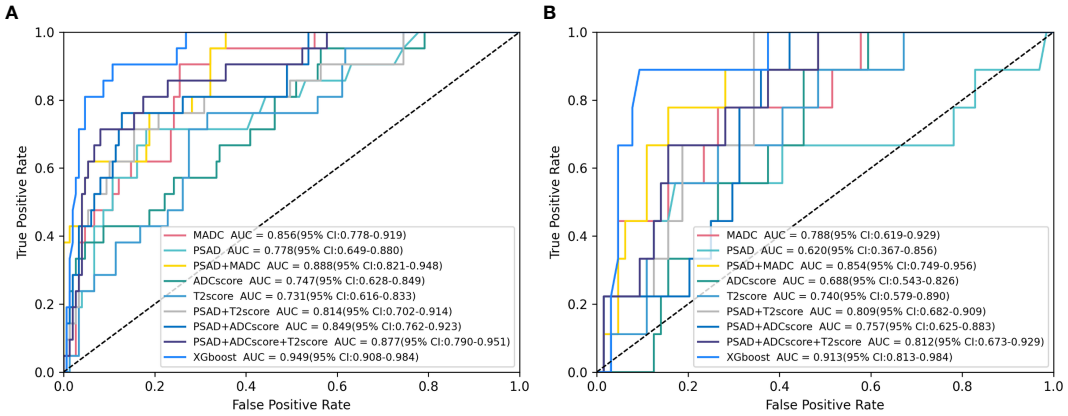

FIGURE 5
Receiver operating characteristic (ROC) analysis of the parameter models in clinically significant prostate cancer (csPCa) of PI-RADS 3 Lesions prediction. **(A, B)** ROC curves for selected logistic models and XGboost models tested for csPCa prediction in the **(A)** training cohort and **(B)** testing cohort. Plus signs indicate parameter combinations in the multivariable models, and data in brackets are 95% confidence intervals. See Table 4 for corresponding area under the ROC curve (AUC) values and additional models.

findings do not necessarily discourage further progression to a biopsy, potentially leading to overtreatment (37). Integrating MRI findings with PSAD may mitigate these concerns. PSAD also constitutes an essential component of the best-performing XGboost model in this study, and has been extensively investigated in several studies (38–40). A large multi-institutional collaborative study showed that among the men with a solitary PI-RADS 3 lesion on MRI, nearly 87% of those with a low PSAD had no or only GG1 prostate cancer. In contrast, as PSAD increases, the rate of csPCa detection increases to more than one-third of men biopsied (37). Several studies have identified an independent association of PSAD with csPCa, even in patients with serum PSA levels slightly exceeding or within the normal range–a common occurrence across various clinical scenarios, such as early diagnosis, repeat biopsy, and active surveillance (38). Roscigno et al. (39) reported that higher PSAD was associated with an elevated risk of reclassification, with 0.20 as the threshold in definitive or follow-up biopsy. Washino et al. (40) increased the negative predictive value (NPV) of PI-RADS from 0.84 to 0.96 by using PSAD with a cut-off value of 0.15 ng/mL/cc. Ullrich et al. (41) concluded that if the PSAD cut-off was 0.15 ng/mL^2, 53% of patients with a PI-RADS v2 score of 3 would have avoided biopsy.

In our study, the predictive performance of radiomics machine learning models did not surpass that of the comprehensive model combining clinical variables and radiological features (MADC + PSAD). This may change with the development of next-generation machine learning techniques for larger-scale cohorts in multicentric setups, as machine learning methods rely on large amounts of training and testing data. These tools typically do not require segmentation or handcrafted radiomic features. In the current study, more traditional machine learning methods were used due to the relatively small sample size and number of csPCa cases.

Our study had several limitations. The retrospective design of this study, combined with the lack of results from radical prostatectomy specimens as a reference standard, means that selection bias and biopsy bias are potential issues. In addition, the PI-RADS 3 dataset is notably small and imbalanced. A more sizable, balanced study group would better facilitate radiomic analyses and aid in formulating robust predictive models. Lastly, identifying PI-RADS 3 lesions can prove challenging, making some lesions ambiguous.

5 Conclusions

Radiomics–based algorithms, notably the XGboost models, demonstrated substantial proficiency in predicting csPCa in PI-RADS 3 lesions in TZ. This could potentially elevate the rate of prostate-positive biopsy for PI-RADS 3 while decreasing the incidence of unnecessary biopsies. Predictions yielded by the XGboost classifier could serve as a crucial reference for clinical decision-making. However, in the current cohort, no additional benefits of the radiomic classifiers were observed over the combined model of clinical and radiological findings, suggesting the mean ADC+PSAD as the most generalized and optimal choice for quantitative prostate assessment.

Data availability statement

The original contributions presented in the study are included in the article/supplementary material. Further inquiries can be directed to the corresponding authors.

Ethics statement

The studies involving humans were approved by ethics committee of Fuqing City Hospital Affiliated to Fujian Medical University. The studies were conducted in accordance with the local

legislation and institutional requirements. The participants provided their written informed consent to participate in this study. Written informed consent was obtained from the individual(s) for the publication of any potentially identifiable images or data included in this article.

Author contributions

T-HC and Y-SL established the central thrust of our study. Y-YZ and M-LX drafted the manuscript, which was revised by ZX, and L-JD. Y-FL and J-LC analyzed the research data. All authors contributed to the article and approved the submitted version.

Funding

Our study was funded by the Fuzhou Health System Science and Technology Plan Project (2022-S-wq-17) and the Startup Fund for scientific research of Fujian Medical University (No. 2019QH1097).

Acknowledgments

We are extremely grateful for the support and help from our department at the First Affiliated Hospital of Fujian Medical University.

Conflict of interest

The authors declare that the research was conducted in the absence of any commercial or financial relationships that could be construed as a potential conflict of interest.

Publisher's note

References

1. Siegel RL, Miller KD, Fuchs HE, Jemal A. Cancer statistics, 2022. *CA Cancer J Clin* (2022) 72:7–33. doi: 10.3322/caac.21708

2. Siegel RL, Miller KD, Fuchs HE, Jemal A. Cancer statistics, 2021. *CA Cancer J Clin* (2021) 71:7–33. doi: 10.3322/caac.21654

3. Ferlay J, Ervik M, Lam F, Colombet M, Mery L, Piñeros M, et al. *Global cancer observatory: cancer today*. International Agency for Research on Cancer: Lyon, France (2020). Available at: https://gco.iarc.fr/today.

4. Engel H, Oerther B, Reisert M, Kellner E, Sigle A, Gratzke C, et al. Quantitative analysis of diffusion weighted imaging may improve risk stratification of prostatic transition zone lesions. *In Vivo* (2022) 36:2323–31. doi: 10.21873/invivo.12963

5. Pepe P, Garufi A, Priolo GD, Galia A, Fraggetta F, Pennisi M. Is it time to perform only magnetic resonance imaging targeted cores? Our experience with 1,032 men who underwent prostate biopsy. *J Urol* (2018) 200(4):774–8. doi: 10.1016/j.juro.2018.04.061

6. Turkbey B, Rosenkrantz AB, Haider MA, Padhani AR, Villeirs G, Macura KJ, et al. Prostate imaging reporting and data system version 2.1: 2019 update of prostate imaging reporting and data system version 2. *Eur Urol* (2019) 76:340–51. doi: 10.1016/j.eururo.2019.02.033

7. Wang ZB, Wei CG, Zhang YY, Pan P, Dai GC, Tu J, et al. The Role of PSA Density among PI-RADS v2.1 Categories to Avoid an Unnecessary Transition Zone Biopsy in Patients with PSA 4-20 ng/mL. *BioMed Res Int* (2021) 2021:3995789. doi: 10.1155/2021/3995789

8. Oerther B, Engel H, Bamberg F, Sigle A, Gratzke C, Benndorf M. Cancer detection rates of the PI-RADSv2.1 assessment categories: systematic review and meta-analysis on lesion level and patient level. *Prostate Cancer Prostatic Dis* (2022) 25:256–63. doi: 10.1038/s41391-021-00417-1

9. Moldovan PC, Van den Broeck T, Sylvester R, Marconi L, Bellmunt J, van den Bergh RCN, et al. What is the negative predictive value of multiparametric magnetic resonance imaging in excluding prostate cancer at biopsy? A systematic review and meta-analysis from the European association of urology prostate cancer guidelines panel. *Eur Urol* (2017) 72:250–66. doi: 10.1016/j.eururo.2017.02.026

10. Thaiss WM, Moser S, Hepp T, Kruck S, Rausch S, Scharpf M, et al. Head-to-head comparison of biparametric versus multiparametric MRI of the prostate before robot-assisted transperineal fusion prostate biopsy. *World J Urol* (2022) 40:2431–8. doi: 10.1007/s00345-022-04120-1

11. Stabile A, Dell'Oglio P, De Cobelli F, Esposito A, Gandaglia G, Fossati N, et al. Association between prostate imaging reporting and data system (PI-RADS) score for the index lesion and multifocal, clinically significant prostate cancer. *Eur Urol Oncol* (2018) 1:29–36. doi: 10.1016/j.euo.2018.01.002

12. Weinreb JC. Organized chaos: does PI-RADS version 2 work in the transition zone? *Radiology* (2018) 288:492–4. doi: 10.1148/radiol.2018180123

13. Woźnicki P, Westhoff N, Huber T, Riffel P, Froelich MF, Gresser E, et al. Multiparametric MRI for prostate cancer characterization: combined use of radiomics model with PI-RADS and clinical parameters. *Cancers (Basel)* (2020) 12:1767. doi: 10.3390/cancers12071767

14. Wu M, Krishna S, Thornhill RE, Flood TA, McInnes MDF, Schieda N. Transition zone prostate cancer: Logistic regression and machine-learning models of quantitative ADC, shape and texture features are highly accurate for diagnosis. *J Magn Reson Imaging* (2019) 50:940–50. doi: 10.1002/jmri.26674

15. Zhang KS, Schelb P, Kohl S, Radtke JP, Wiesenfarth M, Schimmöller L, et al. Improvement of PI-RADS-dependent prostate cancer classification by quantitative image assessment using radiomics or mean ADC. *Magn Reson Imaging* (2021) 82:9–17. doi: 10.1016/j.mri.2021.06.013

16. Hectors SJ, Chen C, Chen J, Wang J, Gordon S, Yu M, et al. Magnetic resonance imaging radiomics-based machine learning prediction of clinically significant prostate cancer in equivocal PI-RADS 3 lesions. *J Magn Reson Imaging* (2021) 54:1466–73. doi: 10.1002/jmri.27692

17. Kan Y, Zhang Q, Hao J, Wang W, Zhuang J, Gao J, et al. Clinico-radiological characteristic-based machine learning in reducing unnecessary prostate biopsies of PI-RADS 3 lesions with dual validation. *Eur Radiol* (2020) 30:6274–84. doi: 10.1007/s00330-020-06958-8

18. Barentsz JO, Richenberg J, Clements R, Choyke P, Verma S, Villeirs G, et al. ESUR prostate MR guidelines 2012. *Eur Radiol* (2012) 22:746–57. doi: 10.1007/s00330-011-2377-y

19. Jin P, Yang L, Qiao X, Hu C, Hu C, Wang X, et al. Utility of clinical-radiomic model to identify clinically significant prostate cancer in biparametric MRI PI-RADS V2.1 category 3 lesions. *Front Oncol* (2022) 12:840786. doi: 10.3389/fonc.2022.840786

20. Westphalen AC, McCulloch CE, Anaokar JM, Arora S, Barashi NS, Barentsz JO, et al. Variability of the positive predictive value of PI-RADS for prostate MRI across 26 centers: experience of the society of abdominal radiology prostate cancer disease-focused panel. *Radiology* (2020) 296:76–84. doi: 10.1148/radiol.2020190646

21. Ganeshan B, Goh V, Mandeville HC, Ng QS, Hoskin PJ, Miles KA. Non-small cell lung cancer: histopathologic correlates for texture parameters at CT. *Radiology* (2013) 266:326–36. doi: 10.1148/radiol.12112428

22. Liddell H, Jyoti R, Haxhimolla HZ. Mp-MRI prostate characterised PIRADS 3 lesions are associated with a low risk of clinically significant prostate cancer - A retrospective review of 92 biopsied PIRADS 3 lesions. *Curr Urol* (2015) 8:96–100. doi: 10.1159/000365697

23. Xiong H, He X, Guo D. Value of MRI texture analysis for predicting high-grade prostate cancer. *Clin Imaging* (2021) 72:168–74. doi: 10.1016/j.clinimag.2020.10.028

24. Hou Y, Bao ML, Wu CJ, Zhang J, Zhang YD, Shi HB. A radiomics machine learning-based redefining score robustly identifies clinically significant prostate cancer in equivocal PI-RADS score 3 lesions. *Abdom Radiol (NY)* (2020) 45:4223–34. doi: 10.1007/s00261-020-02678-1

25. Li J, Weng Z, Xu H, Zhang Z, Miao H, Chen W, et al. Support Vector Machines (SVM) classification of prostate cancer Gleason score in central gland using

multiparametric magnetic resonance images: A cross-validated study. *Eur J Radiol* (2018) 98:61–7. doi: 10.1016/j.ejrad.2017.11.001

26. Schelb P, Kohl S, Radtke JP, Wiesenfarth M, Kickingereder P, Bickelhaupt S, et al. Classification of Cancer at Prostate MRI: Deep Learning versus Clinical PI-RADS Assessment. *Radiology* (2019) 293:607–17. doi: 10.1148/radiol.2019190938

27. Huang Z, Hu C, Chi C, Jiang Z, Tong Y, Zhao C. An artificial intelligence model for predicting 1-year survival of bone metastases in non-small-cell lung cancer patients based on XGBoost algorithm. *BioMed Res Int* (2020) 2020:3462363. doi: 10.1155/2020/3462363

28. Zhang Y, Feng T, Wang S, Dong R, Yang J, Su J, et al. A novel XGBoost method to identify cancer tissue-of-origin based on copy number variations. *Front Genet* (2020) 11:585029. doi: 10.3389/fgene.2020.585029

29. Sheridan AD, Nath SK, Syed JS, Aneja S, Sprenkle PC, Weinreb JC, et al. Risk of clinically significant prostate cancer associated with prostate imaging reporting and data system category 3 (Equivocal) lesions identified on multiparametric prostate MRI. *AJR Am J Roentgenol* (2018) 210:347–57. doi: 10.2214/AJR.17.18516

30. Lim CS, Abreu-Gomez J, Leblond MA, Carrion I, Vesprini D, Schieda N, et al. When to biopsy Prostate Imaging and Data Reporting System version 2 (PI-RADSv2) assessment category 3 lesions? Use of clinical and imaging variables to predict cancer diagnosis at targeted biopsy. *Can Urol Assoc J* (2021) 15:115–21. doi: 10.5489/cuaj.6781

31. Brancato V, Aiello M, Basso L, Monti S, Palumbo L, Di Costanzo G, et al. Evaluation of a multiparametric MRI radiomic-based approach for stratification of equivocal PI-RADS 3 and upgraded PI-RADS 4 prostatic lesions. *Sci Rep* (2021) 11:643. doi: 10.1038/s41598-020-80749-5

32. Schieda N, Lim CS, Zabihollahy F, Abreu-Gomez J, Krishna S, Woo S, et al. Quantitative prostate MRI. *J Magn Reson Imaging* (2021) 53:1632–45. doi: 10.1002/jmri.27191

33. Tavakoli AA, Hielscher T, Badura P, Görtz M, Kuder TA, Gnirs R, et al. Contribution of dynamic contrast-enhanced and diffusion MRI to PI-RADS for detecting clinically significant prostate cancer. *Radiology* (2023) 306:186–99. doi: 10.1148/radiol.212692

34. Surov A, Meyer HJ, Wienke A. Correlations between apparent diffusion coefficient and gleason score in prostate cancer: A systematic review. *Eur Urol Oncol* (2020) 3:489–97. doi: 10.1016/j.euo.2018.12.006

35. Lim C, Flood TA, Hakim SW, Shabana WM, Quon JS, El-Khodary M, et al. Evaluation of apparent diffusion coefficient and MR volumetry as independent associative factors for extra-prostatic extension (EPE) in prostatic carcinoma. *J Magn Reson Imaging* (2016) 43:726–36. doi: 10.1002/jmri.25033

36. Bonekamp D, Kohl S, Wiesenfarth M, chelb P, Radtke JP, Götz M, et al. Radiomic machine learning for characterization of prostate lesions with MRI: comparison to ADC values. *Radiology* (2018) 289:128–37. doi: 10.1148/radiol.2018173064

37. Drevik J, Dalimov Z, Uzzo R, Danella J, Guzzo T, Belkoff L, et al. Utility of PSA density in patients with PI-RADS 3 lesions across a large multi-institutional collaborative. *Urol Oncol* (2022) 40:490.e1–6. doi: 10.1016/j.urolonc.2022.08.003

38. Galosi AB, Palagonia E, Scarcella S, Cimadamore A, Lacetera V, Delle Fave RF, et al. Detection limits of significant prostate cancer using multiparametric MR and digital rectal examination in men with low serum PSA: Up-date of the Italian Society of Integrated Diagnostic in Urology. *Arch Ital Urol Androl* (2021) 93:92–100. doi: 10.4081/aiua.2021.1.92

39. Roscigno M, Stabile A, Lughezzani G, Pepe P, Galosi AB, Naselli A, et al. The use of multiparametric magnetic resonance imaging for follow-up of patients included in active surveillance protocol. Can PSA density discriminate patients at different risk of reclassification? *Clin Genitourin Cancer* (2020) 18:e698–704. doi: 10.1016/j.clgc.2020.04.006

40. Washino S, Okochi T, Saito K, Konishi T, Hirai M, Kobayashi Y, et al. Combination of prostate imaging reporting and data system (PI-RADS) score and prostate-specific antigen (PSA) density predicts biopsy outcome in prostate biopsy naïve patients. *BJU Int* (2017) 119:225–33. doi: 10.1111/bju.13465

41. Ullrich T, Quentin M, Arsov C, Schmaltz AK, Tschischka A, Laqua N, et al. Risk stratification of equivocal lesions on multiparametric magnetic resonance imaging of the prostate. *J Urol* (2018) 199:691–8. doi: 10.1016/j.juro.2017.09.074

10.3389/fonc.2023.1247682

Appendix

APPENDIX 1 Acquisition Parameters of the Multiparametric MRI Protocol for both institution.

Parameter	T2WI		DWI	
	Institution 1	Institution 2	Institution 1	Institution 2
Echo time (msec)	72	93	72	93
Repetition time (msec)	4000	5960	4000	6900
Flip angle (°)	90	150	–	–
Matrix	128×128	256×256	128×128	256×256
Field of view (mm2)	360×360	160×160	360×360	190×260
Number of slices	36	40	32	40
Slice thickness (mm)	4	3	4	3
spacing between slices	0.5	0	1	0
b-values (s/mm2)	–	–	100/800/2000	50/800/1500

frontiers | Frontiers in Oncology

TYPE Original Research
PUBLISHED 14 March 2024
DOI 10.3389/fonc.2024.1287995

OPEN ACCESS

EDITED BY
Fabio Grizzi,
Humanitas Research Hospital, Italy

REVIEWED BY
Biagio Barone,
Azienda Ospedaliera di Caserta, Italy
Shady Saikali,
AdventHealth, United States
Jeffrey Tuan,
National Cancer Centre Singapore, Singapore

*CORRESPONDENCE
Ming-Xu Da
ldyy_damx@lzu.edu.cn
Feng-Hai Zhou
ldyy_zhoufh@lzu.edu.cn

†These authors have contributed equally to this work

RECEIVED 03 September 2023
ACCEPTED 25 January 2024
PUBLISHED 14 March 2024

CITATION
Zhou C, Zhang Y-F, Guo S, Huang Y-Q, Qiao X-N, Wang R, Zhao L-P, Chang D-H, Zhao L-M, Da M-X and Zhou F-H (2024) Multimodal data integration for predicting progression risk in castration-resistant prostate cancer using deep learning: a multicenter retrospective study. *Front. Oncol.* 14:1287995. doi: 10.3389/fonc.2024.1287995

Multimodal data integration for predicting progression risk in castration-resistant prostate cancer using deep learning: a multicenter retrospective study

Chuan Zhou[1,2†], Yun-Feng Zhang[3†], Sheng Guo[3], Yu-Qian Huang[4], Xiao-Ni Qiao[5], Rong Wang[1,6], Lian-Ping Zhao[3,6], De-Hui Chang[3,5], Li-Ming Zhao[7], Ming-Xu Da[1,2,3*] and Feng-Hai Zhou[1,2,3,8*]

[1]The First Clinical Medical College of Lanzhou University, Lanzhou, China, [2]National Health Commission of People's Republic of China (NHC) Key Laboratory of Diagnosis and Therapy of Gastrointestinal Tumor, Gansu Provincial Hospital, Lanzhou, China, [3]The First Clinical Medical College of Gansu University of Chinese Medicine, Lanzhou, China, [4]Department of Center of Medical Cosmetology, Chengdu Second People's Hospital, Chengdu, China, [5]Department of Urology, The 940 Hospital of Joint Logistics Support Force of Chinese PLA, Lanzhou, China, [6]Department of Radiology, Gansu Provincial Hospital, Lanzhou, China, [7]Department of Urology, Second People's Hospital of Gansu Province, Lanzhou, China, [8]Department of Urology, Gansu Provincial Hospital, Lanzhou, China

Purpose: Patients with advanced prostate cancer (PCa) often develop castration-resistant PCa (CRPC) with poor prognosis. Prognostic information obtained from multiparametric magnetic resonance imaging (mpMRI) and histopathology specimens can be effectively utilized through artificial intelligence (AI) techniques. The objective of this study is to construct an AI-based CRPC progress prediction model by integrating multimodal data.

Methods and materials: Data from 399 patients diagnosed with PCa at three medical centers between January 2018 and January 2021 were collected retrospectively. We delineated regions of interest (ROIs) from 3 MRI sequences viz, T2WI, DWI, and ADC and utilized a cropping tool to extract the largest section of each ROI. We selected representative pathological hematoxylin and eosin (H&E) slides for deep-learning model training. A joint combined model nomogram was constructed. ROC curves and calibration curves were plotted to assess the predictive performance and goodness of fit of the model. We generated decision curve analysis (DCA) curves and Kaplan–Meier (KM) survival curves to evaluate the clinical net benefit of the model and its association with progression-free survival (PFS).

Results: The AUC of the machine learning (ML) model was 0.755. The best deep learning (DL) model for radiomics and pathomics was the ResNet-50 model, with an AUC of 0.768 and 0.752, respectively. The nomogram graph showed that DL model contributed the most, and the AUC for the combined model was 0.86. The calibration curves and DCA indicate that the combined model had a good calibration ability and net clinical benefit. The KM curve indicated that the model integrating multimodal data can guide patient prognosis and management strategies.

Conclusion: The integration of multimodal data effectively improves the prediction of risk for the progression of PCa to CRPC.

KEYWORDS

radiomics, pathomics, castration-resistant prostate cancer, deep learning, multi-modal

1 Introduction

Prostate cancer (PCa) affects men worldwide and is a significant health concern, with a global incidence rate of 13.5% (1). Additionally, the mortality rate of 6.7% makes PCa the fifth leading cause of death among men (2). Androgen deprivation therapy (ADT) is considered the primary treatment modality for men diagnosed with advanced symptomatic PCa, also known as castration-sensitive PCa (CSPC) (3). However, subsequent to the initial favorable treatment response, it is frequently observed in PCa patients that there is a decline in response and eventual progression to CRPC, which is characterized by a dismal prognosis (3). The median duration and mean survival period of patients until progression to CRPC range from 18 to 24 months and 24 to 30 months (4, 5), respectively. The status of the depot condition (testosterone [TST] 50 ng/dL or 1.7 nmol/L) and subsequent disease development (a sustained rise in prostate-specific antigen [PSA] and progression seen in images) are now the two most important criteria for detecting CRPC. However, tailored precision medicine is limited by the use of monomodal indicators such as PSA and serum testosterone (6, 7). The early detection of CRPC can help physicians determine the optimal timing for administering second-line therapies, possibly increasing the survival rate among patients. Predicting the risk of CRPC is an important factor affecting prognosis in patients with severe PCa. There is an urgent need for early diagnosis and precise management of CRPC.

Despite advancements in technology, there are still persistent challenges in accurately detecting, characterizing, and monitoring cancers (8). The assessment of diseases through radiographic methods primarily relies on visual evaluations, which can be enhanced by advanced computational analyses. Notably, AI holds the potential to significantly improve the qualitative interpretation of cancer imaging by expert clinicians (9). This includes the ability to accurately delineate tumor volumes over time, infer the tumor's genotype and biological progression from its radiographic phenotype, and predict clinical outcomes (10). Radiomics, and pathomics have rapidly emerged as cutting-edge techniques to aid and enhance the interpretation of vast medical imaging data, which may benefit clinical applications. The techniques have the ability to directly process images, giving rise to numerous subdomains for further research (11). Clinical outcomes, such as survival, response to treatment, and recurrence, may be accurately predicted using AI models that use multimodal data (12–14). The utilization of radiomics and pathomics exhibits significant promise in enhancing clinical decision-making processes and ultimately enhancing patient outcomes via medical imaging techniques (15–17).

Hence, to effectively and precisely anticipate the likelihood of developing CRPC without invasive procedures. We constructed radiomics and pathomics prediction models based on deep-learning algorithms and investigated their application value in clinical decision-making and the prognosis of PCa. This may allow more accurate prediction of the risk of CRPC and provide a reference for accurate diagnosis and treatment of PCa.

2 Materials and methods

Clinicopathological data from patients with PCa were acquired retrospectively from the electronic medical record system of the three centers (center A; center B; center C) after receiving approval from the ethics committee of the local institution. This retrospective study was also approved by the Ethics Committee of the Gansu Provincial Geriatrics Association (2022-61), and the requirement for informed consent was waived. Our research program was designed based on the AI model of a local institution.

2.1 Participants

We conducted a retrospective study including patients with a pathologically confirmed diagnosis of PCa from the three centers between January 2018 and February 2021. The inclusion criteria were (a) first pathological diagnosis of PCa; (b) use of the same ADT treatment regimen; (c) availability of all MRI scans within 30

Abbreviations: ADC, apparent diffusion coefficient; ADT, Androgen deprivation therapy; AI, Artificial intelligence; AUC, area under the curve; CNN, Convolutional Neural Network; CRPC, castration-resistant prostate cancer; CSPC, castration-sensitive prostate cancer; DCA, decision curve analysis; DICOM, Digital Imaging and Communications in Medicine; DTL, deep transfer learning; DWI, diffusion-weighted imaging; Grad-CAM, The Gradient-weighted Class Activation Mapping; KM curve, Kaplan–Meier curve; LASSO, The least absolute shrinkage and selection operator; LR, logistic regression; MRI, magnetic resonance imaging; PCa, prostate cancer; PFS, progression-free survival; PI-RADS-V2, Prostate Imaging Reporting and Data System Version 2; PSA, prostate-specific antigen; ROI, regions of interest; SVM, support vector machines; T2WI, T2-weighted.

days of PCa diagnosis to exclude confounding effects of medication on measurements; and (d) no missing stained tissue slides. The exclusion criteria were (a) missing clinical information; (b) poor quality of MRI images (inability to identify the specific location of the lesion); (c) poor quality of stained tissue slides (uneven staining); and (d) missing follow-up information.

Clinical data from 399 patients with PCa were collected, including 254 from the Gansu Provincial Hospital (Center A), 112 from the 940 Hospital of Joint Logistics Support Force of Chinese PLA (Center B), and 33 from the Second People's Hospital of Gansu Province (Center C). Figure 1 shows the flowchart for patient recruitment.

2.2 Prostate tumor segmentation

A radiologist (R.W) with 5 years of experience in prostate MRI diagnosis and a urologist (FH.Z) with 30 years of experience in PCa MRI diagnosis were involved in delineating the regions of interest (ROIs). Disagreements regarding individual lesions were resolved after consultation with a third radiologist (LP. Z), and a consensus was attained. The radiologist were unaware of the patients' CRPC status and adhered to the guidelines outlined the Prostate Imaging Reporting and Data System Version 2 (PI-RADS-V2). Once the delineation of the Region of Interest (ROI) was finalized, a random screening of the 11 features extracted from the ADC sequences was performed. Subsequently, Mann-Whitney U tests were conducted on both sets of features to ascertain the presence of any potential bias in the results obtained by the two experts (R.W and FH.Z) during the delineation process. The main sequence parameters of mp-MRI in Supplementary Table 1. The ITK-SNAP software, version 4.0.0 (http://itk-snap.org), was used to annotate the ROIs for each patient from three sequences, including T2-weighted (T2WI), diffusion-weighted imaging (DWI), and apparent diffusion coefficient (ADC). The volume of interest was created by overlapping the ROIs of each patient. To pretrain the DL model, 2-dimensional (2D) ROIs were extracted from the original images of the three sequences by using a clipping tool based on the tumor's 3D segmentation mask. The standard protocol of Digital Imaging and Communications in Medicine (DICOM) is commonly used for managing medical imaging information and related data. To ensure data quality, we standardized it to a resampling format with a resolution of 1 cm × 1 cm × 1 cm and performed N4 bias correction on all images before delineation.

A pathologist (X.Z) selected a histopathological hematoxylin and eosin (H&E) slide (20×10 magnification) of a typical tumor area as the pathological image for the patient. To prevent data heterogeneity, we used Photoshop to adjust each histopathological slide to the same pixel size (640×480) for pretraining the DL model.

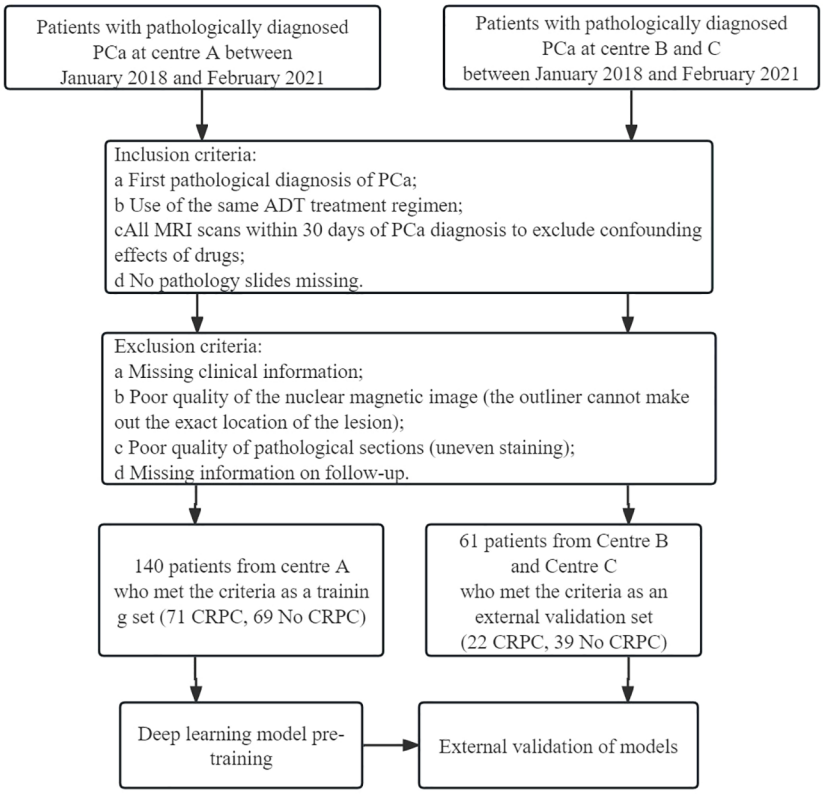

FIGURE 1
Flow chart of patient recruitment. Center **(A)** Gansu Provincial Hospital; Center **(B)** The 940 Hospital of Joint Logistics Support Force of Chinese PLA; Center **(C)** Second People's Hospital of Gansu Province.

Overall, 141 patients from Center A were included in the training group, while 60 patients from Center B and Center C were included in the external validation group for building ML and DL models.

2.3 Signature construction

2.3.1 Radiomics signature construction

PyRadiomics (http://www.radiomics.io/pyradiomics.html) was used for extracting radiomics features. Additionally, the Z-score was employed for dataset standardization ([column−mean]/standard). The method involved using the Spearman correlation coefficient to evaluate the consistency among observers in feature extraction. Features with a correlation coefficient greater than 0.9 were considered reliable and formed a feature set for subsequent analysis. Normalization was performed by subtracting the mean value of each feature and dividing it by the standard deviation. The least absolute shrinkage and selection operator (LASSO) algorithm was used for feature selection and construction, with multiple iterations to assess the importance of each feature. Lastly, ML classifiers, such as logistic regression (LR) and support vector machines (SVM), were utilized to build the predictive models.

2.3.2 DL signature construction

In this study, ResNet-50, ResNet-34, ResNet-18, Vgg19, and other deep transfer learning (DTL) models were used for model pretraining. The number of iterations (epochs) was set to 100, with a batch size of 32. Imagenet was employed as the regularization method. To enhance the interpretability of the model's decision-making process, we applied the Gradient-weighted Class Activation Mapping (Grad-CAM) method for visual analysis of the model. This method utilizes the gradient information from the last convolutional layer of the neural network to generate a weighted fusion of the class activation map. This class activation map highlights the important regions of the classified target image, thereby allowing us to better understand the decision-making principles of the model.

2.3.3 Construction of nomogram

We integrated radiomics models, DL models, and pathomics models to construct a nomogram and investigated the contributions of various modalities in the joint model.

2.4 Model evaluation

To evaluate the predictive performance of the models, we plotted ROC curves for each model and calculated the area under the curve (AUC) values. Decision curve analysis (DCA) curves and calibration curves were used to assess the net clinical benefit and goodness of fit of the joint model. Kaplan–Meier (KM) curves were used to evaluate its relationship with progression-free survival (PFS).

2.5 Statistical analysis

Statistical Package for Social Sciences (SPSS) 23.0 and R statistical software (version 3.6.1 R, https://www.r-project.org/) were used for statistical analysis. The Kolmogorov–Smirnov test was used to evaluate the normality of the measures, and those that conformed to a normal distribution were expressed as $x \pm s$. The measures that did not conform to a normal distribution were expressed as the median (upper and lower quartiles). An independent samples t-test (normally distributed with equal variance) or Mann–Whitney U-test (skewed distribution or unequal variance) was used to compare the measures. Multi-factor LR analysis was used to screen out the independent predictors to construct the prediction model and plot the nomogram. The AUC of the receiver operating characteristics (ROC) was calculated to evaluate the discriminative power of the model. A DCA curve was plotted to compare the clinical value of the model. A p-value of <0.05 indicated a statistically significant difference.

3 Results

3.1 Clinical characteristics

The study flow is shown in Figure 2. A total of 198 patients were excluded for not meeting the inclusion criteria, and 201 patients were included; 93 included patients progressed to CRPC. Statistical analysis revealed no significant differences in clinical features between the training and validation groups (Table 1).

3.2 Feature selection and signature construction

We extracted 2553 radiomic features using PyRadiomics. According to the ROI results presented by the two experts, a random selection of 11 features derived from ADC sequences was subjected to a Mann-Whitney U test. The analysis revealed no statistically significant distinction between the two groups of features (Supplementary Table 2). Seven radiomic features were selected using the LASSO algorithm (Figures 3A–C). Three 2D ROIs with maximum cross-sections were chosen, and different deep-learning models were used for pretraining and external validation. Model evaluation (Table 2) demonstrated that ResNet-50 had better overall performance in the external validation set, with the lowest loss value. This indicates that ResNet-50 had fewer errors during the training process and converged faster than any other Convolutional Neural Network(CNN)model (Figures 4A, B). In terms of model interpretability, each model had distinct attention regions in the samples. In comparison, ResNet-50 had clearer attention regions primarily focused on the internal regions of the tumor, while the tumor regions in the surrounding tissue were not activated (Figure 5). Furthermore, the ResNet-50 model performed better in the ADC sequence among the three sequences (Table 3).

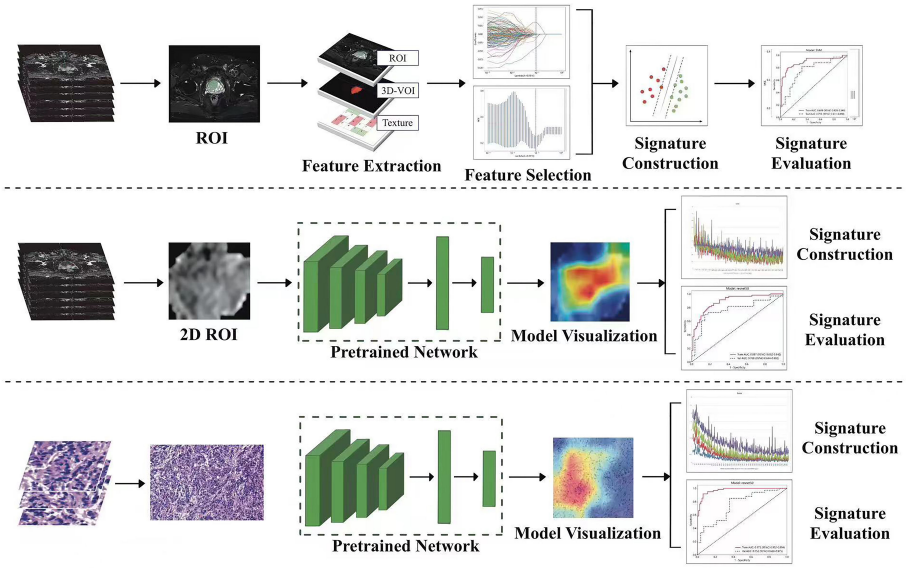

FIGURE 2
Schematic outline of the study. SVM, support vector machine; ROI, region of interest.

TABLE 1 Comparison of clinical data of patients with prostate cancer in the training set and validation set.

Characteristic	Training Set (n=140)	External Validation Set (n=61)	t/Z/X^2 Value	*P* Value
Age			0.000[c]	0.985
≤65	30	13		
>65	110	48		
BMI			0.563[c]	0.755
<25	96	40		
25-30	40	20		
>30	4	1		
BM			0.394[c]	0.530
yes	71	28		
no	69	33		
Gleason Score			0.915[c]	0.822
≤6	4	3		
3+4	15	7		
4+3	13	4		
≥8	108	47		
tPSA	61.99(31.49,100.00)	55.11(29.88,100.00)	-0.357[b]	0.721
Volume	46.30(32.13,67.18)	40.30(29.65,62.99)	-0.939[b]	0.348
PASD	1.11(0.59,1.94)	1.23(0.45,2.05)	-0.302[b]	0.763
ALP	84.00(64.25,130.75)	94.00(70.00,129.00)	-1.002[b]	0.316

(Continued)

TABLE 1 Continued

Characteristic	Training Set (n=140)	External Validation Set (n=61)	t/Z/X^2 Value	*P* Value
Fbg	3.44(2.82,4.36)	3.37(2.88,4.35)	-0.514[b]	0.607
NEUT	3.57(2.91,4.82)	3.57(2.70,4.95)	-0.444[b]	0.657
Lym	1.36(0.93,1.85)	1.38(1.02,1.95)	-0.866[b]	0.386
M	0.44(0.35,0.56)	0.44(0.36,0.57)	-0.381[b]	0.703
Hb	142.00(126.25,154.00)	141.00(125.50,152.00)	-0.499[b]	0.618
PLT	173.50(137.00,215.25)	170.00(144.50,211.00)	-0.070[b]	0.944
SII	753.01±784.31	592.98±480.61	-1.769[a]	0.079
TST	11.20(1.13,18.98)	1.50(1.00,14.75)	-1.737[b]	0.082

a:statistical analysis performed using T-test;b:statistical analysis performed using Mann-Whitney test.c: statistical analysis performed using X^2 test. BMI, Body Mass Index; BM, Bone Metastasis; PSAD, PSA density; ALP, Alkaline phosphatase; Fbg, Fibrinogen; NEUT, Neutrophil; Lym, lymphocyte; M, Monocyte; Hb, Hemoglobin; PLT, Platelet; SII, Systemic immune inflammatory index, SII= PLT* NLR; TST, testosterone.

3.3 Validation of radiomics and pathomics signature

The predictive performance of the models was evaluated using ROC analysis. The best ML model for radiomics was SVM, with an AUC of 0.755 (Figure 6A). For DTL and pathomics, the best model was ResNet-50, with AUC values of 0.768, 0.714, 0.684, and 0.752 (Figures 6B–E). The nomogram graph showed that DTL contributed the most in the combined model (Figure 7), and the AUC of the combined model was 0.86 (Figure 8). Calibration curve

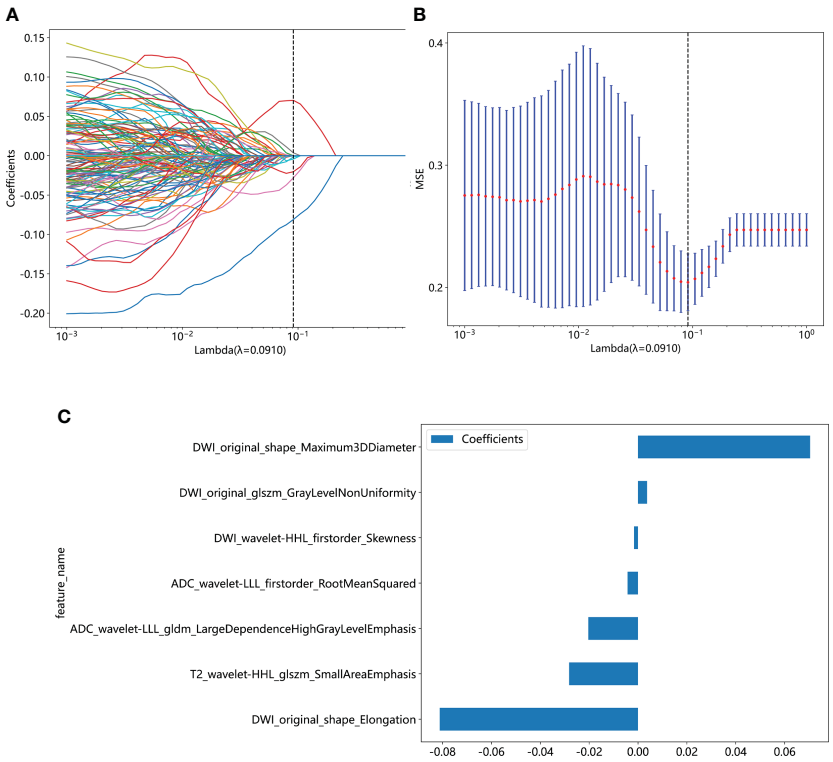

FIGURE 3
(A) Coefficient profiles of the features in the LASSO model are shown. Each feature is represented by a different color line indicating its corresponding coefficient. **(B)** Tuning parameter (λ) selection in the LASSO model. **(C)** Weights for each feature in the model. LASSO, least absolute shrinkage and selection operator.

10.3389/fonc.2024.1287995

TABLE 2 Performance of different DL models.

	Model Name	Acc	AUC	95%CI	Sensitivity	Specificity	PPV	NPV	Precision	Recall	F1	Threshold	Cohort
0	resnet18	0.572	0.643	0.5514-0.7339	0.983	0.226	0.500	0.955	0.500	0.983	0.663	0.154	Train
1	resnet18	0.770	0.810	0.6693-0.9198	0.879	0.643	0.744	0.818	0.744	0.879	0.806	0.471	Test
2	resnet34	0.935	0.978	0.9584-0.9976	0.949	0.929	0.903	0.961	0.903	0.949	0.926	0.465	Train
3	resnet34	0.689	0.698	0.5663-0.8298	0.455	0.964	0.937	0.600	0.937	0.455	0.612	0.502	Test
4	resnet50	0.804	0.887	0.8318-0.9423	0.864	0.759	0.729	0.882	0.729	0.864	0.791	0.382	Train
5	resnet50	0.770	0.768	0.6436-0.8921	0.697	0.857	0.852	0.706	0.852	0.697	0.767	0.515	Test
6	vgg19	0.681	0.709	0.6213-0.7962	0.610	0.734	0.632	0.716	0.632	0.610	0.621	0.444	Train
7	vgg19	0.754	0.728	0.5948-0.8608	0.909	0.751	0.714	0.842	0.714	0.909	0.800	0.508	Test

analysis showed that the joint model has a good fit and strong calibration capability (Figure 9). The DCA curve showed that all models had good clinical net benefit, with the combined model showing higher net benefit (Figure 10).

3.4 Prognosis

In the classification study of CRPC risks, a total of 87 patients experienced tumor progression-related events. The KM curve analysis showed that the joint model suggests significantly lower PFS for patients at high risk of CRPC compared to those at low risk (Figure 11).

4 Discussion

To our knowledge, in this retrospective cohort study conducted across multiple centers, a novel prediction model was developed and validated for the first time. This model integrated radiomics, DTL, and pathomics data to provide strong predictive capabilities in primary prostate cancer progressing to CRPC following two years of ADT. The utilization of multiparametric radiological modeling, as employed in this investigation, may aid urologist in evaluating the probability of CRPC progression and formulating personalized treatment strategies.

The prognosis of CRPC is notably unfavorable, and the challenges in its treatment are diverse among patients (18). The acquisition of reliable data from an initial diagnosis of localized PCa managed with ADT is constrained in clinical practice (19). Previous research has demonstrated a significant correlation between N-glycan score and adverse prognosis in CRPC (20). Additionally, the assessment of skeletal muscle index and skeletal muscle attenuation holds predictive value for the prognosis of metastatic CRPC (21). PSA nadir and Grade 5 were both associated with CRPC progression (22). It was also established that AR-V7 mRNA, significantly predicted biochemical recurrences and CRPC progression (23). However, none of these findings provided specific and prospective indications regarding the likelihood of castration-CRPC progression in patients with PCa. Our approach demonstrated significant predictive performance and provided therapeutic advantage. In addition, the calibration curve and KM survival curve were well-suited for the model and provided useful predictive information for patients with PCa. This finding could potentially be attributed to the multimodal data integration and the selection of suitable AI methodologies.

4.1 Multimodal data integration

Data fusion addresses inference problems by amalgamating data from various modalities that provide different viewpoints on a shared phenomenon (24, 25). Consequently, the integration of multiple modalities may facilitate the resolution of such challenges with

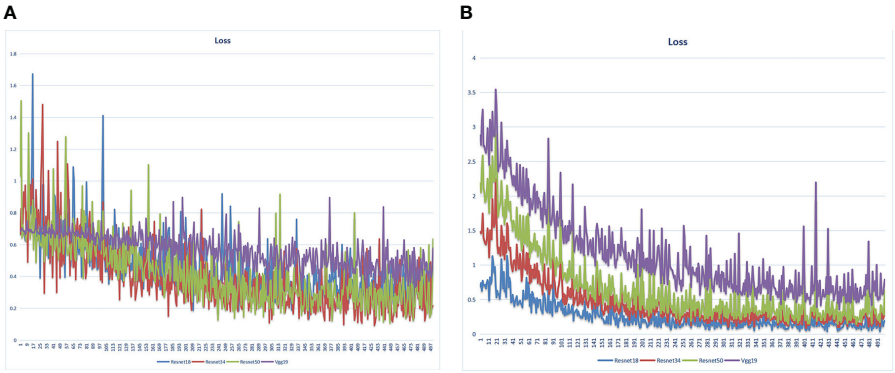

FIGURE 4
Loss value of different DL models in the training set varied with the iteration steps. **(A)** radiomics model **(B)** pathomics model.

greater precision compared to the utilization of singular modalities (26). This is particularly important in medicine, as similar results from different measurement techniques might provide different conclusions (27, 28). In recent years, the growing prevalence of original studies utilizing imaging and pathology images in the field of prostate cancer has created an opportunity for AI technology to demonstrate its potential (29, 30). Additionally, DL approaches have direct applications for segmentation, multimodal data integration and model construction (31).

We used late-stage fusion, also known as decision-level fusion, to train a separate model for each modality and then aggregate the predictions from each model to produce a final prediction. Aggregation can be done by averaging, majority voting, and Bayesian-based rules among other methods (32). During the data collection phase, we found that some of the data were missing and incomplete, while late fusion still maintained the predictive power. Since each model is trained individually, aggregation methods, such as majority voting, can be applied even if one mode is missing. In contrast, if the unimodal data do not complement one another or have weak interdependencies, late fusion may be preferred due to its simpler design and fewer parameters in comparison to other fusion procedures. This is also advantageous in instances with insufficient

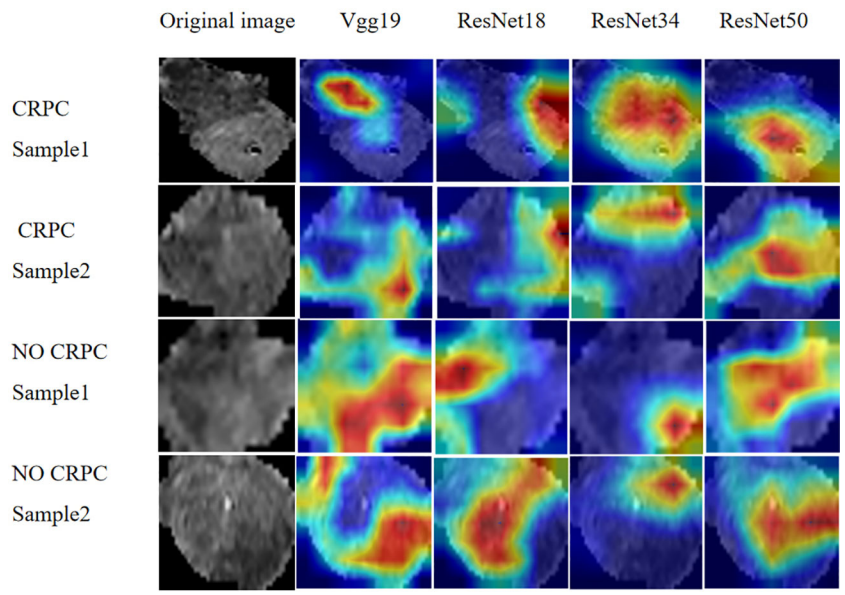

FIGURE 5
Regions of attention in prostate cancer MRI analysis with different DL models. MRI, magnetic resonance imaging.

10.3389/fonc.2024.1287995

TABLE 3 Performance of ResNet-50 in different sequences.

Sequence	Acc	AUC	95%CI	Sensitivity	Specificity	PPV	NPV	Precision	Recall	F1	Thres-hold	Cohort
T2	0.843	0.921	0.878-0.963	0.867	0.825	0.788	0.892	0.788	0.867	0.825	0.405	Train
	0.738	0.684	0.545-0.823	0.758	0.714	0.758	0.714	0.758	0.758	0.758	0.386	Test
DWI	0.686	0.710	0.620-0.799	0.741	0.646	0.606	0.773	0.606	0.741	0.667	0.368	Train
	0.689	0.714	0.584-0.845	0.727	0.643	0.706	0.667	0.706	0.727	0.716	0.534	Test
ADC	0.804	0.887	0.832-0.942	0.864	0.759	0.729	0.882	0.729	0.864	0.791	0.382	Train
	0.770	0.768	0.644-0.892	0.697	0.857	0.852	0.706	0.852	0.697	0.767	0.515	Test

data. In this study, MRI and H&E tissue sections were weakly complementary to each other, and hence our post-fusion model demonstrated good predictive ability. Examples of late fusion include the integration of imaging data with non-imaging inputs, such as the fusion of MRI scans and PSA blood tests for PCa diagnosis (33). Survival prediction using the fusion of genomics and histology profiles by Chen et al. was also performed (34).

4.2 Supervised method

In this study, we selected a supervised AI approach for training radiomics models using radiology image annotations with patient outcomes to input data into predefined labels (e.g., cancer/non-cancer) (35). Since the feature extraction was not part of the learning process, the models typically had more simple architecture and lower computation costs. An additional benefit was a high level of interpretability because the predictive features could be related to the data. In contrast, the feature extraction was time-consuming and could translate human bias to the models. Based on the sample size included in this study, the supervised method was sufficient due to its simplicity and ability to learn from our radiomics model.

Self-supervised techniques effectively leverage accessible unlabeled data to acquire superior image features, subsequently transferring this acquired knowledge to supervised models. Consequently, supervised methods like CNNs are employed to address diverse pretexting tasks, wherein labels are automatically generated from the data (36). Notably, self-supervised methods are particularly well-suited for more robust computational systems and higher-resolution images (37, 38).

4.3 Model selection for DL

DL is the current state-of-the-art ML algorithm, which simulates the connections between the neurons of the human brain. It learns and extracts complex high-level features from the input data through multi-layer neural networks, thus realizing automatic classification, recognition, and prediction of data. Traditional deep CNNs often encounter the issues of gradient vanishing or gradient explosion as the number of network layers increases, leading to challenging model training. ResNet addresses this problem by introducing the concept of residual connections. The structure promotes the flow of gradients and information transfer, thereby facilitating the training of deeper networks. In this study, we selected DL models including ResNet-50, ResNet-34, ResNet-18, and Vgg19 for pre-training. Comparing these models revealed that ResNet-50 outperformed the others. The main advantage of ResNet-50 lies in its ability to effectively train very deep neural networks while avoiding issues such as gradient vanishing and gradient explosion. Consequently, it excels in image classification tasks and can manage large and complex datasets. Due to its versatile application and remarkable performance, ResNet-50 serves as a benchmark model in various computer vision tasks and is widely

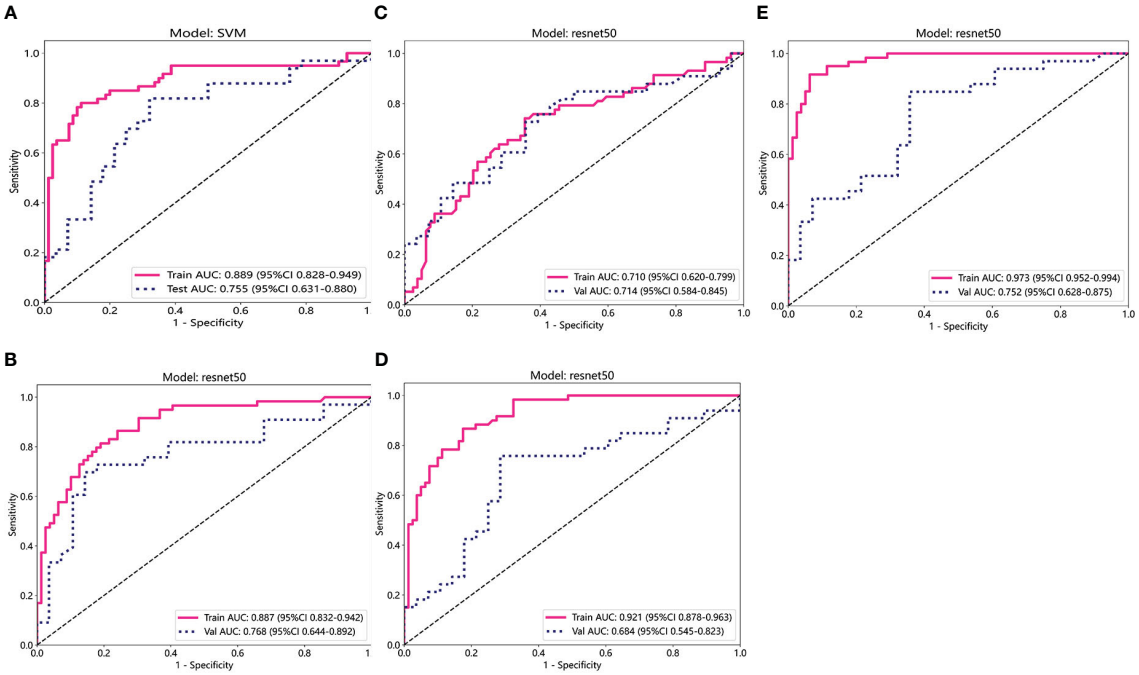

FIGURE 6
ROC curve analysis for each model. **(A)** Radiomics. **(B-D)** DL (ADC, DWI, and T2WI) **(E)** Pathomics. T2WI, T2-weighted imaging; DWI, diffusion-weighted imaging; ADC, apparent diffusion coefficient images; ROC, receiver operating characteristic.

utilized in target detection, image segmentation, and image generation. In Lei et al.'s training study of MRI DL involving 396 patients with PCa, training a DL model for PCa classification using pairs of ResNet-50 anti-paradigms improved the generalization and classification abilities of the model (39). In another pathomics study, texture features captured using the ResNet DL framework were able to better distinguish unique Gleason patterns (40).

4.4 Limitations

The study has limitations. First, this is a retrospective study from a multicenter institution, and potential biases, such as differences in MRI acquisition parameters, are inevitable. However, as mentioned previously, we completed the data alignment and pre-processed the images to minimize the impact of these differences on the results. Second,

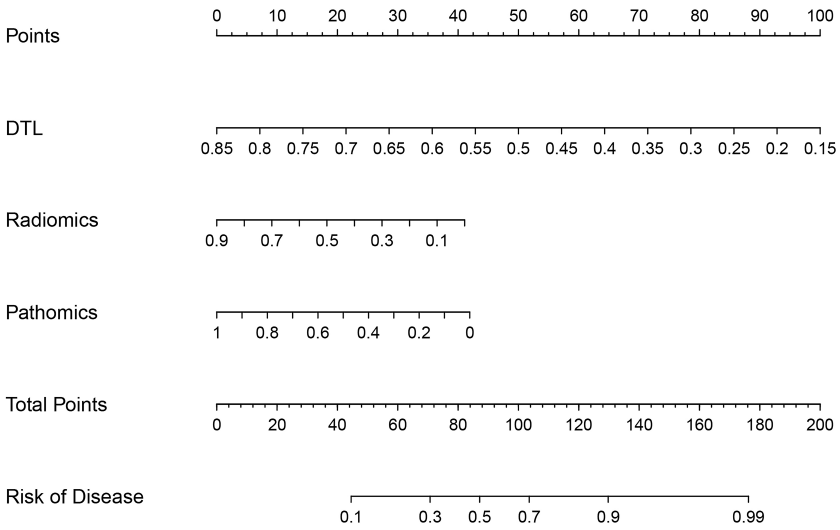

FIGURE 7
Nomodiagram of the combined model.

10.3389/fonc.2024.1287995

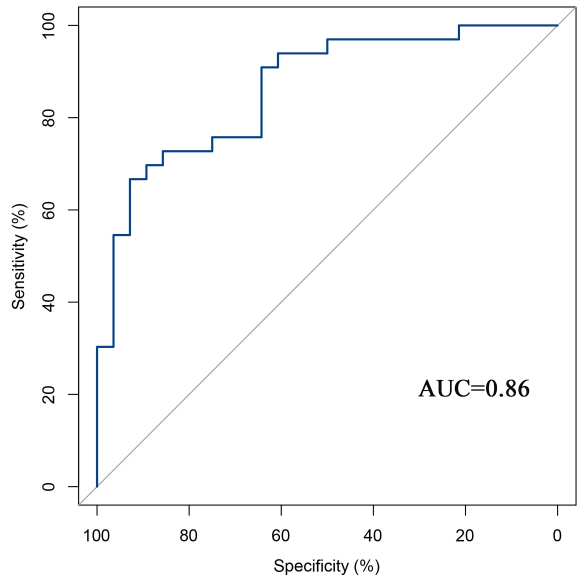

FIGURE 8
ROC curve analysis for the combined model.

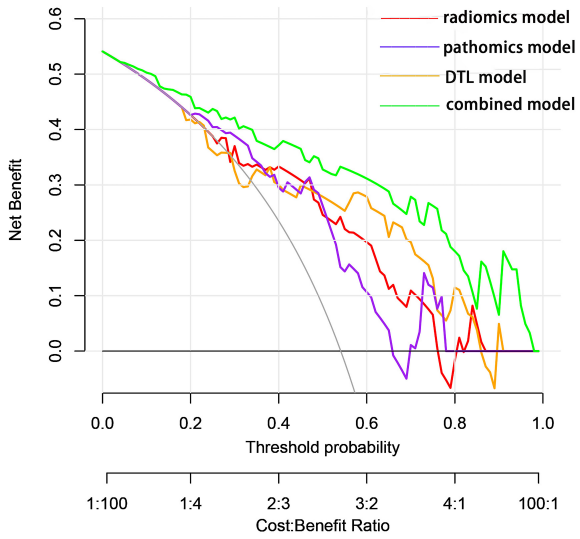

FIGURE 10
Decision curves showed that each model could achieve clinical benefit and that the net benefit of the combined model was better.

key prognostic factors in clinical characterization were not considered in this study due to incomplete clinical data for most patients. Third, our sample size was relatively small, and the number of patients with different Gleason score classifications was unevenly distributed, which may affect the stability and reproducibility of our model. Therefore, the results of this study need to be validated externally using a large sample and a multi-region, multicenter institution in the future.

5 Conclusions

In summary, we collected a multimodal dataset from patients who developed CRPC and used it to develop and integrate radiological and histopathological models to improve CRPC risk prediction. This result encourages to conduct further large-scale studies utilizing multimodal DL.

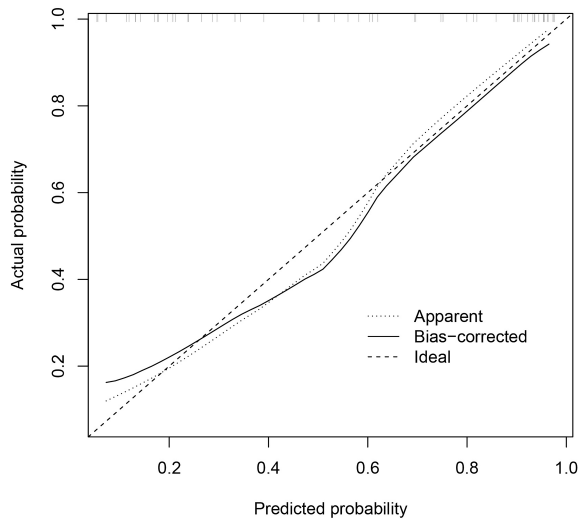

FIGURE 9
Calibration curve of the combined model indicates a better agreement between the predicted probabilities and the actual observed frequencies.

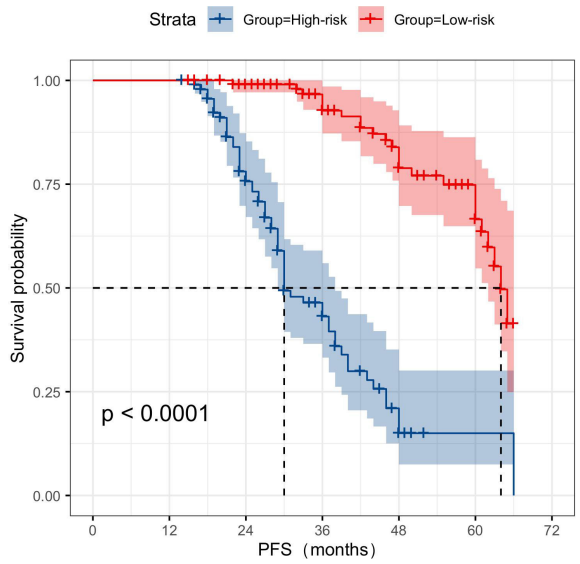

FIGURE 11
KM survival curve analysis demonstrates that multimodal data can serve as a reliable predictor of the risk of CRPC occurrence. CRPC, castration-resistant prostate cancer.

Data availability statement

The original contributions presented in the study are included in the article/Supplementary Material. Further inquiries can be directed to the corresponding authors.

Ethics statement

The studies involving humans were approved by The Ethics Committee of the Gansu Provincial Geriatrics Association (2022-61). The studies were conducted in accordance with the local legislation and institutional requirements. Written informed consent for participation in this study was provided by the participants' legal guardians/next of kin. Written informed consent was obtained from the individual(s) for the publication of any potentially identifiable images or data included in this article.

Author contributions

CZ: Conceptualization, Data curation, Funding acquisition, Investigation, Software, Supervision, Validation, Writing – original draft, Writing – review & editing. Y-FZ: Data curation, Formal analysis, Investigation, Methodology, Software, Validation, Visualization, Writing – original draft. SG: Data curation, Formal analysis, Investigation, Methodology, Software, Writing – review & editing. Y-QH: Data curation, Formal analysis, Investigation, Methodology. X-NQ: Investigation, Methodology, Writing – review & editing. RW: Investigation, Methodology, Writing – review & editing. L-PZ: Investigation, Methodology, Writing – review & editing. D-HC: Resources, Writing – review & editing. L-MZ: Resources, Writing – review & editing. M-XD: Conceptualization, Funding acquisition, Resources, Writing – review & editing, Data curation, Formal analysis, Visualization, Writing – original draft. F-HZ: Conceptualization, Funding acquisition, Resources, Supervision, Writing – review & editing.

Funding

The author(s) declare financial support was received for the research, authorship, and/or publication of this article. This work was funded by grants from the following sources: National Natural Science Foundation of China (No.81860047), The Natural Science Foundation of Gansu Province (No.22JR5RA650), Key Science and Technology Program in Gansu Province (NO.21YF5FA016).

Acknowledgments

We thank for Chinese Medical Association of Gansu Province Geriatrics Society providing guidance and suggestions during the project. We thank for Dr.Yu-Qian Huang contributed to all the Figures in this paper.

Conflict of interest

The authors declare that the research was conducted in the absence of any commercial or financial relationships that could be construed as a potential conflict of interest.

Publisher's note

Supplementary material

The Supplementary Material for this article can be found online at: https://www.frontiersin.org/articles/10.3389/fonc.2024.1287995/full#supplementary-material

References

1. Bray F, Ferlay J, Soerjomataram I, Siegel RL, Torre LA, Jemal A. Global cancer statistics 2018: GLOBOCAN estimates of incidence and mortality worldwide for 36 cancers in 185 countries. *CA Cancer J Clin* (2018) 68(6):394–424. doi: 10.3322/caac.21492

2. Sung H, Ferlay J, Siegel RL, Laversanne M M, Soerjomataram I, Jemal A, et al. Global cancer statistics 2020: GLOBOCAN estimates of incidence and mortality worldwide for 36 cancers in 185 countries. *CA Cancer J Clin* (2021) 71(3):209–49. doi: 10.3322/caac.21660

3. Pernigoni N, Zagato E, Calcinotto A, Troiani M, Mestre RP, Calì B, et al. Commensal bacteria promote endocrine resistance in prostate cancer through androgen biosynthesis. *Science* (2021) 374(6564):216–24. doi: 10.1126/science.abf8403

4. Ryan CJ, Smith MR, Fizazi K, Saad F, Mulders PF, Sternberg CN, et al. Abiraterone acetate plus prednisone versus placebo plus prednisone in chemotherapy-naive men with metastatic castration-resistant prostate cancer (COU-AA-302): final overall survival analysis of a randomised, double-blind, placebo-controlled phase 3 study. *Lancet Oncol* (2015) 16(2):152–60. doi: 10.1016/S1470-2045(14)71205-7

5. Harris WP, Mostaghel EA, Nelson PS, Montgomery B. Androgen deprivation therapy: progress in understanding mechanisms of resistance and optimizing androgen depletion. *Nat Clin Pract Urol* (2009) 6(2):76–85. doi: 10.1038/ncpuro1296

6. Cornford P, van den Bergh R, Briers E, Van den Broeck T, Cumberbatch MG, De Santis M, et al. EAU-EANM-ESTRO-ESUR-SIOG guidelines on prostate cancer. Part II-2020 update: treatment of relapsing and metastatic prostate cancer. *Eur Urol* (2021) 79(2):263–82. doi: 10.1016/j.eururo.2020.09.046

7. Heidenreich A, Bastian PJ, Bellmunt J, Bolla M, Joniau S, van der Kwast T, et al. EAU guidelines on prostate cancer. Part II: Treatment of advanced, relapsing, and castration-resistant prostate cancer. *Eur Urol* (2014) 65(2):467–79. doi: 10.1016/j.eururo.2013.11.002

8. Aerts HJ, Velazquez ER, Leijenaar RT, Parmar C, Grossmann P, Carvalho S, et al. Decoding tumour phenotype by noninvasive imaging using a quantitative radiomics approach. *Nat Commun* (2014) 5:4006. doi: 10.1038/ncomms5006

9. Hosny A, Parmar C, Quackenbush J, Schwartz LH, Aerts H. Artificial intelligence in radiology. *Nat Rev Cancer* (2018) 18(8):500–10. doi: 10.1038/s41568-018-0016-5

10. Boeken T, Feydy J, Lecler A, Soyer P, Feydy A, Barat M, et al. Artificial intelligence in diagnostic and interventional radiology: Where are we now. *Diagn Interv Imaging* (2023) 104(1):1–5. doi: 10.1016/j.diii.2022.11.004

11. van Timmeren JE, Cester D, Tanadini-Lang S, Alkadhi H, Baessler B. Radiomics in medical imaging-"how-to" guide and critical reflection. *Insights Imaging* (2020) 11(1):91. doi: 10.1186/s13244-020-00887-2

12. Lai YH, Chen WN, Hsu TC, Lin C, Tsao Y, Wu S. Overall survival prediction of non-small cell lung cancer by integrating microarray and clinical data with deep learning. *Sci Rep* (2020) 10(1):4679. doi: 10.1038/s41598-020-61588-w

13. Echle A, Grabsch HI, Quirke P, van den Brandt PA, West NP, Hutchins GGA, et al. Clinical-grade detection of microsatellite instability in colorectal tumors by deep learning. *Gastroenterology* (2020) 159(4):1406–1416.e11. doi: 10.1053/j.gastro.2020.06.021

14. Stahlschmidt SR, Ulfenborg B, Synnergren J. Multimodal deep learning for biomedical data fusion: a review. *Brief Bioinform* (2022) 23(2):bbab569. doi: 10.1093/bib/bbab569

15. Wang R, Dai W, Gong J, Huang M, Hu T, Li H, et al. Development of a novel combined nomogram model integrating deep learning-pathomics, radiomics and immunoscore to predict postoperative outcome of colorectal cancer lung metastasis patients. *J Hematol Oncol* (2022) 15(1):11. doi: 10.1186/s13045-022-01225-3

16. Bera K, Braman N, Gupta A, Velcheti V, Madabhushi A. Predicting cancer outcomes with radiomics and artificial intelligence in radiology. *Nat Rev Clin Oncol* (2022) 19(2):132–46. doi: 10.1038/s41571-021-00560-7

17. Bi WL, Hosny A, Schabath MB, Giger ML, Birkbak NJ, Mehrtash A, et al. Artificial intelligence in cancer imaging: Clinical challenges and applications. *CA Cancer J Clin* (2019) 69(2):127–57. doi: 10.3322/caac.21552

18. Xiong Y, Yuan L, Chen S, Xu H, Peng T, Ju L, et al. WFDC2 suppresses prostate cancer metastasis by modulating EGFR signaling inactivation. *Cell Death Dis* (2020) 11 (7):537. doi: 10.1038/s41419-020-02752-y

19. Cheng Q, Butler W, Zhou Y, Zhang H, Tang L, Perkinson K, et al. Pre-existing castration-resistant prostate cancer-like cells in primary prostate cancer promote resistance to hormonal therapy. *Eur Urol* (2022) 81(5):446–55. doi: 10.1016/j.eururo.2021.12.039

20. Matsumoto T, Hatakeyama S, Yoneyama T, Tobisawa Y, Ishibashi Y, Yamamoto H, et al. Serum N-glycan profiling is a potential biomarker for castration-resistant prostate cancer. *Sci Rep* (2019) 9(1):16761. doi: 10.1038/s41598-019-53384-y

21. Lee J, Park JS, Heo JE, Ahn HK, Jang WS, Ham WS, et al. Muscle characteristics obtained using computed tomography as prognosticators in patients with castration-resistant prostate cancer. *Cancers (Basel)* (2020) 12(7):1864. doi: 10.3390/cancers12071864

22. Nakamura K, Norihisa Y, Ikeda I, Inokuchi H, Aizawa R, Kamoto T, et al. Ten-year outcomes of whole-pelvic intensity-modulated radiation therapy for prostate cancer with regional lymph node metastasis. *Cancer Med* (2023) 12(7):7859–67. doi: 10.1002/cam4.5554

23. Khurana N, Kim H, Chandra PK, Talwar S, Sharma P, Abdel-Mageed AB, et al. Multimodal actions of the phytochemical sulforaphane suppress both AR and AR-V7 in 22Rv1 cells: Advocating a potent pharmaceutical combination against castration-resistant prostate cancer. *Oncol Rep* (2017) 38(5):2774–86. doi: 10.3892/or.2017.5932

24. Llinas J, Hall DL. An introduction to multisensor data fusion. *Proc IEEE* (1997) 85(1):6–23. doi: 10.1109/5.554205

25. Iv WCS, Kapoor R, Ghosh P. Multimodal classification: current landscape, taxonomy and future directions. *ACM Computing Surveys (CSUR)* (2021) 55(7):1-3. doi: 10.1145/3543848

26. Durrant-Whyte HF. Sensor models and multisensor integration. *Int J Robotics Res* (1988) 7(6):97–113. doi: 10.1177/027836498800700608

27. Boehm KM, Khosravi P, Vanguri R, Gao J, Shah SP. Harnessing multimodal data integration to advance precision oncology. *Nat Rev Cancer* (2022) 22(2):114–26. doi: 10.1038/s41568-021-00408-3

28. Boehm KM, Aherne EA, Ellenson L, Nikolovski I, Alghamdi M, Vázquez-García I, et al. Multimodal data integration using machine learning improves risk stratification of high-grade serous ovarian cancer. *Nat Cancer* (2022) 3(6):723–33. doi: 10.1038/s43018-022-00388-9

29. Barone B, Napolitano L, Calace FP, Del Biondo D, Napodano G, Grillo M, et al. Reliability of multiparametric magnetic resonance imaging in patients with a previous negative biopsy: comparison with biopsy-naïve patients in the detection of clinically significant prostate cancer. *Diagnostics (Basel)* (2023) 13(11):1939. doi: 10.3390/diagnostics13111939

30. Massanova M, Vere R, Robertson S, Crocetto F, Barone B, Dutto L, et al. Clinical and prostate multiparametric magnetic resonance imaging findings as predictors of general and clinically significant prostate cancer risk: A retrospective single-center study. *Curr Urol* (2023) 17(3):147–52. doi: 10.1097/CU9.0000000000000173

31. Abrol A, Fu Z, Salman M, Silva R, Du Y, Plis S, et al. Deep learning encodes robust discriminative neuroimaging representations to outperform standard machine learning. *Nat Commun* (2021) 12(1):353. doi: 10.1038/s41467-020-20655-6

32. Ramanathan TT, Hossen Md.J, Sayeed Md.S. Naïve bayes based multiple parallel fuzzy reasoning method for medical diagnosis. *J Eng Sci Technol* (2022) 17(1):0472–90.

33. Reda I, Khalil A, Elmogy M, Abou El-Fetouh A, Shalaby A, Abou El-Ghar M, et al. Deep learning role in early diagnosis of prostate cancer. *Technol Cancer Res Treat* (2018) 17:1533034618775530. doi: 10.1177/1533034618775530

34. Chen RJ, Lu MY, Wang J, Williamson D, Rodig SJ, Lindeman NI, et al. Pathomic fusion: an integrated framework for fusing histopathology and genomic features for cancer diagnosis and prognosis. *IEEE Trans Med Imaging* (2022) 41(4):757–70. doi: 10.1109/TMI.2020.3021387

35. Bertsimas D, Wiberg H. Machine learning in oncology: methods, applications, and challenges. *JCO Clin Cancer Inform* (2020) 4:885–94. doi: 10.1200/CCI.20.00072

36. Jing L, Tian Y. Self-supervised visual feature learning with deep neural networks: A survey. *IEEE Trans Pattern Anal Mach Intell* (2021) 43(11):4037–58. doi: 10.1109/TPAMI.2020.2992393

37. Li P, He Y, Wang P, Wang J, Shi G, Chen Y. Synthesizing multi-frame high-resolution fluorescein angiography images from retinal fundus images using generative adversarial networks. *BioMed Eng Online* (2023) 22(1):16. doi: 10.1186/s12938-023-01070-6

38. Eun DI, Jang R, Ha WS, Lee H, Jung SC, Kim N. Deep-learning-based image quality enhancement of compressed sensing magnetic resonance imaging of vessel wall: comparison of self-supervised and unsupervised approaches. *Sci Rep* (2020) 10 (1):13950. doi: 10.1038/s41598-020-69932-w

39. Hu L, Zhou DW, Guo XY, Xu WH, Wei LM, Zhao JG. Adversarial training for prostate cancer classification using magnetic resonance imaging. *Quant Imaging Med Surg* (2022) 12(6):3276–87. doi: 10.21037/qims-21-1089

40. Duenweg SR, Brehler M, Bobholz SA, Lowman AK, Winiarz A, Kyereme F, et al. Comparison of a machine and deep learning model for automated tumor annotation on digitized whole slide prostate cancer histology. *PloS One* (2023) 18(3):e0278084. doi: 10.1371/journal.pone.0278084

Frontiers in Oncology

Advances knowledge of carcinogenesis and tumor progression for better treatment and management

The third most-cited oncology journal, which highlights research in carcinogenesis and tumor progression, bridging the gap between basic research and applications to imrpove diagnosis, therapeutics and management strategies.

Discover the latest Research Topics

See more →

Frontiers

Avenue du Tribunal-Fédéral 34
1005 Lausanne, Switzerland
frontiersin.org

Contact us

+41 (0)21 510 17 00
frontiersin.org/about/contact